GROWTH AND EVOLUTION OF NANOLAYERS OF METAL AND METAL NANOPARTICLES ON SOLID SUBSTRATES

Thesis submitted for the degree of
DOCTOR OF PHILOSOPHY(SCIENCE)

in
PHYSICS

by
MALA MUKHOPADHYAY

Department of Physics
University of Calcutta
August, 2019

To my Family

ACKNOWLEDGEMENT

First of all, I express my sincere gratitude to my thesis supervisor Prof. Satyajit Hazra for his sincere guidance, inspiration and patience through out the research work giving me extraordinary experiences as well as for introducing me to the fascinating field of Surface and Nano Science and the evolving X-ray scattering techniques to probe them. I am very much grateful to him for providing me in depth knowledge base in Synchrotron X-ray scattering techniques. Whatever knowledge I have gained during this period of research regarding the use of X-ray scattering techniques to probe structures of matter is due to him.

I am also indebted to Saha Institute of Nuclear Physics for providing my adequate financial support as Junior and Senior Research Fellowship for the research period of five years and providing me all the facilities which an experimental research student needs. I am also thankful to Department of Science and Technology (DST), Govt. of India for providing me sufficient financial support to perform our experiments at Synchrotron Source.

I would like to thank the former Directors, Prof. M. K. Sanyal and Prof. A. K. Mohanty, and the present Director Prof. Gautam Bhattacharyya, Saha Institute of Nuclear Physics, for giving me the opportunity to work in the institute and utilize its resources and also for providing me all kinds of necessary financial support. I express my sincere gratitude to Prof. Alokmay Datta and Prof. P.M.G. Nambissan for extending the UV-vis spectroscopy facilities, Dr. S.V. Roth for his help in GISAXS measurements at PETRA-III, DESY. I must also thank Dr. B. Satpati for TEM. I would like to thank the Center for Research in Nanoscience and Nanotechnology, University of Calcutta for providing the TEM facility. The

financial supports received from SINP under the DST-DESY project for carrying out experiments at DESY, Germany are thankfully acknowledged.

I thankfully acknowledge Mr. Susanta Banerjee, Mr. Avijit Das, Mr. Goutam Sarkar, Dr. Ramkrishna Dev Das, Mr. Souvik Banerjee, Mr. Syamaprasad Mallik and Mr. Subir Roy for their help in solving different technical difficulties. I am honestly thankful to Mr. Jishnu Basu and all the other members of our workshop for their support in fabricating instrumental accessories for my experimental works. I am thankful to Mr. Mukul Chandra Das and Mr. Subhasish Sanyal for their support in official matters. I will be ever thankful to Mantu-da, Haren-Da and Gobardhan-Da for their wholehearted support in several non-academic routine matters.

I am deeply indebted to my seniors, Ishani-di and Paramita-di, for teaching me the basics of the experimental procedures and helping me out with their invaluable suggestions whenever I asked for it. It is my pleasure to specially acknowledge my friends Moumita, Sushmita, Debasree, Rajeswari, Niyaz and Uttam for the extremely healthy ambience and spontaneous help for professional as well as personal problems. I would like to thank Madhumita for being the first person to teach me how to prepare AuNPs. I will be ever so grateful to my seniors at the Surface Physics and Material Science Division, Maidul-da, Abhishekh-da, Santanu-da, Shirshendu-da, Arpan-da, Shyamal-da, Nupur-di, Tanusree-di and Manjula-di for every little help I have received from them during my Ph.D. days. Special thanks goes to Sumona-di, Sudipta-di and Sruti for being on my side through thick and thin. I want to express my gratitude to all my seniors and juniors fellows in this division for their cooperation and for creating a congenial atmosphere of collective work. I am also thankful to all my friends inside and outside my Institute for their wholehearted support.

I have spent a very good time in SINP hostel and the attitude of the boarders have been very cordial for making “the living” better. I am also thankful to hostel cooks, Shakti-da, Suresh-da and Kartik-da for providing excellent healthy food.

There are, of course, many more people in my division and institute than I have mentioned here, who have helped me in some way or the other during the years I have spent at SINP.

Lastly, I must thank my parents who have been my main motivation for continuing with higher studies and without whose wholehearted support and encouragement I would never have been able to complete my doctoral research.

Kolkata, August 2019 Mala Mukhopadhyay

Table of abbreviations

AFM	Atomic force microscopy
AuNP	Gold nanoparticle
BAM	Brewster angle microscopy
DT-AuNP	Dodecanethiol capped gold nanoparticle
EDP	Electron density profile
FWHM	Full width at half maxima
GID	Grazing incidence X-ray diffraction
GISAXS	Grazing incidence small angle X-ray scattering
LB	Langmuir-Blodgett
LS	Langmuir-Schaefer
MNP	Metal nanoparticle
NP	Nanoparticle
SAM	Self-assembled monolayers
SAXS	Small angle X-ray scattering
SEM	Scanning electron microscopy
SPM	Scanning probe microscopy
SPR	Surface plasmon resonance
STM	Scanning tunneling microscopy
TEM	Transmission electron microscopy
UV-Vis	Ultra violet visible
XR	X-ray reflectivity
XRD	X-ray diffraction

CONTENTS

1 INTRODUCTION 1

1.1 Nanostructures: concept and perspectives . . . 1

1.1.1 Effect of low-dimensionality on physical properties . . . 2

1.2 Metal and MNPs: preliminary concepts . . . 3

1.2.1 Gold nanostructures: an emerging field . . . 4

1.2.2 Historical introduction . . . 4

1.2.3 General background: quantum size effect and application . 5

1.3 Deposition of thin films on solid substrates . . . 7

1.4 Nanolayers of AuNPs . . . 8

1.4.1 Thin films of AuNPs: a short review . . . 8

1.5 Substrate surface . . . 11

1.5.1 Si surface: native oxide . . . 12

1.5.2 Si surface: passivation . . . 13

1.5.2.1 Hydrogen passivation . . . 14

1.5.2.2 OTS passivation . . . 15

1.6 Growth and evolution of self-organised AuNPs nanolayer . . . 16

1.6.1 Growth of highly-ordered assembly of AuNPs . . . 16

1.6.2 Probing order in self-assembled AuNPs layers . . . 19

1.6.3 Reciprocal space information . . . 20

1.6.4 Real space imaging . . . 21

1.7 Our work and the present thesis . . . 22

1.7.1 Goal of the thesis . . . 22

1.7.2 Outline of the thesis . . . 23

2 EXPERIMENTAL SECTION 27

2.1 Si surface cleaning . . . 27

2.1.1 Ultrasonic cleaning . . . 27
2.1.2 RCA cleaning . . . 27
2.2 Substrate surface modification . . . 28
2.2.1 H-Si substrates . . . 28
2.2.2 OTS-Si substrates . . . 29
2.3 Nanolayers of DT-AuNPs . . . 29
2.3.1 Preparation of DT-AuNPs . . . 29
2.3.2 Characterization of AuNPs . . . 31
2.3.2.1 UV-vis spectroscopy . . . 31
2.3.2.1.1 Basic principles . . . 32
2.3.2.1.2 Instrument . . . 33
2.3.2.2 Transmission electron microscopy . . . 34
2.3.2.2.1 Basic principles . . . 35
2.3.3 Thin film deposition techniques . . . 36
2.3.4 Langmuir monolayer . . . 36
2.3.4.1 LB deposition technique . . . 37
2.3.4.2 LS deposition technique . . . 38
2.4 Nanolayers of metal . . . 41
2.4.1 Deposition by magnetron sputtering . . . 41
2.4.1.1 Principle of sputtering deposition . . . 42
2.4.1.2 Instrument . . . 43
2.5 Thin film characterization . . . 44
2.5.1 Microscopic measurement techniques . . . 44
2.5.1.1 Scanning electron microscopy . . . 44
2.5.1.1.1 Basic formalism . . . 45
2.5.1.1.2 SEM instrument . . . 46
2.5.1.2 Atomic force microscopy . . . 47
2.5.1.2.1 Basic principles . . . 48
2.5.1.2.2 Modes of operation . . . 50

(a) Contact mode 50
(b) Non-contact mode 51
(c) Tapping or intermittent-contact mode 52
2.5.1.2.3 Details of AFM used in present experiments 53
2.5.1.2.4 Statistical analysis of images 53
3 X-RAY SCATTERING TECHNIQUE 56
3.1 X-ray reflectivity 56
3.1.1 Dynamical theory of X-ray scattering 57
3.1.2 Fresnel reflection from a flat surface 59
3.1.3 XR from a heterogeneous multi layered system 62
3.1.4 Scattering from rough interface 63
3.1.5 Resolution function 66
3.1.6 Kinematical theory or Born approximation 68
3.1.7 Data correction 69
3.2 Off-specular scattering or diffuse scattering 70
3.2.1 Born approximation 71
3.2.1.1 Bare substrate interface 73
3.2.2 Grazing incidence small angle X-ray scattering 74
3.2.2.1 Resolution limit along q_y-direction in GISAXS . . . 78
3.3 Fitting of data and modelling 79
3.4 X-ray scattering instrument 80
3.4.1 Versatile X-ray diffractometer 81
3.4.2 Synchrotron X-ray sources 83
3.4.2.1 General principles 83
3.4.2.2 P03 beamline at PETRA III 85
4 STRUCTURE OF SINGLE-TRANSFERRED DT-AUNPS LS FILMS AND GROWTH OF LANGMUIR MONOLAYERS 87
4.1 Introduction 87
4.2 Experimental details 90

4.2.0.1 Size of DT-AuNPs from UV-vis and TEM 90
4.2.1 Preparation of DT-AuNPs/H-Si LS films 91
4.2.2 Characterization of DT-AuNPs/H-Si LS films 91
4.3 Results and discussion 93
4.3.1 Out-of-plane structure from XR 93
4.3.2 In-plane structure from GISAXS 94
4.3.2.1 GISAXS line profiles 97
4.3.3 Topography from SEM 105
4.3.4 Topography from AFM 105
4.3.5 Structures of LS and Langmuir films 108
4.4 Conclusions 111
5 INTERFACIAL AND THERMAL ENERGY DRIVEN GROWTH AND EVOLUTION OF LS MONOLAYERS OF DT-AUNPS 113
5.1 Introduction 113
5.2 Experimental details 116
5.2.1 Preparation of DT-AuNPs LS films 116
5.2.2 Characterization of DT-AuNPs LS films 116
5.3 Results and discussion 117
5.3.1 AFM and topography 117
5.3.2 XR and EDPs 117
5.3.3 EDP: time dependence 122
5.3.4 Growth and evolution: control mechanism 127
5.4 Conclusions 132
6 EVOLUTION OF LIGANT-CAPPED NANOPARTICLE MULTILAYERS TOWARD A NEAR UNIQUE THICKNESS 133
6.1 Introduction 133
6.2 Experimental details 135
6.2.1 Preparation of *m*T−DT-AuNP/H-Si LS films 135
6.2.2 Characterization of *m*T−DT-AuNP/H-Si LS films 135

6.3 Results and discussion . . . 137
6.3.1 XR studies of the as-grown films . . . 137
6.3.2 GISAXS studies of the as-grown films . . . 139
6.3.3 XR studies of the films after a month . . . 141
6.3.4 XR studies of the films after a year . . . 143
6.3.5 Growth and stability of *m*T−AuNP/H-Si LS films . . . 147
6.3.6 Evolution toward a near unique thickness . . . 149
6.4 Conclusions . . . 152
7 X-RAY RADIATION INDUCED STRUCTURAL MODIFICATION OF THIOL-COATED AU-NANOPARTICLE LS FILMS 154
7.1 Introduction . . . 154
7.2 Experimental details . . . 156
7.2.1 Preparation of DT-AuNP/H-Si LS films . . . 156
7.2.2 Characterization of DT-AuNPs/H-Si LS films . . . 157
7.3 Results and discussion . . . 159
7.3.1 GISAXS studies of the films . . . 159
7.4 Conclusions . . . 165
8 GROWTH AND EVOLUTION OF GOLD NANOLAYERS ON NATIVE OXIDE COATED SI SUBSTRATES 166
8.1 Introduction . . . 166
8.2 Experimental details . . . 167
8.2.1 Preparation of Au/O-Si films . . . 167
8.2.2 Characterization of Au/O-Si films by XR . . . 168
8.3 Results and discussion . . . 168
8.3.1 XR studies of the as-grown films . . . 168
8.3.2 Au/O-Si nanolayers within a day . . . 168
8.3.3 Au/O-Si nanolayers after sixth months . . . 171
8.3.4 Au/O-Si nanolayers after AR-treatment . . . 174
8.4 Conclusions . . . 174

9 SUMMARY 176
9.1 General conclusions 176
9.2 Scope for future studies 177
Publications 179

1

INTRODUCTION

1.1 Nanostructures: concept and perspectives

"Nanoscience and technology will change the nature of almost every human-made object in the 21^{st} century" [1]. Nanoscience is defined as the study of low dimensional systems or nanomaterials which demonstrate properties that are sometimes completely different from the bulk one. Nanomaterials are essentially materials whose dimension in one, two or in all three directions is reduced to nanometer length scale and accordingly can be nanolayers (2D), nanowires or nanorods (1D) and NPs or nanodots (0D) [2, 3].

Nanoscience has provided immense weightage to the areas of design, characterization, production and application of structures, devices and systems by controlling shape and size at the nanometer (nm) length scale [4]. Among these low dimensional systems, nanolayers grown on semiconductor substrates have received much attention due to their significant importance in different device applications such as electronics, optoelectronics, biosensors, catalysis, integrated circuits, etc. [5–7]. Also the nanolayers are ideal system to study physics of 2D-system. The nanolayers can be grown as a thin film of a single material or an assembly/organization of NPs. Structure of the layer can be modified and even can be made smooth by incorporation of certain layer at the film-substrate interface. This suggests that the structure of overlayer or nanolayer is strongly dependent on the nature of the underlying substrate surface where it is grown. That means both the substrate surface and the nanolayer-substrate interface plays significant role in the growth and stability of the overlayer.

The growth and structure or morphology of such nanolayers and their stability or evolution can be different for each other, which are very important for their novel properties and related applications [8, 9]. For example, the growth and structure of initial nanolayers of simple metals on semiconductor substrates can be layered (wetted) or island (dewetted), textured or nontextured, having sharp or interdiffused interface [10–12]. The evolution of such structures with time is expected to be different. Similarly, the growth and structure i.e. the initial organization of very stable NP can be different: it can have different interparticle-separations, different correlation lengths (to form domains of different size and shape) and even different networks. Such organization can even change with time. The collective properties of the NPs strongly depend on this organization and thus needs special attention [13, 14].

1.1.1 Effect of low-dimensionality on physical properties

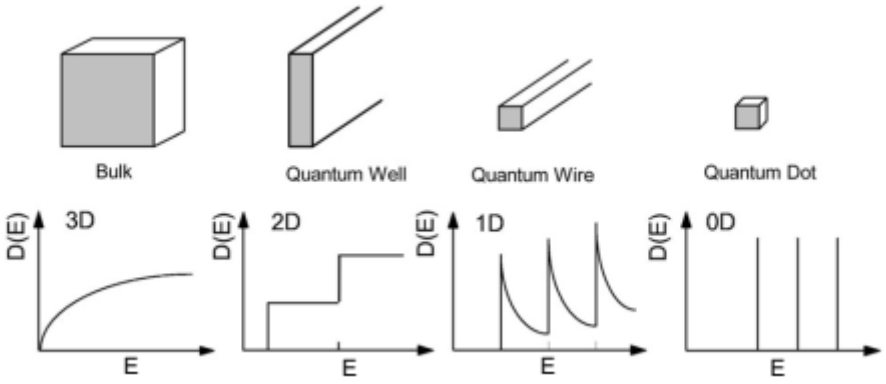

Figure 1: Dimensionality of structures and corresponding density of states. [15]

As the dimensions of materials are reduced down to the nanoscale their properties often change from that of their bulk counterparts. Nanomaterials have a larger surface area to volume ratio as the radius decreases. Since a larger proportion of its atoms are located on the surface of the nanomaterial/AuNP than is the case for a larger particle, it becomes more chemically reactive compared to the bulk one resulting in enhanced electrical properties. At low dimension the quantum affects dominates affecting the optical and magnetic properties of

materials as well [2–4]. Thus particle size, composition and topology are the three parameters that determine electronic, magnetic, and optical properties.

NPs includes metallic, carbon based, semiconducting, magnetic, polymeric and hybrid NPs [16–22]. Till date many research has been performed in the field of NPs structure fabrication, assembly, and utilization. Many other morphologies such as nanowires, nanorods, nanocapsules, nanofibers, nanotubes [23] and nanocomposites, having at least one component with nanoscale dimensions, can be achieved by using synthetic methods. Example of this hybrid material i.e. nanocomposites is polymers with either inorganic NPs or CNTs [24] which exhibit enhanced properties. Thin solid films, such as Langmuir–Blodgett films (LBFs) [25], SAMs [26, 27], two-dimensional supramolecular assemblies [28, 29] and Nanopatterned surfaces [30] are the other examples of nanostructured materials. Monolayer graphene [31], is the extreme limit of nanoscaling which possesses great electrical and mechanical properties [32].

1.2 Metal and MNPs: preliminary concepts

MNPs are important in technology not only by giving a higher number density of molecules at the surface but also by preserving the nanodimension of the cluster in case of monolayer-protected metal clusters such as amines, alkanethiols and various polymers, including conjugated polymers [33, 34]. Generally, MNPs with different sizes and shapes like spheres, rods, and pyramids, possess different properties [35, 36]. Spherical NPs are explored widely due to ease of synthesis procedure. They can be obtained in both homogeneous aqueous phases (using reducers as citrate and borohydride or amines) and aqueous/organic phases [16, 36].

Among different MNPs, Noble MNPs is very sensible to the environment. Due to this sensibility, it has been broadly investigated and used for chemical and biological sensing as MNPs dispersions, arrays of different geometries and

even single NP [37, 38]. Noble MNP is also best known for it's SPR property which originates due to collective resonant oscillation of conduction electrons under optical excitation. This oscillation is directly related to the size, shape and arrangements of NPs as well as on local dielectric environment [39]. The size and shape of the MNPs, deposited upon solid substrates, by thermal evaporation and electrodeposition [40, 41] can't be controlled effectively.

So to precisely control the shape and size of the particle, the as-synthesized MNPs are self assembled upon solid substrates. But the drawback of this method is poor control over the interparticle packing distance and lack of reproducibility, which may lead to loss of near-field coupling effect [42]. Langmuir–Blodgett technique has been used widely for AuNP/nanosheet assembly [43, 44] to build up NP monolayer films with precisely-controlled NP density and interparticle distance.

1.2.1 Gold nanostructures: an emerging field

1.2.2 Historical introduction

There are old materials used by ancient Chinese and Egyptians in the fifth or fourth century BC. There are also evidences showing that ancient Romans used gold colloids to stain glass red or mauve. However, modern nanotechnology was founded with the discovery of ruby AuNPs and the reversible color change of the thin films of these AuNPs upon mechanical compression reported by Michael Faraday in 1857 [45]. Many efforts have been devoted for tailoring the properties of AuNPs for specific applications. Different synthetic routes, such as Turkevich method, Brust method, Perrault method and many other newly created approaches [45–49] have been used to control the morphology, solubility, surface functionality and stability of AuNPs.

AuNPs are very stable metal colloids and have a number of fascinating properties. Due to these reasons the application of AuNPs is increasing day by

day. Throughout history, soluble gold colloids have been used for the treatment of various diseases such as tumors, epilepsy, and for the detection of syphilis, with varying degrees of success and for coloring ceramics and glass, [46]. The Purple of Cassius is a gold-colloid-based coloring agent for enamel and glass popular in the 17th Century. Research concerned with AuNPs underwent a renaissance in the early 1950's. AuNPs have been most intensively studied for the past 10 years as revealed from a number of review artic1es [46, 50, 51], published on this topic.

1.2.3 General background: quantum size effect and application

It has been predicted that due to quantum-mechanical effects, NPs (diameter range 1-10 nm which is intermediate between the molecular size and that of the bulk metal one) would display electronic structures, reflecting the electronic band structure of the NPs. The resulting physical properties are completely different from both the bulk metal nor those and the molecular compounds. The properties/nature of the NP strongly depend on it's size and shape, interparticle distance, nature of the capping agent (the organic shell) [52]. As the particle size decreases the de Broglie wavelength of the valence electron reaches to the same order and the particle behaves as a 0D quantum dot (or box). Due to this quantum size effect, electrons show a characteristic collective oscillation frequency, resulting into the so-called plasmon resonance band (PRB). For AuNPs (5-20 nm-diameter range), PRB is observed near 530 nm. The pioneering work by Schmid and co-workers on well-defined phosphine-stabilized gold clusters showed the properties of quantum-dot particles for the first time [53, 54].

The existence of the plasmon band in AuNP systems has been exploited for many potential applications, especially in the fields of sensors and biology. One example is the functionalization of AuNPs with oligonuc1eotides [55]. DNA-formed assemblies of AuNPs have been used as a colorimetric detector of DNA hybridization, based on the sensitivity of the plasmon band resonance to aggregation which results to a red shift of the SPR peak. Also due to this size-dependent

quantization effect, single-electron transitions can be observed between a tip and NP when thermal energy fluctuation is small enough. AuNPs, having quantum confinement properties, possess an interesting The optoelectronic properties which make them good candidate for electronics and photonics applications [56–59]. Most of the current AuNP applications are based on their inherent electronic and optical characteristics. These arise mainly from the quantum size effect present in NPs [60].

In NPs, a gap exists between the valence band and the conduction band, unlike in bulk metals. The energy level spacings can also change with temperature resulting in a large variation of electrical and optical properties. This made the NPs great practical interest for applications (transistors, switches, electrometers, oscillators, biosensors, catalysis) [61–64]. AuNPs have been reported to be used as sensors to detect organic vapours and ions [65–68]. The mechanism behind the sensing is that the NPs bind to the ions of interest in a bidentate fashion and changing the solution colour [69]. In case of the vapour sensors, electrical resistance of the AuNP films changes after the solvent vapours absorption [66, 70]. For alkylthiol coated gold and silver NPs in Langmuir films [71, 72] reversible metal-insulator transitions have been reported under ambient conditions.

Another fascinating property of AuNPs lies in the accommodation of different redox states. The transition from metal-like capacitive charging to redox-like charging was observed with alkanethiolate-AuNPs of low dispersity in an electrochemical setup for Coulomb staircase experiments [73] where additional peaks have been observed in controlled atmosphere and reduced temperature conditions. Thus, AuNPs behave as delocalized redox molecules, well known in inorganic and organometallic electrochemistry similarly as transition metal clusters and bi-sandwich complexes.

Arrays of closely spaced AuNPs on substrates being potential candidate for wave guides in optical devices have been explored theoretically and experimentally as [57, 58]. The coherent propagation of energy along the array of NPs [56]

occurs due to the coupling of the plasmon band resonance between adjacent NPs. For preparation of non-linear optical devices [74, 75], AuNPs dispersed in glass materials have also been studied also. Although gold is known to be a stable metals (mostly inert to oxidation), AuNPs act as good catalysts in absorption reactions such as CO oxidation, NO reduction, CO_2 hydrogenation and catalytic combustion of methanol [76, 77].

1.3 Deposition of thin films on solid substrates

The properties of a thin film of a given nanostructured material depend on the film's real structure which mainly varies due to deposition procedure. Commonly known as "bottom-up" and "top-down" methods are used for formation of nanostructures.

In "top-down" [78] strategy, the various kind of lithography techniques are used to pattern materials having long-range order. On the other hand, bottom-up is used in different methods of molecular synthesis, colloid chemistry [46], polymer science [79], and related areas to produce structures having nanometer length scale. Top-down lithography techniques now reach the sub-micron scale, but metallic and semi-conductor NPs can bridge the 1-100 nm gap.

NPs are a bottom-up alternative to top-down fabrication methods such as lithography techniques vastly used in semiconductor industry. One particular challenge lies in the organization of NPs into controlled architectures in 1D, 2D, and 3D. Three types of ultrathin films used for such potential applications are LB Films [80], SAM [81] and two-dimensional supramolecular assemblies [29].

Top-down approaches are good for producing structures with long-range order and for making macroscopic connections, while bottom-up approaches are best suited for assembly and establishing short-range order at nanoscale dimensions. In the process of bottom-up approach the physical forces operating at nanoscale i.e., hydrogen bonding, van der Waals, electrostatic, $\Pi - \Pi$ interactions,

hydrophilic–hydrophilic, and hydrophobic–hydrophobic plays important role for self assembling and combining basic units to larger stable structures which leads to thin film deposition. So, both of the strategies have advantages along with disadvantages. Despite the practical importance, the fundamental understanding of surface and interface phenomena is rather slow, as the progress of surface science is taking shape through trial-and-error empirical approaches. This is due to the complexity of studying the surface-interface phenomena.

1.4 Nanolayers of AuNPs

1.4.1 Thin films of AuNPs: a short review

AuNPs have been deposited extensively to grow thin films on various kinds of substrates. Different solid substrates are reportedly used as base materials for thin film deposition of nanostructured Au such as Si [82],various molecular silicon substrates [83], TiO_2 [84], $BaTiO_3$ [85], $SrTiO_3$ [86], Al_2O_3 [87]. The aim of depositing AuNPs on various surfaces has been physical studies [88, 89] as well as derivation of SAM [90]. Among all, the Au/Si interface, being the most studied metal-semiconductor contact [91–103], is a model system for investigating the Schottky-barrier formation as well as the nature of p-d hybridization process [97, 98]. Although, Au is a very stable, non reactive noble metal, and yet it has been reported to be very reactive with complex behaviour on a Si surface even when deposited at room temperature. Researchers have also used ammonium salts [104], and various forms of carbon ([60] fullerene [105], nanotubes [106], and diamond [107]) for depositing Au nanolayers especially AuNPs.

AuNPs have been manipulated to form highly ordered 1D [108, 109], 2D [110], or 3D [111, 112], nano networks and superstructures [113, 114]. Thin films of AuNPs have been prepared using various methods [115–121]. Formation of AuNPs monolayers has been reported at the liquid interface [122] and also from the gas phase [123]. There are many reports of the preparation, characterization,

and study of AuNPs dispersed within mesoporous silica, $Au@SiO_2$ [124, 125] such as, 2- and 5-nm AuNPs have been inserted to mesoporous silica materials by the Somorjai group [126].

Films of AuNPs linked with alkanedithiols have been deposited on nanoporous supports. Heat treatment of these AuNPs dispersed into thin films also have been studied [127]. The Brust-Schiffrin method has been used typically by most of the groups to synthesize alkanethiol-stabilized AuNPs [16]. This two-phase reduction method has triumphed over many other alternatives because of its simplicity.

AuNPs experience both long range vdW attractions and short range steric repulsion, after solvent evaporation. [128–130]. Such complex interaction leads to the formation of self-assembled disk-like islands of monolayer height around different points, which on further compression formed a thermodynamically stable 2D-network of buckled or flipped disk-like islands. [131] Thiol-capped AuNPs (DT-AuNPs) have been reported to form self-assembled 2D structures, [46, 132, 133] due to the complex balance of long range van der Waals (vdW) attractions and short range steric repulsion of the DT-AuNPs[134–137] initiated by solvent evaporation. [128–130] Such 2D structures formed at air/water interface, known as Langmuir monolayers, can be readily transferred onto a solid substrate using LB and LS techniques to grow uniform nanostructures over large areas [133, 138–141] compared to the other deposition techniques. In that sense, separation between particles and their local ordering as well as long-range ordering and/or connectivity become very important, especially for the preparation of organized structures in large areas.

Understanding and controlling the final structures of the films on solid substrates, which actually decide the new collective phenomena arising from interparticle coupling effects, [46, 138, 142] are of utmost importance for their practical uses. There is growing interest for the assembly and study of AuNPs on silanized glass plates [121, 143]. The LB films on hydrophilic Si substrates show nanopatterns formation due to drying mediated agglomeration of AuNPs in presence

of hydrophobic-hydrophilic interaction between thiols and substrate. [144] The LS films on carbon coated grids have been studied mainly using TEM, which show the ordering of the AuNPs. It is known that the hydrophobic strength of the substrate can be tuned through termination or passivation of the substrate, differently, which essentially modifies the surface free energy or contact angle. [145, 146]

Optical microscopy or BAM has been used to monitor the structures of such films in the micrometer length scales [147, 148] while the scattering, especially GISAXS has been used mainly to monitor the particle arrangement and the interparticle separation. In some cases, the presence of islands or domains have been predicted indirectly from the width of the interparticle separation peak [149, 150] or from the analyzed correlation length, [151] as expected. [152]

However, the complete structures of the Langmuir films (i.e. the size of the islands and their separation or connectivity) at different surface pressure (Π) have never been evident clearly, which is particularly important for the small size AuNPs where the long range van der Waals (vdW) attraction is weak compare to the thermal energies.

Also, no systematic work has been carried out to compare the structures of the DT-AuNPs LS films grown on different hydrophobic (strength) substrates as well as to find out and compare the structural stability/instability of the films at ambient condition. The ambient conditions can change the passivation of the substrate with time, even in presence of a film, which in turn can influence the structure of the film. For examples, oxide layer has been found to grow on Si substrates by replacing the passivated H, Br or Cl atoms, in presence of metal (Au, Ag), metal-organic (NiA LB) or organic-inorganic (CTAB-silica) nanolayer films to change the film-structures. [146] Also, the ambient condition can directly change the structure of the film, through oxidation (due to ambient oxygen), interdiffusion (due to ambient pressure), fluctuation, diffusion or reorganization (due to room temperature thermal energy or solvent evaporation), etc. For

examples, oxidation of metal nanolayers, such as Fe, Cu, Ni, etc. are very common, while interdiffusion of Au inside H-Si substrate and reorganization of DT-AuNPs on O-Si substrate have been reported, [153] all of which lead to the change in the film-structure with time at ambient condition.

It is well known that the long keeping time of any transferred film may cause some structural changes (toward energy minimum state) as the transfer process itself is not always carried out under equilibrium conditions. The multilayers of AuNPs formed on the hydrophobic substrates become thermodynamically unstable. As found from previous reports, the instability in Au nanolayer arises due to the presence of room-temperature thermal energy, kT (where k is the Boltzmann constant and T is the room temperature) [91], due to the degradation of thiols at ambient conditions [154, 155] and also due to the change in the substrate surface energy, $\Delta\gamma$ [156], which induces diffusion in the AuNPs. So, finding the energy minimum state or structure and understanding the actual process involved in the evolution of differently deposited nanolayer films are very important also.

1.5 Substrate surface

Among different semiconductor substrates, Si is the widely popular and most studied substrate for its versatile use in the microelectronics industry, most notably as transistors, precisely because of the way its surface oxide leads to unique electrical properties [157]. The removal of surface oxide by wet chemical surface passivation technique is as important as oxidation for the development of the microelectronic industry [158] and facilitating the attachment of nanolayers critical for optoelectronic devices, sensors, etc. [6, 7].

Substrate surface is modified through different ways; passivation by different elements like H, Br, Cl, etc. [91, 159–161] and also creating atomically thin layer. Sometimes self-assembled monolayer (silane) is grown also as a

substrate treatment. Thus changing the free energy or polarity of the surface, the hydrophilic-hydrophobic nature of the surface can be tuned [91, 162, 163]. To make the substrate more hydrophobic prior to film deposition either a self-assembled monolayer (silane) is deposited on the substrate surface as well as wet chemical process is used to make a surface hydrophobic. In many cases HF treatment is done to prepare a hydrophobic Si surface. In the following we will give a brief review of such Si surface.

1.5.1 Si surface: native oxide

Silicon oxides can be categorised into different classes such as native oxide, thermal oxide, chemical vapor deposition (CVD) oxide and anodized oxide. Here growth of native oxide on Si substrate will be discussed. Native oxide grows spontaneously on a clean silicon surface exposed in an ambient environment (air or water). Native oxide, being inert in most solutions, allows the silicon surface to be used as an electronic material in processing and application. The presence of native oxide controls precisely the thickness and quality of very thin gate oxides and gives an increase in contact resistance. The control of native oxide growth rate on Si surfaces is of great importance in the fabrication of ultra-large scale integrated devices, especially with a decrease in pattern dimension.

Silicon surface has a large number of dangling bonds which are very unstable due to lack of electron pairing. As a result a clean Si surface is normally very reactive toward the atoms, molecules or particles, coming in contact with the surface. Oxygen (given in Table 1) present in the ambient condition reacts with these bonds and saturate them forming a very thin native oxide layer. The thickness of the native oxide films formed in water is similar to that in air, ranging from 5 to 10 Å. The thickness, coverage and growth rates of native oxides depend on substrate surface condition and the environmental conditions.

Table 1: The covalent atomic radii (R_a), the electronegativity (δ) in Pauling scale, the bond-energy (DB) with Si and the bond-length (BL) with Si for different elements. [165]

Element	R_a (Å)	DB (kJ/mole)	LB (Å)	δ
Si	1.11	222	2.33	1.90
O	0.73	452	1.63	3.44
H	0.37	318	1.48	2.20
Cl	0.99	381	2.02	3.16
F	0.71	565	1.60	3.98

1.5.2 Si surface: passivation

Surface passivation has been found to be an absolutely essential process, for example, in the manufacturing of microdisk lasers [164]. Silicon surfaces are chemically passivated to prevent contamination between processing steps. In this technique, the Si surface is rendered chemically passive by terminating the bonds on the surface with selective atoms or groups like, -OH, -H, -Cl, etc. Different routes are used to passivate Si surface like gas phase reactions in ultra high vacuum (UHV) condition and wet chemical process. The second one is the most easy and popular because of many applications in semiconductor industry. Si substrates being extremely sensitive to the environment (due to the presence of broken bonds at the surface) when exposed into the air it readily covered by very thin native oxide layer. The reactivity of the clean Si surface when operated in ambient condition, can be dramatically lowered by saturating the surface with monovalent atoms such as H, Br or Cl specially. Such passivated surfaces are expected to be non-reactive since all surface atoms achieve nearly ideal coordination. But after a certain time interval, these surfaces again start to react with oxygen in ambient condition.

Passivated by different materials and their stability depends on many factors like the relative electronegativity (δ), bond-energy (DB) with Si and the atomic size (Ra). Values of such parameters, obtained from different sources (essential in the description of passivation mechanism) are listed in the Table 1.

1.5.2.1 Hydrogen passivation

When etched by hydrofluoric acid (HF), clean Si surface is terminated by a single hydrogen layer that effectively prevents oxidation and chemical contamination of the substrate. In this process, the native oxide layer is first removed and then the substrate surface is predominantly terminated by hydrogen atom. Since the number of dangling bonds are different for (100) and (111) Si surface the H-passivation mechanism is different. The ideal (100) Si surface tends to be terminated by SiH_2 but for (111) it is by SiH or SiH_3. Although, the Si(111) surface can be made atomically smooth with an ideal H termination in buffered HF solutions but the technologically important Si(100) surfaces becomes atomically rough upon HF etching. The coexistence of mono-, di-, and even trihydride species are found to be less stable toward contamination/reoxidation in air [162]. Since the late 1980s it has been well accepted that a Si surface is H-terminated instead of having F- bonded to the Si atoms when immersing in HF solution.

Although the mechanism has not been completely understood, the etching process of SiO_2 from a Si surface can be described in the following steps: Firstly, the oxide layer is rapidly dissolved and forms SiF_2^{-6} ions in HF solution and the surface becomes temporarily F-terminated. Though the Si-F bond energy (DB, given in Table 1) is very large but F-termination is not stable. Because of the large electro negativity of F compared to Si, Si-F bond polarizes the Si-Si back bonds [166] which allows the insertion of HF into the Si-Si bond leading to fluorination of the surface silicon atoms and hydrogenation of the second-layer silicon atoms. As a result, H-terminated Si surface is formed as shown schematically in Fig. 2 with the removal of the surface silicon atom as SiF_4.

The freshly prepared H-passivated Si substrate is hydrophobic in nature [162]. Further, the stability of H-terminated Si(100) and (111) surfaces stored in air has been studied [166, 167]. When stored in ambient condition, the water present in air is predominantly involved in the oxidation of surface Si atoms. The native oxide again starts to grow when most of the surface Si atoms are oxidized.

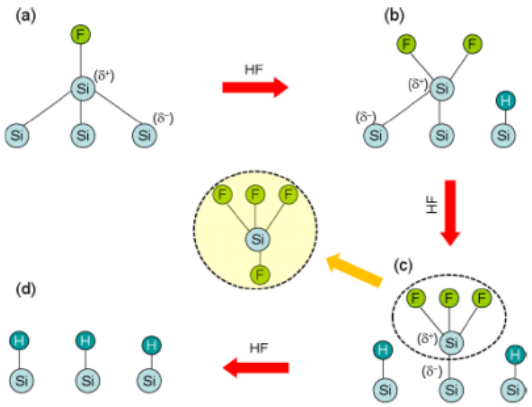

Figure 2: Schematic of hydrogen passivation mechanism of Si surface by HF. [165]

1.5.2.2 OTS passivation

Different organic compounds are used to form SAM on silicon surface. Monolayers of long aliphatic chains such as alkanethiols and alkyltrichloro or alkyltrialkoxysilanes [168, 169], have received much attention due to their stability and resistance to various perturbing conditions. Alkanethiols are used mainly for metallic surfaces but alkyltrialkoxysilanes/alkyltrichloro are used for hydroxylic materials such as glass/silica based substrates [170, 171]. Thus the passivating compounds are chosen based on the nature of the substrate surface. Octadecyltrichlorosilane (OTS) is the most extensively used surface active reagent for creating SAMs on different types of substrates [172, 173].

The true mechanism by which OTS interacts with a hydroxylic surface is complex ant still an area of research. The commonly accepted process comprises of three steps. Initially, the chloro moieties of OTS are hydrolyzed to produce silanetriol. Then, they physisorb onto the Si surface and they finally form Sisilane–O–Sisilane and Sisilane–O–Si via hydrogen bonding and cross-linked covalent bonds [80]. However, Angst-Simmons and Britcher et al proposed a slightly different mechanism [174, 175]. They proposed that the hydrolysis of the chloro groups on OTS occurs in the bulk solution instead of the substrate surface. The surface coverage of OTS depends on several variables like temperature, reaction time, nature of the solvent, degree of hydration of the substrates,

pretreatment of the substrate surface, pH of the environment, as well as the nature and morphology of the oxide layer on the substrate [80, 168]. Researchers found that a full-coverage layer of OTS cannot be fully cross-linked [172, 176] and greater packing densities of OTS on silica based substrates could be achieved with bicyclohexyl or toluene as solvent in comparison with hexadecane [177].

1.6 Growth and evolution of self-organised AuNPs nanolayer

1.6.1 Growth of highly-ordered assembly of AuNPs

Attempts have been made to assemble NPs in two-dimensional structures by a variety of methods like (i) self-assembly of the particles during solvent evaporation [178], (ii) immobilization by covalent attachment at the surface of the SAM [179], (iii) surface modified polymers [180], (iv) electrophoretic assembly onto suitable substrates [181], (v) electrostatic attachment to Langmuir monolayers at the air–water interface [182–184], (vi) air–organic solvent interface [185], (vii) diffusion into ionizable fatty lipid films [186, 187] and (viii) spin coating [188]. The degree of control over molecular-level organization of amphiphiles and ions that may be exercised at the air–water interface has resulted in its extensive use in the organization of large inorganic ions [189, 190], and biological macromolecules [191, 192].

Fendler and co-workers first demonstrated that surface-modified hydrophobic colloidal NPs may also be organized at the air–water interface more specifically, on the surface of water and that multilayer films of the NPs could be formed on suitable substrates by the LB technique [193]. A number of other groups have now used this method to form multilayer films of AuNPs [72, 194–196], polymer-capped platinum colloidal particles [197].

Compared to lithographic patterning, bottom-up selfassembly of MNPs into 2D arrays is a more cost effective and widely used approach to prepare chip-size substrates with sub-10 nm inter-particle spacing for efficient SERS sensing [198, 199]. With the creation of <10 nm inter-particle spacing, high electromagnetic field enhancements are achieved more easily over large areas in the assembled structures [199]. Among numerous assembly techniques developed to assemble MNPs into ordered arrays [200–202], an efficient way to create monolayers of NPs is using the air–water interface through either Langmuir–Blodgett or Langmuir–Schaefer techniques.

Chemically synthesized highly monodisperse NPs are in the core of many novel and emerging applications [203, 204]. One of their fascinating properties is the ability of spontaneous self assembly into large arrays that offers an accessible route to design regular macroscopic NP layers [129, 202, 205]. In particular, freely floating self-assembled NP layers at the air/ water interface also known as the NP Langmuir films in analogy to the molecular Langmuir films attract permanent attention. They offer an easy and uncomplicated way to obtain large scale self-assembled templates of nanomaterials. For example, the NP templates of plasmonic NPs provide a key to enhanced power conversion efficiency of future solar cells or may serve as unique substrates for the surface enhanced Raman scattering spectroscopy.

The LB technique, a room temperature deposition process, may be used to deposit monolayer and multilayer films of organic materials permitting the manipulation of organic molecules on the nanometer scale. Thus intriguing superlattice architectures are assembled [206]. Using this technique, nanolayer of soft materials are grown on semiconductor substrates which have huge potential applications in variety of fields such as sensors, corrosions, photoresists and in the studies of non-linear optics. These ordered arrays of oriented amphiphilic molecules may be useful as insulating or patterning layers in microelectronics, as model systems for studies of 2D phases and as molecular templates for protein

crystallization. The potential of LB films for these applications is sensitive to the details of their molecular packing; in particular, they require that the layers have a defect-free, periodic structure.

Structure of soft nanostructured materials like LB films is strongly related to two main factors: (i) the structure or order of the starting Langmuir monolayer and (ii) the substrate-surface condition where it is transferred. The structure of the Langmuir monolayer can be tuned by changing the surface pressure. As the LB/LS film deals with the amphiphilic molecules having both hydrophobic and hydrophilic parts or spherical hydrophobic NPs, its structure can be modified by changing the nature of the substrate surface. As mentioned before, such modification of surface can be easily done by passivation through wet chemical reaction as discussed in 1.5.2. Furthermore, growth of SAM on the Si surface [26, 81] can modify the nature of the substrate surface. This is the well known technique. But in some work [172, 173], the wet chemical passivation technique has been used to modify the growth of LB films. However, not much work has been carried out to investigate the structure and stability of LB films on wet chemically passivated or terminated Si surface.

Ordering of insoluble monolayers of amphiphilic molecules or hydrophobic NPs on air/water interface leads to wrinkled/buckled patterns. The SAM organization is governed by the growth equations [207] as well as the experimental parameters associated with the process. The interplay of several interfacial forces [208, 209] are the driving force for assembling complex, gradually evolving structures or patterns. Researchers studied different systems and concluded differently about the reason behind generation of ordering in the system. Hydrodynamic mechanisms like Marangoni effect is a popular phenomena driven by surface tension gradients that induce instabilities in the liquid films. Maillard et. al. reported the formation of micrometer rings and hexagonal arrays made of nanocrystals of different sizes, shapes and materials [210] by controlling the solvent evaporation rates. Self assembly formation governed kinetically [129] as

well as coalescence of nearest nucleation sites [211] was reported. Stephan Herminghaus et. al. studied emerging structures in liquid crystal and liquid metal films, similar to those found for spinodal decomposition in mixtures [212]. The de wetting proceeds via unstable surface waves on the liquid. Coexistence of different kinds of ordering/ patterning reported by Stannard et. al. indicates a sharp transition in dewetting mechanism depending upon the deposition conditions as well as chemical potential [213]. Schneider et. al. reported [214] a surface dynamics governed by a substrate strain mediated spinodal decomposition mechanism leading to pattern formation in organic monolayer.

1.6.2 Probing order in self-assembled AuNPs layers

For a precise characterization and structural property measurements of self-assembled AuNPs is absolutely essential. To find out the growth, structure and ordering of self-assembled nanostructures ; the real space (through microscopy measurements) and reciprocal space information (through scattering measurements) have been investigated to realize and understand the processes involved in growth and evolution of nanolayer films. Further, by investigating systematic changes in the parameters effecting the self-assembling processes using real as well as reciprocal-space measurement techniques, the optimal value of the relevant parameters, that lead to improved, defect-free fabrication of SAM, can be determined.

The structures of the Langmuir films of DT-AuNPs have been studied using microscopy and scattering techniques. Optical microscopy or BAM has been used to monitor the structures of such films in the micrometer length scales [147, 148] while the scattering, especially GISAXS has been used mainly to monitor the particle arrangement and the interparticle separation. In some cases, the presence of islands or domains have been predicted indirectly from the width of the interparticle separation peak [149, 150] or from the analyzed correlation length, [151] as expected [152]. However, the complete structures of the Langmuir films (i.e.

the size of the islands and their separation or connectivity) at different surface pressure (Π) have never been evident clearly, which is particularly important for the small size AuNPs where the long range van der Waals (vdW) attraction is weak compare to the thermal energies. The structures of the LB and LS films of DT-AuNPs have also been studied directly. The LB films on hydrophilic Si substrates show nanopatterns formation due to drying mediated agglomeration of AuNPs in presence of hydrophobic-hydrophilic interaction between thiols and substrate. [144] The LS films on carbon coated grids have been studied mainly using TEM, which show the ordering of the AuNPs.

Previous reports confirm the evolution of DT-AUNPs under thermal treatment in solutions from the smaller-sized to larger-sized nanocrystals with the integrity of the final encapsulating shell structures maintained and formation of the long-range ordering of the thiolate-encapsulated nanocrystals [215–217].

1.6.3 Reciprocal space information

The reciprocal space measurements are done mainly on the basis of scattering techniques, using the statistically averaged information over a large area (compared to the dimension of nanostructured units) of the specimen under consideration. Being powerful and non-destructive tool, scattering techniques are used to probe the structure in both plane and our of plane direction. Electrons, photons, neutrons or ions are used as the probing agent depending on the type of information that needs to be extracted from the specimen. It is mandatory that the wavelength of the incident radiation or particle be comparable to the periodicity of the material structure in real space.

X-rays, because of the higher penetration depth, provide detailed structural information about the buried interfaces and multilayers. Electrons and neutrons are also used in microstructural characterization in a manner similar to X-rays. Pradeep et. al. studied the dynamics of alkyl chains in monolayer-protected Au and Ag clusters and silver thiolates using neutron scattering technique [218].

X-rays are surface sensitive at a low angle of incidence. The self-affine in-plane interfacial correlation function for LB multilayers have been observed by Gibaud et al using x-ray scattering [219]. Fukuto et. al. studied the Langmuir films of gold nanoparticles derivatized with acid-terminated alkylthiol chains using X-ray scattering such as XR, GID and reported formation of 2D hexagonal structure with only short-range order. [149] Grazing incidence geometry makes the X-rays sensitive to the in plane structure by its low penetration depth below the critical angle and plays a crucial role for studying structure and ordering of the films [159, 161]. Specular XR and GISAXS techniques have been used extensively in our measurements. XR [220, 221] is the most powerful and non-destructive tool to investigate the structure of the thin films. Analysis of XR profiles provides an EDP, i.e., in-plane (x-y) average electron density (ρ) as a function of depth (z) [161]. Film thickness, electron density, and interfacial roughness are estimated from the EDP. Thus information about surface and interface of nanolayer/Si systems are extracted in angstrom resolution [222] and also the evolution of the structure. Details regarding the X-ray scattering technique and the theoretical formalism of scattering will be discussed in Chapter 3.

1.6.4 Real space imaging

Real space imaging, done mainly based on imaging or microscopic techniques, provides information about the structure of a small area of the specimen under investigation. The most widely used real space imaging techniques are TEM, AFM and SEM. The direct image of the structure obtained from these microscopy techniques includes defects or mixtures of different structures during growth.

In a TEM, high energy electrons (typically 20-200 keV) are used to obtain images of the sample in both direct imaging mode as well as from diffraction patterns for crystalline samples [223]. Hazra et. al. measured the size of DT-AuNPs by TEM [153]. In a Scanning Electron Microscope (SEM) the energy of the electrons are lower (about 10-50 keV) than those used in a TEM. The

SEM operates by detecting the secondary electrons emitted from the sample surface and the the contrast provides the local surface morphology [224]. Li et al [225], used X-ray diffuse scattering and AFM to obtain the interfacial correlation function of LB films of different thickness. Muszynski et. al. presented AFM image of a graphene sheet modified with gold nanoparticles [226]. The AFM is quite versatile and simply by changing the material and configuration of the tip, different characteristics of the sample can be investigated [227, 228].

1.7 Our work and the present thesis

1.7.1 Goal of the thesis

In this thesis work, the primary objective is to study the initial morphology or structure of deposited nanolayers (of simple metals such as Au or of NPs such as thiol capped Au NPs, etc.) on solid substrates and its evolution to understand and control the growth of interesting low dimensional structures, using recently developed powerful scattering techniques, namely XR [229, 230] grazing incidence XRD and GISAXS) [231] with complementary real space imaging techniques, namely AFM, STM and SEM.

Indeed, formation of 2D-network of disk-like islands in the thiol-coated AuNPs (DT-AuNPs) LS films on H-Si substrates is clearly evident from the GISAXS and AFM measurements [161]. Such study also infers that the growth of DT-AuNP Langmuir films is through networked disk-like islands, the size and networking of which increases while the interparticle separation decreases or increases due to further interdigitation or buckling. Evolution in the out-of-plane structures of the LS films with time in ambient conditions is evident from XR techniques, which is due to room-temperature thermal energy and/or substrate surface instability. Evolution in the in-plane structures of the LS films with time under X-ray radiation is evident from GISAXS techniques, where within disk-like islands relatively large correlation appear in expense of original particle-particle

correlation due to the growth of AuNPs. In case of Au nanolayers on O-Si substrates, the thickness of the interdiffused Au layer (which is Gaussian shaped in nature) [91] is found to vary with the deposition conditions.

We have used the TEM, SEM and AFM extensively for characterization as well as measurements of our samples. The working principle, basic design, modes of usage and relevant theoretical aspects of TEM and AFM will provided in details in Chapter 2. X-ray scattering combined with surface imaging techniques like SEM, AFM etc. promises better understanding of growth, structure and evolution of nanolayer/Si system and deeper insight into the processes related or responsible to those.

1.7.2 Outline of the thesis

This thesis has been divided into nine chapters including the Introduction (**Chapter 1**).

Chapter 2 is devoted to the brief description of the experimental techniques and instruments used during the period of this dissertation for synthesis, characterization and fabrication of thin films of nanostructured materials. This includes the basic working principle and a brief outline of the instrumentation. The major experimental techniques,viz. X-ray scattering and SPM techniques, have been elucidated in details.

Chapter 3 is based on the theoretical formalism behind X-ray scattering which has been used extensively in our case to probe structure of matter in a precise and nondestructive manner, the major scattering techniques used in our experiments to probe both out-of-plane and in-plane structuring for surfaces/interfaces and the modeling and fitting of data to extract usable information from such scattering techniques.

Chapter 4 to **Chapter 6** present the original research as published in the 3 peer reviewed journal publications with some relevant explanatory material. **Chapter 4** is based on the ordering and pattern formation in transferred monolayers

of AuNPs and addresses the complex nature of morphology and structure of a deposited monolayer of AuNP on a solid substrate from water surface. Systematic X-ray scattering and AFM measurements give insight into the gross in-plane and out-of-plane morphological structuring. The microscopic details about the in-plane structural symmetry in monolayers of AuNPs, transferred from water surface to solid substrate using LS technique, is discussed using synchrotron X-ray scattering as well as complimentary microscopic techniques. The results demonstrate the formation of monolayers, made of networked disk-like islands (as evident from GISAXS and AFM). The size of islands (ξ or ξ_h) increases with the increase of Π-value. The islands are again made of DT-AuNPs, self-assembled into hexagonal-like close pack with inter-digitization. The average separation between DT-AuNPs (d) either decreases or increases with Π-value depending upon the competitive effects of packing and flipping due to compression. The observed structures of the LS films, at least in the initial stages, can be considered to represent the structures of the Langmuir films, which are of immense importance not only for the understanding of the self-assembly process of AuNPs at air-water interface but also for their use as template to grow nanodevices with interesting properties arise from collective phenomenon.

Chapter 5 addresses the ordering in hydrophobic nanolayers at variously passivated silicon surfaces. The effects of hydrophobic strength of the substrate and ambient conditions on the structures and stability of DT-AuNP LS films were monitored using the XR technique for the formation of controlled 2D-structures on solid substrates through a single transfer LS process. The results provide initial coverages of the monolayer films on different substrates. At ambient conditions, all films evolved with time to change the initial film-thickness. But finally, all the films formed nearly similar vertically expanded monolayer structures, though the evolution paths are different, which is quite interesting and requires further investigation.

Chapter 6 deals with the structural evolution of multi-transferred LS films of AuNPs on H-passivated Si substrates have been investigated using XR and GISAXS techniques. The observation reveals that the number of layers transferred onto the substrate is proportional to the number of transfer but the coverage of the layer decreases considerably with the increase in the number of layer. Such fractional coverage multilayered structures are quite unstable at ambient conditions. The instability mainly arises from three factors: (i) the room-temperature thermal energy (kT) induced fluctuation, (ii) the change in substrate surface energy ($\delta\gamma$) induced repulsion and (iii) the dissimilar film-substrate and film-air interfacial interactions induced attraction toward substrate. Such instability, in one hand, creates hindrance in the control and formation of desired 3D-nanostructures through bottom-up approach. On the other hand, same instability decreases the film-thickness and tries to form a near unique thickness (NUT) through reorganization of AuNPs for different duration.

Chapter 7 is based on X-ray radiation evolution of thiol capped AuNPs. The structural evolution of single-transferred LS films of AuNPs on H-passivated Si substrates under the synchrotron irradiation have been investigated using GISAXS techniques. The GISAXS measurements were carried out using intense x-ray beam of small divergence (from P03 beamline of Petra-3) to enhanced in-plane resolution limit and by shifting the sample in-plane to minimize the effect of beam induced damage. Initially at $t \approx 0$, the films are predominantly of monolayer structures made of networked disk-like islands which are made of self-assembled and close packed DT-AuNPs as revealed from the eartier studies described in Chapter 4. But during irradiation the AuNPs melts to form cluster of larger size. The dimension of the newly developed clusters is almost same for LS films deposited at different Π values. The growth of new correlated clusters almost saturates after a characteristic time as well as the melting rate also follows linear path after a certain characteristic time. All the films shows a certain phase transition after a particular time interval of starting the irradiation process.

In **Chapter 8** the growth and evolution of Au nanolayers on native oxide coated Si surfaces have been presented. The Au/Si interfaces for Au nanolayers deposited at different power and time duration using magnetron sputtering technique have been studied by using XR technique. The result obtained from EDP shows formation of sharp interface of inter diffused Au layer between Au/Si system. The interface shows interesting evolution with time for a fixed deposition power. The nature and thickness of the interface investigated for a fixed deposition time and different wattages as well as for a fixed wattage and different time duration. The origin behind such evolution has been discussed in this chapter.

Chapter 9 concludes the thesis with a brief summary of the major experimental findings from our experiments to investigate ordering and pattern formation in self-assembled nanostructured materials.

2

EXPERIMENTAL SECTION

In this chapter we will discuss in details about the sample preparation and their characterization. Basic principles of the techniques involved in the work have been portrayed together with brief description of the instrumentation.

2.1 Si surface cleaning

2.1.1 Ultrasonic cleaning

Cleaning of sample substrates using sonication technique is done initially to remove the organic contaminants from the substrate surface. In this cleaning process, substrate is kept into trichloroethane/acetone (for about 10 min) and methyl/ ethyl alcohol (for about 10 min) solution separately and placed into the water bath. Using sound energy in the ultrasonic frequency (>20 kHz)range is used to agitate the particles of organic contaminants only, preserving the native-oxide layer on the surface.

2.1.2 RCA cleaning

The RCA (Radio Corporation of America) cleaning technique [232] is a standard set of wafer cleaning process which needs to be performed before any application in semiconductor technology.

In the first step is the standard cleaning process Si substrates are cleaned in a solution of ammonium hydroxide (NH_4OH, Merck, 30 %), hydrogen peroxide (H_2O_2, Merck, 30%) and Milli-Q water (H_2O), with a proportion of 1 : 1 : 2,

by volume of chemical agents, at a temperature of approx. 80 °C for about 10 minutes. The solution removes organic contaminants and forms a continuous thin silicon oxide layer on the substrate surface. Thus it is proved to be a very efficient method for removing organic contaminants and as well as in the formation of continuous oxide layer.

The second treatment step exposes the rinsed wafer to a solution, which is a hot mixture of H_2O_2 (30%), HCl (37%), and H_2O in the proportion of 1 : 1 : 6. This cleaning solution is designed to remove the metallic contaminants.

2.2 Substrate surface modification

Substrate preparation essentially means the preparation of the surface of Si substrate. Depending upon the treatment procedure, one can get differently terminated or passivated Si substrate. In the following we will discuss briefly the preparation procedure for different types of passivated or terminated Si substrates (X-Si, where X = H and OTS), which are of our interest.

2.2.1 H-Si substrates

The Si substrates are treated with HF solution after ultrasonic cleaning. Since the etching of Si substrate strongly depends on the concentration of HF solution and the time of immersion into it [161, 233], we have optimized the concentration and deposition time by using XR measurements. The minimum thickness of oxide layer and least surface surface roughness condition as obtained from XR calculation has been opted which comes from using 10% HF solution and 60 sec immersion time. Such substrates are labelled as H-Si, as HF treatment produce H-passivated surface after removing oxide layer. The HF etching has been performed just before the deposition of nanolayers because the Si surface are very reactive due to the open and unsaturated dangling bonds after the etching. This step has to be performed in HF resistant plastic beaker.

2.2.2 OTS-Si substrates

Si substrates is immersed in trichloro(octadecyl)silane [n-OTS, $CH_3(CH_2)_{17}SiCl_3$] solution to prepare OTS (of monolayer thickness) self-assembled Si (OTS-Si) substrates [234, 235]. Before that they are treated for 15 min at 80 °C in a mixture of concentrated ammonia (25% NH_4OH): concentrated hydrogen peroxide (31%): water with a volume ratio of 1:1:5. This helps to grow a thin oxide layer with lots of silanol (Si-OH) groups. These groups are needed for OTS adsorption. After rinsing the substrates further with deionised water and drying in nitrogen flow, the substrates are now immediately subjected to silanization. OTS solution in toluene of desired mM concentration is used for silanization.

2.3 Nanolayers of DT-AuNPs

2.3.1 Preparation of DT-AuNPs

There are many conventional methods for synthesis of AuNPs like bottom-up approach [46], reduction of $AuHCl_4$ by using citrate [236] or Schmid's cluster method for studying quantum-dot nanomaterial [237]. However The AuNPs synthesized for our experiments have been done following the path breaking Brust method [33, 238]. It's known as a two phase reduction process.

In this method gold ions first transferred to an organic phase, followed by reduction reaction in the presence of capping agent like alkanethiols having sulphur with a strong affinity toward the gold core and attach themselves to their surfaces progressing further growth. The size of AuNPs could be varied by tuning the gold to thiol molar ratio.

A typical preparation involves the mixing of 1 mL of 25 mM aqueous solution (golden yellow in color) of $HAuCl_4$ (Hydrogen tetrachloroaurate) and toluene solution of the well known phase transfer reagent Tetra-octyl Ammonium Bromide (TOABr), 220 mg in 5mL solvent, in a beaker. Toluene floats over the aqueous solution. The liquid is then stirred vigorously with the help of a magnetic stirrer for

some minutes. Immediately after shaking the beaker the transparent toluene layer becomes light brown in color and $HAuCl_4$ is rendered colorless due to transfer of gold ions from the aqueous layer to the toluene layer in a process known as phase separation. In the next step 82 μ L of Dodecanethiol is added to the solution drop by drop with continuous stirring. The toluene layer gradually becomes milky in color. Then 5 mL aqueous solution of 80 mg of $NaBH_4$ (Sodium Borohydride) is added as a reducing agent with rapid shaking resulting in production of dark brown color toluene solution. The color signifies the formation of AuNPs in the solution. The reaction proceeds as

$$AuCl_4^-(aq) + N(C_8H_{17})^4 + T \longrightarrow N(C_8H_{17})4AuCl_4(T)$$

$$mAuCl_4^-(T) + nC_{12}H_{25}SH(T) + 3me^- \longrightarrow 4mCl^-(aq) + Au_m(C_{12}H_{25}SH)_n(T)$$

where aq is aqueous phase and T is toluene. The solution is then rinsed and washed thoroughly with water and precipitated with excess of Ethanol. The precipitated AuNPs are then filtered out using a filtration set-up on a filter paper (shown in Fig. 3) of intercalated pore size 0.45 μm and stored on it for further usage.

All the chemicals used were freshly bought from Aldrich, USA. AuNPs of different core sizes could be successfully synthesized by tuning the molar ratios of Gold to Dodecanethiol (Au:Thiol). The AuNPs remain in the form of a dark brown film on the filter paper and are stable for years. When using for experiments a small section of the filter paper containing the AuNPs is cut off and immersed in a known quantity of toluene.The AuNPs disperse in the solution. The density of the AuNPs in the toluene solution can be calculated easily which will be further used to calculate surface pressure Π of Langmuir monolayer.

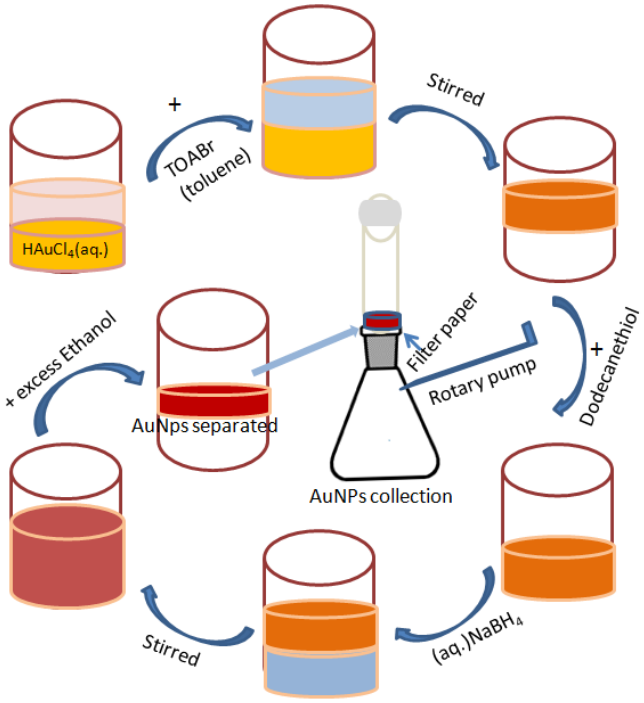

Figure 3: Schematic Representation of the Brust method.

2.3.2 Characterization of AuNPs

The shape, size distribution and degree of polydispersity of the synthesized Au AuNPs have been characterized by using different techniques.

2.3.2.1 UV-vis spectroscopy

Ultraviolet-visible spectroscopy (UV-Vis) involves the spectroscopy of photons in the UV-Visible region. Metals have unique optical properties [239] compared to other materials which are actually manifestations of the conduction electrons which is subject to modification on reducing the shape and size [239]. The optical spectra of noble-metal clusters exhibit pronounced resonance lines caused by collective excitations of surface conduction electrons (as shown in Fig. 4) in presence of electromagnetic radiation. These excitations are known as surface plasmons [60, 239, 240]. Surface plasmons oscillate with a resonance frequency at a peak value when the wavelength of the e.m. radiation λ exactly matches with the diameter d of the clusters. Mie theory provides the exact relation of d

and λ by solving Maxwell's equations [241]. Under certain approximations for small spherical particles the Full Width at Half Maximum (FWHM), Γ of surface plasmon peak, a Lorentzian provides [239],

$$d = \frac{2v_F}{\Gamma}$$

where v_F is the Fermi velocity of the bulk metal. The amplitude of the peak is proportional to the concentration of the solution. The peak position changes with the density of electrons, size and shape of the charge distribution and also on the dielectric constant of the surrounding medium [60, 242, 243].

Similar to nanoclusters, optical properties of AuNPs are also sensitive to size, shape, concentration, agglomeration state, and refractive index near the AuNP surface, which makes UV-vis spectroscopy a valuable tool for identifying, characterizing, and studying these materials. A strong band in the visible region of the absorption spectra of AuNPs arises from the surface plasmons in response to an external e.m. field [240, 244]. We have used this technique to observe the plasmon modes of the AuNPs and determine their sizes.

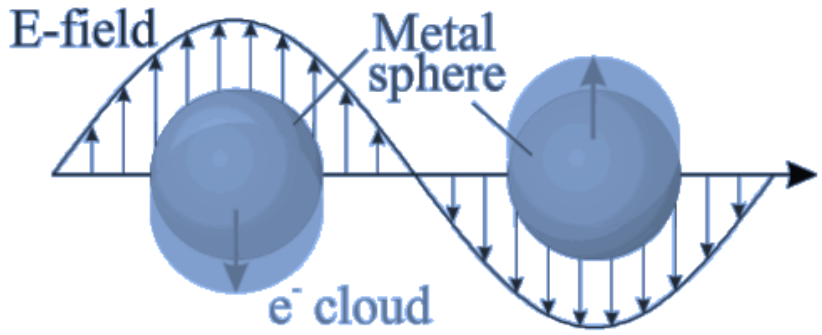

Figure 4: Schematic of plasmon oscillation in a metal sphere [242].

2.3.2.1.1 Basic principles A typical UV-Visible spectrometer (see Fig. 5 for schematics) comprises of the following major components: (a) A radiation source which provides illumination of the appropriate wavelengths (usually tungsten-iodine or xenon lamp), (b) a Czerny-Turner monochromator [245] which selects

the wavelength of interest, (c) a Chopper, (d) a detector/amplifier system (usually a Si photo diode), which measures the amount of light transmitted by the sample and (e) the sample compartment (quartz cuvettes) to place the sample to be studied.

The sample is placed between the source and detector, and the intensity of the radiation beam is measured after passing through the sample w.r.t. an unaffected reference beam. The sample beam interacts with the sample exposing it to ultraviolet light of continuously changing wavelength. The chopper is used here to separate the reference beam from the sample beam, allowing only one to reach the photomultiplier at any given time. When the emitted wavelength corresponds to the energy level which promotes an electron to a higher molecular orbital, energy is absorbed. The detector in transmission mode records the ratio between reference (I_0) and sample beam (I) intensities. And in a typical absorbance mode, the photons that are not absorbed or scattered by the sample are measured which is equal to $-\log_{10}(I/I_0)$. The quartz cuvettes accommodates samples in the form of films and liquids and has a lid to protect the detector from strong external light.

2.3.2.1.2 Instrument All measurements related to the thesis were performed on dilute solutions of the AuNPs in toluene using a UV-vis spectrophotometer, Lambda 750, Perkin Elmer, USA (schematics shown in Fig. 5), in transmission mode to determine their size. It is suitable for measurements in the scanning wavelength range between 190 and 3300 nm with a resolution of 0.17 - 5.00 nm.

We have worked with thiol-capped Au AuNPs dissolved in toluene. Absorption spectra was recorded taking toluene as a reference. The scan range used for our measurements was 300-800 nm with a Tungsten-Iodine lamp. To calculate the average size of the AuNPs after a linear background subtraction around the plasmon peak absorbance is plotted as a function of angular frequencies, $\omega = 2\pi c/\lambda$. Then Γ was obtained from its Lorentzian fit. The diameter d was found ≈ 1.5 nm.

Considering the chain length of the capping layer of dodecanethiol as ≈ 1.0 nm, the size of AuNPs was obtained as ≈ 2.5 nm.

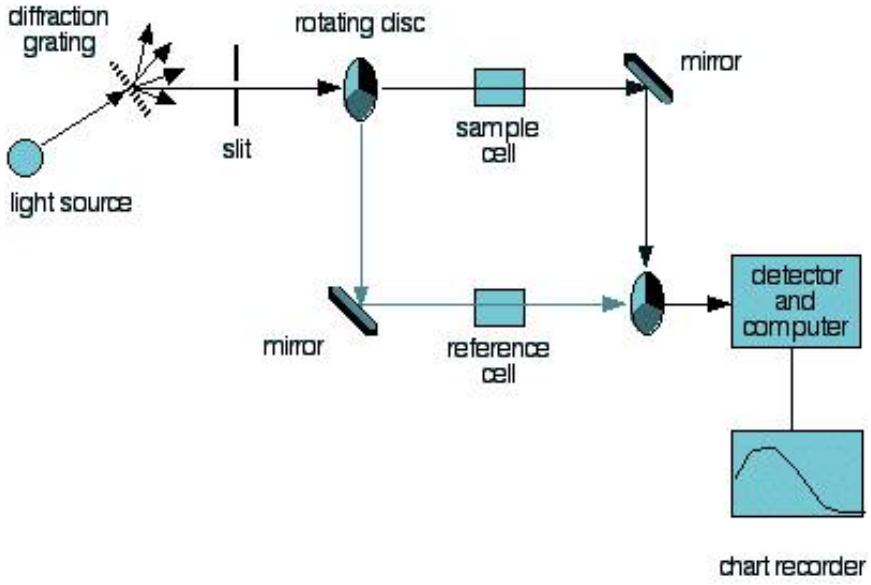

Figure 5: Schematic Representation of the Basic Uv-Vis Spectrometer Components [246].

2.3.2.2 Transmission electron microscopy

Both the high resolution real space information from image mode as well as reciprocal space information in diffraction mode can be obtained from TEM using a single sample [223] by passing a beam of electrons. This technique offers a high magnification ranging from 50 to 10^6. When electrons are accelerated to a high energy value (few hundreds of keV) and focused on a material, they can scatter or backscatter elastically as well as inelastically, or produce many interactions, which are source of different signals such as X-rays, Auger electrons or light [223, 247]. The different kind of information is obtained by probing differently generated signals after interaction of electron beam with the sample. Like, diffraction pattern is obtained from elastically scattered electrons which undergoes no loss of energy during the interaction process. On the other hand, inelastic collisions between electrons originated due to heterogeneities such as grain boundaries, dislocations, second phase particles, defects, density variations

etc. cause complex absorption and scattering effects [223] leading to a spatial variation in the intensity of the transmitted electrons.

The high magnification or resolution of TEM is associated with the very small de-Broglie wavelength of electron given by

$$\lambda = \frac{h}{\sqrt{2meV}} = \frac{1.23}{\sqrt{V}}nm$$

where me and e are the electron mass and charge, h is Plank's constant, and V is the accelerating potential. Hence only a hundred volts are needed to accelerate electrons to wavelength comparable to atomic length scales. The higher the operating voltage of a TEM instrument, the greater is its lateral spatial resolution. In TEM one can switch between imaging the sample and viewing its diffraction pattern by changing the strength of the intermediate lens [247]. The shortcomings of TEM are its limited depth resolution and radiation damage of organic specimens [247, 248]. The most common mode of operation for a TEM is the bright field imaging mode. In this mode the contrast is formed directly by scattering and absorption of electrons [247] in the sample. Thus thicker regions of the sample, or regions with a higher electron density will appear dark, whilst regions with no sample or lower electron density regions in the sample in the beam path will appear bright—hence the term "bright field". These contrast differences provide information on the structure, texture, shape and size of the sample.

2.3.2.2.1 Basic principles A typical schematic of the imaging system in TEM is shown in Fig. 6. The basic principles of functioning is same as the optical microscope. Electrons are emitted in the electron gun by thermionic, Schottky, or field emission and accelerated to high energies (200 keV) by an electric field. Field emission gun provides better resolution with higher brightness than the thermionic systems. The accelerated electrons are projected onto the sample through the condenser lenses. The aperture and illumination area is controlled by

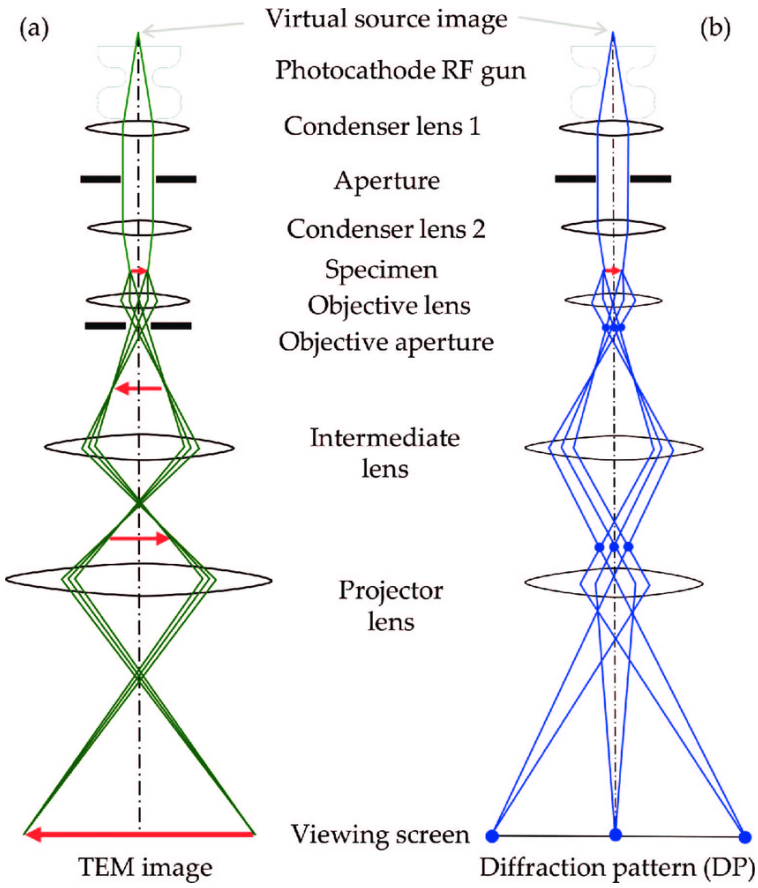

Figure 6: Schematic Representation of the Basic Transmission Electron Microscope Components in both image and diffraction mode [249].

the three- or four-stage condenser-lens system. The electron intensity distribution behind the specimen focused by the objective lens system composed of multiple lenses [247] onto a fluorescent screen [shown in Fig. 6]. The image can be recorded by direct exposure of a photographic emulsion or an image plate inside the vacuum, or digitally via a fluorescent screen coupled by a fiber-optic plate to a CCD camera. A JEOL-JEM 2010 Transmission Electron Microscope operated at 200 kV was used in our experiments.

2.3.3 Thin film deposition techniques

2.3.4 Langmuir monolayer

The molecules having a polar and hydrophilic head part in one side and hydrophobic tail e.g. long chain fatty acid or alcohol on the other side, [206] can

align themselves to form a surface of one molecular layer when spread over water or formed at the water-air interface. This monolayer of insoluble amphiphiles at the air/water interface is known as a Langmuir monolayer [Fig. 7 (a)]. A Langmuir monolayer is generally prepared by placing a known number of water insoluble molecules on the surface of an aqueous subphase; a measured volume of a dilute solution is deposited drop by drop. The monolayer spreads spontaneously onto the clean water surface and the volatile organic solvent, e.g. chloroform, methanol, or benzene, evaporates after some time. For convenience and cleanliness, the subphase is generally contained in a Teflon (PTFE) container, known as trough. Since the number of molecules added to the surface is known, the monolayer area is generally expressed as area per molecule. Measurement of the force exerted on a hydrophilic plate (made of e.g. filter paper or Wilhelmy plate) passing through the air/water interface is the most common method of determining the surface tension (γ). The force measurement is made using an electrobalance or a sensitive spring with a position sensor. The surface pressure (Π) is then calculated as $\Pi = \gamma_0 - \gamma$ where γ_0 is the surface tension of the bare subphase.

There are two possible methods of transferring the monolayers from the liquid–air interface onto a solid substrate. The most conventional method that is used is the vertical deposition of the substrate (Langmuir–Blodgett method). The second method is the horizontal deposition of the substrate onto the Langmuir film, which is known as the Langmuir–Schaefer method.

2.3.4.1 LB deposition technique

The LB technique was pioneered by Irving Langmuir and Katharine Blodgett [250–252]. Films can be transferred to a solid substrate by passing it through the Langmuir monolayer and known as LB films [206, 253]. These can be single layered or multilayered depending upon the number of passes made through the water surface. The commonest form of LB film deposition is shown in

[Fig. 7 (b-d)]. It involves the vertical movement of a solid substrate through the monolayer/air interface [253]. For LB film deposition, holding the Langmuir layer

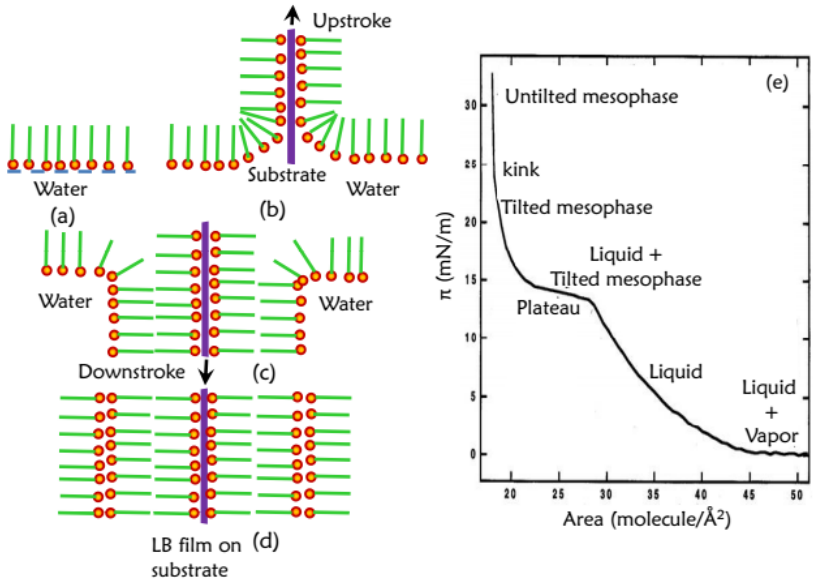

Figure 7: (a) Langmuir monolayer of amphiphilic molecules, (b-d) LB deposition schematics and (e) Π-A isotherm showing thermodynamic phase transition in the monolayer.

at a constant surface pressure, a solid substrate is dipped through the air/water interface at a controlled speed . Surface pressure (Π) is measured as a function of molecular area (A) at constant temperature, known as a Π - A isotherm. This is the standard thermodynamic measurement made on Langmuir monolayers [see Fig. 7 (e)]. It can be considered as a 2-D equivalent of a pressure-volume isotherm curve. Thermodynamic phase transition in the monolayer similar to Gas↔ Liquid ↔ Solid, are generally reflected in an isotherm as singularities such as flat regions (plateaus) or kinks (changes in slope) as shown in Fig. 7 (e).

2.3.4.2 LS deposition technique

The AuNPs which have been synthesized and well characterized are now cast as thin films to carry out experiments. We have prepared thin films of AuNPs mostly by horizontal lift-off of the the compressed insoluble monolayer of AuNPs at the air-water interface in a Langmuir trough using the LS technique [254].In the Langmuir–Schaefer method, a flat substrate is placed horizontally onto a

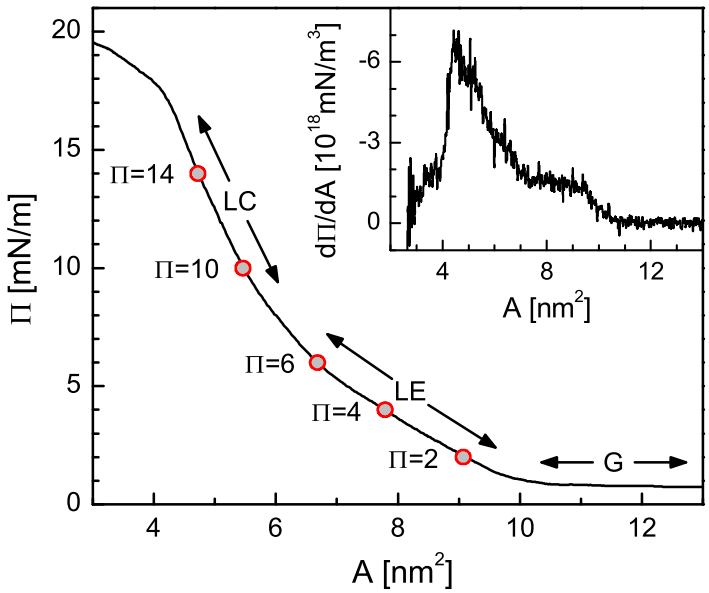

Figure 8: Pressure-area ($\Pi - A$) isotherm of DT-AuNPs layer, recorded at the Langmuir trough, showing various phases, namely gaseous (G), liquid-expended (LE) and liquid-compressed (LC). Inset: corresponding derivative curve to emphasize the changes.

compressed monolayer on the liquid–air interface. When the substrate is lifted horizontally and separated from the water subphase, the monolayer is transferred onto the substrate. In this technique the floating Langmuir monolayer is less affected by the disruptive forces than in the LB method.

A Langmuir trough (KSV 5000 alternating trough) was used for deposition of monolayer films [see Fig. 10] of thiol encapsulated AuNPs on Si substrates at desired surface pressures and temperatures [refer to Fig. 10 for schematics of the experiment].

About 1500 μL of the solution (AuNPs in toluene with concentration 0.25 mg/ml) was spread on the trough and the hydrophobic dodecanethiol encapsulated AuNPS lay suspended at the air-water interface [159–161] once the solvent evaporated. The solution has been spread dropwise on different parts of the trough using a micro pipette containing 100 μL of the solution at a time and then some time is allowed for the complete evaporation of the solvent. The amount of solvent spread decides the initial average area available to each molecule in the monolayer. If M is the molecular weight of the AuNPs, ρ is the concentration of the AuNPs solution and V be the volume of the solution and total surface

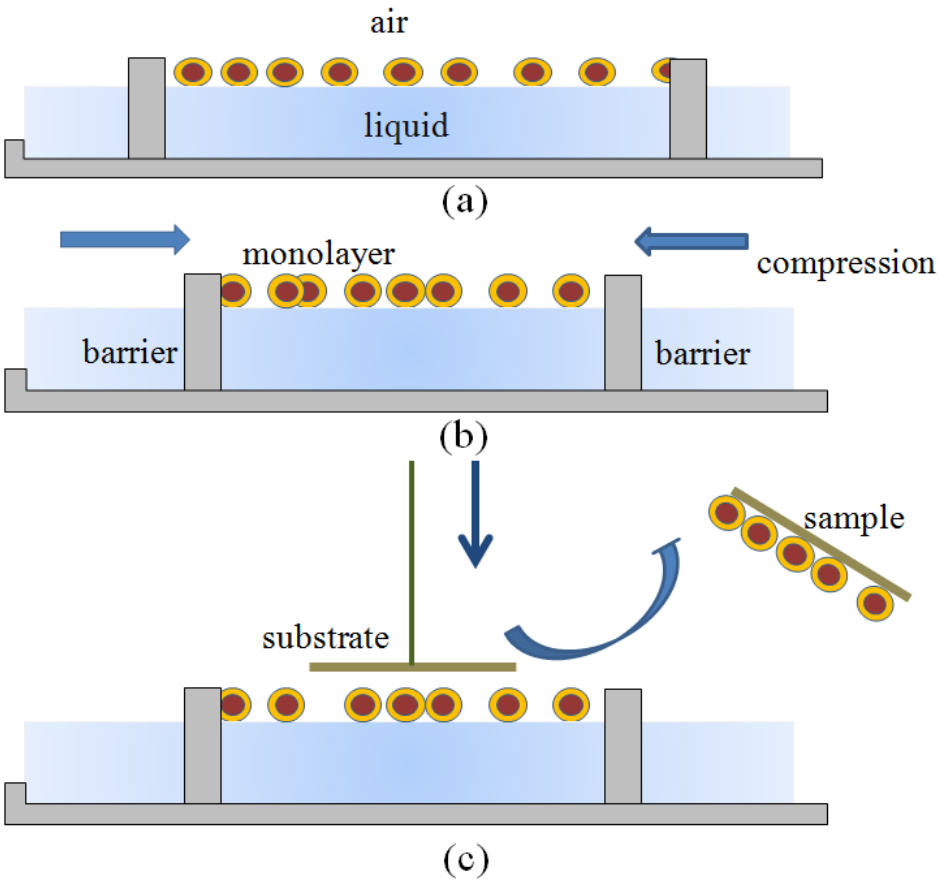

Figure 9: (a) Langmuir monolayer of hydrophobic AuNPs, (b) Compression and formation of monolayer (c) LS deposition of the monolayer on the substrate.

area covered by the monolayer is S (which is basically the area of the trough), then the area per molecule can be calculated using $A = SM/\rho V$. Here ρ and V are selected in such a way so that the area per molecule is large enough for the monolayer to be in the G phase. Various phases obtained in a typical $\Pi - A$ isotherm of AuNPs is shown in Fig. 8.

In gaseous state (G) the molecules are well separated whereas in liquid-expended state or extended monolayer phase (LE) they come closer to interact. On further reduction of the molecular area, a condensed phase, liquid-compressed (LC) is obtained where molecules are closely packed. Above a critical surface pressure,Π_c the monolayer starts buckling or collapsing. Below Π_c the isotherms are reversible on compression and decompression depending upon the stability of the monolayer. Film deposition corresponding to pressures at different phases has been done in the present thesis work. Prior to deposition the substrate has

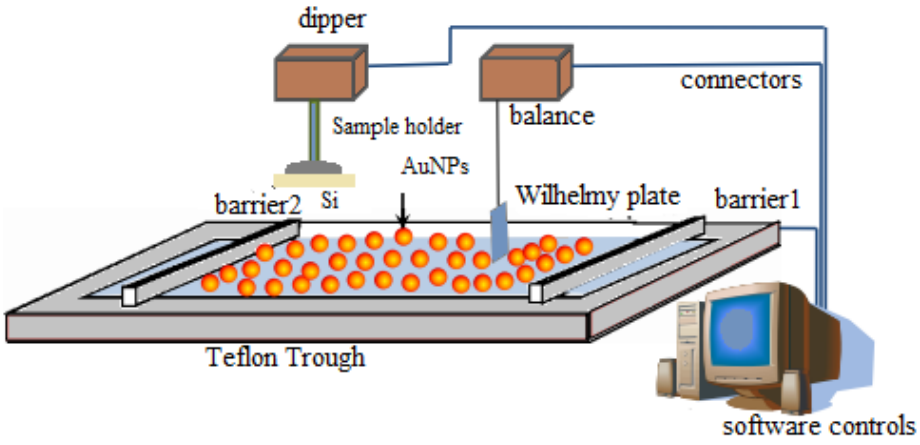

Figure 10: The schematics of the experiment for transfer of thin film of AuNPs to solid substrate from water surface using LS method

been chemically treated. Hydrophobic silicon substrates were then attached horizontally to a homemade Teflon substrate holder(vacuum chunk) which is attached to the clip of the trough dipper. The substrate holder thus can be moved up and down with desired speed. At the time of film deposition, top water surface was properly cleaned and the substrate holder was approached toward the air-water interface very slowly in a parallel manner until it just touched the interface. After few seconds the substrate again was drawn backwards. Transfer onto Si (100) were done at room temperature, with the substrate moving at the rate of 1 mm/min, in this LS method [254] at a desired surface pressure. The reproducibility of the film was monitored by measuring the XR profile.

2.4 Nanolayers of metal

2.4.1 Deposition by magnetron sputtering

The magnetron sputtering is a very simple and reliable process which is used from several years for industrial deposition of thin films and coatings. Magnetron sputtering has emerged to complement other vacuum coating techniques such as thermal evaporation and electron-beam evaporation. Magnetron sputtering has many advantages like high deposition rates, broad range of sputtering metals,

alloys or compoun. High-purity uniform films can be deposited with excellent coverage of steps and small features. Thus sputtering is a very powerful technique which can be used in a wide range of applications.

2.4.1.1 Principle of sputtering deposition

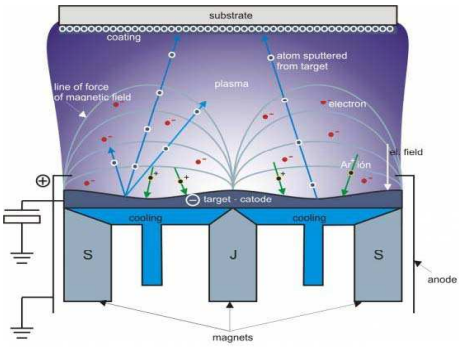

Figure 11: Schematic view of magnetron sputtering

Within the sputtering process a DC voltage is applied across the two electrodes in a gas at low pressure to accelerate the gas ions out of a plasma toward a target (cathode) consisting of the material to be deposited. This gas further becomes ionised making plasma which strikes the target. Material is detached ('sputtered') from the target and afterwards deposited on a substrate in the vicinity. This process is known as DC sputtering.

The ignition of plasma is done by feeding up argon Ar) into the chamber. In the DC-sputtering a negative potential U up to some hundred Volts is applied to the target. As a result, the Ar^- ions (already present in the system due to cosmic radiation) are accelerated toward the target and set material free producing secondary electrons which further further ionize the gas. The gas pressure p and the electrode distance d determine a break-through voltage U_D from which on a self sustaining glow discharge starts- following the Eqn.

$$U_D = A\frac{pd}{\ln(pd) + B} \tag{2–1}$$

where, A and B are materials constants. This is Paschen's Law. Graphically spoken the ionization probability rises with an increase in pressure and hence the number of ions and the conductivity of the gas also increases. The break through voltage drops. For a sufficient ionization rate a stable burning plasma results, where from a sufficient amount of ions is available for sputtering of the material.

To increase the ionization rate by emitted secondary electrons even further, a ring magnet below the target is used to create magnetically confinement plasma. The strong magnetic field generated by magnetron traps the electrons in a spiral shape increasing the probability of confinement of plasma near the target. This eventually increases the deposition rate. So the technique is called *magnetron sputtering*.

The DC-sputtering is restricted to the conducting materials like metals or doped semiconductors. For preparing dielectric films another method called radio frequency, *RF-sputtering* is used. A periodically reversible high frequency voltage is applied to the target here to charge neutralize the surface of the target made of insulating material. Hereby also sputtering of non-conducting materials is possible.

2.4.1.2 Instrument

The instrument used to grow metal nanolayers is a magnetron sputtering unit (PLS 500, Pfeiffer Vacuum) shown in Fig. 12. The system has three major units (a) pumping system; (b) sputtering chamber; and (c) control panel. The main chamber, shown in Fig. 12, can be evacuated to a base pressure of $\approx 1 \times 10^{-6}$ mbar with the help of a turbo molecular pump (Pfeiffer, TMH 520) backed by a rotary pump (Pfeiffer, DUO 016 B). Different types of gases like Ar, N_2, etc. can be introduced into the main chamber for plasma discharge. The gas flow rate is controlled by a mass flow controller. Two DC and one RF sputtering units are availabe which can be operated at different wattage. The maximum power that can be applied to the dc magnetron is 0.5 kW. Both static and rotational modes

Figure 12: Left: Magnetron sputtering instrument (PLS 500). Right: Inside view of the deposition chamber

available for the sample stage. In our study, as we have used more than one samples for deposition at a time using the rotation mode to get smooth films of uniform thickness for all samples..

2.5 Thin film characterization

2.5.1 Microscopic measurement techniques

2.5.1.1 Scanning electron microscopy

To overcome the limitations of the light microscopes such associated with the magnification and resolution power, Scanning electron microscope (SEM) were developed [224]. SEM comes under the category of electron microscopes. A beam of highly energetic electrons is used to image the specimen on a very fine scale and to get it's structure and composition. The analysis provides information related to the topography, morphology, composition and the crystallographic orientation of the sample [255]. There are two kinds of electron microscope namely Transmission electron microscope (TEM) and Scanning electron microscope (SEM) that are

commonly used in the surface science. In our work, we have used SEM to characterize the surface morphology of the metal nanolayers.

2.5.1.1.1 Basic formalism Electron column, scanning unit, detector(s), display, and vacuum unit are the main parts of a typical SEM instrument. The scanning unit and the detectors are kept in vacuum during operation. A beam of electrons is generated from the electron gun using tungsten tip located at the top of the electron column which is always in high vacuum vacuum environment. This beam is attracted through the anode, condensed by a magnetic lens and focused as a very fine probe (<10 nm in diameter) on the specimen by the objective lens. The scan coils are energized (by varying the voltage produced by the scan generator $\sim$ 1-40 kV) and create a magnetic field, which deflects the beam back and forth in a controlled pattern. Once the beam hits the sample, the electrons interact with the surface atoms of solid specimens and produces a variety of signals such as secondary electrons, high-energy backscattered electrons, characteristics X-rays, visible light. The emitted signals escape from the sample surface with specific angles with the incident electrons.

As for as the SEM is concerned, when the electron beam hits the sample surface, the secondary electrons produced from the sample are collected by the secondary electron detector or the backscatter detector, which has been converted into a signal resulting in an 2D intensity map in the viewing screen known as SEM image. The resulting image is generally straightforward to interpret, at least for topographic imaging of objects at low magnifications. The schematic of various components of a SEM instrument is shown in the Fig. 13.

A very important point in the study of SEM is that the sample should be conductive to avoid electron cloud accumulation on the top of the specimen which ultimately results in lower contrast of the image. And for this reason conductive tape is pasted in the lower face of the insulator/semiconductor sample surface before the process of imaging.

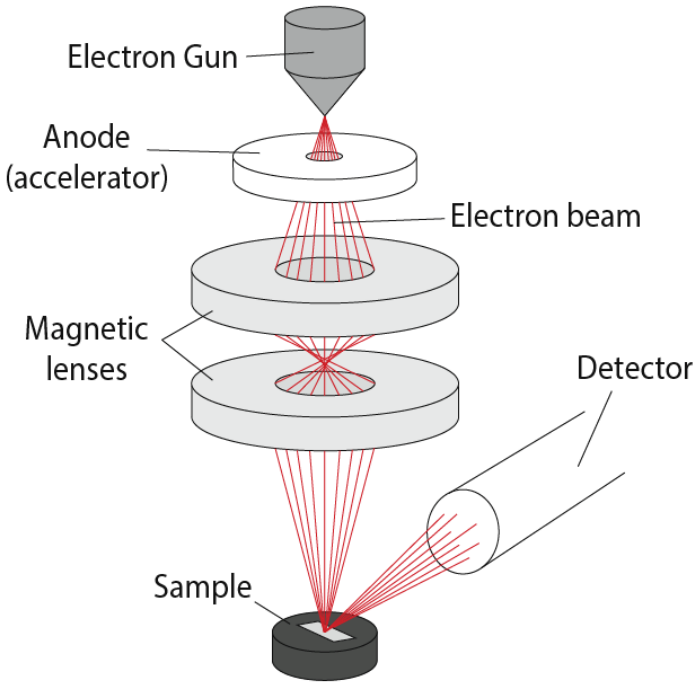

Figure 13: Schematic Representation of the Basic SEM Components [256].

2.5.1.1.2 SEM instrument FEI Quanta 200F schottkey field emission gun (FEG). Scanning Electron Microscope has been used in our divisional laboratory to image the topography of thin films in large scale. The photograph of the instrument is shown in the Fig. 14. The instrument can be operated in three different vacuum modes as per necessity depending upon the nature of the samples:High Vacuum (HV) for observing conducting sample, Low Vacuum (LV) and environmental SEM (ESEM) for scanning nonconducting materials without having any metal coating on the sample. It also possesses different types of detectors like Everhart-Thornly detector (ETD), large-field gaseous secondary electron detector (LFD) and solid state detector (SSD). The accelerating voltage of the electron beam can be varied from 0.2 kV to 30 kV. For low and high vacuum modes, the spatial resolution of the microscope is 3.5 nm at 3 kV and 2 nm at 30 kV respectively. We have imaged the AuNPS films using operating voltage= 5 kV while the pressure is kept at 0.37 torr.

Figure 14: Scanning Electron Microscope

2.5.1.2 Atomic force microscopy

SPM is a branch of microscopy that forms images of surfaces using a physical probe that scans the specimen and AFM is one member in the family. SPM, founded with the invention of the scanning tunneling microscope in 1981 [257]. An image of the surface is obtained in AFM by mechanically moving the probe in a raster scan of the specimen, line by line, and recording the probe-surface interaction as a function of position [227, 228]. By changing the probe material and configuration, detection scheme is modified to determine different characteristics of a sample.

AFM has a widespread usage in real space imaging of a large variety of specimens spanning across vast boundaries of physical, chemical, material and biological science. Also, it can be used both in ambient conditions as well as in vacuum according to the specific requirement of the experiment. Basic principle

governing the mechanism and modes of operation are being discussed in the following sections.

2.5.1.2.1 Basic principles In AFM, a sharp tip mounted on a cantilever is allowed to scan over a sample surface and deflection of the tip due to its interaction with the sample surface atoms is monitored. Schematics of AFM is shown in Fig. 15. Under normal working conditions the interaction forces between the tip

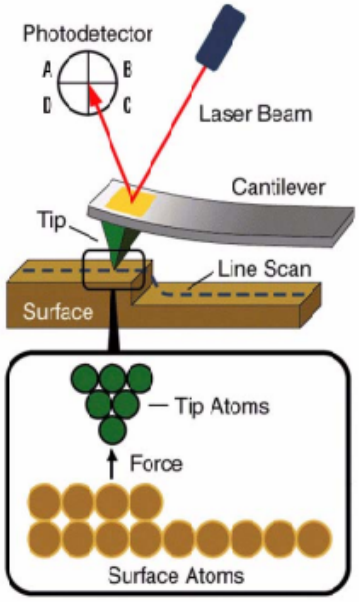

Figure 15: Working principle of AFM [258].

and sample atoms bend the cantilever following Hooke's law.

$$F = -\kappa x \tag{2–2}$$

The cantilever deflection is detected by an 'optical lever' principle and converted into an electrical signal to produce the images. In the optical lever setup, a laser beam reflected from the backside of the cantilever is made incident on a Position Sensitive Photo Detector (PSPD). As the cantilever deflects, the angle of reflected beam changes and the spot falls on a different part of the detector. Generally the detector is made of four quadrants (shown in Fig. 15) and the signals from the four quadrants are compared to calculate the position of the laser spot. The

spring constant of the cantilever should be small enough to allow detection of small forces and its resonant frequency should be high to minimize sensitivity to mechanical vibration. The scanning (tip or sample movement) is performed by an extremely precise positioning device made from piezo-electric ceramics, most often in the form of a tube scanner. The scanner is capable of sub-Angstrom resolution in X, Y and Z-directions. To control the relative position of the tip with respect to the sample accurately, good vibration isolation of the microscope has to be ensured.

In AFM, the force F(r) which acts between the tip and sample is used as the imaging signal. For two electrically neutral and non-magnetic bodies held at a distance of the order of several nanometers, the van der Waals forces usually dominate the Pauli repulsion due to overlapping electron orbitals. The force can be derived from the Lenard-Jones potential V(r) where

$$V(r) \propto [(\sigma/r)^{12} - (\sigma/r)^{6}] \tag{2–3}$$

σ is the finite distance at which the inter-particle potential is zero and r is the distance between the particles. Thus using the relation the force can be written as

$$\begin{aligned} F(r) &= -\partial V(r)/\partial r \\ &\propto [\sigma^{6}/r^{7} - \sigma^{12}/r^{13}] \end{aligned} \tag{2–4}$$

The variation of interaction force with the distance is depicted in Fig. 16. For larger r weak attractive force exists between the tip and sample. As they are gradually brought closer the attractive force between them increases until the electron clouds begin to repel each other electro statically. This electrostatic repulsion gradually weakens the attractive force as the inter-atomic separation continues to decrease. When the distance between the atoms reaches a couple of Angstroms, the interatomic force becomes zero. And the force acting is totally Van

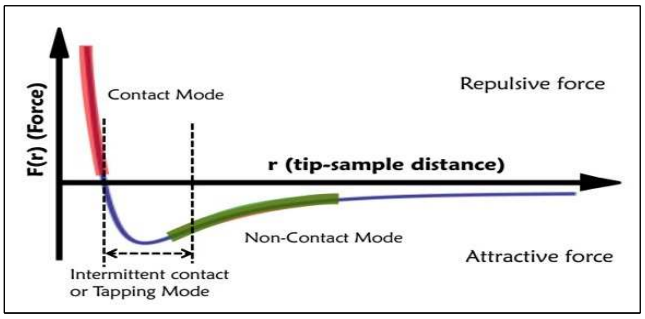

Figure 16: Variation of inter-atomic forces with distance. Working regime for the different modes of AFM.

der Waals repulsive force. In AFM, the tip-sample interaction force is measured and mapped to generate the three dimensional images of the surface.

2.5.1.2.2 Modes of operation There are various modes of operation of the AFM among which (a) contact mode, (b)non-contact mode and (c) tapping mode are frequently used to probe surfaces.

(a) Contact mode Contact mode is the simplest and fastest mode of AFM operation since the deflection of the cantilever gives us the topography of the sample directly. In contact mode, the tip and the sample remain in close contact (within a few Å) during the scanning, i.e. the force experienced by the tip is the Van der Waals force [as shown in Fig. 16]. In this mode, imaging can be done in two different methods:

1. *Constant force imaging:* The force between tip and sample remains same during scanning that means the cantilever deflection is maintained at a constant value. A feedback circuit connected to the z-piezo-drive is used to adjust the height of the tip. Voltages applied to the x and y piezoelectric drives determine the corresponding positions along the both axis. The signal obtained in terms of voltages can finally be translated into 'topography' h(x, y) provided that the sensitivities of the three orthogonal piezoelectric drives are known.

2. *Constant height imaging:* In this method the scanning at a constant height arises the variation in tip-sample interaction force which reflects the atomic-scale

topography of the sample. The feedback loop is turned off in this mode setting and the image signal comes entirely from the deflection of the cantilever.

The constant height mode suffers from the disadvantage that any steep step in the sample surface may cause the tip to crash against the sample and thus damage the tip. So the constant force mode is the most commonly used mode of operation. But, constant height mode is often used for taking atomic scale images of atomically flat surfaces, where the force variation is small. This is also efficient where high scan speed is essential. A significant disadvantage of the contact mode is the dragging motion of the probe tip, combined with adhesive forces between the tip and the surface which can cause substantial damage to both sample and probe and creates artefacts in the resulting image. Thus this mode is not an ideal one to perform high resolution topographic imaging of surfaces of soft materials which can easily be damaged or of over-layers those are loosely bounded to the substrates.

(b) Non-contact mode Non-contact AFM (NC-AFM) mode is a vibrating cantilever technique in which an AFM cantilever is made to vibrate above the sample surface at such a distance that the forces of interaction remain in the attractive force regime of the inter-atomic force curve as indicated in Fig. 16. Since the force is very small, this mode is advantageous for studying soft or elastic samples. To avoid pulling and crushing at sample surface stiffer cantilever is used. The NC-AFM signal is very small in value and difficult to measure. So a sensitive AC detection scheme is used for NC-AFM operation. The cantilever vibrates slightly above its resonant frequency (typically from 100 to 400 Hz) with an amplitude of a few nm. When comes in close proximity of the sample, the resonant frequency of the cantilever is decreased by Van der Waal's force resulting in a change in oscillation amplitude. By monitoring changes in resonance frequency/vibrational amplitude of the cantilever which results in force gradient, the tip-to-sample spacing or sample topography is mapped. By keeping the resonant frequency or amplitude constant, the average tip-to-sample distance

is mained at a constant value in this mode. As with contact AFM, the voltage applied to the scanner is used to generate the topography. Although this mode does not suffer from the tip to sample degradation effects as seen in contact AFM, the contact AFM provides better resolution than the NC-AFM. This is because the attractive Van der Waal's forces are substantially weaker than the forces used by contact mode. Hence, even when the sample-tip separation is successfully maintained, non-contact mode provides substantially lower resolution than the contact mode. Ultra-high vacuum conditions and active anti-vibration devices is needed to diminish moise effects and for smooth functioning of this mode. Due to these disadvantages, applications for non-contact mode AFM imaging have been somewhat limited.

(c) Tapping or intermittent-contact mode Tapping mode imaging is implemented in ambient condition. The stiff cantilever oscillates at or near it's resonance frequency with a high amplitude (typically greater than 20 nm) at a very close separation with the sample. The oscillating tip is then moved toward the surface until it begins to lightly touch, or 'tap' the surface intermittently reducing the oscillation. The amplitude of oscillation changes when the tip scans over the bumps or depressions. A constant oscillation amplitude and thus a constant tip-sample interaction is maintained during scanning with the help of the feedback circuit by adjusting the tip-sample separation.

The advantage of this mode is that it inherently prevents the tip from sticking to the surface and making damages during scans. Unlike contact and non-contact modes, when the tip contacts the surface, it has sufficient oscillation amplitude to overcome the tip-sample adhesion forces. Also, the surface material is not pulled sideways by lateral forces since the applied force is largely vertical. As a result lateral forces are virtually eliminated and the possibility of tip crashes is avoided. Damage and distortion to the sample can be minimized also. For these reasons, tapping mode AFM is well suited for the study of polymer, AuNPs, soft matter and fragile objects.

2.5.1.2.3 Details of AFM used in present experiments The detailed top surface morphologies of the films in the present thesis have been mapped in tapping mode using the Agilent 5500 SPM using etched Si cantilever in ambient conditions (see Fig. 17). Details of the measurements have been discussed in corresponding

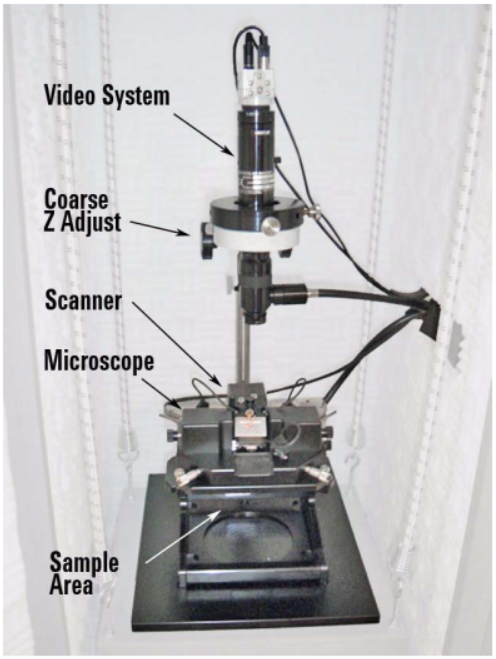

Figure 17: Components of Agilent 5500 SPM [258].

chapters.

2.5.1.2.4 Statistical analysis of images WSXM software has been used to process and further analyse AFM images [259]. Height information of each point in x-y plane within the scan resolution limit is stored in the AFM image in height mode. Using this information roughness, height correlation function etc. can be analysed [260]. For example, considering an AFM scan with digitized data consisting of $N \times N$ points in the x-y plane, the r.m.s. roughness can be calculated as

$$\sigma = \frac{1}{N}\sqrt{[\sum_{i=1}^{N}\sum_{j=1}^{N} h(x_i, y_j) - h_{av}]^2}$$

where,$h(x_i, y_j)$ denotes height at a point (x_i, y_j) and h_{av} is the average height of the scan area. Using r.m.s. roughness only height-height correlation C(X, Y) function

can be calculated since it only deals with height fluctuations along vertical direction. These experimentally obtained correlation functions are then fitted with different types of surface correlation functions such as Gaussian, exponential, power-law, self-affine, liquid-like, self-affine liquid-like etc. to characterize the surface under observation [260].

All the positional correlations between different points which give the surface quantities like featured wavelength, homogeneity and lateral correlation length remain unidentified. This can be attained by transforming the height profile in the reciprocal space or Fourier space. The 2D finite length FFT (Fast Fourier Transform) for a square image is given by:

$$H(q_x, q_y) = \int_{-L/2}^{L/2} \int_{-L/2}^{L/2} h(x, y) \exp^{-i(q_x x + q_y y)} \, dxdy \tag{2–5}$$

where, the image size L $\times$ L. q_x and q_y are the reciprocal wave vector components along x-axis and y-axis respectively. For isotropic sample, periodicity is same in all direction. So only one dimensional PSD is sufficient. The spots in FFT image describe the preferred orientation of structures on surface, whereas its position determines the characteristic spatial frequency i.e., wavelength of the structures. The width of the spot gives the homogeneity and the spatial correlation among the periodicities on the surface. The presence of additional spots in FFT, multiple of the first one, denote the higher lateral ordering of the structures. Higher number of spots indicate the better lateral ordering. However, for better quantitative estimation of these quantities, the one dimensional PSD (q_y) function [261, 262] can be considered. It can be noted that the PSD is the angular averaged distribution of the Fourier transformed AFM image [260], which can be expressed in its limiting integral form for continuous data as

$$\mathrm{PSD}(q_y) = \lim_{L \to \infty} \frac{1}{L} \left| \int_{-L/2}^{L/2} dy \, h(y) \, e^{-iq_y y} \right|^2 \tag{2–6}$$

where L is the scan length, $q_y = 2\pi f_y \sin\theta$ with scattering angle θ and spatial frequency f_y due to periodicity along y direction. And h(y) is the surface roughness height as a function of distance y. The above PSD is for one-dimension i.e. along a line in y direction. The first peak position in the PSD profile gives the wavelength of structures. The lateral ordering of structures can be quantified by estimating lateral correlation length (ξ) which can be extracted from the first order peak. If more than one lateral correlation lengths exist in the system, by further modelling the definite structures can be found. Detailed modelling will be discussed in corresponding chapter.

3

X-RAY SCATTERING TECHNIQUE

Since the discovery of X-rays in 1895 by W. C. Röntgen [263], it has been used extensively as a probe in characterizing atomic, molecular and supramolecular structures of matter. X-rays are a form of electromagnetic radiation with wavelengths in the range of 1 to 100 Å, corresponding to frequencies in the range 30×10^{15} to 30×10^{18} Hz and energies in the range 120 eV to 120 keV.Among this range X-rays of wavelengths 50 Å to 5 Å are termed as Soft X-rays and 5 Å to 0.5 Å are termed as Hard X-rays depending upon their penetrating power through matter [264].

X-rays can interact with matter through different mechanisms [265]. Nowadays, the availability of intense X-rays from the modern synchrotron sources have accelerated the usage of X-rays in the determination of interfacial structures of solids as well as liquids. There are various types of X-ray scattering techniques, called - XRD, grazing incidence diffraction, SAXS, GISAXS, XR, diffuse scattering, etc. In this chapter we have discussed the theoretical formalism behind X-ray scattering,the major scattering techniques used (XR and GISAXS) and the modeling/fitting of data to extract usable information from such scattering techniques.

3.1 X-ray reflectivity

XR is a surface sensitive tool which is generally used in different areas specially for studying thin films or multilayers of metals and MNPs or soft matter (polymers, surfactants, biological systems, etc.) at both solid and liquid interfaces. X-ray

radiation under specular condition (keeping reflected angle same as incident angle) is used here to probe the thickness and electron density along the in-depth direction of the thin films of nm range. Due to non destructive nature XR is used vastly for surface structure characterization.

We have discussed here two theoretical formalisms of XR. The first approach is Dynamical Theory. It is based on Maxwell's equations. Reflectivity calculation incorporates multiple scattering [221, 265, 266]. The second approach, known as Kinematical Theory or Born Approximation [221, 265], on the other hand, greatly simplifies the expression for the intensity of specular reflectivity. When X-rays scatter from rough surfaces, interact strongly with matter. Using the corresponding boundary conditions over random surfaces, several simplifying assumptions are taken to get to the solution of the relevant wave equations.

3.1.1 Dynamical theory of X-ray scattering

X-ray interacts with matter in atomic level when it propagates through it. Basically, when an electromagnetic (EM) plane wave like X-ray penetrates into a medium of refraction index n(**r**), it propagates according to the Helmholtz equation [221, 230, 267] given by

$$\Delta\mathbf{E(r)} + k^2 n(\mathbf{r})^2 \mathbf{E(r)} = 0 \tag{3–1}$$

where, $k = 2\pi/\lambda$, the modulus of the wave vector k_i, λ is the X-ray wavelength and the electric field is described by $\boldsymbol{E}(\boldsymbol{r}) = \boldsymbol{E_0}\exp(i\boldsymbol{k_i}.\boldsymbol{r})$. Considering N atoms per unit cell as harmonic oscillators with the resonance frequencies ω_j [268, 269], the refraction index is given by,

$$n^2(r) = 1 + N\frac{e^2}{\epsilon_0 m}\sum_{j=1}^{N}\frac{f_j(\omega)}{\omega_j^2 - \omega^2 - 2i\omega\eta_j} \tag{3–2}$$

where e and m are the charge and mass of the electron, respectively,ω is the frequency of the wave, η_j is the damping factor and f_j is the forced oscillation strength of electrons of each single atom. It should be noted that f_j are com-

plex numbers as $f_j = f_j^0 + f_j'(E) + if_j''(E)$ with the dispersion and absorption corrections $f_j'(E)$ and $f_j''(E)$, respectively which depend on the radiation energy E. Since for X-ray, $\omega > \omega_j$, the refraction index may be rewritten as,

$$n(r) = 1 - \delta(r) + i\beta(r) \tag{3–3}$$

where the dispersion and absorption terms are

$$\begin{aligned} \delta(r) &= \frac{\lambda^2}{2\pi}\rho(r)\sum_{j=1}^{N}\frac{f_j^0 + f_j'(E)}{Z} \\ \beta(r) &= \frac{\lambda^2}{2\pi}\rho(r)\sum_{j=1}^{N}\frac{f_j''(E)}{Z} = \frac{\lambda}{4\pi}\mu(r) \end{aligned}$$

$\rho(\boldsymbol{r}) = r_e\varrho(\boldsymbol{r})$ is the scattering length density (SLD), r_e is the classical electron radius as $r_e = e^2/4\pi\epsilon_0 mc^2 = 2.814 \times 10^{-5}$Å. $\varrho(\boldsymbol{r})$ denotes the electron density and $Z = \sum_j Z_j$ is the total number of electrons per unit cell. Neglecting f_j'(E) and approximating $f_j^0(E) \approx Z_j$,

$$n(r) = 1 - \frac{\lambda^2}{2\pi}\rho(\mathbf{r}) + i\frac{\lambda}{4\pi}\mu(\mathbf{r}) \tag{3–4}$$

where μ(r) is the linear absorption coefficient. The dispersion δ is of the order of 10^{-6} for X-ray (wavelength $\lambda \sim 1.54$ Å) and the absorption β is of 10^{-8} order, generally one or two orders smaller than δ. Both the parameters are proportional to the electron density $\varrho(\mathbf{r})$. In such a case we can ignore the β i.e the complex part of the refractive index and the real part become slightly less than 1. Therefore in case of refraction of X-ray from vacuum (n=1) to any medium, vacuum acts like a denser medium. At this point it can be noted that the complex part of n become more important for elements with high atomic number or when the wavelength of the X-ray become large (soft X-ray). Since $n \approx 1$ for X-ray and smaller than unity, there exists a critical angle α_c , below which the real part of $k_{t,z}$ vanishes and the incident wave completely reflected back from the interface

into the vacuum i.e. the total external reflection ($r \approx 1$) occurs [221, 267, 268]. Since the angle α_c is very small as n is close to unity we can expand cos α_c is its series form. Considering only the quadratic term and neglecting higher orders term of α_c we can can write [221, 267, 268],

$$\alpha_c \approx \sqrt{2}\delta \approx \sqrt{\frac{\lambda^2}{2\pi}\rho_e} \tag{3–5}$$

The typical value of $\alpha_c \simeq 0.1^\circ$ to 0.5°. For Si, $\delta_{Si} = 7.6 \times 10^{-6}$and corresponding $\alpha_c = 0.223^\circ$ with q_c = 0.0316 Å^{-1} for $\lambda = 1.54$Å. For a multilayer film, the overall critical angle is determined by the layer having the highest value of δ.

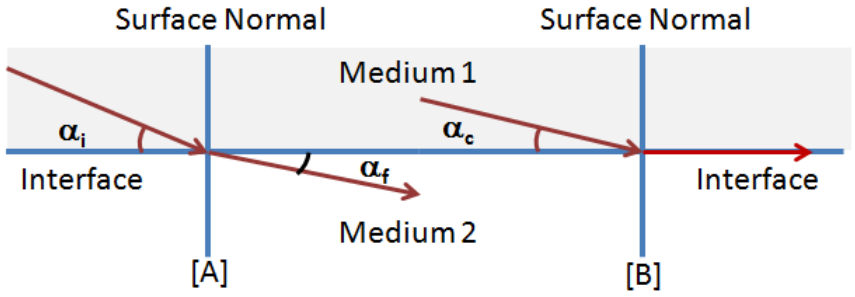

Figure 18: [A]Schematic representation of X-ray refraction by an interface with a grazing incident angle α_i.[B] the critical angle of incidence α_c for the total external reflection.

3.1.2 Fresnel reflection from a flat surface

When a plane EM wave

$$\boldsymbol{E_i}(\boldsymbol{r}) = \boldsymbol{E_0} \exp(i\boldsymbol{k_i}.\boldsymbol{r}) \tag{3–6}$$

hits a smooth vacuum/medium interface of refraction index n at grazing angle α_i, it splits into two wave components a) reflected wave and b) transmitted wave as shown in Fig.19. Here all the angles are taken with reference to surface plane as conventionally. The vectors of electric fields of these two wave components are given by

$$\boldsymbol{E_r}(\boldsymbol{r}) = r_{s,p}\boldsymbol{E_i}(\boldsymbol{r}) \exp(i\boldsymbol{q_i}.\boldsymbol{r}) \tag{3–7}$$

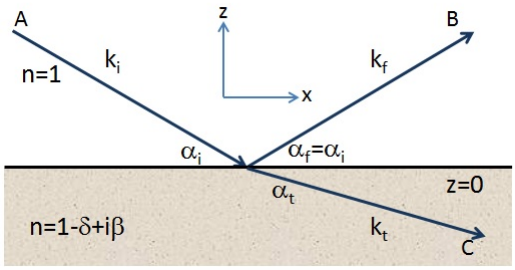

Figure 19: A plane electromagnetic wave with wavevector k_i hits a surface at a grazing angle α_i. The wave splits into a reflected ($\alpha_f = \alpha_i$) and a refracted wave transmitted at the angle α_t [221].

and

$$\boldsymbol{E_t}(\boldsymbol{r}) = t_{s,p}\boldsymbol{E_i}(\boldsymbol{r})\exp[i(\boldsymbol{k_t} - \boldsymbol{k_i}).\boldsymbol{r}] \tag{3–8}$$

where, $\boldsymbol{k_i} = k(\cos\alpha_i, 0, -\sin\alpha_i)$, $\boldsymbol{k_r} = k(\cos\alpha_i, 0, \sin\alpha_i)$, $\boldsymbol{k_t} = (k_{t,x}, 0, k_{t,z})$, $k = \mid k_i \mid = \mid k_r \mid = 2\pi/\lambda = \mid k_t \mid /n$ and $r_{s,p}, t_{s,p}$ and $\boldsymbol{q} = (\boldsymbol{k_f} - \boldsymbol{k_i})$ are the reflection coefficient, transmission coefficient and wave vector transfer, respectively. By Fresnel formulas on classical optics, in case of s - and p - polarization,$r_{s,p}$ and $t_{s,p}$ are given as

$$r_s = \frac{k_{i,z} - k_{t,z}}{k_{i,z} + k_{t,z}}, r_p = \frac{n^2k_{i,z} - k_{t,z}}{n^2k_{i,z} + k_{t,z}}, t_s = \frac{2k_{i,z}}{k_{i,z} + k_{t,z}}, t_p = \frac{2k_{i,z}}{n^2k_{i,z} + k_{t,z}}$$

where $k_{i,z} = ksin\alpha_i$ and $k_{t,z} = nksin\alpha_t = k(n^2 - cos^2\alpha_i)^{1/2}$ are z-components of the incoming and transmitted wave vectors, respectively.

In case of small angle of incidence one arrives at the expression of the specular XR i.e. the Fresnel reflectivity, for an interface separating the two media as a function of wave-transfer vector, which is given by, $R_F = \mid r \mid^2$ is given by,

$$R_F(q_z) = \mid \frac{q_z^2 - \sqrt{q_z^2 - q_c^2 - \frac{32i\pi^2\beta}{\lambda^2}}}{q_z^2 + \sqrt{q_z^2 - q_c^2 - \frac{32i\pi^2\beta}{\lambda^2}}} \mid^2 \tag{3–9}$$

where $q_z = 2ksin\alpha_i$, the z-component of the wavevector transfer q and $q_c = 2ksin\alpha_c$, the critical wave vector transfer that is related to the SLD and given by $q_c = \sqrt{16\pi\rho}$. When wave-vector transfer is large compared to q_c i.e.$q_z \gg q_c$ more

specifically $q_z > 3q_c$, the following asymptotic behaviour of Fresnel reflectivity (R_F) is observed.

$$R_F(q_z) = [(\frac{q_c}{2q_z})^4] \tag{3–10}$$

Therefore, for high value of q_z, the reflectivity for an ideally sharp interface will vary with q_z^{-4}.

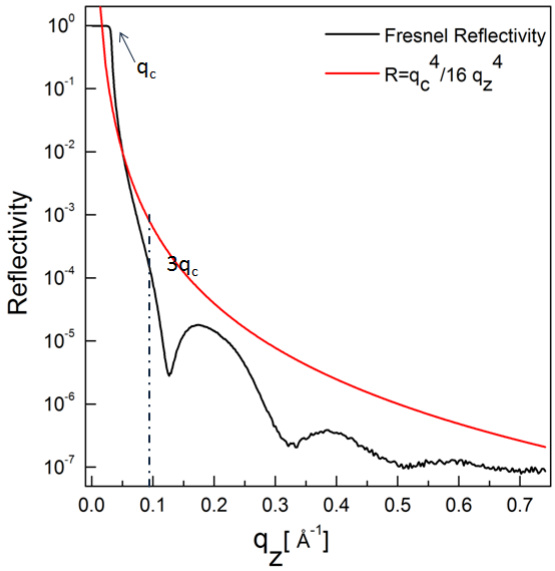

Figure 20: Calculated Fresnel reflectivity for a flat silicon surface. Red line shows the asymptotic curve given by Eq. 3–10. Black line shows the experimental Reflectivity for a monolayer of OTS on flat silicon surface.

It can be seen from Fig.20 that the reflectivity curve or reflectivity profile consists of three different regimes: It starts with a plateau of total external reflection R = 1 for $q < q_c$ which is followed by a region of very steep decrease when $q = q_c$ and finally the region where R follows $1/q^4$ power law for $q > 3q_c$. It is worth noting that if the value of q_c is measured experimentally, this immediately yields the value of the electron density in the material [265] since, $q_c = 3.75 \times 10^{-2}\sqrt{\rho_e}$ where ρ_e is the electron density in the units e/Å^3 .

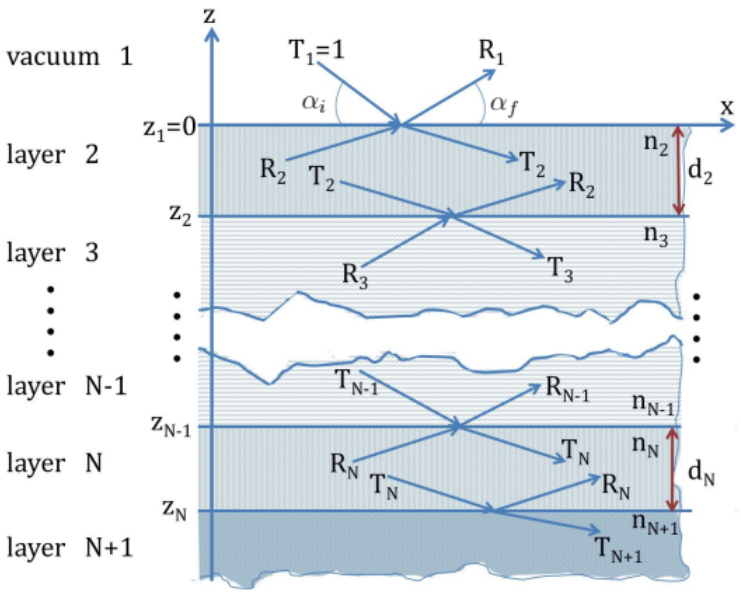

Figure 21: Sketch of a system consisting of N+1 layers with N interfaces. In the case of reflectivity the condition $\alpha_i = \alpha_f$ holds. The incident wave amplitude is normalized to unity, $T_1 = 1$. No wave is reflected from the substrate, i.e. $R_{N+1} = 0$ [221].

3.1.3 XR from a heterogeneous multi layered system

The formalism for describing the scattering at a single sharp interface has been extended to the multilayer system with arbitrary number of homogeneous layers having sharp interfaces, by applying the boundary conditions for electric and magnetic fields at each of the interfaces between the slabs of constant electron density, as shown in Fig.21. The transmission and reflection coefficients of two succeeding layers are coupled via matrices by F. Abèles (1950) and L. G. Parratt (1954) who developed a recursive formalism for analysing the scattering. The ratio of the reflected to transmitted wave amplitudes for the lower interface of j^{th} layer is given by the recursion formula (Parratt's recursion formula) as

$$X_j = \frac{R_j}{T_j} = \exp(-2ik_{z,j}z_j)\frac{r_{j,j+1} + X_{j+1}\exp(2ik_{z,j+1}z_j)}{1 + r_{j,j+1}X_{j+1}\exp(2ik_{z,j+1}z_j)} \tag{3–11}$$

where $r_{j,j+1} = (k_{z,j} - k_{z,j+1})/(k_{z,j} + k_{z,j+1})$ is the Fresnel coefficient of interface j and $k_{z,j} = k\sqrt{n_j^2 - cos^2\alpha_i}$ is the z - component of the wave vector in layer j

of refraction index n_j. Since there is no reflection from the substrate, $R_{N+1} = X_{N+1} = 0$.

The specular reflection intensity R is obtained from Eq. after N iterations and is given as

$$R = \mid X_0 \mid^2 = \mid R_0 \mid^2$$

with the value of R_1 and considering $T_1 = 1$, the amplitudes R_j and T_j for all layers are given recursively by

$$R_{j+1} = \frac{1}{t_{j+1,j}}\{T_j r_{j+1,j} \exp[-i(k_{z,j+1} + k_{z,j})z_j] + R_j exp[-i(k_{z,j+1} - k_{z,j})z_j]\} \quad (3\text{–}12)$$

and

$$T_{j+1} = \frac{1}{t_{j+1,j}}\{T_j \exp[i(k_{z,j+1} - k_{z,j})z_j] + R_j r_{j+1,j} \exp[i(k_{z,j+1} + k_{z,j})z_j]\} \quad (3\text{–}13)$$

with the Fresnel transmission coefficient $t_{j+1,j} = 1 + r_{j,j+1}$ at the interface j.

The reflectivity thus obtained displays oscillations due to interference of waves reflected from the top and bottom interfaces. These are known as Kiessig fringes [270]. From the period $\delta\alpha_i$ the layer thickness may be estimated via $d = 2\pi/\delta q_z \approx \lambda/(2\delta\alpha_i)$, where $q_z = 2k \sin\alpha_i$ is the wave vector transfer as defined before.

3.1.4 Scattering from rough interface

The formalism described in above section, only deals with the sharp interfaces of the system. However, real system involves roughness at surfaces/interfaces. Thus, further modification/correction of the formalism is necessary to describe a realistic systems. A density fluctuations around a rough interface z_j is shown in Fig.22. So, the sample structure, averaged over (x, y), can be expressed as

$$n_j(z) = \iint n_j(x, y, z)dydx \quad (3\text{–}14)$$

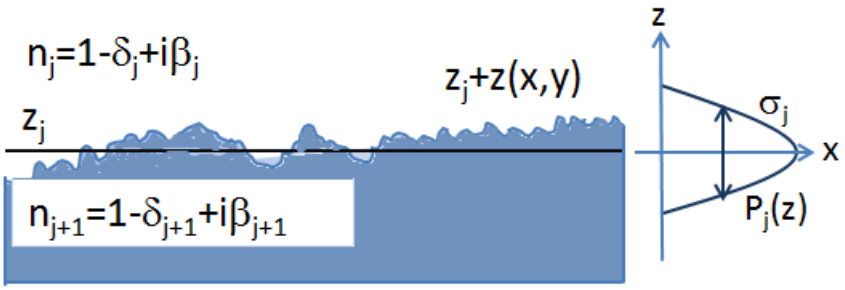

Figure 22: Rough interface with mean z coordinate z_j and fluctuations z(x, y) around this value. The surface is replaced by an ensemble of smooth surfaces at coordinates z_j + z with probability density P_j(z) [221].

The influence of roughness on the reflected intensity may be estimated by averaging the right hand sides of Eqs.3–12 and 3–13. If the sharp interface is replaced by an ensemble of interfaces within z and $z_j + z$ with a probability distribution function of $P_j(z)$, the mean value is given by

$$\mu_j = \int z P_j(z) dz \tag{3–15}$$

and root-mean-square (rms) roughness as

$$\sigma_j^2 = \int (z - \mu_j)^2 P_j(z) dz$$

. with the function $f_j(k)$ is defined as

$$f_j(k) = < \exp -ik(z - \mu_j) >_{P_j(z)} = \exp(ik\mu_j) \int \exp(-ik_z) P_j(z) dz$$

After averaging Eqs.3–12 and 3–13 we get

$$R_{j+1} = \frac{1}{\tilde{t}_{j+1,j}} T_j \tilde{r}_{j+1,j} \exp[-i(k_{z,j+1} + k_{z,j})zj] + R_j \exp[-i(k_{z,j+1} - k_{z,j})z_j]$$

$$T_{j+1} = \frac{1}{f_t \tilde{t}_{j+1,j}} T_j \exp[i(k_{z,j+1} - k_{z,j})z_j + R_j f_r \tilde{r}_{j+1,j} \exp[i(k - z, j + 1 + k_{z,j})z_j]$$

with the respective modified Fresnel coefficients for the rough interface as

$$\tilde{r}_{j+1,j} = \frac{f_j(k_{z,j+1} + k_{z,j})}{f_j(k_{z,j+1} - k_{z,j})} r_{j+1,j}$$

$$\tilde{t}_{j+1,j} = \frac{1}{f_j(k_{z,j+1} - k_{z,j})} t_{j+1,j}$$

. here $r_{j+1,j}$ and $t_{j+1,j}$ are those for smooth interfaces as calculated before and

$$f_r = \frac{f_j(k_{z,j+1} - k_{z,j})}{f_j(-k_{z,j+1} + k_{z,j})} \frac{f_j(-k_{z,j+1} - k_{z,j})}{f_j(k_{z,j+1} + k_{z,j})}$$

$$f_t = \frac{f_j(k_{z,j+1} - k_{z,j})}{f_j(-k_{z,j+1} + k_{z,j})}$$

However, for X-ray, we approximate f_r and f_t as unity. If a continuous refractive-index profile between layers j and j + 1 is taken as

$$n_j(z) = \frac{n_j + n_{j+1}}{2} - \frac{n_j - n_{j+1}}{2} \operatorname{erf}(\frac{z - z_j}{\sqrt{2}\sigma_j})$$

the error function may be defined by

$$\operatorname{erf}(z) = \frac{2}{\sqrt{\pi}} \int_0^z \exp(-t^2) dt,$$

with a Gaussian probability density $P_j(z)$ at μ_j = 0 is expressed as

$$P_j(z) = \frac{1}{\sqrt{2\pi\sigma_i}} \exp(-\frac{z^2}{2\sigma_j^2})$$

So, the modified Fresnel coefficients are given as

$$\tilde{r}_{j,j+1} = r_{j,j+1} \exp(-2k_{z,j}k_{z,j+1}\sigma_j^2) \tag{3–16}$$

$$\tilde{t}_{j,j+1} = t_{j,j+1} \exp[(k_{z,j} - k_{z,j+1})^2 \sigma_j^2 / 2]$$

It should be noted that in the case of a single surface, these coefficients directly describe the reflectivity and transmittance of that interface. A comprehensive overview about scattering from rough interfaces is given in Ref. [221].

The parameter σ_j is the measure of roughness between j th and (j+1)th interfaces, and roughness acts like a Debye-Waller Factor [267]. σ_j is actually the Root Mean Square (RMS)fluctuation of the interface with respect to the average interface. Equation3–16 also explains the observation that reflectance of rough surface $r_{j,\tilde{j+1}}$ deviates more from the reflectance for smooth surface $r_{j,j+1}$ as $k_{z,j+1}$ and $k_{z,j}$ increase with $k_{z,0}$ (or k_z). For a surface separating two media (as shown in Figure 22), Equation3–16 can be simplified [271] as

$$R_{rough}(q_z) = R_F(q_z)\exp[-2k_z^2\sigma_{1,2}^2] = R_F(q_z)\exp[-q_z^2\sigma_{1,2}^2/2] \tag{3–17}$$

where $R_F(q_z)$ is the Fresnel reflectivity given in Equation 3–10 and $\sigma_{1,2}$ represents surface roughness at the interface of the two media. In general, the roughness of the film surface brings down the reflectivity curve faster while the roughness of the interface of the film and the substrate reduces the amplitude of multilayer peaks.

3.1.5 Resolution function

In all the previous calculation of reflectivity for flat surface, homogeneous medium and heterogeneous system it has been assumed that the beam is monochromatic, perfectly collimated and the detector is a point detector. Whereas in the actual experimental situation there is some amount of dispersion in wavelength, divergence in beam and finiteness in the size of source and detector.

In all the theoretical formalism X-ray beam is assumed to be monochromatic and collimated. The detector used to catch the reflected beam is a point detector. But due to wavelength dispersion, divergence in beam and finiteness in the size of source and detector,the practical reflectivity data does not match with the

simulated one using the above theoretical approaches. For this purpose a resolution function, taking into account the experimental situations like wavelength dispersion $\Delta\lambda/\lambda$ angular divergence of incident beam ($\Delta\alpha_i$) and outgoing beam ($\Delta\alpha_f$), is convoluted with calculated reflectivity profile as $R(q_z) \otimes \Re(q_z)$. The resolution function is given by [221, 265],

$$\Re(q_z) = \frac{1}{\sqrt{2\pi}\sigma_s} \exp(-\frac{(q_z - q'_z)^2}{2\sigma_s^2}) \tag{3–18}$$

Therefore the resolution function is given by an Gaussian function. The standard deviation σ_s is related to the FWHM δq_z of the Gaussian function by the relation $\sigma_s = \Delta q_z/(2\sqrt{2log2})$. Δq_z is a function of the geometry of experimental set-up and $\Delta\lambda/\lambda$. Usually during XR experiments, the detector slits perpendicular to the scattering plane is kept widely open to integrate out the component of $\boldsymbol{q}$ perpendicular to the scattering plane. Considering the x-z plane as the scattering plane, q_z can be written as ,

$$q_z = \frac{2\pi}{\lambda}(\sin\alpha_i + \sin\alpha_f) = k(\sin\alpha_i + \sin\alpha_f)$$

where k is the magnitude of incident or reflected wave vector and is related to wavelength λ by the relation

$$k = 2\pi/\lambda$$

. Differentiating above Eqn. we get,

$$dq_z = k(\cos\alpha_i d\alpha_i + \cos\alpha_f d\alpha_f) + dk(\sin\alpha_i + \sin\alpha_f) \tag{3–19}$$

Since $d\alpha_i$ and $d\alpha_f$ are randomly distributed, first moment of distribution $\langle\Delta\alpha_i\rangle = \langle\Delta\alpha_f\rangle = 0$ and Δq_z is given by,

$$\Delta q_z^2 = k^2(\cos^2\alpha_i\Delta\alpha_i^2 + \cos^2\alpha_f\Delta\alpha_f^2) + \Delta k^2(\sin\alpha_i + \sin\alpha_f)^2 \tag{3–20}$$

In the XR set up used for our experiment, distance between X-ray source and sample was kept equal to the distance between sample and detector. In this geometry $\Delta\alpha_i = \Delta\alpha_f = \Delta\theta$. The $\Delta\theta$ can be calculated from the profile of direct beam. Therefore in specular condition Eq.3–20 becomes,

$$\Delta q_z = k[2\cos^2\theta\Delta\theta^2 + (\frac{\delta k}{k})^2 4\sin^2\theta]^{1/2} \tag{3–21}$$

The first term in Eqn.3–21 comes due to the presence of angular divergence of the source and detector and the second term represents the dispersion in wavelength. For perfectly monochromatic X-ray source the wavelength dispersion term vanishes.

3.1.6 Kinematical theory or Born approximation

As revealed from the name, three approximations are used in this approach called Born Approximation. First one is not taking account the multiple Scattering at the interfaces. Secondly, the effects of refraction at the interfaces are neglected. Third assumption is that reflection coefficient at each interface is proportional to the difference of electron density.

So, if we consider the multilayered system to be made of an infinite number of thin layers, using the reflectance of a single layer derived in Eqn.3–12, the total reflectance of the system using Born Approximation transforms into an integral over z; and the reflectance takes the form

$$R(q_{z,0}) = \frac{(4\pi r_e)^2}{q_z^4} \mid \int_{-\infty}^{-\infty} \frac{d\rho(z)}{dz}\, exp[iq_{z,0}z]dz \mid^2 \tag{3–22}$$

where, $\rho(z)$ is the ED at depth z (from top of the sample) averaged over the x-y plane, $r_e = e^2/m_e c^2 = 2.818 \times 10^5$ Å is classical radius of electron or the Thomson

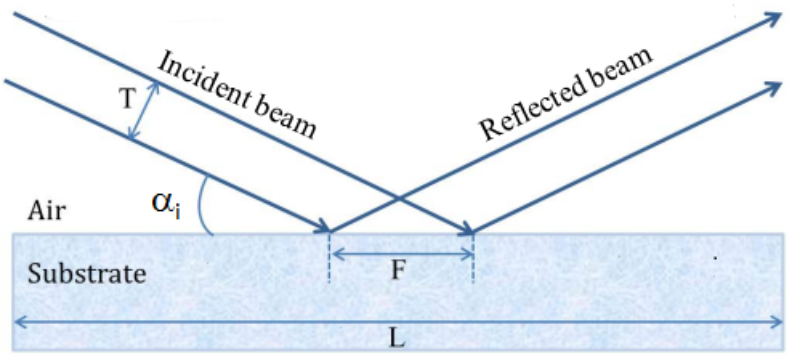

Figure 23: Schematic diagram of the footprint of a beam of size T incident on a substrate of length L at an angle α_i

scattering length. In the simplest possible situation where scattering from a bare substrate is considered, the ED is a step function and the above equation becomes

$$R(q_{z,0}) = R_F(q_{z,0}) \mid \frac{1}{\rho_\infty} \int_{-\infty}^{-\infty} \frac{d\rho(z)}{dz} \, exp[iq_{z,0}z]dz \mid^2 \quad (3\text{–}23)$$

$$= R_F(q_{z,0}) \mid F(q_{z,0}) \mid^2 \quad (3\text{–}24)$$

This analytical equation is popularly known as the Master Formula with ρ_∞ being the electron density of the substrate and $R_F(q_{z,0})$ as the Fresnel reflectivity which does not hold at small angle. And $F(q_{z,0})$ is called the structure factor obtained from the Fourier transform of the derivative of the EDP ρ(z). But near the critical angle where multiple scattering is quite strong, there is a obvious mismatch between the calculated reflectivity using dynamical approach and Born approximation .

3.1.7 Data correction

Since the beam size used in XR experiments is finite, at the grazing incidence the footprint of the beam can be greater than the substrate [221] and there occurs a loss of reflected intensity. This loss is corrected in the footprint correction before fitting the experimental data using theoretical models . As shown in Fig.23 a beam of dimension 'T' incidents on the sample of length 'L' with an angle α_i

making a footprint of size 'T' on the sample. The footprint 'F' of the beam of thickness 'T' can be written as ,

$$F = T / \sin \alpha_i$$

.

Now for $\alpha_i < \alpha_{min}$ the footprint of the beam becomes wider than the dimension of sample. The loss of incident counts are then corrected for this incident angle below α_{min} by multiplying the reflected intensity at any angle α_i with the factor $T/L \sin \alpha_i$. The thickness of the incident beam is an intrinsic property and depends also on the aperture of the slit. Generally for rectangular slit, the aperture of the slit is taken as the thickness of the beam. However,essentially the incident slit aperture is chosen properly such that $F < L$ for $\alpha_i = \alpha_c$ where α_c is the critical angle.

3.2 Off-specular scattering or diffuse scattering

As discussed in the XR section,in case of specular X-ray scattering experiments we consider only specularly scattered data of the X-ray. But due to a finite roughness at film surfaces, the intensity of specularly reflected part damps and this missing intensity is scattered at the reflected angle $\alpha_f \neq \alpha_i$ i.e. in off specular direction [221, 265], as shown in Fig.24. Study of the diffusely scattered intensity gives information about the in-plane density correlation of the films which is used for shape analysis at surface or buried interfaces. The off-specularly scattered data is collected by varying the angle of the sample with respect to the incident beam while source and detector is kept at fixed positions i.e. by taking rocking curve of the sample. For XR technique only the z-component of momentum transfer vector (q_z) have non-zero value which gives us the in-depth information. While for rocking curve since $\alpha_f \neq \alpha_i$ x-component of momentum transfer vector

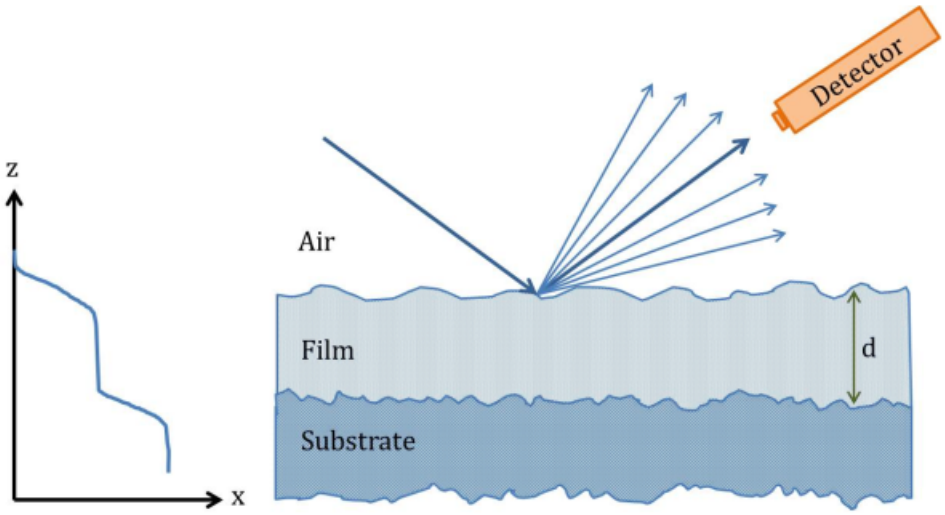

Figure 24: Schematic diagram of off-specularly reflected X-ray

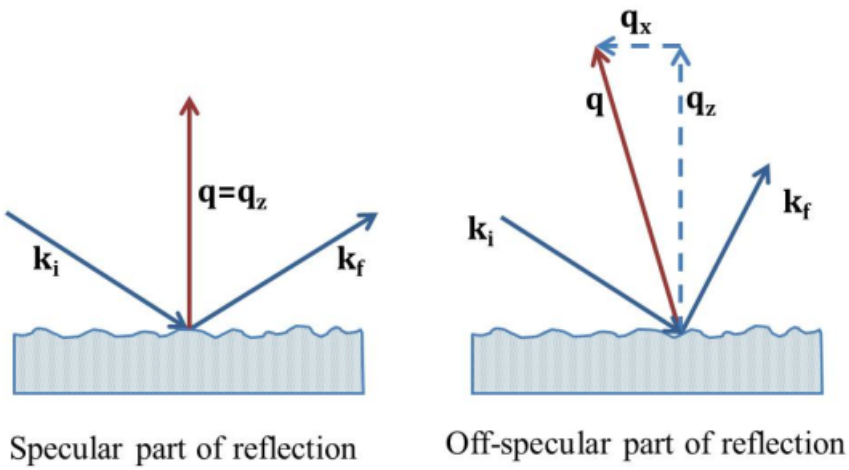

Figure 25: Resultant momentum transfer vector for specular and off-specular part of reflected ray. Figure on the right side indicates non-zero q_x for off-specular reflection

(q_x) also has non-zero value, as shown in Fig.25, and thus probes the in-plane information.

3.2.1 Born approximation

Specular reflectivity from perfectly smooth surface/interface, following the first-order Born approximation (refer to Eqn.3–22) needs to consider only the FT of the gradient of ED along the depth (z-axis), however, to study the in-plane structure of a surface/interface by off-specular reflectivity [221, 265, 272–275] the in-plane

density variation along lateral direction has to be included. Considering the three dimensional density function as $\rho(\boldsymbol{r}) = \rho(x,y,z) = \rho(z) + \Delta\rho$. Here $\Delta\rho$ is the lateral fluctuation of density and $\rho(z) =< \rho(x,y,z) >_{(x,y)}$is the vertical part of the density. So Eqn.3–22 can be written as

$$R(\boldsymbol{q}) \propto \left| \int d\boldsymbol{r}\rho(\boldsymbol{r}) \exp^{i\boldsymbol{q}.\boldsymbol{r}} \right|^2 \tag{3–25}$$

$$\propto \int\int \rho(\boldsymbol{r})\rho(\boldsymbol{r'}) \exp^{[i\boldsymbol{q}.(\boldsymbol{r}-\boldsymbol{r'})]} d\boldsymbol{r}d\boldsymbol{r'} \tag{3–26}$$

In order to proceed further we need to introduce the statistical description of an interface. Considering the difference in heights for the surface/interface at two different positions (x, y) and (x′, y′) as a Gaussian random variable, a height difference correlation function can be defined as

$$g(\boldsymbol{R}) = g(X,Y) =< [h(x,y) - h(x',y')]^2 > \tag{3–27}$$

where, the height h(x, y) is defined from an average value of z for a surface/interface. $R = (X,Y)$ with X = x-x′ and Y = y-y′. The average is taken over all pairs of points on the surface. Further, g(X, Y) in Eqn.3–27 can be expanded as

$$g(\boldsymbol{R}) = 2[\sigma^2 - C(\boldsymbol{R})] \tag{3–28}$$

where, rms roughness σ is defined by $\sigma = \sqrt{< h(0)^2 >} = \sqrt{< h(\boldsymbol{R})^2 >}$ and $C(\boldsymbol{R}) =< h(0)h(\boldsymbol{R}) >$ is height-height correlation function.

So introducing this height difference in Eqn. 3–26 we get

$$\begin{aligned} R(\boldsymbol{q}) &\propto \int\int \rho(\boldsymbol{r})\rho(\boldsymbol{r'}) \exp^{[i\boldsymbol{q}.(\boldsymbol{r}-\boldsymbol{r'})]} \\ &\propto \int \rho(\boldsymbol{r})d\boldsymbol{r} \int \rho(\boldsymbol{r'})d\boldsymbol{r'} \exp^{-iq_z^2 g(X,Y)/2} \exp^{i[q_x X + q_y Y]} \end{aligned} \tag{3–29}$$

where, $\boldsymbol{q}.\boldsymbol{r}$ is taken as $q_z h(x,y) + q_x x + q_y y$ and, $\exp[iq_z(h(x,y) - h(x',y')] =< \exp[iq_z(h(0,0) - h(x,y))] >= \exp[-iq_z^2 g(X,Y)/2]$ since Gaussian distribution is assumed.

3.2.1.1 Bare substrate interface

As revealed from Eqn.3–26 the scattering intensity depends on electron density of the sample. In the simplest possible situation where scattering from a bare substrate is considered, the ED is a step function:

$$\begin{aligned} \rho(\boldsymbol{r}) &= \Delta\rho \quad , \; z > 0 \\ &= 0 \quad , \; z \leq 0 \end{aligned}$$

Applying this, Eqn.3–29 can be written in three dimension as

$$R(\boldsymbol{q}) \approx \frac{(\Delta\rho)^2}{q_z^2} \int\int dxdy \int\int dx'dy' \exp^{-iq_z^2 g(X,Y)/2} \exp^{i[q_x X + q_y Y]} \tag{3–30}$$

By performing appropriate change of variables and using Eqn.3–28 one can write, Eqn.3–30 as

$$\begin{aligned} R(\boldsymbol{q}) &\propto \frac{(\Delta\rho)^2}{q_z^2} \int\int dXdY \exp^{i[q_x X + q_y Y - \frac{q_z^2 g(\boldsymbol{R})}{2}]} \\ &\propto \frac{(\Delta\rho)^2 \exp^{-q_z^2\sigma^2}}{q_z^2} \int \exp^{q_z^2 C(\boldsymbol{R})} \exp^{i[q_\parallel.\boldsymbol{R}]} \, d\boldsymbol{R} \\ &\propto R(\boldsymbol{q})^{spec} + R(\boldsymbol{q})^{diff} \end{aligned} \tag{3–31}$$

Here the specular part of the scattered intensity is defined as

$$R(\boldsymbol{q})^{spec} \propto \frac{(\Delta\rho)^2 \exp^{-q_z^2\sigma^2}}{q_z^2} \int \exp^{i[q_\parallel.\boldsymbol{R}]} \, d\boldsymbol{R} \tag{3–32}$$

And the Diffuse reflectivity part,

$$R(\boldsymbol{q})^{diff} \propto \frac{(\Delta\rho)^2 \exp^{-q_z^2\sigma^2}}{q_z^2} \int F(q_z, \boldsymbol{R}) \exp^{i[q_\parallel.\boldsymbol{R}]} \tag{3–33}$$

where, $q_{\parallel} = (X, Y)$ and $F(q_z, \boldsymbol{R}) = \exp^{q_z^2 C(\boldsymbol{R})} - 1$. It can be concluded from the above Eqn. that $R(\boldsymbol{q})^{diff}$ can be obtained with different form of $g(\boldsymbol{R})$ for different type of surfaces/interfaces. It is proportional to $\Delta\rho$. Also it is evident that $R(\boldsymbol{q})^{diff}$ is not proportional to PSD i.e. Fourier transform of $C(\boldsymbol{R})$. The important parameter which is the cut-off length for height-height correlation of a surface roughness is the correlation length, ξ (for $R << \xi$, the surface is self-affine, whereas for $R >> \xi$, the surface appears to be smooth). Eqn.3–28 can be written as,

$$g(\boldsymbol{R}) \approx 2\sigma^2(1 - \exp^{-(\boldsymbol{R}/\xi)^{2H}}) \tag{3–34}$$

with $C(\boldsymbol{R}) = \sigma^2 \exp^{-(\boldsymbol{R}/\xi)^{2H}}$. H is called the Hurst parameter or roughness exponent.

In this thesis work we have employed this technique to study the in-plane structural evolution of AuNPs thin films for different Π values. For a completely flat surface rocking curve would be a perfectly delta function. Width of the rocking curve can be directly related to the roughness of the surface while the shape of the curve can give an insight about the presence of any surface features. Studying the evolution of rocking curve with different surface pressure and for different time of exposure, in this thesis work, we have probed the evolution of surface structure of the films qualitatively.

3.2.2 Grazing incidence small angle X-ray scattering

The GISAXS geometry used for characterization of the samples is shown schematically in Fig.26. GISAXS as an advanced scattering technique is performed in reflection geometry and gives results in reciprocal space. The surface of the sample is defined as the x-y plane and the plane of the incident X-ray beam (of wavelength λ) is defined as the x-z plane. α_i is the incident angle with the x -y plane and α_f and ϕ are the exit angles with the x - y and x - z planes, respectively. In GISAXS technique, we can measure the diffuse scattering around the specularly reflected beam at fixed incidence angle α_i. The scattering angles

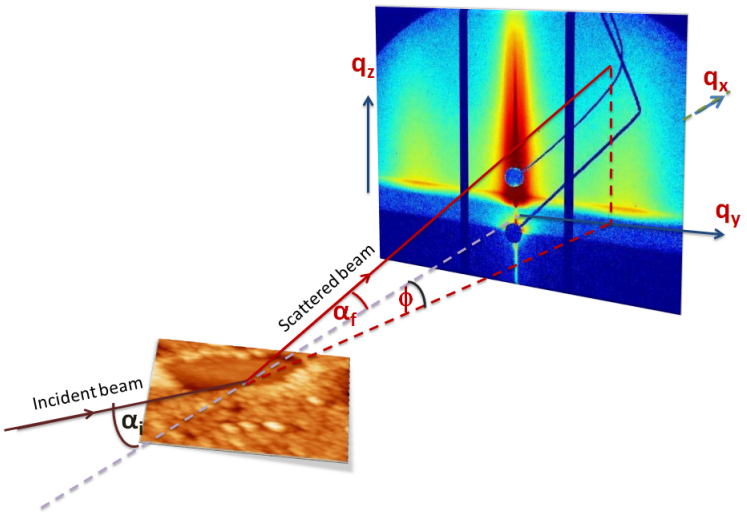

Figure 26: Schematic of the scattering geometry used to perform GISAXS measurements.

(α_f and ϕ) are related to the components of the wave vector transfer, $\boldsymbol{q}$ (q_x, q_y, q_z), by the following relations

$$q_x = (2\pi/\lambda)(\cos\alpha_f \cos\phi - \cos\alpha_i) \quad (3\text{–}35)$$

$$q_y = (2\pi/\lambda)(\cos\alpha_f \sin\phi) \quad (3\text{–}36)$$

$$q_z = (2\pi/\lambda)(\sin\alpha_f + \sin\alpha_i) \quad (3\text{–}37)$$

The scattered beam intensity is a function of α_f and ϕ. In a conventional GISAXS experiment, the recorded data is labeled and analyzed as a map of the (q_y, q_z) reciprocal plane by varying α_f and ϕ. In a typical GISAXS pattern the presence of two sharp peaks is obvious due to the transmitted and specularly reflected beams apart from specular rod or broad hump arising from diffuse scattering. The z=o sample surface is called the horizon while an enhancement of scattering, the so-called Yoneda peak, is found at an exit angle α_f close to the angle of total external reflection α_c. For specular scattering part, the wave vector components $q_x = q_y = 0$ and $q_z \neq 0$ here reveals a depth sensitive information only. With off-specular scattering, the lateral component is $q_{\|} = (q_x, q_y) \neq 0$ probing the in-plane structure of the sample.

GISAXS measurements performed at laboratory sources are very limited. So GISAXS experiments are done using synchrotron sources. In our GISAXS experiments, we are not interested in the specular reflection and have focused only on the diffuse scattering part. We are mainly in a search of the hints coming arising due to in-plane structure of the thin film which can be derived from the Bragg spot present in the q_y - q_z reciprocal space in GISAXS pattern.

GISAXS is used to probe the morphology both parallel to (along q_y) and perpendicular to (along q_z) the sample surface at length scales typically ranging from a few nm to a few hundred nm.For GISAXS all angles are assumed to be small (less than a few degrees). In that case

$$q_x \simeq 0 \tag{3–38}$$

$$q_y \simeq (2\pi/\lambda)\sin\phi \simeq (2\pi/\lambda)\phi \tag{3–39}$$

$$q_z \simeq (2\pi/\lambda)\alpha_f \tag{3–40}$$

i.e., the reciprocal space scales with the angular coordinates.

From GISAXS data we can find out the geometry, size distributions and spatial correlations present in the thin films on nanometer length scales. Either a Linear Position Sensitive Detector (PSD) or a 2D Area Detector is employed for recording data in this geometry. In our GISAXS measurement beam-stops are used to block the direct beam and the specularly reflected beam from hitting the 2-D detector to avoid the detector saturation as several orders of magnitude in intensity separate the diffuse scattering from the specular reflectivity. The GISAXS pattern recorded on the 2d detector is symmetric with respect to the scattering plane. Due to refraction and reflection effects the Yoneda peak, which is the maximum of the off-specular diffuse scattering intensity, is located at the critical angle for total external reflection, i.e, at α_c.

As the angle of incidence in GISAXS study is kept close to the critical angle, the kinematical approximation of single scattering, the so-called Born approximation

does not expected to be valid for GISAXS analysis and one has to consider the distorted wave Born approximation (DWBA) [273, 276, 277]. DWBA can be thought as a semi-dynamical treatment where the multiple scattering from interfaces is included in the reference state while the roughness leads to a single scattering event between reference states and the roughness is viewed as a perturbation of a known reference state. For poly dispersed systems, the GISAXS intensity is commonly calculated within the local mono disperse approximation, which considers locally mono disperse domains that interfere incoherently [278]

$$I(\boldsymbol{q}) \propto \int_0^\infty \mid F(\boldsymbol{q}) \mid^2 S(\boldsymbol{q}) N(R) dR \tag{3–41}$$

where $F(\boldsymbol{q})$ is the form factor of the scattering objects, $S(\boldsymbol{q})$ is the structure factor due to the spatial correlation, and N(R) is the size distribution function. Single particle form factor is expresses as

$$F(\boldsymbol{q}) = \frac{1}{V_P} \int_{V_P} \exp^{i\boldsymbol{q}.\boldsymbol{r}} d\boldsymbol{r} \tag{3–42}$$

The form factor depends on the morphology, size and shape of the particle through the integral over its volume, V_P. As for example the form factor for a sphere of radius R calculated using the above Eqn. will be

$$F(\boldsymbol{q}) = 3[\frac{\sin(qR) - qR\cos(qR)}{q^3R^3}] \tag{3–43}$$

On the other hand inter particle correlations are accounted for by introducing the structure factor $S(\boldsymbol{q})$ which varies if the distribution of particles changes its nature. Moreover, at grazing incidence conditions, dynamical scattering effects have to be taken into account since the Born approximation (BA) fails in reproducing the measured data so long as $\alpha_{i,f}$ are close to the critical angle of total reflection. Details GISAXS intensity calculation using different particle size and distribution related to thesis work will be discussed in corresponding chapters.

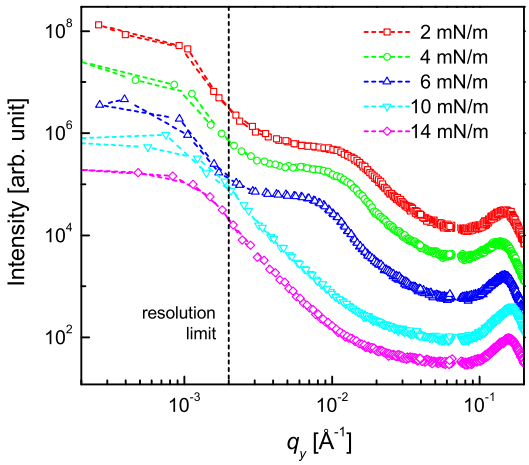

Figure 27: GISAXS line profiles along q_y direction for the DT-AuNPs/H-Si LS films deposited at different surface pressure. Curves are shifted vertically for clarity. The straight dashed line marked the resolution limit along q_y direction.

3.2.2.1 Resolution limit along q_y-direction in GISAXS

The resolution limit along q_y-direction is a very important parameter in understanding the long-range in-plane correlations in a system, such as the domains, if any. Such resolution limit depends upon the detector-to-sample distance, beam-size and most importantly on the beam divergence. Increase in the value of first one and decrease in the values of latter two decreases the value of the resolution limit, which in turn increases the measurement length scale. However, the scattering intensity decreases for the increase in the detector-to-sample distance and for the decrease in the beam size. Thus high intensity, low divergence micro-focused beam is essential which is available at MiNaXS beamline of PETRA-III.[1] The detector-to-sample distance and beam divergence imposed resolution limit along q_y-direction (about 0.002 Å^{-1}), as observed from the GISAXS line profiles, is marked by the vertical line in Fig. 27. Such resolution limit can very well determine any long-range in-plane correlations within 300 mn length scale.

It is necessary to mention that such low value, which is mainly achievable in this beamline (due to very small divergence of the micro-focused beam), is absolutely essential for the direct estimation of the long-range in-plane correlations, such as the domains, if any, along with the short-range in-plane correlations, such as the separation between AuNPs.

3.3 Fitting of data and modelling

The X-ray scattering data collected over a lot of samples using both specular and diffuse scattering techniques is interesting subject to proper extraction of physically relevant parameters from the data. As discussed in the preceding sections, the data extraction process is often non-trivial. The fits are highly dependent on the initial guess model and yield reasonably good results when the final model is not very far off from the initial one.

The aim of a reflectivity measurement is the determination of the unknown density profile of a sample. However, in most of the cases the materials which are involved in the experiments are known beforehand, and hence using their bulk densities we can approximately define their electron density in the film taking account the film thickness, surface coverages, thin film material's weight volume ratios etc.

To verify the uniqueness of the model different formalisms can be used in fitting the experimental data. Several assumptions have been made depending upon the formalism used for the fitting process. In case of XR of thin films deposited on substrates (performed mostly using a lab source of X-rays), the data was first normalized and then incorporating the footprint corrections for individual sample, particularly near the critical angle, the data has been processed. The corrected data has been fitted using Parratt formalism by self-modified code using Fortran 90 as well as using Parratt 32 version 1.6 [279]. During fitting process a constant background is added as well as source resolution has been incorporated. In some cases, both the Parratt as well as the Born formalism were independently used to find the EDP of the sample, and were found to be quite similar. This confirms that the model solution, which has been extracted independently out of two different formalisms, is quite reasonable and the possibility of an erroneous solution can be negated to a large extent.For multilayers or thicker films one has to resort to Parratt formalism only.

The scattering data collected at PETRA III were extracted from the master SPEC file using MATLAB. The geometry of the experimental setup, along with the precise distance between the slits, sample and detector has to be provided to extract the data files from image format to relevant ASCII format. Most of the diffuse scattering data of GISAXS are fitted using self-written (modified) codes using MATLAB. In case of GISAXS data, the scattering cross-section is calculated by assuming an appropriate height-difference correlation function of the scattering surface/interface. Once the starting model seemed reasonably good, the relevant parameters were refined by iterative process till the data was fitted properly. 2D profiles could be generated by integrating over the entire q_z and $q_{||}$ range. For GISAXS data at particular $q_{||}$ value, conformality amongst surfaces was assumed and the fits generated. It is seen that the formalism works nicely for monolayers. The form factor is used to fit the Bragg spot/hump profiles which gives a fair estimate of the particle shape and size. Detailed description of the formalism used to fit the data has been mentioned in the relevant chapters.

3.4 X-ray scattering instrument

In this section we have discussed about the instruments used for X-ray scattering experiments. In my thesis work I have mainly focused on XR and GISAXS measurements.For XR only the lab X-ray source has been used. And for GISAXS measurements we have used synchrotron source since there are huge advantages of using synchrotron X-ray which can not be achieved by lab source. In Synchrotron, X-ray beam is generated with high intensity, higher degree of collimation (i.e. small angular divergence) and lower wavelength dispersion than the lab source. Moreover we can change the wavelength of the incident X-ray according to our needs which is not possible with monochromatic laboratory X-ray source which acts for a fixed energy. Dynamical processes can be probed

more quickly with the help of Highly intense synchrotron X-ray . Here we have discussed different X-ray Scattering set ups one by one.

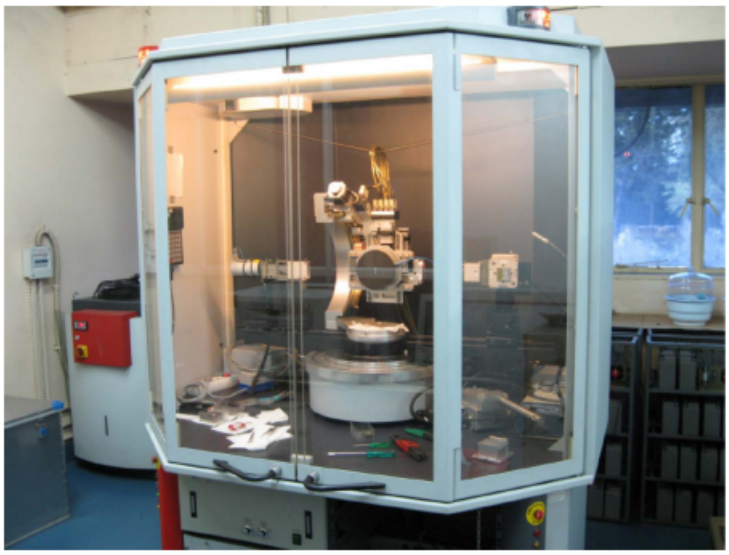

Figure 28: Versatile X-ray Diffractometer

3.4.1 Versatile X-ray diffractometer

Versatile X-ray Diffractometer (VXRD, D8 Discover) from Bruker AXS, Germany has been used in our laboratory to study thickness and structure of AuNps thin films. As source of X-ray the instrument has copper sealed tube [2.2 kW power, $0.04 \times 12\ mm^2$ line focus]. Generated X-ray contains both $K_{\alpha 1}$ and $K_{\alpha 2}$ lines where

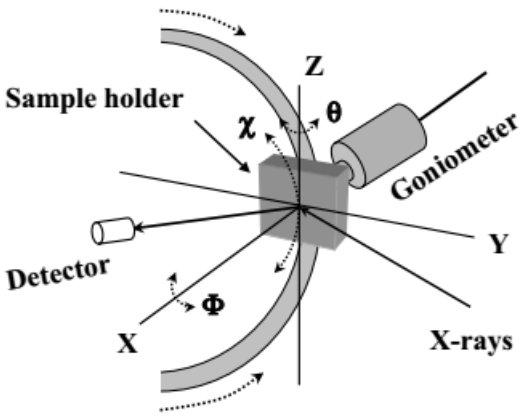

Figure 29: Rotation geometry of the θ, ϕ and χ motors in VXRD setup with 1/4-circle Eulerian cradle.

wavelength of K_α line is λ = 1.54 Å. A Ni/C Góbel mirror is used to enhance Cu k_α radiation. This instrument possesses a 2-circle Huber goniometer (θ and 2θ) and a sample stage with 1/4 circle Eulerian Cradel. The sample stage is usually mounted on the inner θ circle of the goniometer. The goniometer can be used in horizontal $\theta - 2\theta$,vertical $\theta - 2\theta$ and vertical $\theta - \theta$ geometries. The stage is connected to motors for performing 2-circular rotation $\chi(97^\circ)$ and ϕ (360 $^\circ$) and 3-translational movement along X, Y and Z. This sample stage contains a vacuum chuck [suction by rotary pump]. The detector used is a NaI scintillation point detector (with dynamics range of 10^7, count rate $10^5 s^{-1}$ and noise rate 2-10 s^{-1}). The instrument is associated with ERL2000 cooling water unit chiller to maintain the source at a constant temperature. The movements of all parts of the instrument are operated with software controlled stepper motors. The sample is kept along vertical during data collection and the scattering plane lies on the horizontal plane.

A photograph of the instrument is shown in Fig.28 kept in a radiation protection housing. A lead glass window at the front of the radiation protection housing enables the samples to be changed and or the diffractometer mounts to be modified. The window shutter of the X-ray tube stand closes automatically when this window is opened. The laboratory VXRD can also be used for various other purposes; like angle dispersive XR, XRD, small and wide angle X-ray scattering etc.

It is well-known that XR operates in specular region, having both the incident and reflected beams in same scattering plane. This condition makes $\alpha_i = \alpha_f = \theta$. Under such a condition there exists a non-vanishing wave vector component, q_z, which can be equated to $(4\pi/\lambda)\sin\theta$ with resolution $\approx$0.002 Å^{-1}. The qualitative idea about the samples has been obtained from the Kiessig fringes of the XR profiles. To get a qualitative idea the XR profiles have been further analysed.

3.4.2 Synchrotron X-ray sources

3.4.2.1 General principles

Synchrotron radiation takes its name from a specific type of particle accelerator. However, synchrotron radiation has become a generic term to describe radiation from charged particles. In Fig.30 a schematic of the key components of a typical experimental beam line at a third-generation X-ray source is shown. The details will of course vary considerably depending on the particular requirements.

Synchrotron produces linearly polarized X-ray beam rather than the unpolarized one produced in lab source. Also the X-ray beam energy can be tuned at different values for a particular experiment in synchrotron. This is another special advantage of synchrotron source compared to laboratory X-rays where the energy is fixed.

A synchrotron source operates in a specific manner described in the following section: Initially the electrons are accelerated to a high speed in a linear accelerator called, LINAC, to gain energy ($\sim$ GeV). Next the energised electron beam is

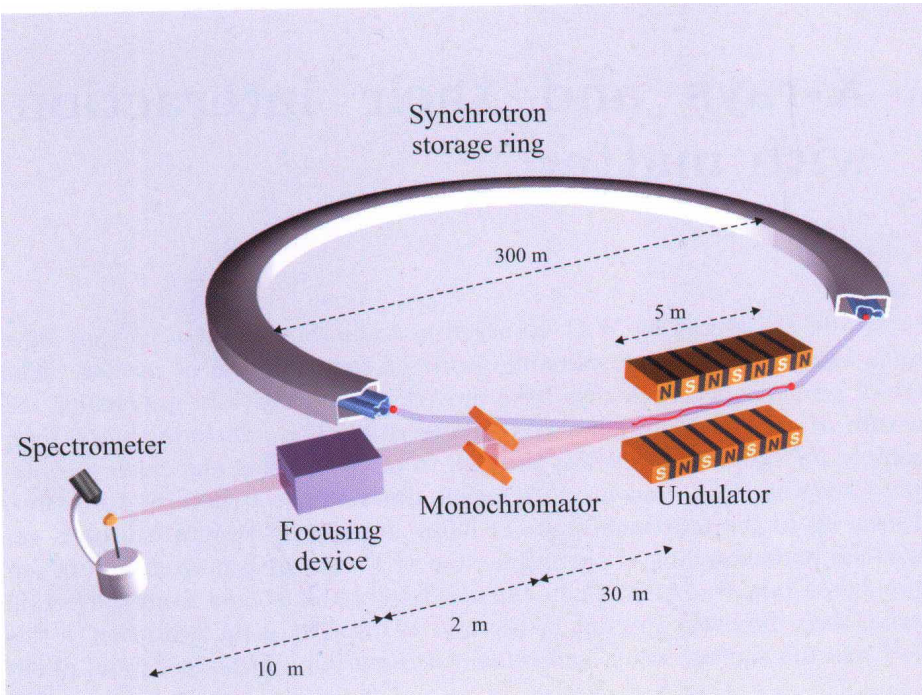

Figure 30: A schematic of a typical X-ray beamline at a third generation X-ray source [267].

transferred to the storage ring where electrons are kept circulating. In second generation synchrotron, bending magnets (installed to make the orbits of electrons a closed one) and in third generation synchrotron, the insertion devices wigglers or undulators produces the alternating strong magnetic field which forces the electrons to follow the curved paths rather than the straight line. And these accelerated electrons radiate covering a broad range of electromagnetic spectrum including X-ray region. This radiation is called Synchrotron radiation, coming out tangentially with the storage ring. So beamlines are set up along that tangential path to collect this radiation. Depending on the number of arranged magnets and spacing between them, the individual emission acts are in phase (undulator) or without a definite phase relation (wiggler). The emission spectrum of synchrotron radiation is well defined [280]. The angular frequency of an electron in the storage ring ω_0 is typically around 10^6 cycles per second, so the hard X-ray frequency cut-off is around 10^{18} cycles per second. To compare different radiation sources the quality of the emitted radiation is characterized by its brilliance:

$$brillance = \frac{dN/dt}{(mrad)^2(mm^2 sourcearea)(0.1\% bandwidth)}$$

Brilliance is the number of photons N, emitted in one second per $1mm^2$ source area, into a radiation cone defined by an spatial opening angle of $1mrad^2$. Then it is normalized on a spectral bandwidth of 0.1% [281]. The brilliance at $K_\alpha$of a fixed tube X-ray source is around 10^7, whereas for rotating anode and 3rd generation synchrotron X-ray sources the values are 10^8 and 10^{20} respectively.

For designing the scattering experiment a well-collimated and monochromatic incident beam of sufficient intensity is needed. After a X-ray beam is extracted from a storage ring, which is considered as white beam, is allowed to pass through a series of vacuum pipes for its conditioning to use it for any particular experiment. The incident beam interacts with the sample and scatters into a definite direction in space. The scattered beam is recorded by a detector. The beam is probed by using various slit systems. Besides this, sophisticated optical elements are used that improves the beam quality and increase the intensity at the

Table 2: P03 Beamline Properties

Source	Type	Undulator
Energy	keV	13
Monochromator	Double crystal	Si(111)
Detector	Type	PILATUS 300k, Dectris
Resolution	Δ E/E	0.5 $\times 10^{-2}$
Image area	pixels	487$\times$ 619
Pixel size	μm	172
Beam Dimension	nm^2	250 $\times$ 350

sample site.This whole section of conditioning a beam is known to be Beamlines. A standard synchrotron beamline consists of the following

The elements of the first group, that increases the beam quality are referred to as monochromators and analysers, since they reduce the energy or angular range accepted by the sample or the detector. Double crystal monochromators extract a particular wavelength from the white beam and align the diffracted beam along the incident one. Collimator is the another optical element that is used for making the beam parallel. The second group of optical elements are flat, parabolic or elliptical mirrors. They collect the photons coming from the incident beam and deflect toward the sample i.e. collimating the beam but with increased angular divergence. Lenses are also used in this purpose. Finally the beam scattered by the sample is detected by 'point-detector' and/or position sensitive detector (PSD) which are attached to a six-circle goniometer.

3.4.2.2 P03 beamline at PETRA III

P03 is the microfocus small- and wide-angle X-ray scattering beamline μ SAXS/WAXS at PETRA III. Among the novel methods that exploit perfectly the most-brilliant beam, are μGISAXS [282] and μSAXS tomography [283], as well as their expansion to nanosized beams [284]. Optics for nanofocusing include KB-mirror, waveguides, and compound refractive lenses. The beamline offers dedicated micro- and nano-focus end stations with a low emittance source and ultra high intensity ideal for both transmission and grazing incidence experiments. The

Nanofocus Endstation (hutch EH2) has been used for our GISAXS experiments. The minimum beam size is 250 nm $\times$ 350 nm and a long focal distance optics is used here to provide a clear working distance of up to 8 cm. Specifications of the synchrotron X-ray scattering facilities used are shown in Table 2.

4

STRUCTURE OF SINGLE-TRANSFERRED DT-AUNPS LS FILMS AND GROWTH OF LANGMUIR MONOLAYERS

4.1 Introduction

MNPs are attracting significant attention because of their unusual optical, magnetic, electronic and catalytic properties. [46, 138, 285–287]. Among them thiol-capped AuNPs (DT-AuNPs) have attracted considerable interest due to their ease of preparation and ability of spontaneous self-assembly into large arrays that offers an accessible route to design regular macroscopic AuNPs layers. [46, 132] New collective phenomena can be explored from such organized structures due to interparticle coupling effect in both in-plane and out-of-plane directions. [46, 129, 132, 138] In that sense, separation between particles and their local ordering as well as long-range ordering and/or connectivity become very important, especially for the preparation of organized structures in large areas.

There are several techniques to prepare packed 2D array or 2D-network pattern from colloidal DT-AuNPs solutions such as drop casting, spin coating, LB and LS depositions, etc. [138, 140, 288]. The LB and LS techniques are especially suitable for the fabrication of uniform nanostructures over large areas, where an ordered AuNP array formed at the air/water interface on a LB trough at an appropriate surface pressure (known as Langmuir film) is transferred onto a solid substrate. [289] Structures of such LB or LS films depend on the initial structures of the Langmuir films, the transfer process and the film-substrate interaction.

The structures of the Langmuir films of DT-AuNPs have been studied using microscopy and scattering techniques. Optical microscopy or BAM has been used to monitor the structures of such films in the micrometer length scales [147, 148] while the scattering, especially GISAXS has been used mainly to monitor the particle arrangement and the interparticle separation. In some cases, the presence of islands or domains have been predicted indirectly from the width of the interparticle separation peak [149, 150] or from the analyzed correlation length, [151] as expected. [152]

However, the complete structures of the Langmuir films (i.e. the size of the islands and their separation or connectivity) at different surface pressure (Π) have never been evident clearly, which is particularly important for the small size AuNPs where the long range van der Waals (vdW) attraction is weak compare to the thermal energies. The structures of the LB and LS films of DT-AuNPs have also been studied directly. The LB films on hydrophilic Si substrates show nanopatterns formation due to drying mediated agglomeration of AuNPs in presence of hydrophobic-hydrophilic interaction between thiols and substrate. [144] The LS films on carbon coated grids have been studied mainly using TEM, which show the ordering of the AuNPs. However, the LS films on large hydrophobic substrate, which is expected to mimic the Langmuir film structure better have never been studied in details using statistically meaningful techniques, such as GISAXS, [290, 291]to have better structural information of the AuNPs Langmuir films, which is otherwise not possible.

The fact that the complete structures of the AuNPs Langmuir or LS films have not been evident so far is mainly associated with the poor resolution limit of the X-ray beam and/or the beam induced damage. Poor resolution limit arises from the relatively broad beam size (used to enhance the beam intensity), relatively large beam divergence (as obtained from most of the sources itself and also due to the use of additional reflecting mirror to impinge the X-ray beam onto the horizontal air/water interface) and relatively small sample-to-detector

distance (required to capture the low scattering intensity). High intensity and small divergence beam of advanced synchrotron sources can, however, create better resolution limit. Even then the requirement of additional reflecting mirror, for the study of Langmuir film, is still a problem. Additionally, intense beam of the advance source can create beam induced damage, especially considering the time required to align the beam on the sample. To minimize the effect of damage, the lateral movement of the beam (or sample) with respect to the sample (or beam) is required for the actual measurements after alignment, which was somehow never considered.

Here we have tried to overcome all such problems by transferring the DT-AuNPs Langmuir films on H-passivated Si substrates using LS techniques and then measuring those close resemblance LS films using GISAXS techniques [292] with high intensity small divergence X-ray beam (having better resolution limit) and by moving the samples laterally before actual measurements (to minimize the beam induced damage). Indeed, a broad peak or shoulder (related to the island separation and/or size), the position of which varies with Π, is observed from such measurements for the first time. Detailed analysis of the GISAXS data correspond to the structures of networked disklike-islands, which are well supported by the AFM images. Further, the present study also infer that the growth of DT-AuNPs Langmuir films is through networked disk-like-islands, the size and networking of which increases while the interparticle separation decreases or increases due to further interdigitization or buckling with Π. This information is important for understanding the self-assembly process and for controlling the nanostructure formation.

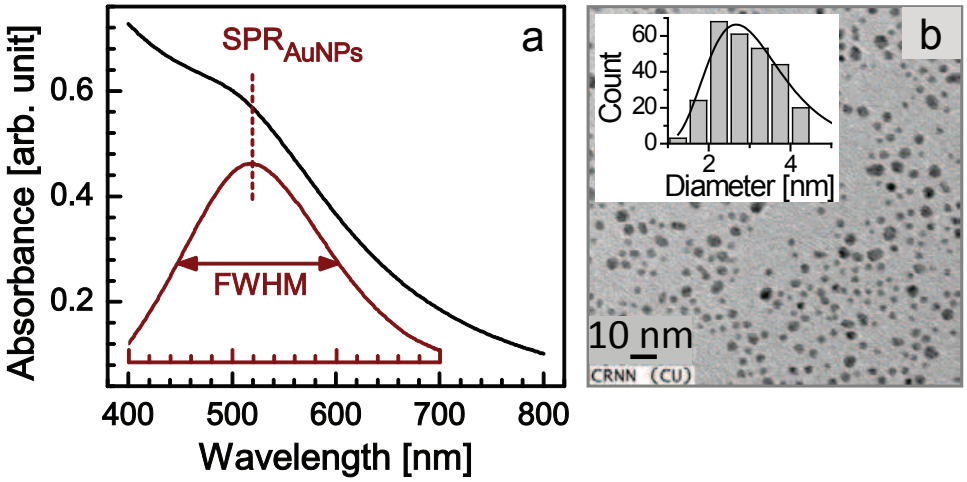

Figure 31: (a) UV-vis spectrum of AuNPs in solution and corresponding background subtracted spectrum to emphasize the SPR peak and its FWHM and (b) typical TEM image of AuNPs in grid and corresponding size histogram in the inset.

4.2 Experimental details

4.2.0.1 Size of DT-AuNPs from UV-vis and TEM

The optical absorption spectra of the thiol-coated Au-AuNPs (DT-AuNPs) in toluene solution were collected with a UV-vis spectrophotometer (Lambda 750, Perkin Elmer), while the transmission electron micrographs of the DT-AuNPs, deposited on a carbon-coated copper grid, were observed using transmission electron microscope (JEM 2100, JEOL). Typical UV-vis spectrum and TEM image for the DT-AuNPs are shown in Fig. 31. A broad hump near 520 nm is observed in the optical absorption spectrum (Fig. 31a), which is a characteristic SPR band of the AuNPs. The peak becomes quite prominent, after subtraction of exponentially decaying background. The size of the core AuNPs ($2R$) is estimated from the full width at half maximum (FWHM) of this peak, which is about 2.5 nm. Formation of AuNPs is also evident from TEM image (Fig. 31b) and corresponding particle size histogram is shown in the inset. The value of $2R$, as estimated from the particle size distribution curve, is 2.5 ± 0.6 nm, which is consistent with the size estimated from optical absorption measurement. The average size of the DT-AuNPs is then about 4.5 nm, as the dodecanethiol capping thickness is nominally assumed to be 1 nm.

4.2.1 Preparation of DT-AuNPs/H-Si LS films

A 1.5 ml toluene solution of DT-AuNPs (0.5 mg/ml) was spread uniformly, using a micropipette, on the surface of Milli-Q water (Milipore) in a Langmuir trough (KSV 5000). It was kept undisturbed for some time to let the toluene evaporate and the hydrophobic DT-AuNPs lay suspended at the air-water interface (at 23°C). A pressure-area (Π-A) isotherm of DT-AuNPs Langmuir monolayer on water surface was recorded (as shown in Fig. 8) by regulating the barrier movement. Π was measured with a Wilhelmy plate. Prior to the DT-AuNPs monolayer deposition, H-terminated Si (H-Si) substrates were prepared through the standard pre-treatment method (discussed in 2.1, 2.2). In short, Si(001) substrates (of size about 15×15 mm^2) were first sonicated in acetone and ethanol solutions to remove organic contaminants and subsequently etched with hydrogen fluoride [HF, Merck, 10%] solution for 60 s at room temperature (25°C) to terminate the Si surface with H after removing the native oxide layer. The DT-AuNPs Langmuir monolayers formed at different pressure were then transferred onto the H-Si substrates using LS deposition technique (discussed in 2.3.4.2). DT-AuNPs/H-Si LS films prepared at Π = 2, 4, 6, 10 and 14 mN/m, as shown in the π-A isotherm of Fig. 8, were used for further analysis.

4.2.2 Characterization of DT-AuNPs/H-Si LS films

The characterization of the DT-AuNPs/H-Si LS films, in reciprocal and real spaces, were carried out using X-ray scattering (XR and GISAXS) and microscopy (SEM and AFM) techniques, respectively. The scattering geometry used for the characterization of samples is already discussed in 3.1, 3.2.2. XR measurements of the films were performed on a versatile x-ray diffractometer (VXRD) setup (discussed in 3.4.1). Resolution of the instrument in this mode is 0.002 Å^{-1}. XR technique essentially provides an electron-density profile (EDP), i.e., in-plane $(x - y)$ average electron density (ρ) as a function of depth (z) in high resolution

(discussed in 3.1). From EDP it is possible to estimate film thickness, electron density, and interfacial roughness.

GISAXS measurements of the films were carried out using a synchrotron source (MiNaXS beam line, PETRA III) at λ = 0.94 Å(discussed in 3.2.2). The sample-to-detector distance was 1721 mm. Corresponding angular resolution (given by the ratio of pixel size and the sample-to-detector distance) is 0.1 mrad. The resolution limit along q_y-direction is less than 0.002 $Å^{-1}$, for the present setup. The resolution limit along q_y-direction is a very important parameter in understanding the long-range in-plane correlations in a system, such as the domains, if any. Such resolution limit depends upon the detector-to-sample distance, beam-size and most importantly on the beam divergence (discussed in 3.2.2).

For the data collection, the incident angle α was kept at 0.25°, slightly greater than the critical angle, α_c, of the sample. Under such grazing incidence, the footprint of the micro-focused beam on the sample, along x-direction, is quite large, as necessary for any statistically relevant information, while along y-direction, is small, which can be used to map the in-plane inhomogeneity, if any. To minimize the effect of the radiation damage of the sample (due to high intensity beam), GISAXS pattern, on a single position, was collected for small time (10 s). To check the in-plane inhomogeneity and/or to enhance the statistics, similar GISAXS patterns were also collected at different positions by moving the sample laterally.

The topography of the DT-AuNPs/H-Si LS films, at large scale, were imaged by scanning electron microscope (Quanta 200 FEG). The detailed top surface morphology of the films were mapped through AFM (5500 AFM, Agilent) technique, few days after deposition. Topographic images were collected in a noncontact (or intermittance contact) mode to minimize the silicon-tip-induced damage of the soft film. Scans of different sizes and in different portions of the sample

were carried out to get statistically meaningful information about the topography. WSXM software [293] has been used for AFM image processing and analysis.

4.3 Results and discussion

4.3.1 Out-of-plane structure from XR

XR data of the DT-AuNPs/H-Si LS films deposited at different Π-values are shown in Fig. 32. Oscillations with more than a single periodicity are observed in all the XR profiles. The periodicity even changes with the films suggesting readily the change in the film with the deposited pressure. However, to get the quantitative information about the films, all XR profiles have been analyzed using Parratt's formalism, [294] after incorporating roughness at each interface. [295] An instrumental resolution in the form of a Gaussian function and a constant

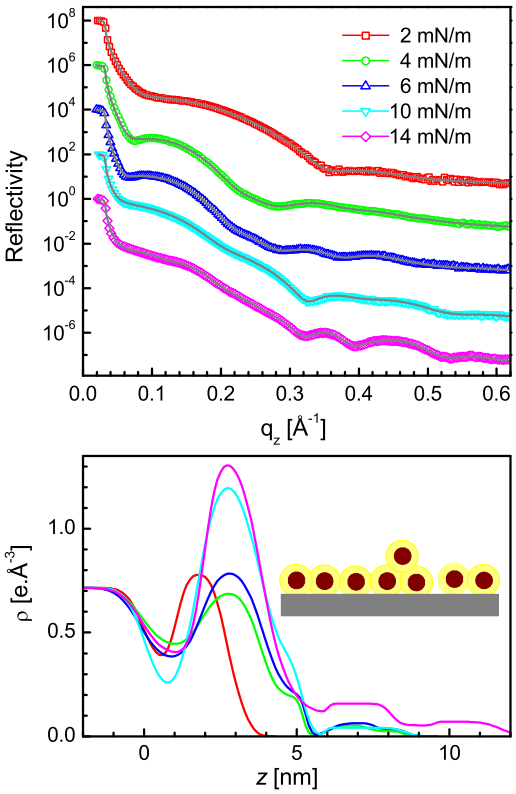

Figure 32: Top: XR data (different symbols) and analyzed curves (solid lines) of DT-AuNPs/H-Si LS films deposited at different surface pressure (Π). Curves are shifted vertically for clarity. Bottom: Corresponding analyzed EDPs and the schematic of the model used for the analysis.

background were also included at the time of data analysis. For the analysis, we started with a monolayer of DT-AuNPs of different thickness and coverage on the Si substrate and then replaced some coverage with bilayer and/or trilayer, according to the fitting requirements. Further, each DT-AuNPs monolayer is divided into three layers, namely thiol-rich low density bottom layer, Au-rich high density middle layer and again thiol-rich low density top layer. The best fit XR profiles along with the corresponding EDPs for all the films are shown in Fig. 32.

It is evident from the EDPs that only monolayer structure is present in the film deposited at Π = 2 mN/m. For the films deposited at Π = 4, 6 and 10 mN/m, a very small amount of bilayer structure and for the film deposited at Π = 14 mN/m, even very small amount of trilayer structure are also present in the films apart from the monolayer structure. In the film deposited at Π = 2 mN/m, the monolayer-coverage is partial (low peak ρ-value) and the monolayer-fluctuation along z-directional is almost negligible (low thickness). In the film deposited at Π = 4 mN/m, there is no increase in the monolayer-coverage rather decreases at the expense of some bilayer structure and some monolayer-fluctuation (increase in monolayer thickness). In the films deposited at Π = 6 and 10 mN/m, only the monolayer-coverage increases further with the Π-value. In the film deposited at Π = 14 mN/m, some trilayer structure is also formed in addition to the further small increase in the monolayer coverage.

4.3.2 In-plane structure from GISAXS

Fig. 33 shows the GISAXS reciprocal space patterns of the DT-AuNPs/H-Si LS films deposited at different surface pressure collected for a short time duration(10 sec). Each sample was moved laterally to get GISAXS patters at different positions and similar pattern was obtained for different positions. Thus we have ascertained the in-plane homogeneity of the GISAXS profiles. Averaging of all these patterns has been taken for better statistics and finally presented in Fig. 33.

In all the profiles for different surface pressures some common signatures has been observed. The most prominent features present are the two diffraction

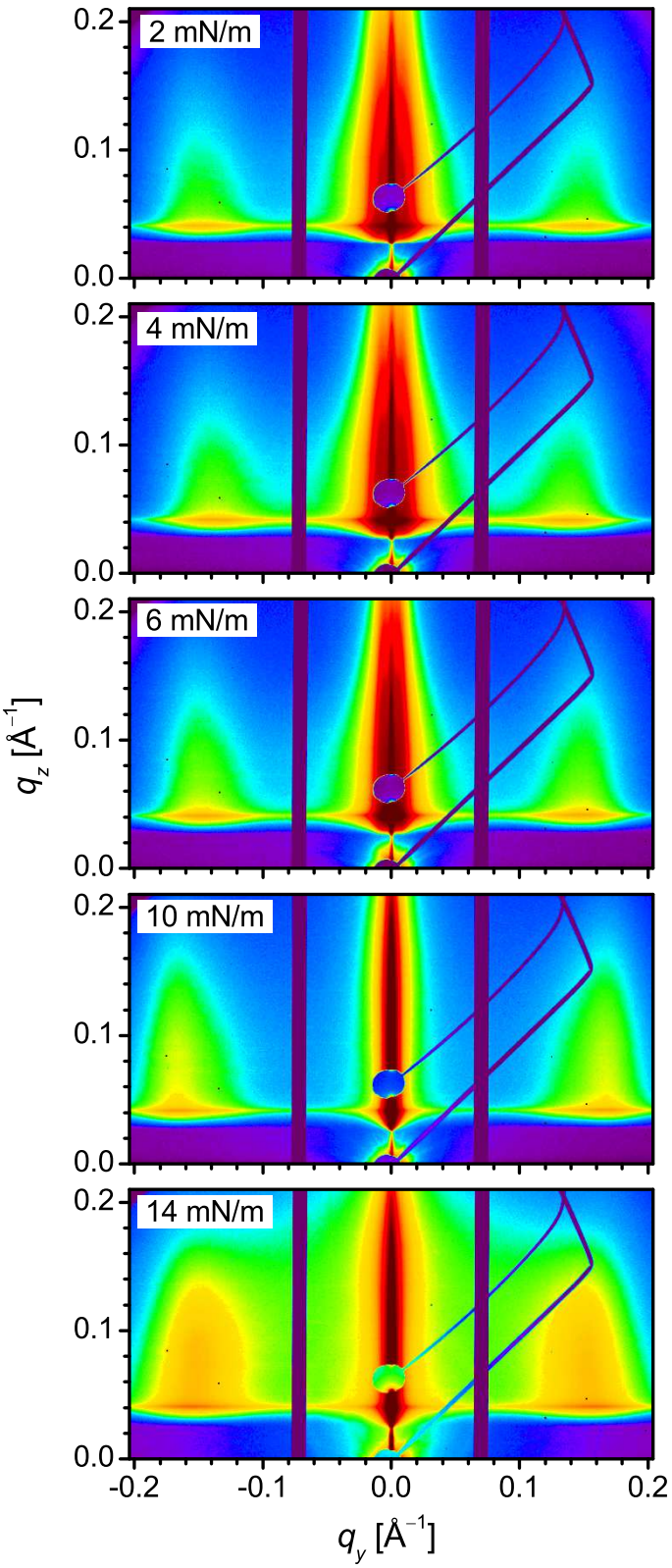

Figure 33: GISAXS patterns of the DT-AuNPs/H-Si LS films deposited at different surface pressure (Π).

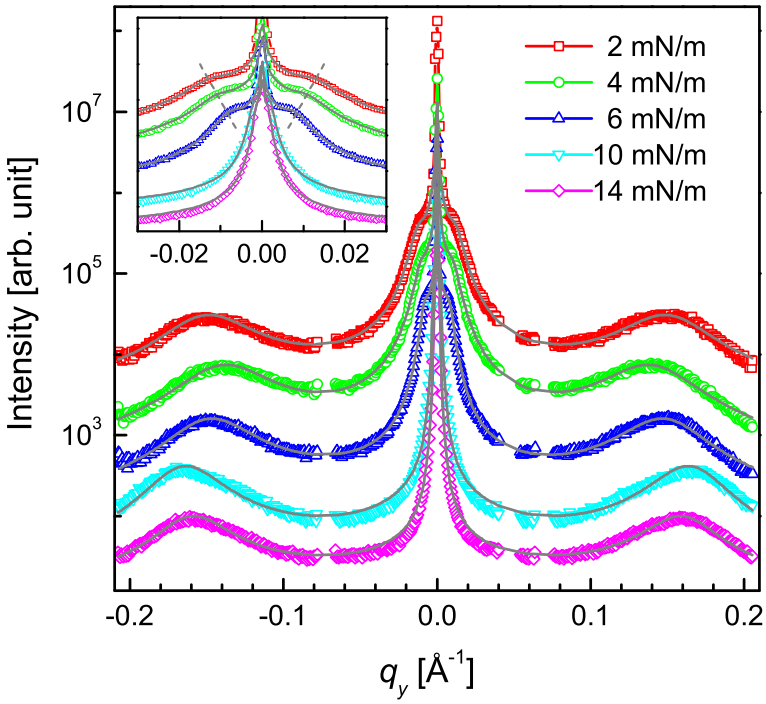

Figure 34: GISAXS line profiles (different symbols) and analyzed curves (solid lines) along the q_y direction (i.e. lateral cut through the first Bragg rod at $q_z \approx 0.04$ Å^{-1}) of the DT-AuNPs/H-Si LS films deposited at different surface pressure (Π). Curves are shifted vertically for clarity. Inset: magnified view of corresponding central portion to have a better idea about the shoulder and their position.

Bragg rods around $q_y = \pm\, 0.15$ Å^{-1} and the intensity of the rods varies with Π value. Secondly, high intensity value is observed near $q_y = 0$, the nature of this intensed rod again changes with Π. To get a better idea about the position and intensity of the Bragg rods in the GISAXS patterns and also the nature of the intensity variation near $q_y = 0$, we have plotted GISAXS line profiles along q_z direction in Figs. 35 and along q_y direction in in Figs. 34. The line profiles have been drawn through the Bragg rods. In case of the line profiles along q_z-direction (in Fig. 35), we have shown only a slow increase in the absolute intensity for change in Π value. This increase in intensity is obvious since with increasing Π value the number of AuNPs present in the film also increases(as observed from the $\Pi - A$ isotherm and EDPs). Now for the line profiles along q_y-direction (in Fig. 34)we have observed peaks around $q_y = \pm\, 0.15$ Å^{-1} which arises due to AuNPs separation. Also broad peaks or shoulders have been found within $q_y = \pm$ 0.02 Å^{-1}. In the inset of Fig. 34 the central portion i.e. around $q_y = \pm\, 0.00$ Å^{-1} is

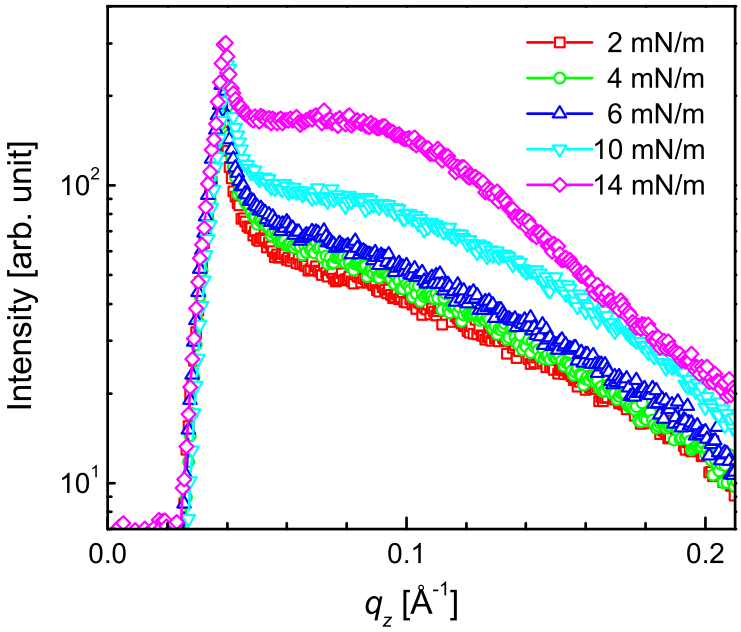

Figure 35: GISAXS line profiles along the q_z direction (i.e. vertical cut along the first Bragg rod at $q_y \approx 0.15$ Å^{-1}) of the DT-AuNPs/H-Si LS films deposited at different surface pressure (Π).

magnified to show the shoulder around $q_y = \pm\ 0.02$ Å^{-1} more prominently. The broad peak is only present in the line profiles for the three low Π valued films and it's position moves toward lower q value with increasing Π value.

4.3.2.1 GISAXS line profiles

The GISAXS line profiles along q_y direction are extracted by integrating different portion of q_z values for the DT-AuNPs/H-Si LS films deposited at three different surface pressure and are shown in Fig. 36. It is clear from the figure that the positions of the shoulders (indicated by dashed lines in Fig. 36) around the central peak, which move toward the center with increasing Π value, remain changed with the q_z value. This indicates that the position of q_z value is not very important for the extraction of horizontal line profile from the GISAXS image.

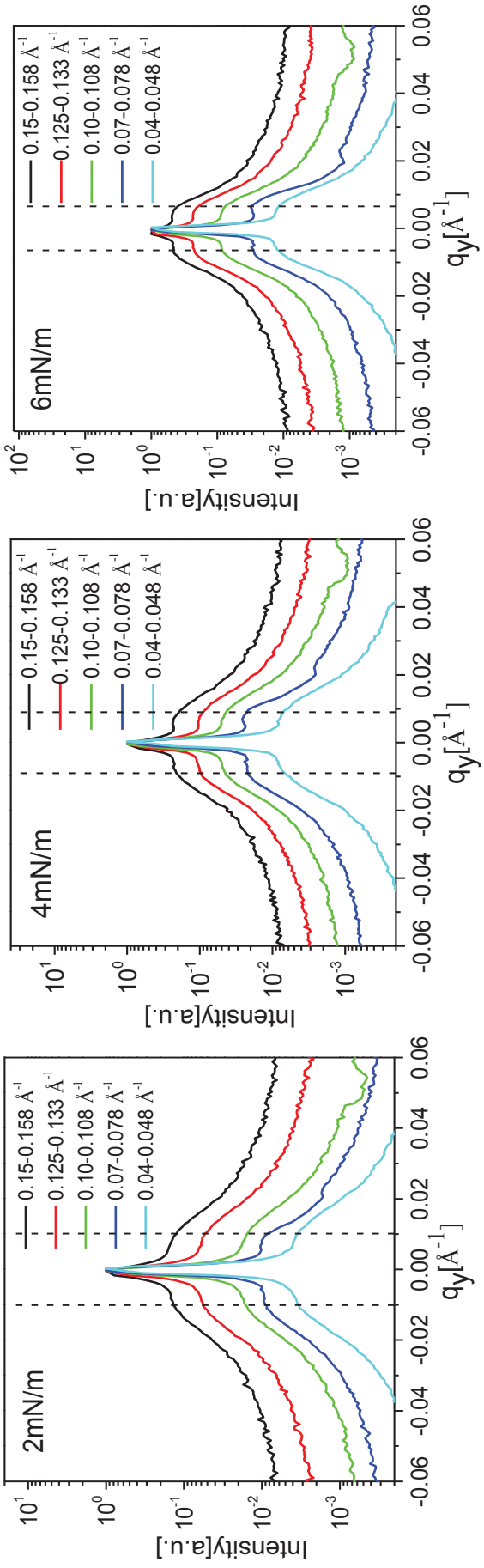

Figure 36: GISAXS line profiles along q_y direction, extracted from different ranges of q_z values, for the DT-AuNPs/H-Si LS films deposited at three different surface pressure. The positions of the correlation peaks are indicated by the dashed lines.

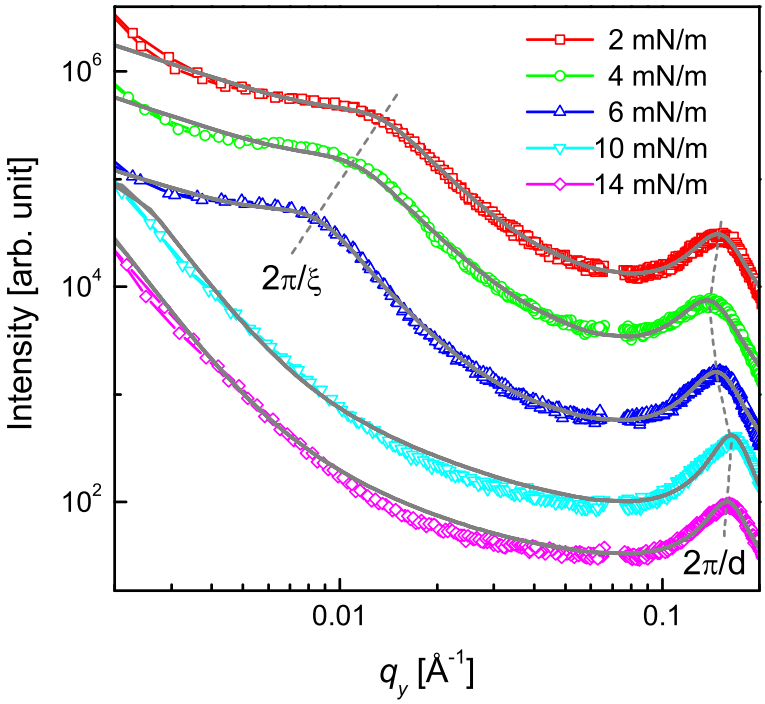

Figure 37: GISAXS line profiles (different symbols) and analyzed curves (solid lines) along the q_y direction (i.e. lateral cut through the first Bragg rod at $q_z \approx 0.04$ Å^{-1}) of the DT-AuNPs/H-Si LS films deposited at different surface pressure (Π) in log-log scale to have a better idea about the in-plane correlation (such ξ and d) in different length scales. Curves are shifted vertically for clarity.

The position of the shoulder, however, remains unchanged with the q_z value (as evident from Fig. 36) and thus the role of q_z is not very crucial for drawing the horizontal line profile from the GISAXS pattern. The shoulder observed in the reciprocal space directly indicates the presence of a certain long range correlation in real space. The evidence of such observation has never been found before. It is clear that the horizontal line profiles are of actual interest and need further analysis and discussion.

The horizontal line profiles, in log-log scale, are shown in Fig. 37, where both peak at large q_y value and broad hump at low q_y value (if present) are clearly visible. The positions of which are marked by the dashed lines and provide the rough estimate of the in-plane AuNPs separation (d) and in-plane correlation length (ξ). For the better estimate of these parameters, quantitative analysis of the horizontal line profiles are necessary. It is known that in the kinematic or Born approximation the measured scattering intensity can be expressed as

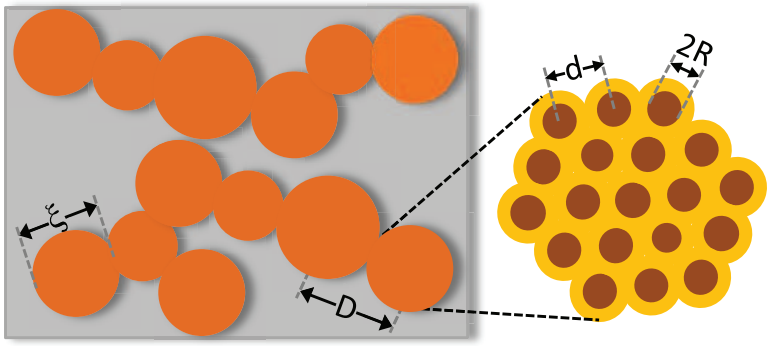

Figure 38: Schematic of the in-plane film structure used for the calculation. It is considered that the film is a network of domains or islands of average size ξ and average separation D, while each domain is composed of DT-AuNPs of average AuNP size $2R$ and average separation d.

the square of total scattering amplitude, which is the Fourier transform of the electron density in the film, as

$$I(\mathbf{q}) = \left| \int d\mathbf{r}\, \rho(\mathbf{r})\, e^{-i\mathbf{q}.\mathbf{r}} \right|^2 = |FT[\rho(\mathbf{r})]|^2 \tag{4–1}$$

where $\rho(r)$ is the electron density, which needs to be modelled. To take care the observed features in the GISAXS line profiles, $\rho(\mathbf{r})$ for the film can be modelled as shown in Fig. 38.

First it is assumed that the film is composed of networked 2D-islands. The islands are disk-like of average size ξ and thickness T (which is the thickness of the film), and their average separation is D (which is $\geq \xi$). Under such conditions, the EDP can be written as [296, 297]

$$\rho(\mathbf{r}) = [\rho_D S_D(\mathbf{r}) \otimes \sum_j \delta(\mathbf{r} - \mathbf{r}_j)].S_F(\mathbf{r}) \tag{4–2}$$

where $S_F(\mathbf{r})$ is related to the dimension of the film (which is limited along z direction to the film thickness), $S_D(\mathbf{r})$ and $\sum \delta(\mathbf{r} - \mathbf{r}_j)$ are related to the average dimension and distribution of the islands having uniform electron density ρ_D. In reality, each island is actually composed of DT-AuNPs. This means that the electron density is not uniform throughout an island, rather high electron density small regions (of size $2R$ due to core AuNPs) are distributed (with

average separation d) within low electron density background (containing thiols). Considering this, the EDP can be expressed as

$$\begin{aligned}\rho(\mathbf{r}) &= [\{\rho_{\mathrm{DT}} + \Delta\rho S_{\mathrm{NP}}(\mathbf{r}) \otimes \sum_k \delta(\mathbf{r}-\mathbf{r}_k)\}.S_{\mathrm{D}}(\mathbf{r}) \otimes \sum_j \delta(\mathbf{r}-\mathbf{r}_j)].S_{\mathrm{F}}(\mathbf{r}) \\ &= [\rho_{\mathrm{DT}}.S_{\mathrm{D}}(\mathbf{r}) \otimes \sum_j \delta(\mathbf{r}-\mathbf{r}_j)].S_{\mathrm{F}}(\mathbf{r}) + [\{\Delta\rho S_{\mathrm{NP}}(\mathbf{r}) \\ &\qquad \otimes \sum_k \delta(\mathbf{r}-\mathbf{r}_k)\}.S_{\mathrm{D}}(\mathbf{r}) \otimes \sum_j \delta(\mathbf{r}-\mathbf{r}_j)].S_{\mathrm{F}}(\mathbf{r})\end{aligned} \tag{4–3}$$

where $S_{\mathrm{NP}}(\mathbf{r})$ and $\sum\delta(\mathbf{r}-\mathbf{r}_j)$ are related to the average dimension and distribution of the AuNPs having electron density contrast $\Delta\rho$ with respect to the thiols electron density of ρ_{DT}. Then the intensity can be written as

$$\begin{aligned}&I(\mathbf{q}) \\ &= |\rho_{\mathrm{DT}} f_{\mathrm{D}}(\mathbf{q}).\sum_j e^{-i\mathbf{q}.\mathbf{r}_j} \otimes f_{\mathrm{F}}(\mathbf{q}) + \{\Delta\rho f_{\mathrm{NP}}(\mathbf{q}).\sum_k e^{-i\mathbf{q}.\mathbf{r}_k}\} \otimes f_{\mathrm{D}}(\mathbf{q}).\sum_j e^{-i\mathbf{q}.\mathbf{r}_j} \otimes f_{\mathrm{F}}(\mathbf{q})|^2 \\ &\approx |\rho_{\mathrm{DT}} f_{\mathrm{D}}(\mathbf{q}).\sum_j e^{-i\mathbf{q}.\mathbf{r}_j} \otimes f_{\mathrm{F}}(\mathbf{q})|^2 + |\{\Delta\rho f_{\mathrm{NP}}(\mathbf{q}).\sum_k e^{-i\mathbf{q}.\mathbf{r}_k}\} \otimes f_{\mathrm{D}}(\mathbf{q}).\sum_j e^{-i\mathbf{q}.\mathbf{r}_j} \otimes f_{\mathrm{F}}(\mathbf{q})|^2 \\ &\approx I_D + I_P\end{aligned} \tag{4–4}$$

where the cross term (which is a coupled expression) has been neglected. Then the contributing terms are I_D and I_P, which are mainly related to the islands and AuNPs, respectively. The term $f(\mathbf{q}) = FT[S(\mathbf{r})]$ gives rise to the form factor and can be determined considering the shape of the islands or AuNPs, while the term $\sum_k e^{-i\mathbf{q}.\mathbf{r}_k} = FT[\sum_j \delta(\mathbf{r}-\mathbf{r}_j)]$ gives rise to the structure factor and can be determined considering the distribution of the islands or AuNPs. It is known that the limited dimension can create a smearing (broadening) effect on the delta-like function, arise for the perfectly ordered arrangement. However, if we consider that the islands have polydispersity in size as well as in separation then the island distribution term should not contribute sharp function. In such a case, square of the island distribution term convoluted with the sample dimension term can

Table 3: Parameters such as the size ($2R$) of the AuNPs as obtained from UV-Vis spectra and TEM measurements, the in-plane separation (d) of the AuNPs, the in-plane size (ξ) and the in-plane separation (D) of the islands as obtained from GISAXS measurements and the in-plane size (ξ_h) and the in-plane separation (D_h) of the islands as obtained from AFM measurements for the DT-AuNPs/H-Si LS films deposited at different surface pressure (Π).

Π (mN/m)	$2R \pm \sigma_{2R}$ (nm)	$d \pm \sigma_d$ (nm)	$\xi \pm \sigma_\xi$ (nm)	$D \pm \sigma_D$ (nm)	$\xi_h \pm \sigma_{\xi_h}$ (nm)	$D_h \pm \sigma_{D_h}$ (nm)
2	2.5 ± 0.6	3.8 ± 0.7	32 ± 12	33 ± 12	33 ± 07	47 ± 16
4	2.5 ± 0.6	4.1 ± 0.8	39 ± 15	44 ± 16	45 ± 12	59 ± 18
6	2.5 ± 0.6	3.9 ± 0.7	54 ± 18	56 ± 19	65 ± 19	80 ± 25
10	2.5 ± 0.6	3.6 ± 0.6	> 100	> 100	79 ± 23	85 ± 30
14	2.5 ± 0.6	3.7 ± 0.6	> 200	> 200	30 ± 09	30 ± 30

be expressed as the Fourier transform of the position-position auto-correlation or pair correlation function of the islands. Similarly, the polydispersity in the size of the AuNPs is present, which will certainly give rise polydispersity in the separation. Even if such polydispersity is less, it is sufficient to destroy any correlation beyond island length scale. In such a case again square of the AuNP distribution term convoluted with the island dimension term can be expressed as the Fourier transform of the pair correlation function of AuNPs. Considering cylindrical islands and spherical AuNPs, the I_D and I_P along in-plane direction can be expressed as

$$
\begin{aligned}
I_D(q_y) &\approx A_D \frac{[\sin(q_y\xi/2) - (q_y\xi/2)\cos(q_y\xi/2)]^2}{(q_y\xi/2)^6} \cdot \frac{1 - e^{-2q_y^2\sigma_D^2}}{1 - 2\cos(q_y D)e^{-q_y^2\sigma_D^2} + e^{-2q_y^2\sigma_D^2}} \\
I_P(q_y) &\approx A_P \frac{[\sin(q_y R) - q_y R\cos(q_y R)]^2}{(q_y R)^6} \cdot \frac{1 - e^{-2q^2\sigma_d^2}}{1 - 2\cos(q_y d)e^{-q_y^2\sigma_d^2} + e^{-2q_y^2\sigma_d^2}} \\
&\quad \cdot \frac{1 - e^{-2q_y^2\sigma_D^2}}{1 - 2\cos(q_y D)e^{-q_y^2\sigma_D^2} + e^{-2q_y^2\sigma_D^2}}
\end{aligned}
\tag{4–5}
$$

where A_D is related to the electron density contrast and number of the domains, while A_P is related to those of the AuNPs, $\xi/2$ and R are the radius of the cylindrical islands and spherical AuNPs, respectively, σ_D and σ_d are the standard deviations of the separations D and d, respectively. Eqs. 4–4 and 4–5 are then used to analyze the GISAXS line profiles along q_y direction. In the actual calculation, Gaussian distributions of the sizes ξ and $2R$ (with σ_ξ and σ_{2R} as their FWHM) are also considered. For the analysis, predetermined value of the parameter $2R$, as obtained from the UV-Vis and TEM measurements, is used. The analyzed curves thus obtained for all the films are shown in Figs. 34 and 37; and corresponding parameters are listed in Table 3.

It is clear from Table 3 that the value of ξ, D and their distributions increases with the increase of Π-value. Also it is found that the value of D is quite close to the value of ξ. However, for the films with high (10 and 14 mN/m) Π-value, as there is no shoulder in the GISAXS line profiles, no definitive value rather the lower limits of these parameters are obtained. The d-values for all the films are found less than the size of the free DT-AuNPs, while the variation of d-value with the surface pressure, although small, show interesting variation. With the increase of the Π-value, the d-value of the film first increases (when Π changes from 2 to 4 mN/m) then decreases gradually (when Π changes from 4 to 10 mN/m) and then again increases (when Π changes from 10 to 14 mN/m). Such variation is quite consistent with the observed EDPs of the films, namely only monolayer structure for the film deposited at Π = 2 mN/m, while partially bilayer structures for the films deposited at Π = 4 to 10 mN/m (thus monolayer structure first become relaxed which then again become compressed with pressure) and partially trilayer structure for the film deposited at Π = 14 mN/m (thus monolayer structure again become slightly relaxed).

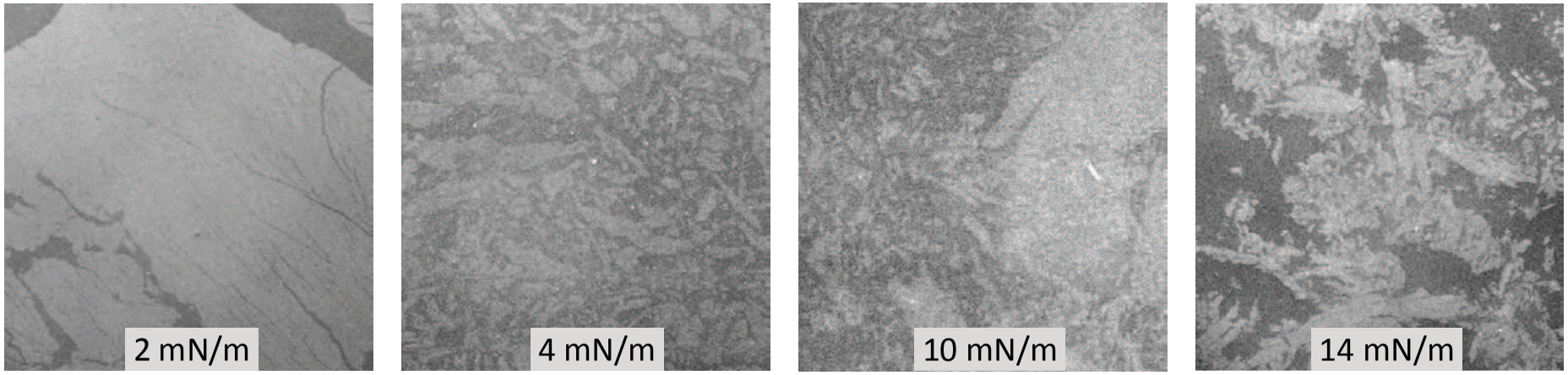

Figure 39: SEM images of the DT-AuNPs/H-Si LS films deposited at different surface pressure, showing topography in large (2.5×2.5 mm^2) scan size.

4.3.3 Topography from SEM

Such SEM images for the DT-AuNPs/H-Si LS films, deposited at four different surface pressure, are shown in Fig. 39. It is clear from the figure that there is no increase in the coverage of the film with surface pressure, at least, in large scale. However, the contrast of the image increases with surface pressure, which is probably associated with the increase in the thickness and/or coverage, in small scale.

4.3.4 Topography from AFM

So far, we have presented the structures of the films obtained from the X-ray scattering study. Although the structures obtained from such reciprocal space mapping is quite complete, nonetheless, it is always demanding to validate it with real space mapping. With this in view, the topography of the films, as imaged using AFM, are presented here. Typical AFM images of the films in different scan ranges are shown in Fig. 40. In the large (5×5 μm^2) scan size, large

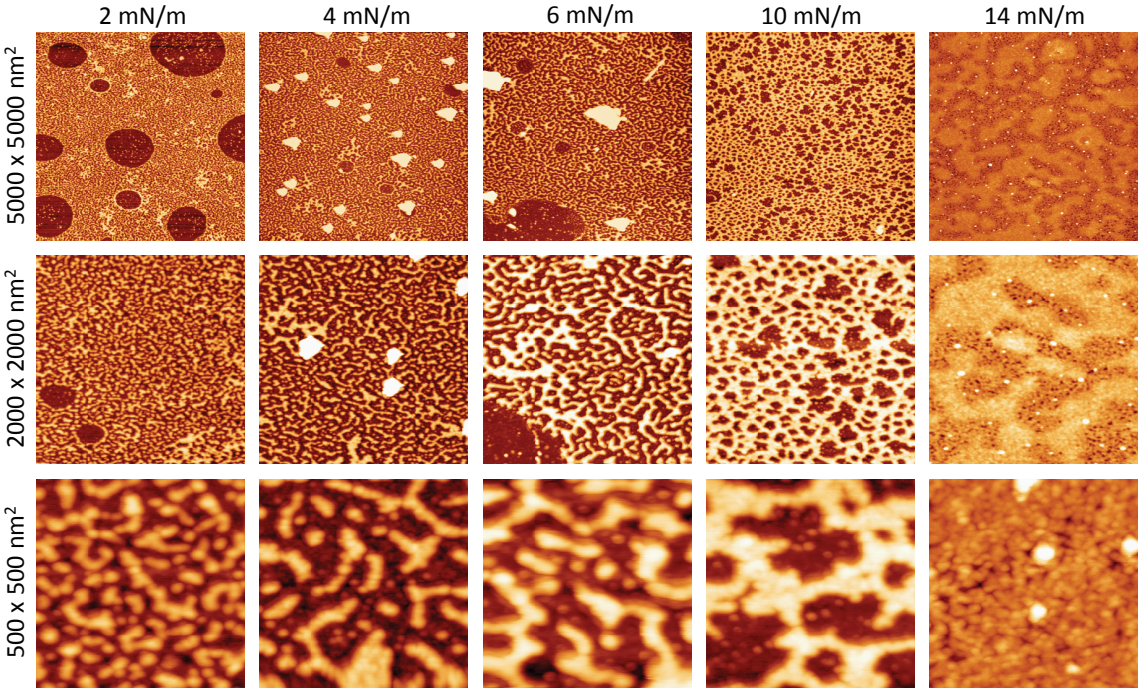

Figure 40: AFM images of the DT-AuNPs/H-Si LS films deposited at different surface pressure (Π) showing topography in three different scan sizes.

voids are observed for the film deposited at Π = 2 mN/m, otherwise film is found uniform. Such uniform portion when magnified (i.e. images of scan size $\leq 2\times2$ μm^2) clearly show the presence of networked 2D-islands of monolayer height. Large voids are however decreases in size and number with the increase of the surface pressure (see 5×5 μm^2 scan size images) and almost vanishes for the films deposited at Π = 10 mN/m. The presence of networked 2D-islands of monolayer height are also evident (in the images of scan size $\leq 2\times2$ μm^2) for the films deposited at higher pressures (Π = 4 to 10 mN/m). The size of which increases with the pressure. However, separate islands are almost invisible for the film deposited at Π = 14 mN/m.

To have a better idea about the average size of the islands, power spectral density (PSD), [298, 299] extracted from the AFM images of different scan size, are plotted in Fig. 41 for all the films.

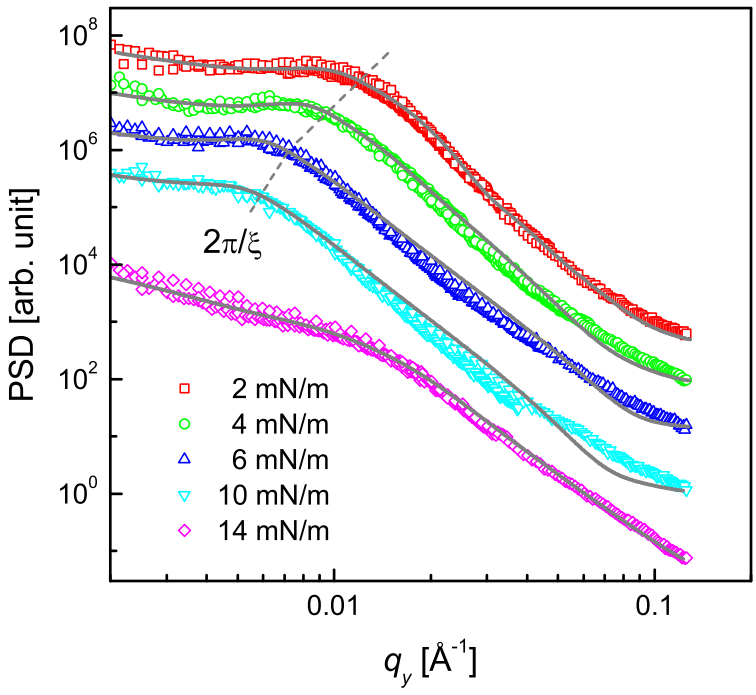

Figure 41: Power spectral density (PSD) profiles (different symbols) and analyzed curves (solid lines) of the DT-AuNPs/H-Si LS films deposited at different surface pressure (Π) obtained from the AFM images of different scan sizes.

It can be noted that the PSD is the angular averaged radial distribution of the Fourier transformed AFM image, which can be expressed as

$$\mathrm{PSD}(q_y) = \lim_{L\to\infty} \frac{1}{2L} \left| \int_{-L}^{L} dr\, z(r)\, e^{-iq_y r} \right|^2 \tag{4–6}$$

where $2L$ is the scan length. In that sense the PSD profile (Eq. 4–6) is similar to the GISAXS in-plane line profile (Eq. 4–1). Only difference is that the PSD (topography) is related to the height-height correlation, while the GISAXS (scattering) intensity is related to the density-density correlation and both become same when density fluctuation creates height fluctuation. In the present system the islands distribution creates density as well as height variation and thus the PSD can be expressed similar to the Eq. 4–5, considering only the island distribution, as

$$\mathrm{PSD}(q_y) \approx A_h \frac{[\sin(q_y\xi_h/2) - (q_y\xi_h/2)\cos(q_y\xi_h/2)]^2}{(q_y\xi_h/2)^6} \cdot \frac{1 - e^{-2q_y^2\sigma_{D_h}^2}}{1 - 2\cos(q_y D_h)e^{-q_y^2\sigma_{D_h}^2} + e^{-2q_y^2\sigma_{D_h}^2}} \tag{4–7}$$

where A_h is related to the height contrast and number, ξ_h is the average size and D_h is the average separation (with σ_{D_h} is its standard deviation) of the islands. Eq. 4–7 is then used to analyze the PSD profiles and for the calculation Gaussian distribution of the size ξ_h (with σ_{ξ_h} as FWHM) is again considered. The analyzed curves thus obtained for all the films are shown in Fig. 41 and corresponding parameters are listed in Table 3.

The values of parameters ξ_h and D_h are found to increase with the increase of Π-value similar to the values of ξ and D, with the exception for the film deposited at Π = 14 mN/m. The values of ξ_h and D_h (and their differences) are found more compared to the definitive values of ξ and D (and their differences) for the films deposited at low Π-values (2 to 6 mN/m), which may be related to the time evolution and/or tip convolution effects. Additionally, AFM was able to estimate the islands size, which GISAXS can not, for the films deposited at high Π-values (10 and 14 mN/m) having large monolayer coverage (as predicted from

EDPs). This is probably related to the relatively enhanced height fluctuation of the islands with time due to interfacial instability. For the film deposited at Π = 10 mN/m, the value of ξ_h is however systematic, which is not the case for the film deposited at Π = 14 mN/m. For the latter the value is found quite low and may be associated with the pressure independent characteristic island size of the DT-AuNPs system on water surface. Such funding is quite interesting and need further verification.

4.3.5 Structures of LS and Langmuir films

Let us now first try to visualize the overall structures of the DT-AuNPs/HSi LS films, by combining the information obtained from different techniques and then discuss its implication in understanding the structures of the DT-AuNPs Langmuir monolayers. It is clear (from the EDP and topography) that the DT-AuNPs/HSi LS films, deposited at different Π-values, are predominantly of monolayer structure. Considering the coverage of the monolayer (as obtained from the EDPs), such films can be categorized into two groups, namely low coverage (for Π = 2 to 6 mN/m) and high coverage (for Π = 10 to 14 mN/m), which is consistent with the classification of the liquid expended (LE) and liquid condensed (LC) phase diagram of the $\Pi - A$ isotherm. However, considering the presence of other structures (namely bilayer, trilayer, etc.), the films can be categorized into three groups, namely only monolayer structure (for Π = 2 mN/m), monolayer plus very small amount of bilayer structure (for Π = 4 to 10 mN/m) and monolayer plus very small amount of bilayer and trilayer structure (for Π = 14 mN/m), which is again consistent with the observed variation in the d-values, namely decrease in d-value associated with the flipping of some DT-AuNPs from monolayer to form bilayer or trilayer.

On the other hand, it is clear (from the in-plane density-density and height-height correlations) that the monolayers are made of networked disk-like islands. The size and separation of which however varies with the Π-values. The size

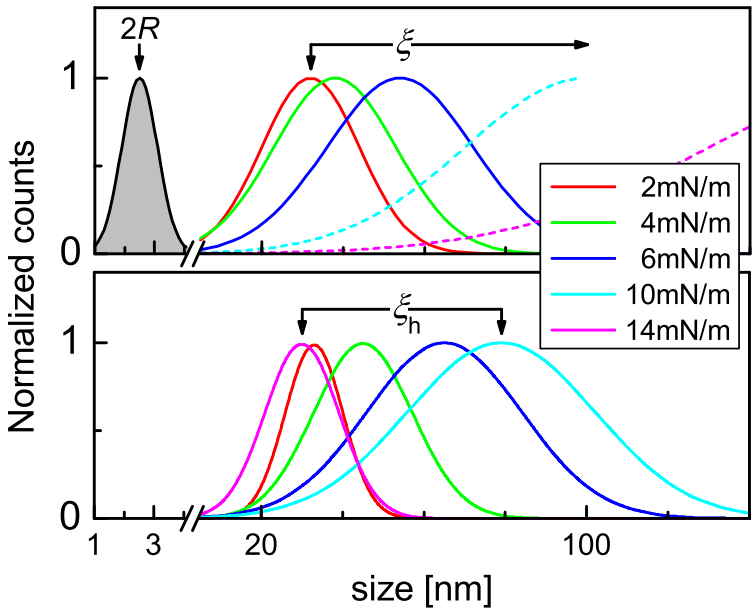

Figure 42: Size distribution of AuNPs ($2R$) as obtained from combined UV-Vis and TEM measurements and in-plane size distribution of islands (ξ and ξ_h) as obtained from GISAXS and AFM measurements for the films deposited at different surface pressure (Π).

distributions of the islands, for the films deposited at different surface pressure (Π), are shown in Fig. 42 along with the size distribution of the AuNPs. Increase in the size of the islands (ξ) is clearly evident from the GISAXS study, although the size estimation is only accurate for the films deposited at low Π-values and approximate for the films deposited at high Π-values, due to the resolution limit. Such variation is also confirmed from the AFM study, however, the sizes, ξ_h, are found slightly more compared to the corresponding sizes, ξ (for the low Π-value films) and can be understood considering time evolution and/or tip convolution effects. Signature of small size islands is found in the film deposited at Π = 14 mN/m from the AFM study, which is quite interesting. Probably such islands are present in all the films, i.e. related to the more pressure independent characteristic nature of the system. However, enhanced height fluctuation of these islands with time, in absence of other feathers, probably helps to express such small islands in the film deposited at Π = 14 mN/m.

Let us now consider that the DT-AuNPs films have been prepared by transferring the Langmuir monolayers on HSi substrates using LS techniques. Such

transfer technique and hydrophobic-hydrophobic interaction (between Langmuir monolayer and HSi substrate) are expected to create least disturbance. Thus it can be considered that the observed structures of the films, at least in the initial stages, are in close resemblance of the Langmuir monolayers. Accordingly, at Π = 2 mN/m, only monolayer height networked islands (of size around 30 nm) having large voids are formed at the air-water interface. On increase of Π from 2 to 4 mN/m, the size of the islands increases (to about 40), the size and number of voids decreases and a very small amount of bilayer is formed through flipping of DT-AuNPs from monolayer. Further increase of Π from 4 to 10 mN/m, the size of the islands increases, while the size and number of voids decreases and almost vanishes at Π = 10 mN/m but the amount of bilayer almost remains same. Increase of Π from 10 to 14 mN/m, the size of the islands increases further and a very small amount of trilayer is also formed through flipping of DT-AuNPs from monolayer.

From the structures it can be inferred that the DT-AuNPs in the water surface first assembled (in a hexagonal close pack) around different points (which act as nucleation centers) to form disk-like islands of monolayer height, probably due to the complex balance of the long range van der Waals interactions, electrostatic forces, and/or short-range steric repulsion of the DT-AuNPs. [135] The critical size of which is related to the size of the AuNPs and the length of the thiols. On compression of the barriers of the LB trough, the size of the islands increases (due to the increase in the local DT-AuNPs concentration), the separation between AuNPs (or d-value) decreases (due to the increase in their packing) and the networking of the islands and some flipping of DT-AuNPs take place.

It is necessary to mentioned that in spite of a large number of in-situ structural study on the thiol coated AuNPs Langmuir monolayers, formation of such networked island structure has never been observed or reported before, which can be understood as follows. BAM has been used extensively, however, it is not expected to resolved such structures, even present, due to its limited spatial

resolution. Also scattering, especially GISAXS, has been used extensively. For this the problem is mainly associated with the poor resolution limit and/or the beam induced damage. Poor resolution limit arises from the relatively broad beam size (used to enhance the beam intensity), relatively large beam divergence (as obtained from most of the sources itself and also due to use of additional reflecting mirror to impinge the x-ray beam onto the horizontal air-water interface) and relatively small sample-to-detector distance (required to capture the low scattering intensity). High intensity and small divergence beam of advanced synchrotron sources can, however, create better resolution limit. Even then the requirement of additional reflecting mirror, for the study of Langmuir monolayer, is still a problem. However, the main problem of the advance source is the high intensity beam induced damage, especially considering the time required to align the beam on the Langmuir monolayer. To minimize the effect of damage, the lateral movement of the beam (or sample) with respect to the sample (or beam) is required after alignment for actual measurement. The inability to move the beam laterally on the Langmuir monolayer surface is the hindrance in the observation of their actual (networked islands) structure. while small size intense P03 beam having better resolution limit and lateral beam movement on the LS film during actual measurements after alignment, help us to observed that.

4.4 Conclusions

The structures of the DT-AuNPs/HSi LS films, deposited at different Π-value, were first estimated using XR and GISAXS techniques and then confirmed using AFM technique. The GISAXS measurements were carried out using intense x-ray beam of small divergence (from P03 beamline of Petra-3) to enhanced in-plane resolution limit and by shifting the sample in-plane to minimize the effect of beam induced damage. It is clear (from XR and AFM) that the films are predominantly of monolayer structures. Such monolayers are made of networked

disk-like islands (as evident from GISAXS and AFM). The size of islands (ξ or ξ_h) increases with the increase of Π-value. The islands are again made of DT-AuNPs, self-assembled into hexagonal-like close pack with inter-digitization. The average separation between DT-AuNPs (d) either decreases or increases with Π-value depending upon the competitive effects of packing and flipping due to compression.

Owing to the least disturbance of the Langmuir films during transfer (using LS technique) onto the HSi substrates (due to the hydrophobic-hydrophobic interaction between Langmuir film and HSi substrate), the observed structures of the LS films, at least in the initial stages, can be considered to represent the structures of the Langmuir films, which are of immense importance not only for the understanding of the self-assembly process of AuNPs at air-water interface but also for their use as template to grow nanodevices with interesting properties arise from collective phenomenon.

5

INTERFACIAL AND THERMAL ENERGY DRIVEN GROWTH AND EVOLUTION OF LS MONOLAYERS OF DT-AUNPS

5.1 Introduction

Low dimensional systems or nanoobjects, having size smaller than certain intrinsic physical length, demonstrate properties that are sometimes completely different from the bulk one. [138, 286, 300] Such nanoobjects can be used as building blocks to form organized structures with useful electronic, optical, and magnetic properties. [46, 301, 302] For examples, thiol-capped AuNPs (DT-AuNPs) have been found to form self-assembled 2D structures, [46, 132, 133] due to the complex balance of long range van der Waals (vdW) attractions and short range steric repulsion of the DT-AuNPs[134–137] initiated by solvent evaporation. [128–130] Such 2D structures formed at air/water interface, known as Langmuir monolayers, can be readily transferred onto a solid substrate using LB and LS techniques to grow uniform nanostructures over large areas. [133, 138–141] Understanding and controlling the final structures of the films on solid substrates, which actually decides the new collective phenomena arises from interparticle coupling effects, [46, 138, 142] are of utmost importance for their practical uses.

The structures of such films on solid substrates will be governed not only by the structures of the Langmuir monolayers but also by the monolayer-substrate interactions during transfer and their evolution with time. As a hydrophilic substrate, due to its repulsive force on the DT-AuNP Langmuir monolayer (for both LB and LS depositions), can perturb and change the monolayer structure,

which with time can evolve further. Also, hydrophilic substrate can trap (or attract) water molecules (from Langmuir trough), which with time evaporates to form drying mediated agglomeration and nanopartterning of DT-AuNPs. [153] Similarly, a hydrophobic substrate, due to its repulsive force on water (for LB deposition), can perturb and change the monolayer structure, which with time can reorganize to release the strain. On the other hand, the hydrophobic substrate, due to its hydrophobic attraction, is expected to create least disturbance on the DT-AuNP Langmuir monolayer (during LS deposition). [133] Although, this is presumably be the better choice for the formation of uniform nanostructures over large areas on solid substrate just by tuning the DT-AuNPs monolayer structures at air/water interface, the question is, in practice, is it really possible? To address this question it is important to know if the hydrophobic strength of the substrates matters at all in creating the least disturbance on the DT-AuNP Langmuir monolayer or not. Also, it is necessary to know if the ambient condition creates any instability in the transferred film to change the structure with time or not.

It is known that the hydrophobic strength of the substrate can be tuned through termination or passivation of the substrate, differently, which essentially modifies the surface free energy or contact angle. [145, 146] Though different terminated substrates have been used for the growth of DT-AuNPs LS films, the carbon coated grids are mostly used as hydrophobic substrates to study the structure of the films, directly, using TEM. DT-AuNPs LS films were also grown on other large hydrophobic substrates, namely H-passivated Si substrates, etc. to study the structure of the films, indirectly, using X-ray scattering techniques, [133] however, no systematic work has been carried out to compare the structures of the DT-AuNPs LS films grown on different hydrophobic (strength) substrates.

On the other hand, the ambient conditions can change the passivation of the substrate with time, even in presence of a film, which in turn can influence the structure of the film. For examples, oxide layer has been found to grow on Si

substrates by replacing the passivated H, Br or Cl atoms, in presence of metal (Au, Ag), metal-organic (NiA LB) or organic-inorganic (CTAB-silica) nanolayer films to change the film-structures. [146] Also, the ambient condition can directly change the structure of the film, through oxidation (due to ambient oxygen), interdiffusion (due to ambient pressure), fluctuation, diffusion or reorganization (due to room temperature thermal energy or solvent evaporation), etc. For examples, oxidation of metal nanolayers, such as Fe, Cu, Ni, etc. are very common, while interdiffusion of Au inside H-Si substrate and reorganization of DT-AuNPs on O-Si substrate have been reported, [153] all of which lead to the change in the film-structure with time at ambient condition. However, no attempt has been made to find out and compare the structural stability/instability of the DT-AuNPs LS films on different hydrophobic substrates at ambient condition.

Here, we have investigated the role of hydrophobic strength of substrate and ambient condition on the structures and stability of DT-AuNPs LS films, using XR technique, [220, 303] to understand the possibility of formation of uniform nanostructures over large areas on solid substrate just by tuning the DT-AuNPs Langmuir monolayer structures. Different initial structures (monolayer or monolayer plus bilayer) are observed for films deposited on different passivated Si substrates, which indeed suggests strongly role of hydrophobic strength in mimicking the Langmuir monolayer structure. Structural evolution of the film is observed with time, which is actually a hindrance in formation of desired nanostructures of DT-AuNPs on solid substrate just by tuning the DT-AuNPs monolayer structures at air/water interface but formation of similar expended monolayer structure of DT-AuNPs is observed through evolution, which is interesting. The probable reasons behind these different observations are discussed.

5.2 Experimental details

5.2.1 Preparation of DT-AuNPs LS films

Prior to the DT-AuNPs monolayer deposition, Si substrates (of size about 15 × 15 mm^2) were first pretreated to prepare H-terminated Si (H-Si) substrates and OTS (of monolayer thickness) self-assembled Si (OTS-Si) substrates (see 2.1, 2.2). The DT-AuNPs Langmuir monolayers formed at different pressure (namely Π = 2, 4, 6, 10 and 14 mN m^{-1}) were then transferred once onto both OTS-Si and H-Si substrates using LS deposition technique (see 2.3.4.2 and are labeled as DT-AuNP/OTS-Si and DT-AuNP/H-Si, respectively.

5.2.2 Characterization of DT-AuNPs LS films

The details evolution of the films with time were characterized using XR techniques, while after evolution were characterized using AFM technique. XR measurements of the films were performed on a VXRD setup (discussed in 3.4.1) to get statistically averaged electron density information. Data were taken in the specular condition, i.e. reflected angle is equal to the incident angle, θ. Under such condition there exists a non-vanishing wave vector component, q_z, which is equal to $(4\pi/\lambda)\sin\theta$ with resolution 0.002 $Å^{-1}$. XR technique essentially provides an EDP, i.e., in-plane $(x-y)$ average electron density (ρ) as a function of depth (z) in high resolution (discussed in 3.1). From EDP it is possible to estimate not only the film thickness, electron density, and interfacial roughness but also the vertical position of the DT-AuNPs in the film and their evolution with time.

The detailed top surface morphology of the films were mapped through AFM (5500 AFM, Agilent) technique,as discussed in 2.5.1.2, a few days after deposition, i.e. after evolution at ambient conditions. Topographic images were collected in a noncontact (or intermittance contact) mode to minimize the silicon-tip-induced damage of the soft film. Scans of different sizes and in different portions of the

sample were carried out to get statistically meaningful information about the topography.

5.3 Results and discussion

5.3.1 AFM and topography

Typical AFM images of the DT-AuNP/OTS-Si LS films obtained after evolution at ambient conditions are presented in Figure 43. The network-like structures of the films with voids are clearly evident from these images. The size of such voids is found quite large in the film deposited at low Π-value (2 mN m^{-1}) but decreases with the increase of Π-value and almost disappear in the film deposited at high Π-value (10 mN m^{-1}). The network-like structures are predominantly of monolayer height with some fraction having height more than that. The contribution of the latter is almost negligible for the film deposited at low Π-value (2 mN m^{-1}) but reasonable for the film deposited at high Π-value (10 mN m^{-1}).

The topography of the DT-AuNP/H-Si LS films obtained after evolution at ambient conditions were presented before, [133] where 2D-network of disk-like islands of monolayer height on H-Si substrates were very much evident. The size of such islands is found to increase with pressure more systematically on H-Si substrates compared to that on OTS-Si substrates.

5.3.2 XR and EDPs

Time evolution XR data of DT-AuNP/OTS-Si and DT-AuNP/H-Si LS films deposited at different Π-values are shown in Figures 44 and 45. Oscillations with slightly different periodicity and amplitude are observed in the XR profiles of the as deposited DT-AuNP/OTS-Si LS films (Figure 44). Such periodicity changes with time suggesting change in the film structure. The change is, however, minimum for the film deposited at high pressure (Π = 10 mN m^{-1}). A broad peak or hump followed by a dip is mainly observed in the XR profiles of DT-AuNP/H-Si

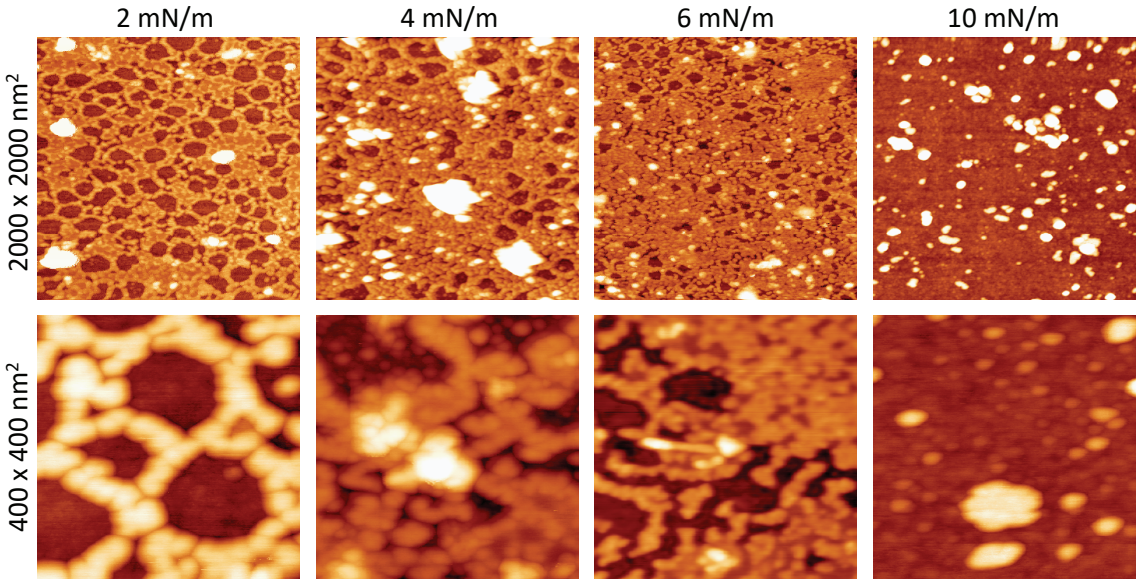

Figure 43: AFM images of the time evolved DT-AuNP/OTS-Si LS films deposited at different surface pressure (Π) showing topography in two different scan sizes.

LS films (Figure 45). The sharpness of the hump and the position of the dip (as indicated by the dashed line) are found to decrease with time. However, the decrease in the position is prominent for the low Π-value film and almost negligible for the high Π-value film suggesting large thickness change for the previous one, while small thickness change for the latter.

To get the quantitative information about the films, all XR profiles have been analyzed using Parratt's formalism, [294] after incorporating roughness at each interface. [12] An instrumental resolution in the form of a Gaussian function and a constant background were also included at the time of data analysis. For the analysis of the XR profiles of DT-AuNP/OTS-Si LS films, first a monolayer of DT-AuNPs of different thickness and coverage on the OTS-Si substrate was considered. Next each DT-AuNPs monolayer was further considered to be made of three layers, namely thiol-rich low density bottom layer, Au-rich high density middle layer and again thiol-rich low density top layer. Also, the OTS-Si substrate was considered to be made of three layers, namely high density Si substrate at the bottom, intermediate density silane related layer at the middle and low density hydrocarbon layer on the top. The starting EDPs of the OTS-Si substrates were used considering ideal SAM structure and then some allowance was given to the

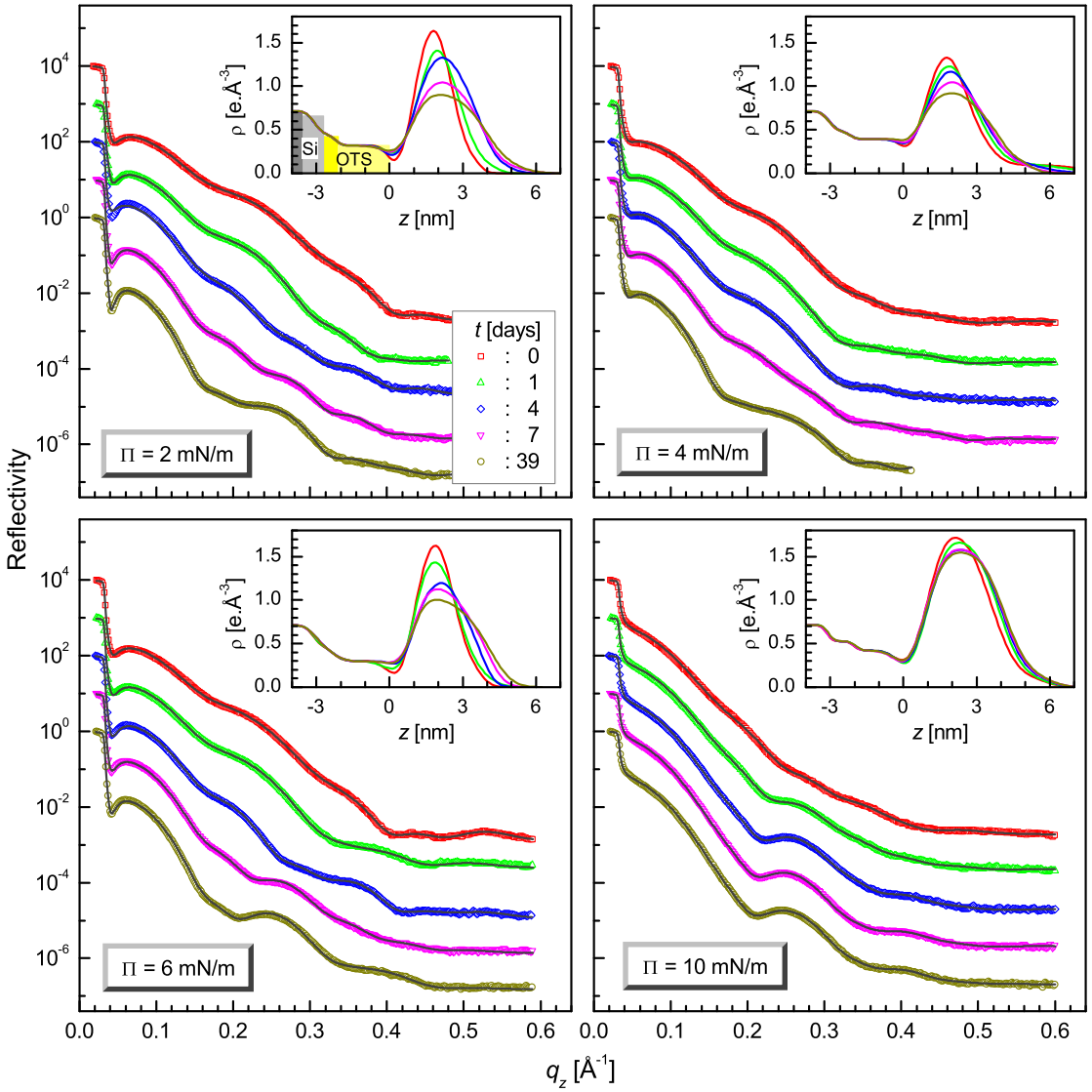

Figure 44: Time evolution XR data (different symbols) and analyzed curves (solid lines) of the DT-AuNP/OTS-Si LS films deposited at different surface pressure (Π). Curves are shifted vertically for clarity. Insets: Corresponding analyzed EDPs.

top two layers to find out the actual EDPs of the OTS-Si substrates for each film from the initially measured XR data. For the analysis of the XR data, measured at the subsequent stages, the initial EDP of the OTS-Si substrate was kept fixed apart from the top roughness. The parameters corresponding to the DT-AuNPs monolayer were, however, varied to fit the XR profiles. The best fit XR profiles along with the corresponding EDPs for all the films are shown in Figure 44.

Similarly, the XR profiles of DT-AuNP/H-Si LS films have been analyzed considering a monolayer of DT-AuNPs of different thickness and coverage on the H-Si substrate first and subsequently a second layer of low coverage was added,

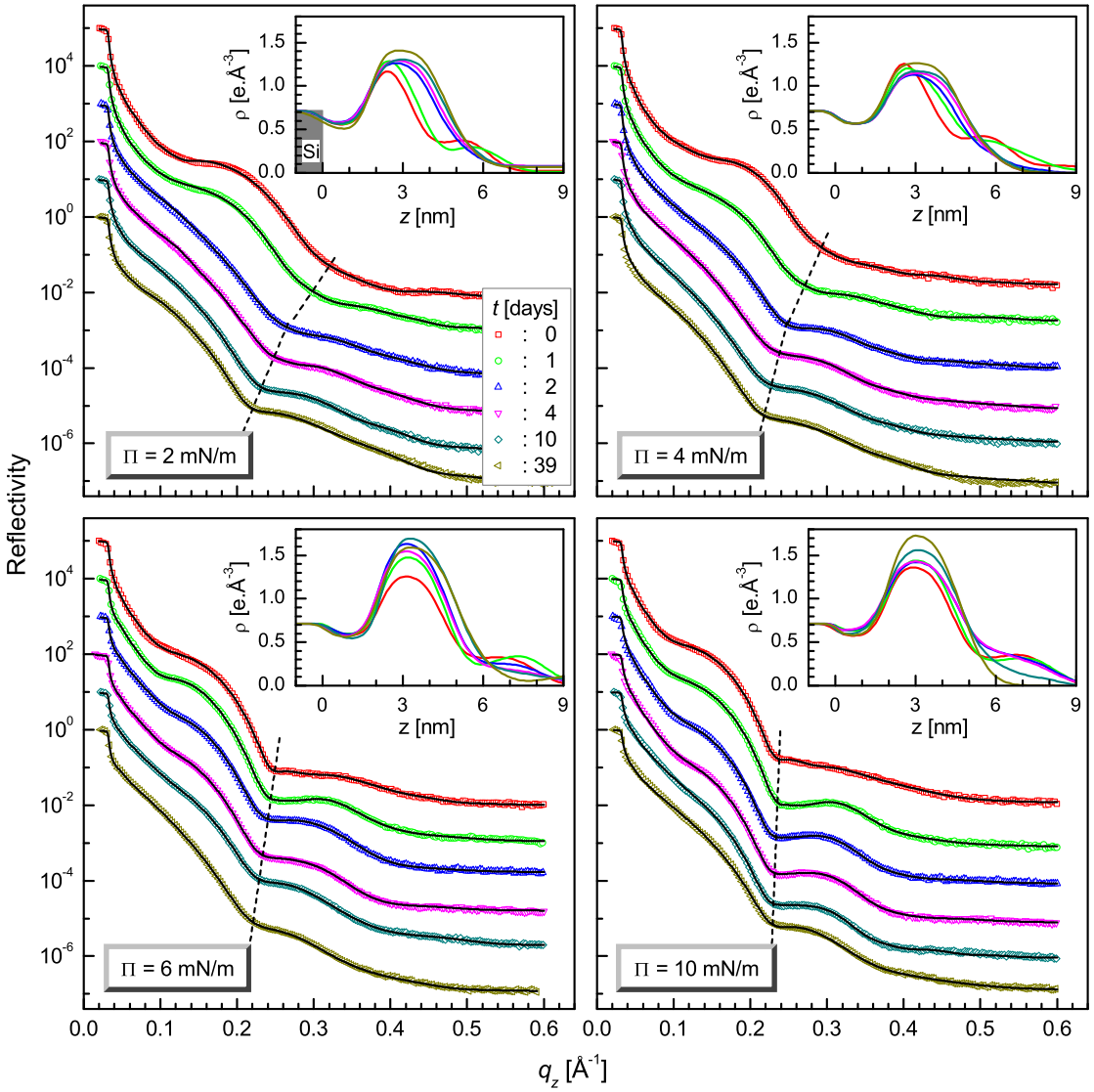

Figure 45: Time evolution XR data (different symbols) and analyzed curves (solid lines) of the DT-AuNP/H-Si LS films deposited at different surface pressure (Π). Curves are shifted vertically for clarity. Insets: Corresponding analyzed EDPs.

if required. Each DT-AuNPs layer was again considered to be made of three layers, as before. The best fit XR profiles along with the corresponding EDPs for all the films thus obtained are shown in Figure 45.

Two peaks (one intense and another weak) are clearly visible (see Figure 45) in the EDPs of the DT-AuNP/H-Si LS films at the initial stages. With time such distinct nature disappears and a rather broad single peak appears. A single peak is only observed (Figure 44) in the EDPs of the DT-AuNP/OTS-Si LS films at all stages. However, the EDP changes with Π-value and time. The change is mainly related to the peak or maximum value of ρ (ρ_m) and its full width at half

Table 4: Parameters such as the peak electron density ($\rho_{m,i}$ and $\rho_{m,f}$), the full width at half maximum of EDP ($w_{h,i}$ and $w_{h,f}$) and the summation of the deconvoluted Gaussian peak electron densities [$(\sum_j \rho_{0j})_i$ and $(\sum_j \rho_{0j})_f$] at initial ($t \approx 0$) and final ($t \approx 39$ days) stages of measurements and the peak-decay or width-growth time (τ) for the DT-AuNP/OTS-Si and/or DT-AuNP/H-Si LS films deposited at different surface pressure (Π).

Table 5: DT-AuNP/OTS-Si

Π (mN m^{-1})	$\rho_{m,i}$ (e Å^{-3})	$\rho_{m,f}$ (e Å^{-3})	$w_{m,i}$ (nm)	$w_{m,f}$ (nm)	τ (days)	$\sum_j \rho_{0j}$ (e Å^{-3})
2	1.62	0.90	1.73	3.31	4.8	1.63
4	1.34	0.92	2.14	3.43	6.0	1.68
6	1.63	1.00	1.82	3.22	4.2	1.70
10	1.72	1.54	2.80	3.40	2.5	2.75

Table 6: DT-AuNP/H-Si

Π (mN m^{-1})	$\rho_{m,i}$ (e Å^{-3})	$\rho_{m,f}$ (e Å^{-3})	$w_{m,i}$ (nm)	$w_{m,f}$ (nm)	$(\sum_j \rho_{0j})_i$ (e Å^{-3})	$(\sum_j \rho_{0j})_f$ (e Å^{-3})
2	1.17	1.41	2.55	3.30	1.91	2.61
4	1.25	1.26	2.62	3.64	2.18	2.44
6	1.25	1.59	3.18	3.44	2.46	3.00
10	1.36	1.72	3.14	3.14	2.74	2.96

maximum (w_h). The variation of these parameters at initial (i) and final (f) stages of measurements are plotted as a function of Π-value in Figure 46 for both the systems, separately and also tabulated in Table 4. It can be observed that for the DT-AuNP/OTS-Si LS system, the $\rho_{m,i}$-value remains almost same ($\sim$1.6 e Å^{-3}) at Π = 2 and 6 mN m^{-1}, but decreases (to $\sim$1.3 e Å^{-3}) at Π = 4 mN m^{-1} and increases (to $\sim$1.7 e Å^{-3}) at Π = 10 mN m^{-1}. Similarly, the $w_{h,i}$-value remains almost same ($\sim$1.7 nm) at Π = 2 and 6 mN m^{-1}, but increases reasonably (to $\sim$2.2 nm) at Π = 4 mN m^{-1} and appreciably (to $\sim$2.8 nm) at Π = 10 mN m^{-1}. This means that both the parameters either remain unchanged or increase with Π-value with some deviation at Π = 4 mN m^{-1} and the combination of both the

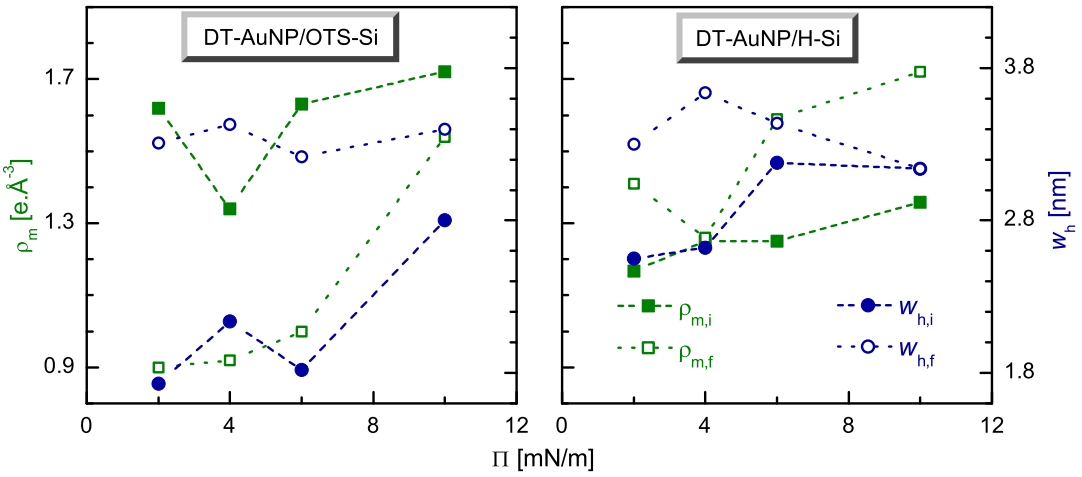

Figure 46: Variation of initial and final peak electron density ($\rho_{m,i}$ and $\rho_{m,f}$) and peak width ($w_{h,i}$ and $w_{h,f}$) of the films with deposited surface pressure (Π) for the DT-AuNP/OTS-Si and DT-AuNP/H-Si LS systems.

parameters apparently suggests a very small increase in the amount of materials in the films upto Π = 6 mN m^{-1} and an appreciable increase there after. On the other hand, the $\rho_{m,f}$-value is found to increase gradually (from 0.9 to 1.5 e Å^{-3}) with the Π-value. The increase is very small upto Π = 6 mN m^{-1} and appreciable after that. While the $w_{h,f}$-value is found quite high (∼3.4 nm) and almost remains unchanged with Π-value. For the DT-AuNP/H-Si LS system, the value of $\rho_{m,i}$ is found to increase from 1.2 to 1.4 e Å^{-3} with the increase of Π-value. Similarly, the value of $w_{h,i}$ (estimated from the width of the intense peak) is found to increase from 2.6 to 3.2 nm with the increase of Π-value. The combination of both the parameters apparently suggests a gradual small increase in the amount of materials in the films with Π-value. On the other hand, the $\rho_{m,f}$-value is found to increase (from 1.2 to 1.7 e Å^{-3}) and the $w_{h,f}$-value is found to decrease (∼3.6 to 3.1 nm) with the increase of Π-value with some deviation at low Π-value.

5.3.3 EDP: time dependence

In order to understand the time dependence nature of the films, the variation of ρ_m and w_h with time (as obtained from Figures 44 and 45) are shown in Figures 47 and 48 for the DT-AuNP/OTS-Si and DT-AuNP/H-Si LS films de-

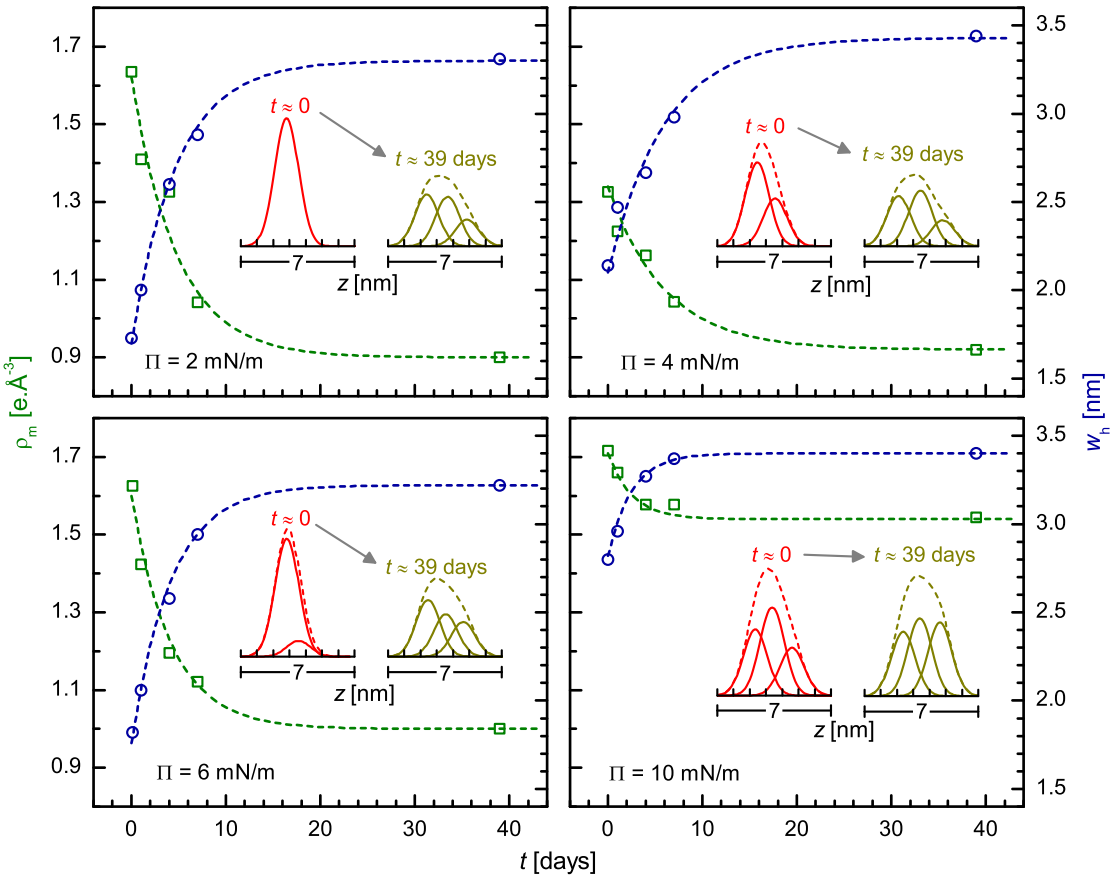

Figure 47: Evolution of peak electron density (ρ_m) and peak width (Δz) with time of the DT-AuNP/OTS-Si LS films deposited at different surface pressure (Π). Dashed lines through the data are the analyzed curves. Insets: corresponding initial ($t \approx 0$) and final ($t \approx 39$ days) EDPs and their Gaussian deconvolution to show the vertical organization of DT-AuNPs and their reorganization with time.

posited at different surface pressure. The variation is found systematic for the DT-AuNP/OTS-Si LS films and quite irregular for the DT-AuNP/H-Si LS films. For the DT-AuNP/OTS-Si LS films, the value of ρ_{m} and w_{h} decreases and increases, respectively, with time, which is initially fast then saturates with time. Such variation of ρ_{m} and w_{h} with time (t) at ambient condition can be expressed quantitatively using standard exponential dependence:

$$\rho_{\mathrm{m}}(t) = \Delta\rho_{\mathrm{m}} e^{-t/\tau} + \rho_{\mathrm{m}\infty} \tag{5–1}$$

$$w_{\mathrm{h}}(t) = w_{\mathrm{ho}} + \Delta w_{\mathrm{h}}(1 - e^{-t/\tau}) \tag{5–2}$$

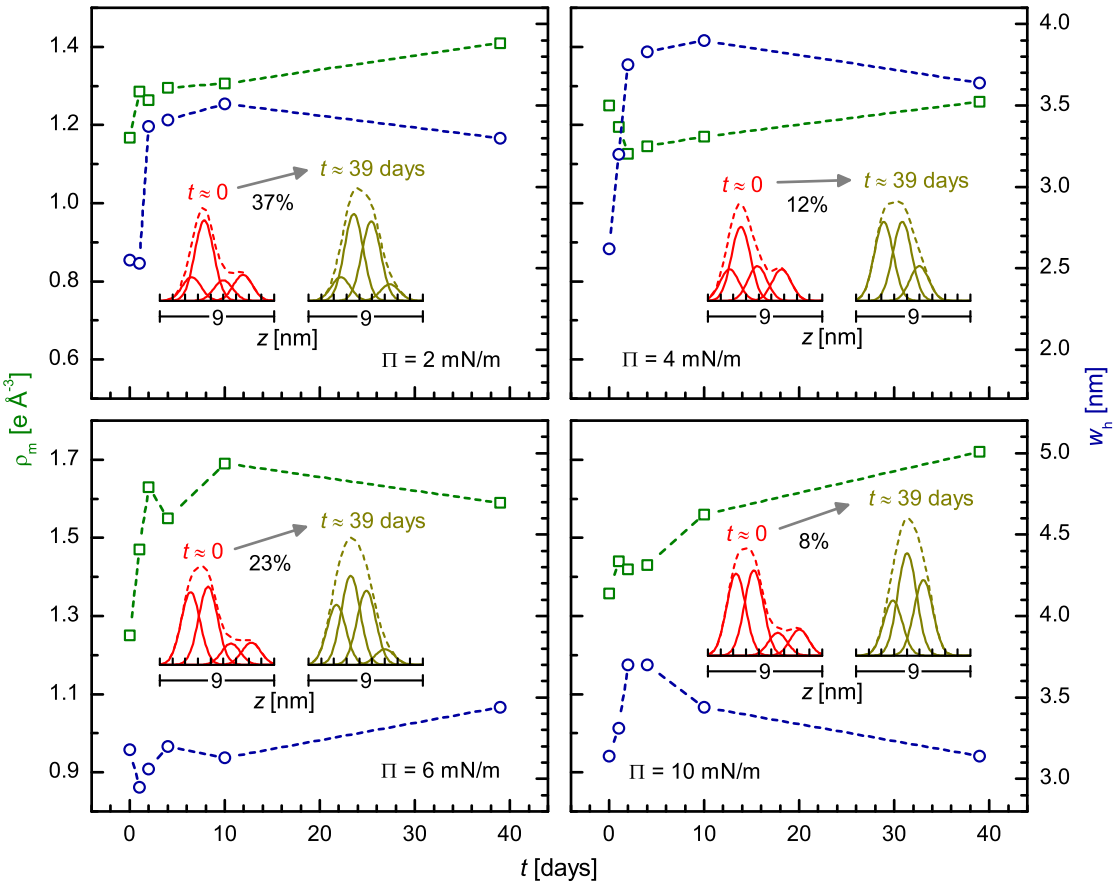

Figure 48: Evolution of peak electron density (ρ_m) and peak width (Δz) with time of the DT-AuNP/H-Si LS film deposited at different surface pressure (Π). Dashed lines through the data are to guide the eyes. Insets: corresponding initial ($t \approx 0$) and final ($t \approx 39$ days) EDPs and their Gaussian deconvolution to show the vertical organization of DT-AuNPs and their reorganization with time. The observed apparent percentage increase in the amount of DT-AuNPs with time is indicated.

where τ in Eq. 5–1 is the decay time and $\Delta\rho_m = \rho_{mo} - \rho_{m\infty}$ is the maximum change in ρ_m with ρ_{mo} is its maximum value at $t \to 0$ and $\rho_{m\infty}$ is its minimum or saturation value at $t \to \infty$, while τ in Eq. 5–2 is the growth time and $\Delta w_h = w_{h\infty} - w_{ho}$ is the maximum change in w_h with w_{ho} is its minimum value at $t \to 0$ and $w_{h\infty}$ is its maximum or saturation value at $t \to \infty$. Considering $\rho_{m0} \approx \rho_{m,i}$, $\rho_{m\infty} \approx \rho_{m,f}$, $w_{h0} \approx w_{h,i}$ and $w_{h\infty} \approx w_{h,f}$, the variations of ρ_m and w_h for the DT-AuNP/OTS-Si LS films have been simulated using Eqs. 5–1 and 5–2, respectively, and the simulated profiles are shown in Figure 47. The values of the parameter τ, used for the simulation, are enlisted in Table 4.

In order to model the evolution of the film with time quantitative reconstructions of EDPs are essential. In general, the depth dependence electron density can be expressed as:

$$\rho(z) = \rho_S(z) + \rho_F(z) \tag{5–3}$$

where the first term of the right hand side corresponds to the substrate of uniform electron density with some variation at the top due to surface roughness and the second term corresponds to the film, which is of prime importance. Here the film is composed of DT-AuNPs, where the EDP of a single DT-AuNP can be calculated considering the core-cell structure and can be approximated with a Gaussian peak function, $\rho_0 \exp(-z/\sigma_0)$, of $\rho_0 \approx 1.8$ e Å^{-3} and $\sigma_0 \approx 1.04$ nm as shown schematically in Figure 49. Accordingly, $\rho_F(z)$ can be expressed as the summation of Gaussian peaks:

$$\rho_F(z) = \sum_j \rho_{0j} \exp\left[-\left(\frac{z - z_{0j}}{\sigma_0}\right)^2\right] \tag{5–4}$$

where ρ_{0j} is the peak value, z_{0j} is the position and σ_0 is the standard deviation or width related term of the jth Gaussian peak. It can be noted that each Gaussian

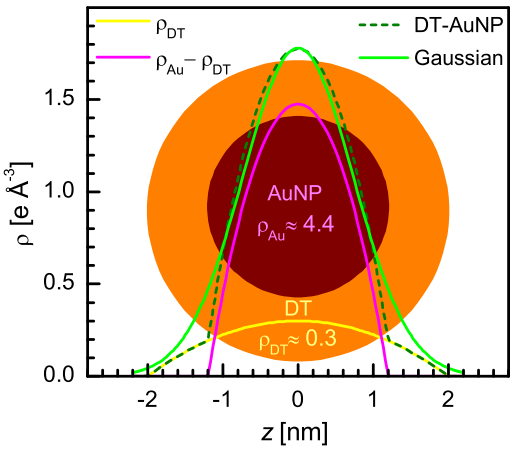

Figure 49: Schematic of a DT-AuNP, where the core is of high density Au ($\rho_{Au} \approx 4.4$ e Å^{-3}) and the coating layer is of low density DT ($\rho_{DT} \approx 0.3$ e Å^{-3}). Corresponding variations of calculated electron density as a function of height (relative to the center of DT-AuNP); for the complete NP of size ≈ 4 nm and $\rho \approx \rho_{DT}$, for the core NP of size ≈ 2.5 nm and $\rho \approx \rho_{Au} - \rho_{DT}$ (≈ 4.1 e Å^{-3}), for the linear combination of them and for the equivalent Gaussian function.

peak in Eq. 5–4 arises from a layer consisting of DT-AuNPs and not simply from single DT-AuNP. Accordingly, $\sigma_0 \approx 1.04$ nm in Eq. 5–4 corresponds to a layer of perfect monolayer thickness, while ρ_{0j} infers about the coverage of DT-AuNPs in the monolayer at z_{0j}. Eq. 5–4 is then used to simulate the EPDs of the films by considering minimum possible number of Gaussian peaks.

Deconvoluted profiles obtained from the simulation of the EDPs for all the films at initial and final stages are shown in Figures 47 and 48. The summation of the deconvoluted Gaussian peak values ($\sum_j \rho_{0j}$) for an EDP, which is correlated to the amount of materials in a film, is expected to be time independent. Although this is the case for the DT-AuNP/OTS-Si LS films but this is not the case for the DT-AuNP/H-Si LS films. Accordingly, only initial $\sum_j \rho_{0j}$ value for the DT-AuNP/OTS-Si LS films and both initial and final $\sum_j \rho_{0j}$ values for the DT-AuNP/H-Si LS films are presented in Table 4.

It is evident from the parameter $\sum_j \rho_{0j}$ in Table 4 that the DT-AuNP/OTS-Si LS films can be categorized into two groups. First group is for low Π values (2, 4 and 6 mN m^{-1}) films, where $\sum_j \rho_{0j} \approx 1.7$ e Å^{-3}, while the second group is for high Π value (10 mN m^{-1}) films, where $\sum_j \rho_{0j} \approx 2.7$ e Å^{-3}. These $\sum_j \rho_{0j}$ values apparently indicate full monolayer coverage for the first group of films and more than monolayer coverage for the second group of films. However, looking at the AFM images (Figure 43) it is clear that for the first group of films, the monolayer coverage is not complete, rather voids are present within network-like structures. The absence of the effect of such voids in the $\sum_j \rho_{0j}$ value suggests that the voids do not contribute in the ρ value estimated from the XR analysis. This is possible if the size of voids is comparable to the coherent length of the X-ray beam, in that case the covered film area and the voids area scattered incoherently [304] and the coherent scattered intensity from the covered film area only contribute in the XR measurements. It can be noted that the signature of incomplete monolayer coverage is also available from the $\Delta\rho_m$ and τ values, namely, the large values indicate less restrictive motion of the DT-AuNPs in the film, which is possible

if the coverage is incomplete, while the small values suggest restricted motion, which is applicable if the coverage is complete. On the other hand, the values of the parameter $\sum_j \rho_{0j}$ for the DT-AuNP/H-Si LS films is neither similar to that of the DT-AuNP/OTS-Si LS films nor time independent. The increase in the value of this parameter can be visualized by the increase in the area of the large size voids, which then, by keeping the film materials constant, decreases the effective in-plane covered area and consequently (considering the incoherent scattering concept as before) increases the $\sum_j \rho_{0j}$ value.

5.3.4 Growth and evolution: control mechanism

Now, let us first try to model the structures of the films and then try to understand their growth, evaluation and control mechanism. The structures of the DT-AuNPs LS films grown at low ($\Pi = 2$ mN m^{-1}) and high ($\Pi = 10$ mN m^{-1}) pressures on two different passivated substrates (OTS-Si and H-Si) at initial

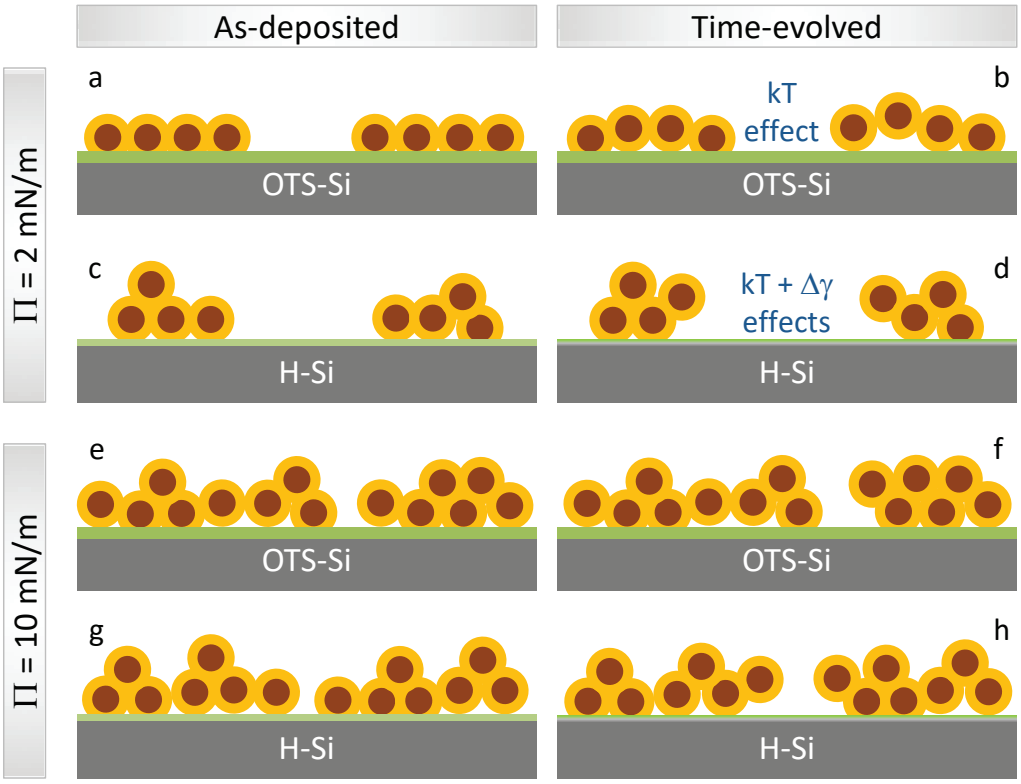

Figure 50: Structural models of the as-deposited ($t \approx 0$) and time-evolved ($t \approx 39$ days) DT-AuNPs LS films deposited at low and high surface pressures (Π) on the OTS-Si and H-Si substrates.

($t \approx 0$) and final ($t \approx 39$ days) stages, as visualized from the analysis, are shown schematically in Figure 50. DT-AuNP/OTS-Si LS film deposited at low pressure formed monolayer structure with large size voids (i.e. partial coverage), where the DT-AuNPs are initially (Figure 50a) placed at same z position to give rise a layer of perfect monolayer thickness and finally (Figure 50b) few are placed at slightly different z positions to give rise a fluctuating monolayer (of thickness intermediate between monolayer and bilayer thickness). DT-AuNP/H-Si LS film deposited at low pressure initially (Figure 50c) formed monolayer plus very small bilayer structure with large size voids (i.e. partial coverage), which with time finally (Figure 50d) become symmetrically fluctuated monolayer structure (of thickness intermediate between monolayer and bilayer thickness) with increased void size. DT-AuNP/OTS-Si LS film deposited at high pressure formed highly fluctuated monolayer structure with negligible voids (i.e. full coverage), where the DT-AuNPs are initially (Figure 50e) accumulated mostly at central position and finally (Figure 50f) distributed evenly to give rise thickness less than bilayer thickness. Finally, DT-AuNP/H-Si LS film deposited at high pressure initially (Figure 50g) formed monolayer plus small bilayer structure with negligible voids (i.e. full coverage), which with time finally (Figure 50h) become more symmetrically fluctuated monolayer structure (of thickness intermediate between monolayer and bilayer thickness) with some voids.

It is known that the DT-AuNPs on the water surface first self-assembled around different points to form disk-like islands of monolayer height [133] (due to the complex balance of long range vdW attractions and short range steric repulsion of the DT-AuNPs[134, 135, 137] initiated by solvent evaporation [128–130] in presence of the hydrophobic repulsion of water), which on compression formed 2D-network of buckled or flipped disk-like islands [133, 151] (due to a combined effect of collision induced coalescence and solid-like behavior resisting deformation of the islands [134]). The interactions between DT-AuNPs in the islands can be described phenomenologically by a potential given by Hamaker. [305, 306]

Considering the size ($2R \approx 2.5$ nm, as estimated from the optical absorption and TEM measurements), the centre-to-centre separation ($D \approx 4$ nm, as estimated from the GISAXS measurements) [133] i.e. the edge-to-edge separation ($\delta = D - 2R \approx 1.5$ nm) and the Hamaker constant ($A \approx 1.95$ eV) [306, 307] of the AuNPs, the interaction potential energy is less than 10 meV. The growth and evaluation of such Langmuir monolayers when transferred onto OTS-Si and H-Si substrates using LS techniques can be understood from the XR data analyses, which are shown schematically in Figure 51. During LS deposition (Figure 51a,b), the DT-AuNPs in Langmuir monolayers, in presence of hydrophobic repulsion of water, feel strong-attraction (Figure 51c) with the relatively strong-hydrophobic OTS-Si substrate (contact angle $\theta_c \approx 110^\circ$), [308, 309] to form (Figure 51e) partially covered monolayer structured (with perfect monolayer thickness) film at low pressure (Figure 50a) and nearly covered buckled monolayer structured (with enhanced monolayer thickness) film at high pressure (Figure 50e), while feel relatively weak-attraction (Figure 51d) with the weak-hydrophobic H-Si substrate ($\theta_c \approx 80^\circ$), [310] to form (Figure 51f) partially covered monolayer plus few bilayer structured film at low pressure (Figure 50c) and nearly covered monolayer plus few bilayer structured film at high pressure (Figure 50g).

After deposition, evolution of film takes place with time (Figure 51g,h). Such evolution is unlikely drying mediated, [153] as no trapped water is expected on the hydrophobic particles and/or substrates. Also, the evolution is unlikely to relax the strain, which may usually arise due to the hydrophobic substrate-water repulsion (for LB deposition) or the substrate-film repulsion (for hydrophilic substrate) during deposition, as such stain is not expected for the LS deposition on hydrophobic substrates. It is expected that at ambient condition, the room temperature (T) supply thermal energy $kT \approx 26$ meV (where k is the Boltzmann constant) to the system, which can change the positions of the DT-AuNPs. The amount and direction of the change, are however, depend upon their interactions in the film. Absence of the hydrophobic repulsive force of water from the top of

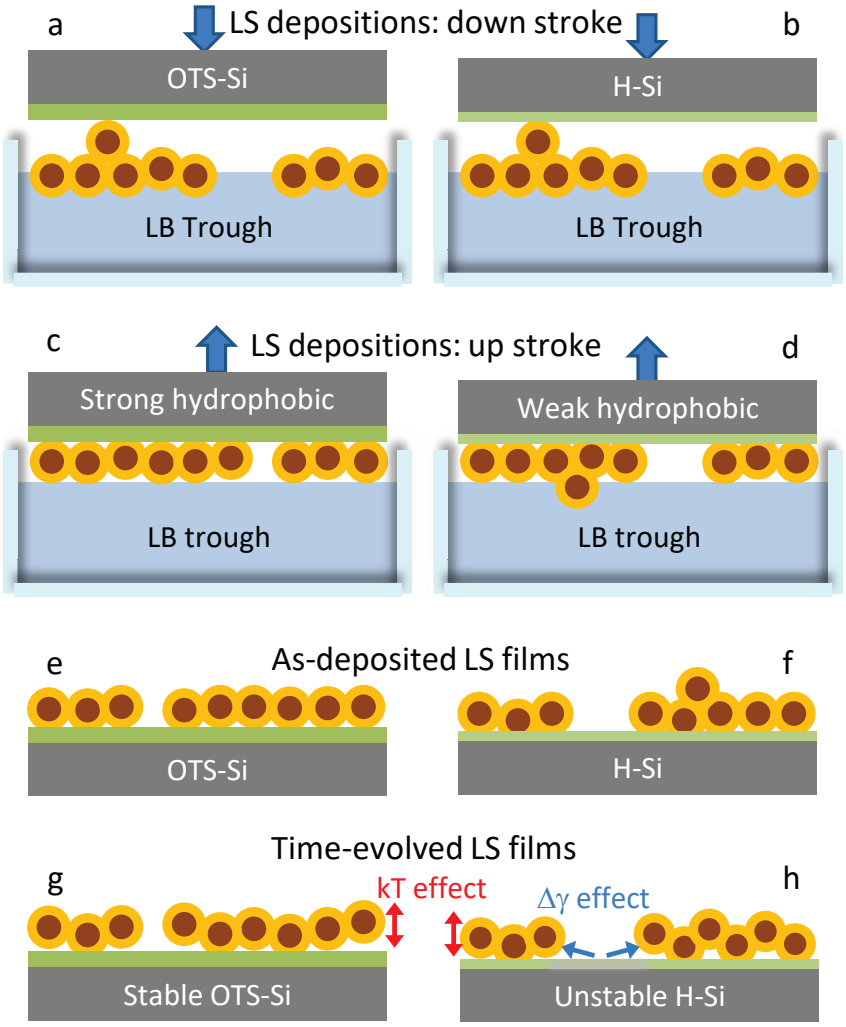

Figure 51: Schematic illustration of the growth and evolution of DT-AuNPs LS films on OTS-Si and H-Si substrates.

the film after deposition (which was present during deposition) probably allows the small thermal energy to fluctuate the DT-AuNPs vertically to enhance the film-thickness with time. Such kT effect is applicable to the films deposited on both the substrates (Figure 51g,h). Additionally, instability of the passivated Si surface, at ambient condition, plays important role. It is known that the OTS-Si substrate is stable [308, 309] but H-Si substrate is not. [12] For the latter, desorption of H atoms followed by the growth of oxide layer takes place with time, which then changes its surface energy or hydrophobic/hydrophilic nature from weak-hydrophobic ($\theta_c \approx 80^\circ$ for H-Si) to weak-hydrophilic ($\theta_c \approx 60^\circ$ for O-Si) or moderate-hydrophilic ($\theta_c \approx 20^\circ$ for OH-Si). [146, 311] Such instability or change in the hydrophobic/hydrophilic nature (i.e. contact angle $\Delta\theta_c$) or

substrate surface energy ($\Delta\gamma$, which is related to $\Delta\theta_c$) can even takes place in presence of a film, may be selectively, which then changes the film-substrate interaction. The change in surface energy will be considerable at the area of voids and accordingly the DT-AuNPs near the periphery of the voids will experience inwards force to enhance the size of the voids. This $\Delta\gamma$ effect is applicable to the films deposited on H-Si substrates (Figure 51h).

The present structural analysis (namely out-of-plane monolayer/bilayer structure and in-plane island size) indicates that the Langmuir monolayer structure is better preserved on the H-Si substrate compared to the OTS-Si substrate at the initial stages, which is quite amazing. The weak-hydrophobic nature of H-Si substrate probably creates the optimum attraction in mimicking the Langmuir monolayer structure. Subsequently, the spherically symmetric DT-AuNPs in the monolayer and/or bilayer positions of a film are found to evolve or fluctuate with time at ambient conditions due to the presence of room temperature thermal energy and/or change in the substrate surface energy (unlike spherically asymmetric amphiphilic molecules, where perfect 2D structure is more favorable), to form extended/broad monolayer or compressed/narrow bilayer structure of thickness $\approx$ 6 nm, which is quite interesting. The kT effect probably fluctuates the DT-AuNPs mainly along vertical direction as observed for the films deposited on the OTS-Si substrates, where the film-thickness changes with time following the exponential growth law. The critical growth time (τ) and the change in the film-thickness are prominent for the film deposited at low pressure, where initial film-coverage and film-thickness are low. The combination of kT and $\Delta\gamma$ effects probably fluctuates the DT-AuNPs in different directions as observed for the films deposited on H-Si substrates. The final thickness, which is more related to the vertical fluctuation, is probably decided by the room temperature thermal energy. However, proper theoretical modeling is needed to support such optimized thickness. Also, further experimental studies are required to find out the uniqueness of such thickness, which are in progress.

5.4 Conclusions

The effects of hydrophobic strength of the substrate and ambient conditions on the structures and stability of DT-AuNP LS films were investigated using the XR technique for the formation of controlled 2D-structures on solid substrates by mimicking the Langmuir monolayer structures through a single transfer process. A partially covered monolayer structured (with perfect monolayer thickness) film at low pressure and nearly covered buckled monolayer structured (with enhanced monolayer thickness) film at high pressure are evident on the OTS-Si substrate, while a partially covered monolayer plus few bilayer structured film at low pressure and nearly covered monolayer plus few bilayer structured film at high pressure are evident on the H-Si substrate at the initial stages. These indicate that during transfer, the OTS-Si substrate, due to its strong-hydrophobic nature ($\theta_c \approx 110^\circ$), creates too much attraction toward the DT-AuNP Langmuir monolayer to vertically squeeze the structure, while the H-Si substrate, due to its weak-hydrophobic nature ($\theta_c \approx 80^\circ$), creates reasonable attraction toward the DT-AuNP Langmuir monolayer to better mimic the structure.

At ambient conditions, all films evolved with time to change the initial film-thickness. The evolution of film-thickness deposited on OTS-Si substrates shows exponential growth due to kT ($\approx$26 meV) energy induced systematic diffusion, while those deposited on H-Si substrates show anomalous evolution due to both kT and $\Delta\gamma$ (related to $\Delta\theta \approx 20^\circ$) energy driven fluctuation. Finally, all the films formed nearly similar vertically expanded monolayer structures, though the evolution paths are different, which is quite interesting and requires further investigation.

6

EVOLUTION OF LIGANT-CAPPED NANOPARTICLE MULTILAYERS TOWARD A NEAR UNIQUE THICKNESS

6.1 Introduction

It is known from earlier studies [144, 306] that, at air/water interface, AuNPs self-assembled to form 2D-structures, which then can be transferred onto solid substrate using LB and LS deposition techniques to grow 2D- and 3D-nanostructures over large areas. [133, 160, 306] Among them, the nanostructures grown on hydrophobic substrates using LS technique are of special interest [133, 160], as the interaction between hydrophobic AuNP-shell and hydrophobic substrate (i.e. between two hydrophobic or similar nature materials) is attractive, it is likely to create least disturbance on the structure during transfer and thus expected to be better controlled. Although some works have been carried out to understand the structure and growth of LS monolayers of AuNPs on hydrophobic substrates (i.e. 2D-nanostructures) [160] but no work has been carried out to understand the growth and stability of LS multilayers of AuNPs on hydrophobic substrates, which is of utmost importance for the formation of desired 3D-nanostructures of specific collective properties through controlled bottom-up technique. The study of LS monolayers of AuNPs on hydrophobic substrates, on the other hand, suggests that the hydrophobic strength apart from the hydrophobic nature of the substrate is responsible for creating minimum disturbance on the Langmuir monolayers [160]. In fact, it was found that the weak-hydrophobic H-passivated Si substrate creates less disturbance, compared to the strong-hydrophobic OTS

self-assembled Si substrate, to better mimic the Langmuir monolayer structures. Such structures were again found to evolve with time at ambient conditions (due to the presence of room temperature thermal energy and/or the change in interfacial energy) to form similar vertically expanded monolayer structures. The condition for obtaining the better mimic structure at the initial stages and the formation of similar vertically expanded monolayer structures through evolution for LS monolayers are interesting and lead to the questions: i) Do the desired 3D-structures can be formed on H-passivated Si substrate through multi-transfer of such Langmuir monolayers, atleast at the initial stages, simply by knowing and controlling the Langmuir monolayer structures, i.e. do the concept of mimic is valid for the multi-transferred LS films? ii) Do the multi-transferred LS films evolved to similar vertically expanded monolayer structures, i.e. do the evolution of multilayer LS films can infer anything about the uniqueness in the thickness of the evolved structure and its possible origin? It can be noted that the long keeping time of the LS film may cause some structural changes (toward energy minimum state) as the transfer process itself is not always carried out under equilibrium conditions. Hence, finding such energy minimum state or structure and the associated process are quite demanding, though challenging.

In this chapter we have addressed these questions by investigating the structures of the multi-transferred LS films of AuNPs on H-Si substrates using complementary XR and GISAXS techniques; and their evolution with time at ambient conditions using XR technique. It is found that the structures of the films, at the initial stages, depend strongly on the surface pressure of Langmuir monolayer and the number of transfer but follow weakly the Langmuir monolayer structure, both in terms of layer coverage and domain structure. On the other hand, it is indeed found that the structure (thickness) of film evolves (decreases) with time at ambient condition to approach toward a near unique thickness (provided the amount of transferred AuNPs in the LS film is within the amount, which can be accommodated). The possible interactions and/or energy, responsible

for the growth of such near unique thickness from different layer-number and layercoverage films, through evolution, are discussed.

6.2 Experimental details

6.2.1 Preparation of mT−DT-AuNP/H-Si LS films

The colloidal DT-AuNPs of core size about 2.5 ± 0.6 nm and overall size about 4.5 ± 0.6 nm were synthesized following a two-phase (water-toluene) reduction of hydrogen tetrachloroaurate by sodium borohydride in presence of dodecanethiol (discussed in 2.3.1). Such DT-AuNPs were spread uniformly on the surface of water (Milli-Q) in a Langmuir trough (KSV 5000) to form Langmuir monolayer. [133] The pressure (Π) of the of DT-AuNPs Langmuir monolayer was regulated using Teflon barriers movement. Prior to the DT-AuNPs monolayer deposition, Si substrates (of size about 15×15 mm^2) were first sonicated in acetone and ethanol solvents to remove organic contaminates and then treated with hydrogen fluoride [HF, Merck, 10%] solution to prepare H-terminated Si (H-Si) substrates (discussed in 2.2). The DT-AuNPs Langmuir monolayers formed at different pressure (namely Π = 2, 4, 6, 10 and 14 mN/m) were then transferred twice and four times onto the H-Si substrates using LS deposition technique (discussed in 2.3.4.2). Such multi-transferred films are labeled as mT−DT-AuNP/H-Si LS films, where m = 2 and 4.

6.2.2 Characterization of mT−DT-AuNP/H-Si LS films

The characterization of mT−DT-AuNP/H-Si LS films, within a day, after a month and after a year of preparation, were carried out using XR technique, while that at the initial stages, were also carried out using complementary GISAXS technique.

XR measurements of the films were performed on a versatile X-ray diffractometer (VXRD) setup (discussed in 3.4.1). VXRD consists of a diffractometer (D8 Discover, Bruker AXS) with enhance Cu Kα radiation (λ = 1.54 Å) (discussed

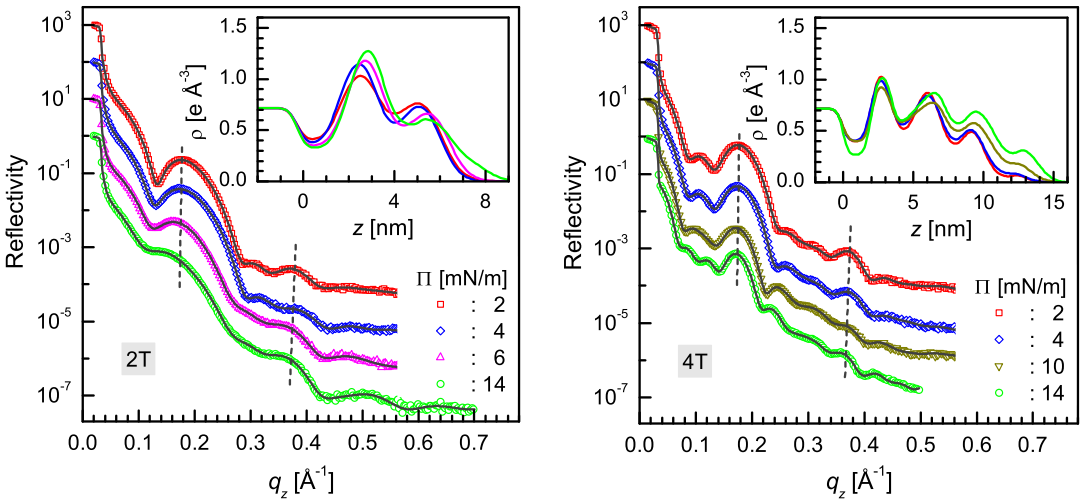

Figure 52: XR data (different symbols) collected within a day ($t < 1$ day) and analyzed curves (solid lines) of multi-transferred (2T- and 4T-) DT-AuNP/H-Si LS films prepared from Langmuir monolayers of different surface pressure (Π). Curves are shifted vertically for clarity. First order and second order psudo-Bragg peaks arising from out-of-plane AuNPs layer separation (d_{out}) are indicated by dashed lines. Insets: corresponding analyzed EDPs.

in 3.4.1). XR technique essentially provides an electron-density profile (EDP), i.e., in-plane ($x - y$) average electron density (ρ) as a function of depth (z) in high resolution. From EDP it is possible to verify the presence of layering in the film, with their number, position and coverage. GISAXS measurements of the films were carried out using a synchrotron source (MiNaXS beam line, PETRA III), (discussed in 3.4.2) at λ = 0.94 Å. The sample-to-detector distance was 1721 mm. Corresponding angular resolution is 0.1 mrad and the resolution limit along q_y-direction is less than 0.002 Å^{-1}. For the data collection, the incident angle α was kept at 0.25°, slightly greater than the critical angle, α_c, of the sample. GISAXS pattern on a particular position was collected for small time (10 s) to minimize the effect of the radiation damage of the sample. Then GISAXS patterns were collected at different lateral positions of a sample to rule out the in-plane inhomogeneity of the sample and to enhance the statistics by averaging.

6.3 Results and discussion

6.3.1 XR studies of the as-grown films

XR data of the mT−DT-AuNP/H-Si LS films deposited at different Π-values and collected within a day (i.e. $t < 1$ day) are shown in Fig. 52. Oscillations with more than a single periodicity are observed in all the XR profiles. The high frequency oscillations are the Keissig fringes corresponding to the total film thickness. The relatively strong peaks near $q_z \approx 0.18$ and 0.37 Å^{-1} (indicated by dashed lines) are the first and second order pseudo-Bragg peaks corresponding to the layered structures of the films. The position and intensity of which change slightly with the Π-value and also with the m-value.

To get the quantitative information about the films, all XR profiles have been analyzed using Parratt's formalism, [294] after incorporating roughness at each interface. [133] An instrumental resolution in the form of a Gaussian function and a constant background were also included at the time of data analysis. For the analysis, 2T− and 4T−DT-AuNP/H-Si LS films are first modelled with two and four layers, respectively, of DT-AuNPs of different thickness and coverage on the Si substrates. Subsequently, considering each DT-AuNPs layer consists of three layers, namely thiol-rich low density bottom layer, Au-rich high density middle layer and again thiol-rich low density top layer; the 2T− and 4T−DT-AuNP/H-Si LS films are actually analyzed using 5 and 9 layers, respectively, of alternate low and high electron densities. The best fit XR profiles along with the corresponding EDPs for the mT−DT-AuNP/H-Si LS films are shown in Fig. 52.

Two and four number of peaks are readily evident in the EDPs (insets of Fig. 52) of the 2T− and 4T−DT-AuNP/H-Si LS films, suggesting bilayer and tetralayer natures, respectively. However, the peak-value (ρ_m) is not same for the different peak positions in a film and also for the similar peak position in different films. The variation of such ρ_m-value for different layer number (n) in the mT−DT-AuNP/H-Si LS films are plotted in Fig. 54 as a function of Π-value.

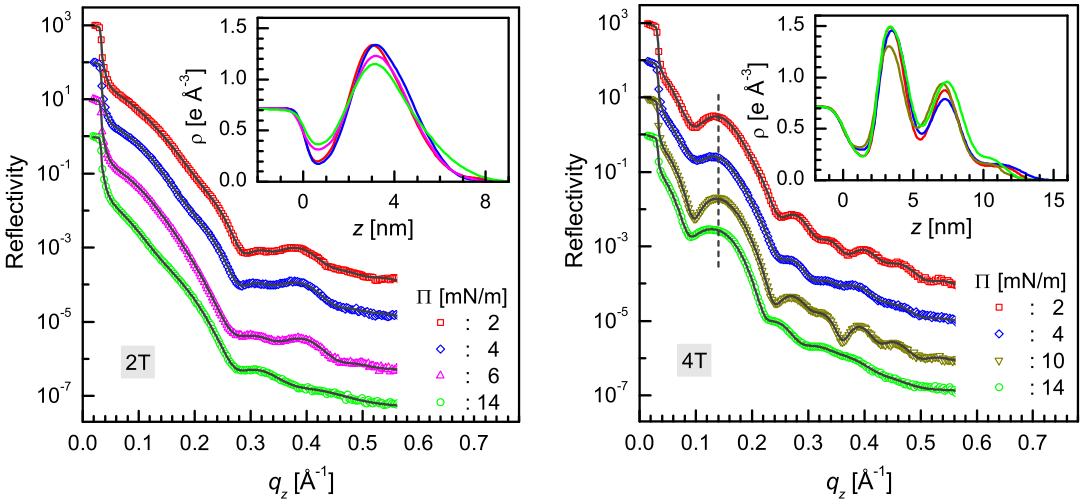

Figure 53: XR data collected after a month (different symbols) and analyzed curves (solid lines) of multi-transferred (2T- and 4T-) DT-AuNP/H-Si LS films prepared from Langmuir monolayers of different surface pressure (Π). Curves are shifted vertically for clarity. Psudo-Bragg peaks due to layered structures of the films are indicated by dashed lines. Insets: corresponding analyzed EDPs.

In case of 2T−DT-AuNP/H-Si LS films, the ρ_m-value for the first layer is found relatively high, which increases initially fast then slow (i.e. exponentially) with Π-value, while that of the second layer is relatively low and decreases exponentially with Π-value. In case of 4T−DT-AuNP/H-Si LS films, however, the ρ_m-value for the first and second layers decreases gradually with Π-value, except for high Π-value, while that for the third and forth layers increases gradually with Π-value.

The variation of the ρ_m-value and the peak position (z_m) with layer number are also plotted in Fig. 54 for the mT−DT-AuNP/H-Si LS films deposited at two extreme Π-values (namely 2 and 14 mN/m). The average out-of-plane separation between the layers (d_{out}) obtained from the slope of the z_m vs n curves for the four films are tabulated in Table 7. The d_{out}-value (∼3.1 nm) is quite small compared to the overall size of the DT-AuNPs ($2R \approx 4.5$ nm) and found to increase with the Π-value and also with the m-value. The average film thickness (D) and the average electron density (ρ_{ave}) obtained from the EDPs are also listed in Table 7. For the 2T−DT-AuNP/H-Si LS films, the ρ_{ave}-value is found unchanged, while the D-value is found to increase slightly with the Π-value, suggesting very small

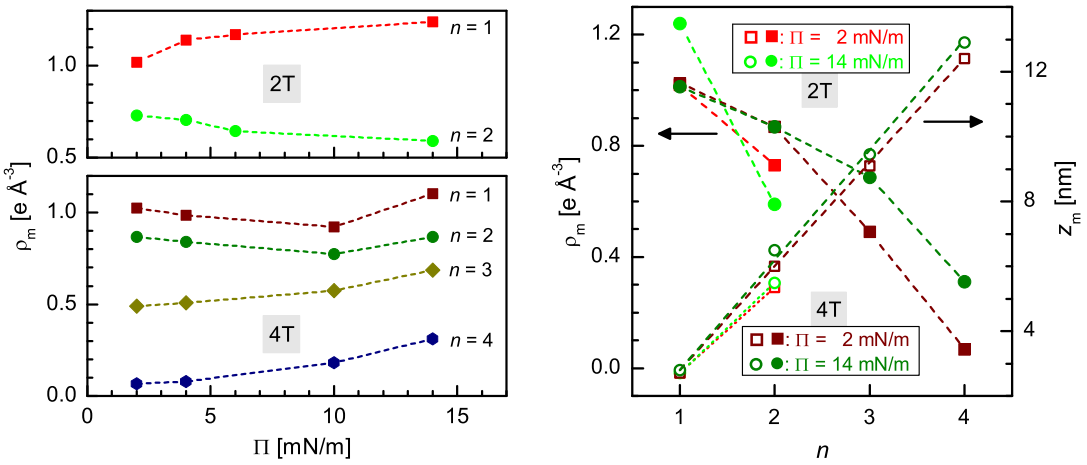

Figure 54: Left: Variation of peak electron density (ρ_m) with deposited surface pressure (Π) for the different layer number (n) in the EDPs of multi-transferred (2T- and 4T-) DT-AuNP/H-Si LS films. Right: Variation of peak electron density (ρ_m) and peak position (z_m) with layer number (n) in the EDPs of multi-transferred (2T- and 4T-) DT-AuNP/H-Si LS films prepared from Langmuir monolayers of two different surface pressure (Π).

increase in the amount of transferred materials. On the other hand, for the 4T−DT-AuNP/H-Si LS films, both (ρ_{ave} and D) values are found to increase with the Π-value, suggesting reasonable increase in the amount of transferred materials. Further the ρ_{ave}-value is found to decrease considerably with the increase of m-value from 2 to 4, suggesting considerable decrease in the amount of materials per transfer with the increase in the number of transfer.

6.3.2 GISAXS studies of the as-grown films

GISAXS patterns of the mT−DT-AuNP/H-Si LS films deposited at two extreme Π-values (2 and 14 mN/m) are shown in Fig. 55. The Bragg rods around $q_y = \pm$ 0.15 Å^{-1} are observed in all the patterns, the intensity and actual position of which varies with Π and m values. To have a better idea about the position and intensity of the Bragg rods, GISAXS line profiles along q_y direction and through the Bragg rods, for all the films, are also plotted in Figs. 55. The line profiles along q_y-direction clearly show peaks around $q_y = \pm$ 0.15 Å^{-1} due to in-plane AuNPs separation (d_{in}). The d_{in}-values obtained from the peak positions are tabulated in Table 7 for four films.

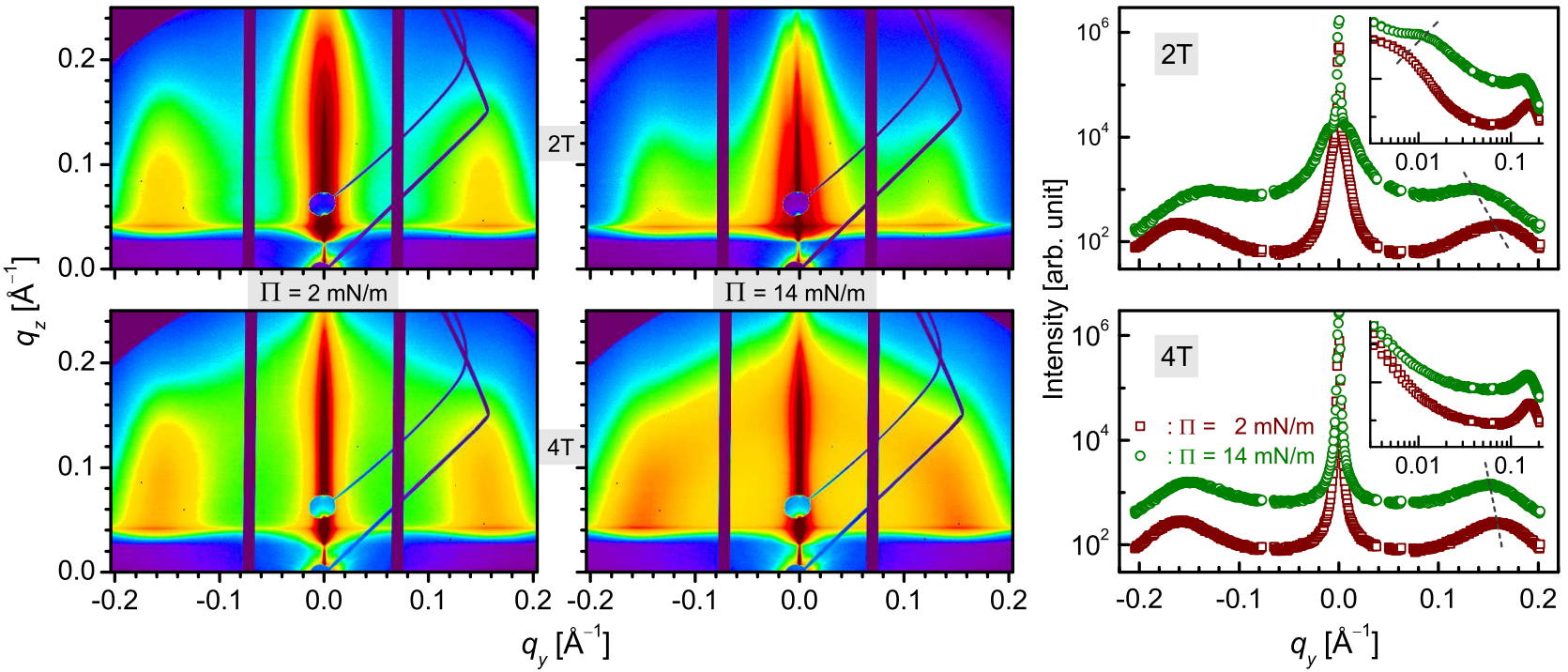

Figure 55: Left panel: GISAXS patterns of multi-transferred (2T- and 4T-) DT-AuNP/H-Si LS films prepared from Langmuir monolayers of two extreme surface pressure (Π). Right panel: Corresponding GISAXS line profiles along the q_y direction (i.e. lateral cut through the first Bragg rod at $q_z \approx 0.04$ Å^{-1}). Peaks arising from in-plane AuNPs separation (d_{in}) are indicated by dashed lines. Insets: log-log plot of the same GISAXS line profiles to have a better idea about the in-plane correlation at different length scales. Broad humps arising from in-plane correlation between domain-like structures are indicated by dashed lines. Curves are shifted vertically for clarity.

The d_{in}-value (∼4.2 nm) is slightly low compared to the $2R$-value but considerably high compared to the d_{out}-value. The d_{in}-value is also found to increase with the Π-value. The increase is, however, small for the 4T−DT-AuNP/H-Si LS films but appreciably for the 2T−DT-AuNP/H-Si LS films. The peak intensity for the 2T−DT-AuNP/H-Si LS films decreases slightly with the increase of Π-value, while for the 4T−DT-AuNP/H-Si LS films increases slightly with the increase of Π-value.

Further, to have a better idea about the different in-plane correlation lengths (especially the larger correlation lengths, which should appear at low q_y values), the log-log plot of the same GISAXS line profiles have been presented in the insets of Fig. 55. A broad hump is observed for the 2T−DT-AuNP/H-Si LS films (shown by the dashed lines), suggesting formation of domainlike structures in these films. The average separations between the domains, as obtained from the hump positions, are about 100 and 50 nm for the films of Π values 2 and 14 mN/m, respectively. This indicates that the separation between the domains decreases with the Π-values, which is probably due to the increase in the number of domains. The information about the domains for the 4T−DT-AuNP/H-Si LS films is however missing.

6.3.3 XR studies of the films after a month

XR data of the mT−DT-AuNP/H-Si LS films deposited at different Π-values and collected after a month (i.e. $t \approx 1$ month) are shown in Fig. 53. Oscillations with more than a single periodicity are observed in all the XR profiles. However, for the 2T−DT-AuNP/H-Si LS films, the oscillations are very weak compared to the as-grown films and even the first order pseudo-Bragg peak is absent, which indicates the absence of multi-layered structure. For the 4T−DT-AuNP/H-Si LS films, though the first order pseudo-Bragg peak is present, it becomes broad and shifts toward lower q_z value, which suggests decrease in the layer number and increase in the layer width. To get the quantitative information of the 2T−

Table 7: Parameters such as the in-plane AuNPs separation (d_{in}) and out-of-plane AuNPs layers separation (d_{out}) at the initial stages; while the total film thickness (D) and the average electron density (ρ_{ave}) at the different aging time (t) for the multi-transferred, mT−DT-AuNP/H-Si LS films deposited at different surface pressure (Π), as obtained from the GISAXS and XR data analysis.

mT	Π	$t < 1$ day			
	[mN/m]	d_{in} [nm]	d_{out} [nm]	D [nm]	ρ_{ave} [e Å^{-3}]
2T	2	3.9	2.8	6.4±0.6	0.73
	14	4.6	2.9	6.8±0.6	0.73
4T	2	4.0	3.2	13.1±0.7	0.49
	14	4.2	3.4	13.9±0.7	0.58

mT	Π	$t \approx 1$ month		$t \approx 1$ year	
	[mN/m]	D [nm]	ρ_{ave} [e Å^{-3}]	D [nm]	ρ_{ave} [e Å^{-3}]
2T	2	4.8±1.0	0.97	4.6±0.9	1.02
	14	5.0±1.2	0.99	4.5±0.8	1.10
4T	2	11.0±1.7	0.59	6.2±1.2	1.03
	14	11.0±1.5	0.70	7.1±1.5	1.08

and 4T−DT-AuNP/H-Si LS films, the XR data are analyzed using 3 and 7 layers, respectively, of alternate low and high electron densities.

The best fit XR profiles along with the corresponding EDPs for the mT−DT-AuNP/H-Si LS films are shown in Fig. 53. Only one and two (with weak third) peaks are observed in the EDPs (insets of Fig. 53) suggesting monolayer and bilayer (with some trilayer) natures of the 2T− and 4T−DT-AuNP/H-Si LS films, respectively, after a month, deviating from the original bilayer and tetralayer natures. The D-value and the ρ_{ave}-value obtained from the EDPs for the four films are also listed in Table 7. For the 2T−DT-AuNP/H-Si LS films, the D-value (∼5 mn) is found to decrease ∼25%, correspondingly the ρ_{ave}-value (∼1 e Å^{-3}) is found to increase ∼30% compared to the values of the as-grown structures. On the other hand, for the 4T−DT-AuNP/H-Si LS films, the D-value becomes about 11 nm for both the films, while the ρ_{ave}-value becomes about 0.6 and 0.7 e Å^{-3}

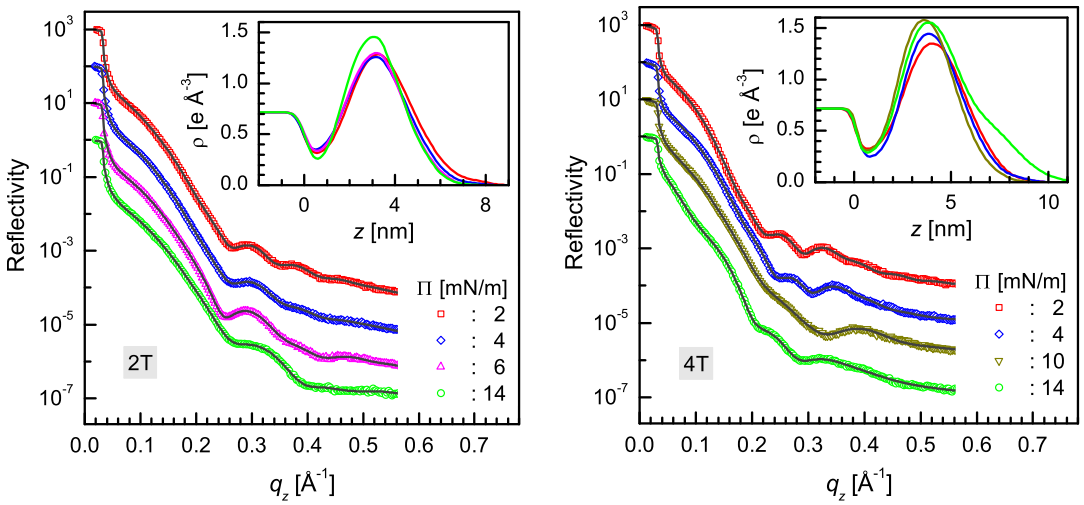

Figure 56: XR data collected after a year (different symbols) and analyzed curves (solid lines) of multi-transferred (2T- and 4T-) DT-AuNP/H-Si LS films prepared from Langmuir monolayers of different surface pressure (Π). Curves are shifted vertically for clarity. Insets: corresponding analyzed EDPs.

for the films of Π = 2 and 14 mN/m, respectively, suggesting ∼20% decrease in the D-value and ∼20% increase in the ρ_{ave}-value of the films after a month.

6.3.4 XR studies of the films after a year

XR data of the mT−DT-AuNP/H-Si LS films deposited at different Π-values and collected after a year (i.e. $t \approx 1$ year) are shown in Fig. 56. Weak oscillations are observed in all the XR profiles but the pseudo-Bragg peak is absent, indicating disappearance of the multi-layered structures of the films. The best fit XR profiles along with the corresponding EDPs for the mT−DT-AuNP/H-Si LS films are also shown in Fig. 56. Single peak is observed in the EDPs (insets of Fig. 56) suggesting monolayer nature of the films, after a year, deviating from the original bilayer and tetralayer natures. The D-value and the ρ_{ave}-value obtained from the EDPs for the four films are listed in Table 7. For the 2T−DT-AuNP/H-Si LS films, the D-value (∼4.5 mn) decreases appreciably (∼30%) compared to the value of the as-grown films, but decreases slightly compared to the value of the films observed after a month, correspondingly the ρ_{ave}-value increases significantly (∼35%) compared to the value of the as-grown films but increases negligibly compared to the value of the films observed after a month. On the other hand, for

the 4T−DT-AuNP/H-Si LS films, the D-value ($\sim$6.5 mn) decreases appreciably ($\sim$50% and $\sim$40%), while the ρ_{ave}-value ($\sim$1.05 e Å^{-3}) increases significantly ($\sim$95% and $\sim$60%) compared to the values of the as-grown films and the films observed after a month.

Table 8: The coverage (C_L) of first (1st), second (2nd), third (3rd) and forth (4th) layers; and the coverage (C_S) of monolayer (ML), bilayer (BL), trilayer (TL) and tetralayer (TtL) thickness structures at the different stages of time (t) in the multi-transferred, mT−DT-AuNP/H-Si LS films deposited at different surface pressure (Π), as obtained from the deconvolution of the analyzed EDPs. Note that C_L can have two values (first one is for closer position compared to other normal position from the substrate), while C_S is the total coverage of similar layered (thickness) structures

mT	Π [mN/m]	t	C_L [%]							
			1st		2nd		3rd		4th	
2T	2	1d	19	60	23	38				
		1m	11	70	46	11				
		1y	17	58	50	17				
	14	1d	17	76	17	31	9	0		
		1m	18	55	43	21	7	0		
		1y	9	58	60	17				
4T	2	1d	17	63	24	47	14	25	2	5
		1m	10	86	22	42	26	7	7	0
		1y	17	47	63	43	14	0		
	14	1d	11	62	34	46	23	37	16	18
		1m	12	80	42	42	40	11	7	0
		1y	14	61	72	45	26	11		

mT	Π [mN/m]	t	C_S [%]				M_T	
			TtL	TL	BL	ML	[M_{MLT}]	[M_{NUT}]
2T	2	1d			57	26	∼1.4	∼0.9
		1m			22	94		
		1y			34	74		
	14	1d		9	39	45	∼1.5	∼1.0
		1m		7	32	59		
		1y			26	92		
4T	2	1d	7	32	25	23	∼1.9	∼1.3
		1m	7	11	45	49		
		1y		14	46	50		
	14	1d	29	24	16	27	∼2.4	∼1.6
		1m	7	16	59	40		
		1y		25	46	62		

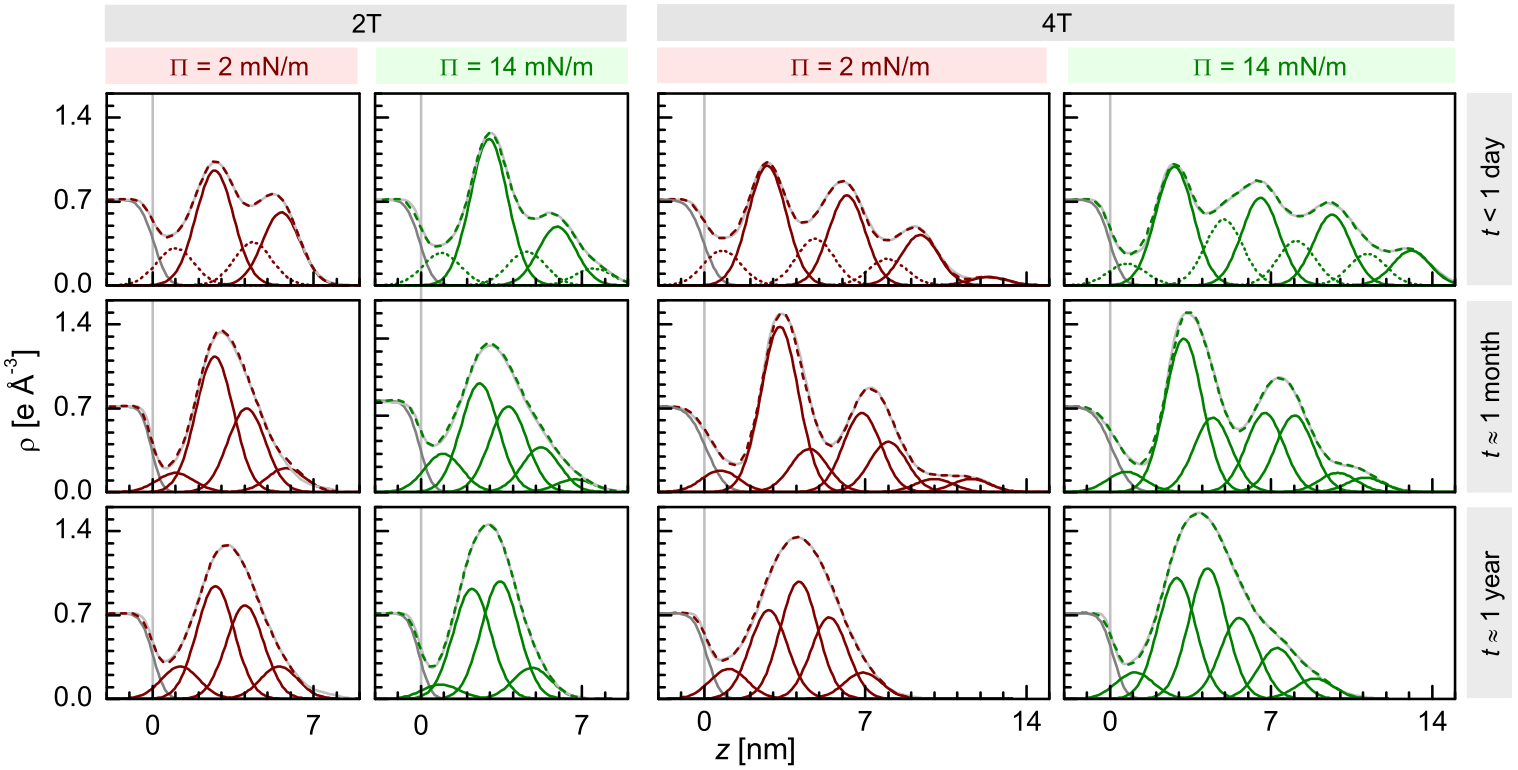

Figure 57: Gaussian deconvoluted EDPs at different stages (t) of multi-transferred (2T- and 4T-) DT-AuNP/H-Si LS films prepared from Langmuir monolayers of two different surface pressure (Π).

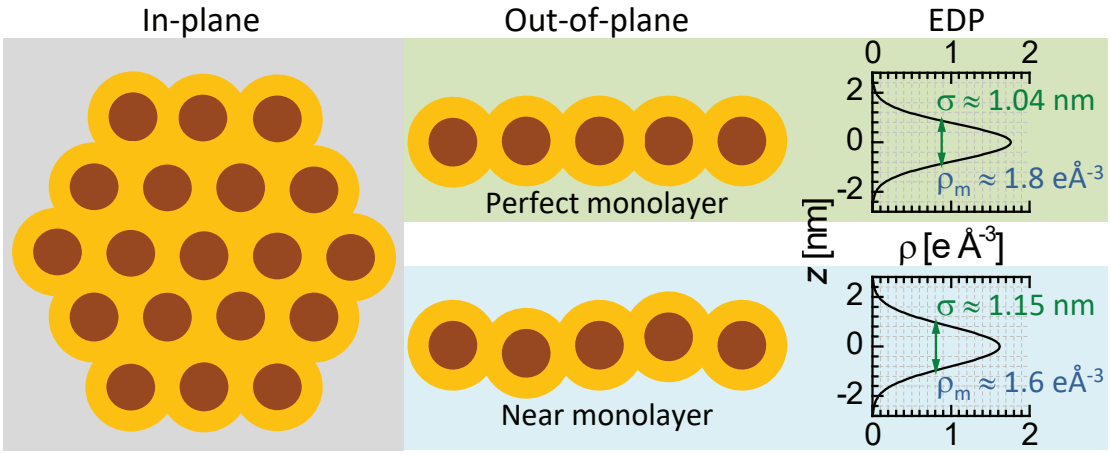

Figure 58: GISAXS line profiles along q_y direction for the DT-AuNPs/H-Si LS films deposited at different surface pressure. Curves are shifted vertically for clarity. The straight dashed line marked the resolution limit along q_y direction.

6.3.5 Growth and stability of mT−AuNP/H-Si LS films

Let us now try to visualize the structures of the mT−DT-AuNP/H-Si LS films at different stages of time from the analyzed EDPs and then discuss their growth and stability/instability. To do this first taking into account that the EDP of a monolayer of DT-AuNPs can be approximated by a simple Gaussian function. It can be noted that each Gaussian peak in the EDP of a monolayer film arises from a layer consisting of DT-AuNPs and not simply from single DT-AuNP. Accordingly, $\sigma_0 \approx 1.04$ nm in Eq. 5–4 corresponds to a layer of perfect monolayer thickness and $\sigma_0 \approx 1.15$ nm in Eq. 5–4 corresponds to a layer of near monolayer thickness as shown schematically in Fig. 58.

Then the analyzed EDP can be expressed using following relation

$$\rho(z) = \frac{\rho_s}{2}\left[1 - erf\left(\frac{z - z_0}{\sigma_s}\right)\right] + \sum_i \rho_i \exp\left[-\left(\frac{z - z_i}{\sigma}\right)^2\right] \qquad (6\text{–}1)$$

where the first term, represented by the error function, corresponds to the substrate of uniform electron density, ρ_s with substrate surface (or film-substrate interface) roughness, σ_s at position, z_0, while the second term, represented by the summation of Gaussian peaks of different intensity (ρ_i) and position (z_i) but of same width or standard deviation (σ), corresponds to the film consists of a

number of similar width (thickness) but different intensity (coverage) DT-AuNPs layers placed at different vertical positions.

Eq. 6–1 is used to simulate the analyzed EPDs. For the simulation, attempted has been made to minimize the number of Gaussian peaks by optimizing the σ value. It has been observed that σ = 1.15 nm, which corresponds to the near monolayer structure (as evident from Fig. 58), can well simulate the analyzed EDPs. Deconvoluted profiles obtained form the simulation of the analyzed EDPs for the mT−DT-AuNP/H-Si LS films (where m = 2 and 4 for Π = 2 and 14 mN/m), at different stages of time, are shown in Fig. 57. It is clear from Fig. 57 that minimum two Gaussian peaks (one intense and another weak) are necessary to simulate each single peak of the analyzed EDPs at the initial stages. The weak peaks are at closer positions (CP) to the substrate compared to the corresponding intense peaks, which are at normal positions (NP). Considering these, the coverage (C_L) of the different layers (with CP first and NP second) are estimated from ρ_i value after normalizing with ρ_{max} = 1.6 e Å^{-3} (corresponding to the cent percent coverage) and are tabulated in Table 8 for the four films at three different stages of time. The coverage (C_S) of different layered (thickness) structures, considering summation of the coverage of similar layered (thickness) structures even at slightly different positions, are also listed in Table 8. Finally, the amount of transferred materials (M_T), as estimated from the C_L or C_S values, are also listed in Table 8.

The values of M_T w.r.t. the full coverage of monolayer thickness (M_{MLT}) indicate that, from Table 8, on average, ∼70% and ∼74% materials (*w.r.t.* monolayer coverage) are transferred each time onto the 2T−DT-AuNP/H-Si LS films deposited at Π = 2 and 14 mN/m, respectively, while ∼48% and ∼60% onto the 4T−DT-AuNP/H-Si LS films.

Such decrease of the transfer ratio with the increase of the transfer number, though creates hindrance in the formation of desire layered structures, is quite natural. The increase of surface pressure is one way in which one can increase

the transfer ratio, to some extent. This is apparent for the 4T-AuNP/HSi LS films, where about 30% tetralayer is observed for the high pressure (P = 14 mN/m) film as oppose to the less than 10% tetralayer for the low pressure (P = 2 mN/m) film. Similarly, by tuning the other deposition conditions, it is possible to further improve the transfer ratio to better attain the desire layered structures.

The ambient conditions, on the other hand, play interesting role on the evolution of the structures of the LS films. The multilayered structures tend toward extended monolayer structures with time, namely for the 2T-AuNP/H-Si LS film deposited at P = 2 mN/m, the bilayer structure decreases (∼30%) and the monolayer structure increases (∼40%). It is found that the final thickness attains by a film depends more on the amount of materials transferred (M_T) than on the number of layers. The film with $M_T \approx 1{:}5\ M_{MLT}$, attains thickness of about 6 nm, is termed as near unique thickness (NUT) with near full coverage, while the films with $M_T < 1{:}5\ M_{MLT}$ also attain the NUT but without full coverage. On the other hand, the films with $M_T > 1{:}5\ M_{MLT}$ try to attain NUT, but unable, as excess amount can not be accommodated within NUT. Accordingly, the tetralayer structure in the 4T-AuNP/H-Si LS film deposited at P = 14 mN/m though decreases (∼ 30%), in fact vanishes, both the bilayer and monolayer structures increase (∼30%). It can be noted that the film of NUT can accommodate about 1.5 times materials compared to that of the film of MLT, i.e. $M_{NUT} \approx 1{:}5 M_{MLT}$. Considering this, the values of M_T are expressed in terms of M_{NUT} in Table 8 for different films.

6.3.6 Evolution toward a near unique thickness

The structures of the *m*T-AuNP/H-Si LS films at a particular stage is modelled considering the values of C_L for different vertically positioned layers at that stage, which are shown schematically in Fig. 59. Such structures of the films at initial stages and their evolution with time can be visualized as follows. On the water surface, AuNPs experience both long range vdW attractions and short range steric

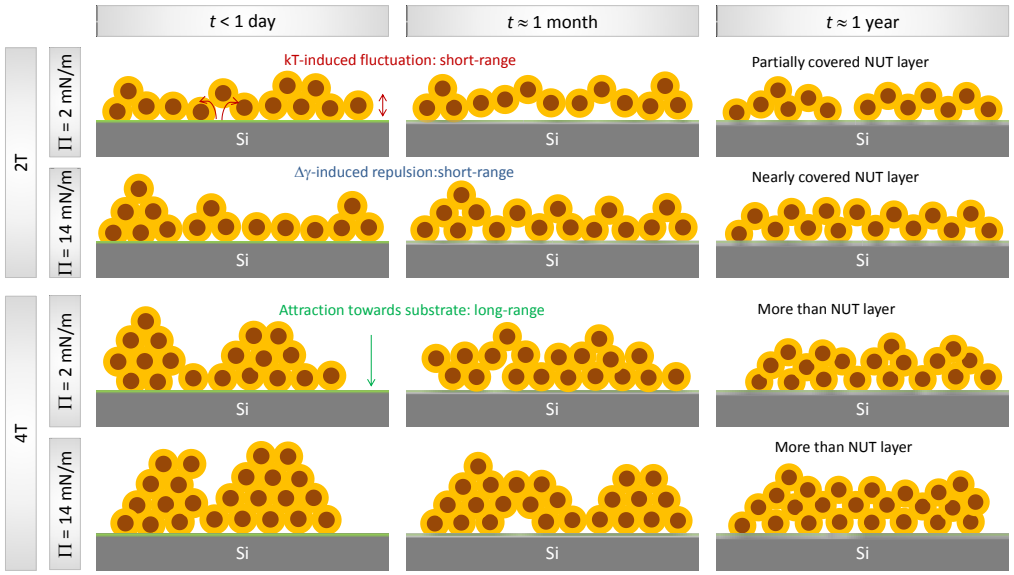

Figure 59: Structural schematics of multi-transferred (2T- and 4T-) DT-AuNP/H-Si LS films prepared from Langmuir monolayers of different surface pressure (Π = 2 and 14 mN/m) at initial stages ($t < 1$ day), after one month ($t \approx 1$ month) and after one year ($t \approx 1$ year).

repulsion, after solvent evaporation. [128, 129] Such complex interaction leads to the formation of self-assembled disk-like islands of monolayer height around different points, which on further compression formed a thermodynamically stable 2D-network of buckled or flipped disk-like islands. [131, 160, 161]

During LS deposition, the hydrophobic terminated Langmuir monolayer feels repulsion from the hydrophilic water and attraction toward the hydrophobic (H-Si or AuNP covered H-Si) substrate, accordingly layer-by-layer (bi-layer and tetra-layer) growth takes place (as shown schematically in Fig. 59 for t $<$ 1 day). However, the multilayers formed on the hydrophobic HSi substrates become thermodynamically unstable. It is well known that the long keeping time of any transferred film may cause some structural changes (toward energy minimum state) as the transfer process itself is not always carried out under equilibrium conditions. However, finding the energy minimum state or structure and understanding the actual process involved in the evolution are very important.

The instability here mainly arises due to the presence of room-temperature thermal energy, kT (where k is the Boltzmann constant and T is the room temperature) [91, 160], due to the degradation of thiols at ambient conditions

and also due to the change in the substrate surface energy, $\delta\gamma$ (as some portion of hydrophobic H-Si surface turn into weak-hydrophilic O-Si surface through H desorption and O adsorption with time) [156, 160], which induces diffusion in the AuNPs. Though the thiol oxidation cannot be ruled out at ambient conditions, [155] it is likely that the oxidation is not completely removing the capping layer of the AuNPs, otherwise continuous growth, due to coalescence of AuNPs with time, would have been taken place, which is not the case here (at least not the dominating effect). Greater coverage of thiols in curved AuNPs (through defective sites) compared to the planer surfaces [154] probably play important role in reducing the oxidation of thiols and maintaining some capping on AuNPs. The certain degradation of thiols (if any) thus considered here to add extra instability in the system and extra diffusion in the AuNPs and not to the coalescence of AuNPs.

Each AuNP in the film then experience hydrophobichydrophobic attractive interaction with other AuNPs and/or H-Si substrate. The AuNPs on the top, where no AuNPs are present above them, experience net attractive force toward the substrate. Such AuNPs, depending upon the availability of nearest void space, start to roll down or move toward the substrate, to reduce the film thickness (from tetralayers and bilayers toward monolayers) and to increase the film coverage (as shown schematically in Fig. 59 for t $\approx$ 1 month and 1 year). However, the $\delta\gamma$-energy in some portion of the substrate surface creates repulsion and the kT-energy creates fluctuation on the AuNPs, which altogether imposes restriction in the thickness-reduction and ideal monolayer formation, rather deviates to form a thermodynamically favourable and relatively stable extended monolayer of NUT. It is necessary to mention that, through reorganization, such NUT layer can be formed if the number (N) of AuNPs in the multilayer is less than (as shown in Fig. 59 for 2T and P = 2 mN/m film) or equals (as shown in Fig. 59 for 2T and P = 14 mN/m film) to the maximum number (N_c) of AuNPs that can be accommodated within NUT. Otherwise (if N $>$ Nc), the evolved-thickness

will increase (as shown in Fig. 59 for 4T films) to accommodate extra particles. The reorganization process (i.e. the duration of reorganization) depends on the number of voids and AuNPs. Accordingly, the reorganization or the thickness-decrease process continues for longer time ($t > 1$ month) for the films with larger number of partial coverage layers (as shown in Fig. 59 for 4T films).

It can be noted that the mechanistic origins for lamellar instability and the convergent reorganization of multilayers proposed here strongly depend on the roles of the thermal fluctuations, the hydrophobic repulsion between AuNPs and degradation of thiols. Hence they call for additional experiments to firmly validate the proposed mechanism. Specifically, it is important to examine how temperature, surface hydrophobicity (which can be controlled by mixing hydrophilic and hydrophobic thiols), and the sizes of AuNPs affect the stability and NUT. Also, the assumption that the degradation of thiols only add extra diffusion in the AuNPs and not to the coalescence, though seems to be valid but deserves direct experimental verification.

6.4 Conclusions

The structural evolution of multi-transferred LS films of AuNPs on H-passivated Si substrates have been investigated using XR and GISAXS techniques. It is found from such structural investigation that the number of layers transferred onto the substrate is proportional to the number of transfer but the coverage of the layer decreases considerably with the increase in the number of layer. Such fractional coverage multilayered structures are quite unstable at ambient conditions. The instability mainly arises from three factors: (i) the room-temperature thermal energy (kT) induced fluctuation, (ii) the change in substrate surface energy ($\delta\gamma$) induced repulsion and (iii) the dissimilar film-substrate and film-air interfacial interactions induced attraction toward substrate. Such instability, in one hand,

creates hindrance in the control and formation of desired 3D-nanostructures through bottom-up approach.

On the other hand, same instability decreases the film-thickness and tries to form a near unique thickness (NUT) through reorganization of AuNPs for different duration. The duration of reorganization increases with the increase of layer number. The value of NUT ($\sim$ 6 nm) is greater than the thickness of ideal monolayer ($\sim$ 4.5 nm) but less than the thickness of ideal bilayer ($\sim$ 9 nm). Such value of NUT is actually related to the size of the AuNPs ($\sim$ 4.5 nm) plus their possible fluctuation ($\sim$1.5 nm) due to kT-energy. The formation of NUT layer (for $N \leq N_c$), through reorganization, is quite distinctive. In fact, the NUT layer is found to evolve through three complex processes and interactions, namely (i) the decrease of thickness (or roll down of top AuNPs through nearest void space) due to the anisotropic hydrophobic-hydrophobic interaction mediated long range attraction toward substrate, (ii) the increase of thickness due to the anisotropic hydrophilic-hydrophobic interaction mediated short range repulsion from substrate and (iii) the increase in thickness due to the kT-energy induced effective outward fluctuation w.r.t. the substrate. However, further experiments are needed to firmly validate the proposed mechanism.

7

X-RAY RADIATION INDUCED STRUCTURAL MODIFICATION OF THIOL-COATED AU-NANOPARTICLE LS FILMS

7.1 Introduction

Monolayer-encapsulated AuNPs are of considerable technological interest because of the potential electronic, optical, magnetic, catalytic and sensing applications emerging from the core–shell combinations. The stability of the AuNPs is critical for all these applications. A controlled self-assembling needs to be guided by a thorough understanding of ordering kinetics.

It is known from earlier studies [144, 306] that, at air/water interface, AuNPs self-assembled to form 2D-structures, which then can be transferred onto solid substrate using LB and LS deposition techniques to grow 2D- and 3D-nanostructures over large areas. [133, 160, 306] Although some works have been carried out to understand the structure, growth and evolution of LS monolayers of AuNPs on hydrophobic substrates (i.e. 2D-nanostructures) [159, 160], which is of utmost importance for the formation of desired 3D-nanostructures of specific collective properties through controlled bottom-up technique. AFM results show that the particle size and interparticle spatial properties are highly dependent on the surface mobility, surface tension, and adsorption energy of AuNPs on the substrate [312].

The structures of the LS films, have been studied using GISAXS techniques [159, 292] with high intensity small divergence X-ray beam (having better resolution limit). GISAXS is widely used to analyze the crystallinity and nanoscale structure in thin films of soft material. But, intense beam of the advance source can create beam induced damage, especially considering the time required to align the beam on the sample. Ionized radiation will generate free radicals that initiate cross-linking and/or chain scission, and structural damage will impact the ordering kinetics, thermodynamics, and crystallinity in organic compounds. As revealed from different studies, radiation damage is a major obstacle for SAXS since the intense beam generates aggregated particles in the solution and SAXS beamlines acknowledge the need to check for and avoid radiation [313–316]. So, exploring the change in the film structure in the presence of X-ray beam is necessary for better understanding of the growth and evolution of LS films of DT-AuNPs.

Previous reports confirm the evolution of DT-AUNPs under thermal treatment in solutions from the smaller-sized to larger-sized nanocrystals with the integrity of the final encapsulating shell structures maintained and formation of the long-range ordering of the thiolate-encapsulated nanocrystals [215–217]. Researchers have seen the irreversibility in conductivity changes for thin, LS deposited thiol encapsulated AuNPs films raised to a high temperature. The conductivity rapidly increases at higher temperature, to values that remain high and are almost linear with temperature as a result of electron hopping in metal AuNP films [317]. The optical properties of 4-methylbenzenethiol encapsulated 3 nm AuNP thin films have been investigated for a range of temperatures [318]. The SPR peak shift is found to be sensitive to temperature, heating time and film thickness. AFM data of the material after heating reveals structural changes corresponding to gold cluster growth following thiol desorption.

Recent work has revealed that electron beam irradiation can modify a AuNP assembly. It was also reported that removal of the organic ligands by heating or

electron beam irradiation leads to coalescence and sintering of metal cores. [319] NPs of 2 nm gold cores encapsulated with alkanethiolate monolayers has been studied in solution phase by Maye et.al. [320] using TEM, XRD, UV-Vis and FTIR spectroscopy. The results demonstrate the evolution in size and shape of the NPs toward monodispersed larger core sizes encapsulated with the thiolate shells. Wang et. al. [321] have also concluded from their studies that surface thermodynamic fluctuations and atomic interaction forces are the causes of the approach and coalescence behavior of the AuNPs. Another group of researchers have shown [322] that with desorption of capping ligands, the steric stability of the nanocrystals decreases and the inclination to aggregation increases. At low temperature, the alkyl chains behave as a solid with a rigid configuration, whereas on heating to 323 K, they behave more as a liquid [323]. Pradeep et al. [218] investigated the temperature-dependent phase behavior and dynamic freedom of alkyl chains coated on silver and gold clusters and reported that at 325 K, about 70% of the chains contribute to the dynamic activity.

From all the previous reports it seems to be of great importance to explore the impact of X-ray beam on the structures of DT-AuNPs LS films during X-ray scattering experiments of the films. Our aim in this chapter is to find out whether the beam induces damage due to thermodynamic fluctuation (beam induced heating) similar to the results as obtained when increasing the temperature in solution phase or something different happens. Here we have studied the films using GISAXS technique since it had been an important experimental tool in the thesis.

7.2 Experimental details

7.2.1 Preparation of DT-AuNP/H-Si LS films

The colloidal AuNPs with a core (Au) size of about 2.5 ± 0.6 nm and an overall (Au plus thiol shell) size of about 4.5 ± 0.6 nm were synthesized (discussed

in 2.3.1). The DT-AuNPs Langmuir monolayers formed at different pressure were transferred onto the H-Si substrates using LS deposition technique (as described in 2.3.4.2). DT-AuNPs/H-Si LS films prepared at Π = 2, 4, 6, 10 and 14 mN/m, as shown in the Π-A isotherm as shown in Fig. 31a, were used for further analysis.

7.2.2 Characterization of DT-AuNPs/H-Si LS films

The characterization of the DT-AuNPs/H-Si LS films were carried out using GISAXS techniques while that at the initial stages, were also carried out using complementary XR technique (discussed in 3.1). The scattering geometry used for the characterization of samples is shown schematically in 3.2.2. GISAXS measurements of the films were carried out using a synchrotron source (MiNaXS beam line, PETRA III) at λ = 0.94 Å(described in 3.2.2). The sample-to-detector distance was 1721 mm. Corresponding angular resolution (given by the ratio of pixel size and the sample-to-detector distance) is 0.1 mrad. The resolution limit along q_y-direction is less than 0.002 $Å^{-1}$ (discussed in 3.2.2.1). It is necessary to mention that such low value, which is mainly achievable in this beamline (due to very small divergence of the micro-focused beam), is absolutely essential for the direct estimation of the long-range in-plane correlations, such as the domains, along with the short-range in-plane correlations, such as the separation between AuNPs.

For the data collection, the incident angle α was kept at 0.25°, slightly greater than the critical angle, α_c, of the sample. Under such grazing incidence, the footprint of the micro-focused beam on the sample, along x-direction, is quite large, as necessary for any statistically relevant information, while along y-direction, is small, which can be used to map the in-plane inhomogeneity, if any. To minimize the effect of the radiation damage of the sample (due to high intensity beam), GISAXS pattern, on a single position, was collected for small time (10 s). To check the in-plane inhomogeneity and/or to enhance the statistics, similar GISAXS patterns were also collected at different positions by moving the

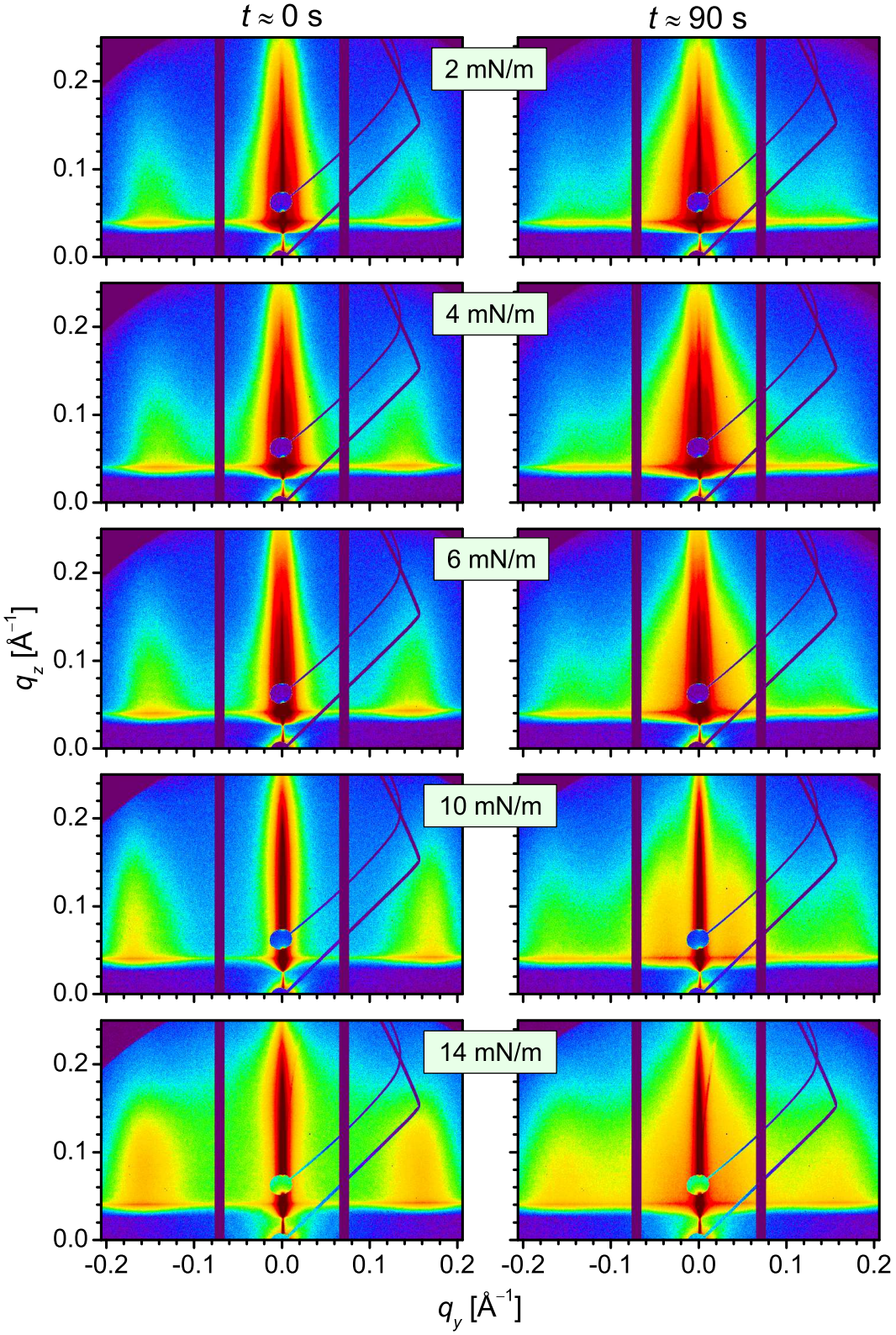

Figure 60: GISAXS patterns, before ($t \approx 0$ s) and after ($t \approx 90$ s) irradiation, of AuNP/H-Si LS monolayers deposited at different surface pressure (Π).

sample laterally. On the other hand. to see the effect of radiation in the structure of the film, GISAXS patterns, on a single position, were collected as a function of irradiation time. Each GISAXS image was collected for 10 s and the collection were carried out one after another upto 100^{th} second.

7.3 Results and discussion

7.3.1 GISAXS studies of the films

Fig. 60 shows the GISAXS reciprocal space patterns of the DT-AuNPs/H-Si LS films before ($t \approx 0$ s) and after ($t \approx 90$ s) the exposure of irradiation, deposited at different surface pressure collected for a short time of exposure(10 sec). The Each sample was moved laterally to get GISAXS patters at different positions and similar pattern was obtained for different positions. Thus we have ascertained the in-plane homogeneity of the GISAXS profiles. Averaging of all these patterns has been taken for better statistics and finally presented in Fig. 60.

In all the profiles for different surface pressures some common signatures has been observed. The most prominent features present are the two diffraction Bragg rods around $q_y = \pm$ 0.15 Å^{-1} and the intensity of the rods varies with Π value. Secondly, high intensity value is observed near q_y = 0, the nature of this intensed rod again changes with Π.

The GISAXS line cuts presented in fig. 61 clearly shows two regions behaving differently with radiation. The higher q value region specially correlation peak (with Gaussian broadening due to particle size distribution) due to the particle particle separation shows a decrease in intensity with time. The small q value region where the correlation peak due to island island separation lies (reported previously) grows in intensity as radiation time increases.

Thus the two regions can be marked as melting of AuNPs and growth of clusters. But the most interesting thing in this radiation induced growth of clusters or new dimensional islands is that it does not affect the initially created

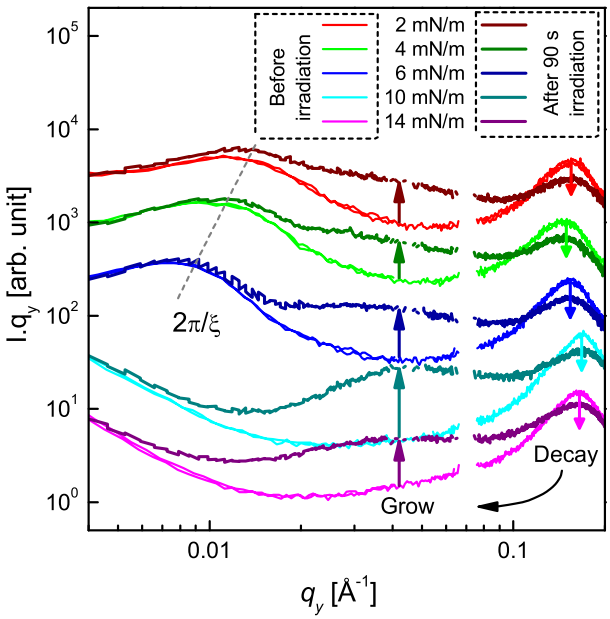

Figure 61: GISAXS line profiles along the q_y direction (*i.e.* lateral cut through the first Bragg rod at $q_z = 0.04$ Å^{-1}), before ($t \approx 0$ s) and after ($t \approx 90$ s) irradiation, of AuNP/H-Si LS monolayers deposited at different surface pressure (Π). Profiles are shifted vertically for clarity. Appearance of peak at $q_y \approx 0.04$ Å^{-1} and decrease in peak intensity at $q_y \approx 0.16$ Å^{-1} due to irradiation are indicted by arrows.

large sized island which is also considered as the building block for the LS films (present and recognised by GISAXS imaging for the LS films deposited at lower Π values i.e. 2, 4 and 6 mN/m. The position of the correlation peak due to growing island is almost same $\sim$0.055 Å^{-1} for all the pressure lying in the isotherm before the collapsing region. So it is evident that the new island growing is almost of equal size for all the pressures. The only difference is that the intensity is higher for higher pressures. For some pressures the higher order diffraction peaks can be observed though very weak in intensity which is due to broad background intensity (mainly the tail due to bigger islands). For Π =22 mN/m, the particle size seems to be more broadly distributed due to high compression and flipping of the monolayer film. But the presence of island is evident.

So it is evident that there is loss of small sized as prepared AuNPs due to radiation damage. It can be also inferred that the lost particles contribute to the formation of new type of ordering in the system may be in terms of spherical island or others. But one thing is definite that such type of ordering does not

destroy the long range ordering already present in the system. So the new long range ordering is growing in such a way that it is not hampering in the old one and same group of AuNPs is contributing in these two types of long range ordering. The newly build large sized particles i.e. AuNPs have the DT shell intact by molecular re-encapsulation process to protect them from further coalescence. This type of behaviour i.e. thermally-induced homo-interparticle coalescence of metal AuNPs at mild temperature elevation (140-160 deg C) is already reported for heat treatment of DT-AuNPs in solution phase [217].

More interesting characteristics can be revealed from the intensity vs. time curves for the growth of islands and lapse of AuNPs (see Fig. 62 and Fig. 63) The growth rate i.e. the slope of the curve is almost same for all the pressures (except 10mN/m) though the coverage and electron density were different initially for all the deposited LS films (reported previously).

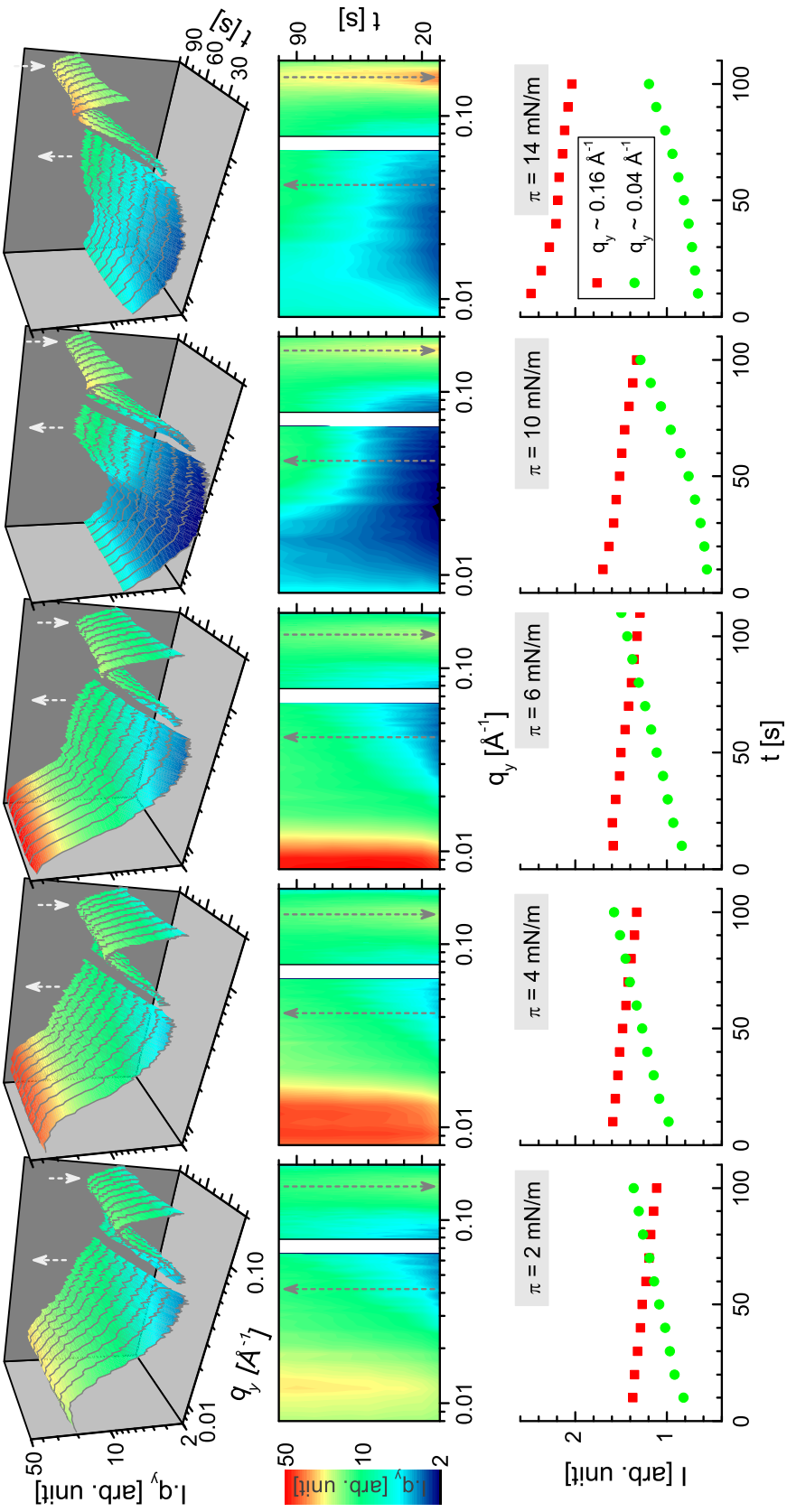

Figure 62: Evolution of GISAXS line profiles with irradiation time for AuNP/H-Si LS monolayers deposited at different surface pressure (Π), presented in 3D and 2D modes. Corresponding evolution of intensities at $q_y \approx 0.04$ and 0.16 Å^{-1} with irradiation time.

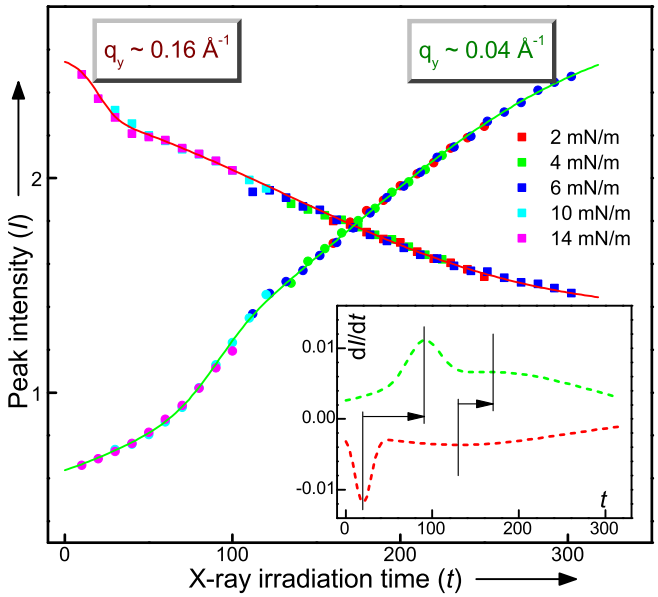

Figure 63: Line profile for Radiation induced Time Evolution of GISAXS patterns measured at surface pressures of 2,4,6,10 and 14 mN/m ($q_y \approx 0.04$ and 0.16 Å^{-1}. Inset: Corresponding derivative curve to emphasize the changes.

The growth of the NPs is, however, taking place within the initially formed disk-like domains. The radiation has no effect on the size of the disk-like domains, neither the size of such domains has any influence in the growth of the NPs. The growth of the AuNPs within disk-like domains can be visualized as the agglomeration of an AuNP with the first nearest neighbors due to radiation induced damage or modification of thiol coated layer, as shown schematically in Fig. 64. Such model suggest that once agglomerated such AuNPs are well separated (with $d' \approx 15$ nm) and thus can not grow further. However, events of agglomeration of AuNP with their first nearest neighbors increases with radiation time and the process continue for long for more covered high pressure films.

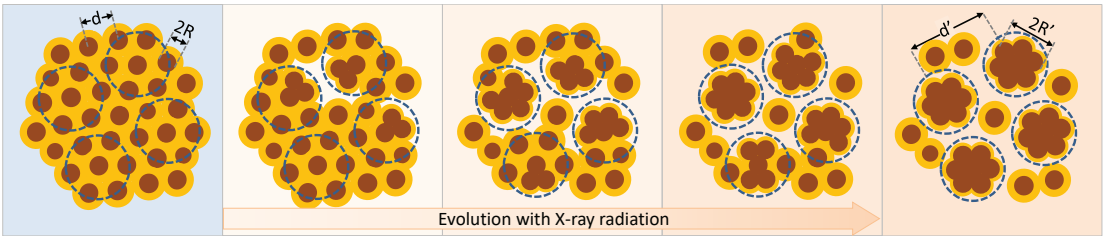

Figure 64: Schematic illustration of the evolution of AuNPs within disklike domains, under X-ray radiation, showing the growth of AuNPs from 2R to 2R′ and the separation from d ≈ 4 nm to d′ ≈ 15 nm.

The sintering of bare metal AuNPs on a support, e.g., catalyst particles, is often modelled in terms of Ostwald ripening, in which individual metal atoms leave a metal particle, diffuse over the support, and attach to another metal particle. Large particles grow at the expense of small particles. However, when the interaction between the AuNPs and the support is weak, the diffusion of a whole particle becomes possible. An alternative sintering mechanism thus arises in which particles diffuse across the surface and collide with other particles, leading to coalescence [324] for particles with a diameter of 5 nm. This surface diffusion is driven by the large surface tension resulting from the small particle size [325]. Even after extended electron beam exposure, the sintering remains localized in a small area and often involves only three or four adjacent AuNPs cores. AuNPs of large cores sinter prior to those of small ones. For particle with a smaller core size of about 2.8 nm, formation of neck is reported between two AuNPs which again reveals a surface diffusion-dominated sintering mechanism [319].

The dominating driving force for the in-plane motion of AuNPs is attributed to the attractive van der Waals interaction between the Au AuNPs leading to their coalescence [326]. At short time scales, it can also be deduced from the analysis of the GISAXS patterns along the q_z direction (form factor) that the diffusion length is less than the average particle separation since the average size of the Au nanoparticles has not changed. In the initial stages of diffusion leading to coalescence, but well before the collision of the nanoparticles, d remains the same due to invariant particle number density. σ_d becomes larger as pairs of particles that are already close together move toward one another and pairs of particles that are already comparatively far apart move still farther apart. Thus, this manifests a constant d accompanied by an increase in σ_d. The resultant change in σ_d is a direct measure of the diffusion length of the nanoparticles. The lateral nanoparticle diffusion or the coalescence coefficient can be defined as [327]

7.4 Conclusions

The structural evolution of single-transferred LS films of AuNPs on H-passivated Si substrates under the synchrotron irradiation have been investigated using GISAXS techniques. The GISAXS measurements were carried out using intense x-ray beam of small divergence (from P03 beamline of Petra-3) to enhanced in-plane resolution limit and by shifting the sample in-plane to minimize the effect of beam induced damage. Initially at $t \approx 0$, the films are predominantly of monolayer structures made of networked disk-like islands which are made of self-assembled and close packed DT-AuNPs as revealed from the eartier studies described in Chapter 4. But during irradiation the AuNPs melts to form cluster of larger size. The dimension of the newly developed clusters is almost same for LS films deposited at different Π values. The growth of new correlated clusters almost saturates after a characteristic time as well as the melting rate also follows linear path after a certain characteristic time. All the films shows a certain phase transition after a particular time interval of starting the irradiation process.

8

GROWTH AND EVOLUTION OF GOLD NANOLAYERS ON NATIVE OXIDE COATED SI SUBSTRATES

8.1 Introduction

The controlled self-assembly of MNPs on semiconductor and oxide surfaces is a research topic of very great current interest. The interface formed due to the deposition of metal atoms on the elemental semiconductor substrates is of immense interest not only to produce control diffused junctions in silicon at very shallow depth from the surface for the newly developed devices but also for the understanding of the morphological stability of the grown low-dimensional structures due to the diffusion even at room temperature [91]. It plays a significant role in the fabrication of micro-electronic devices and interconnects. Au-Si is one such interface, which has long-standing interest for device fabrications [93, 97]. The interface of the substrate plays a major role in the formation of thin Au-Si diffuse layer at room temperature. Dependence of diffusion on passivation has been observed for the Au-Si(001) system [10]. The possibility to understand the inter diffusion and to form control inter diffused nanolayer, created renewed interest to study the Au-Si system. It is known that the presence of a native oxide layer at the interface strongly suppresses the inter diffusion behaviour across a metal-semiconductor interface [10, 328]. But, if the deposited layer thickness is increased, will it affect the inter diffused layer when deposited on native oxide coated Si substrate? This question is unattended till date. Another possibility of more diffusion of Au atoms through the native oxide is suspected when the

bombarding Au ions are more energetic or precisely have a bigger momentum. It is thus suspected that the Au layer thickness and deposition condition also play key role in defining the inter diffused Au layer.

In this paper, our aim is exactly to address the qualitative and quantitative differences between the Au diffusion not only for different coverages but also for different deposition conditions. By monitoring the EDP of inter diffused Au layer as a function of time and studying if the EDP peak is shifting or the FWHM is changing, it is possible to conclude about the growth and evolution of the Au nanolayers as well as the inter diffused Au layers.

8.2 Experimental details

8.2.1 Preparation of Au/O-Si films

In our study, Au films of different thickness were deposited on SiO_2/Si(100) by magnetron sputtering. The change in deposition power indicates different applied voltage difference between the cathode and anode i.e the Au target and Si substrate.

Two sets of samples were prepared by depositing Au films on Si(001) substrates using magnetron sputtering technique (PLS 500, Pfeiffer) at 3.5×10^{-3} mbar Argon pressure. Prior to Au deposition, Si substrates (each of about $10 \times 10 mm^2$ size were sonicated in the presence of trichloroethelene for about 10 min and methyl alcohol (for about 10 min) separately to remove organic contaminants only, preserving the native-oxide layer on the surface. The first set of samples were prepared at a constant time of 60 sec and at different deposition powers (wattages), 15, 20, 25, 35 and 40 Watt(W) respectively. Another set of samples were prepared by fixing the deposition wattage at 25 W but varying the deposition time as 20, 35, 60, 90 and 120 s respectively.

8.2.2 Characterization of Au/O-Si films by XR

The characterization of Au/O-Si films, within a day and after 6 months of preparation, were carried out using XR technique, To monitor the structure of the diffused Au layer in native silicon oxide layer more thoroughly, further XR profiles studies were done after etching the upper Au layer by Aqua Regia (AR) XR measurements of the Au deposited films were carried out using a VXRD setup (already described in 3.4.1). XR profiles were taken for all the films after deposition. treatment.

8.3 Results and discussion

8.3.1 XR studies of the as-grown films

XR data of the Au/O-Si films deposited at different wattage-values, including the corresponding AR treated films, and collected within a day and 6 months are shown in Fig. 65. Films deposited at different wattages are shown separately. Oscillations with more than a single periodicity are observed in all the XR profiles. The high frequency oscillations are the Keissig fringes corresponding to the total film thickness. Similarly the XR profiles of the deposited films with different time duration are shown in Fig. 67.

Both the XR profiles were analysed using the Parratt formalism (described in 3.3) to get the EDPs to understand the nature of diffused Au layer considering three layers (top Au layer, intermediate layer and diffused layer). Fig. 65 and 67 show the XR data along with the analysed curve for the as prepared and AR treated samples.

8.3.2 Au/O-Si nanolayers within a day

From the EDP of the films (deposited at different wattage) just after deposition the electron density and thickness of the upper Au layer seems to increase

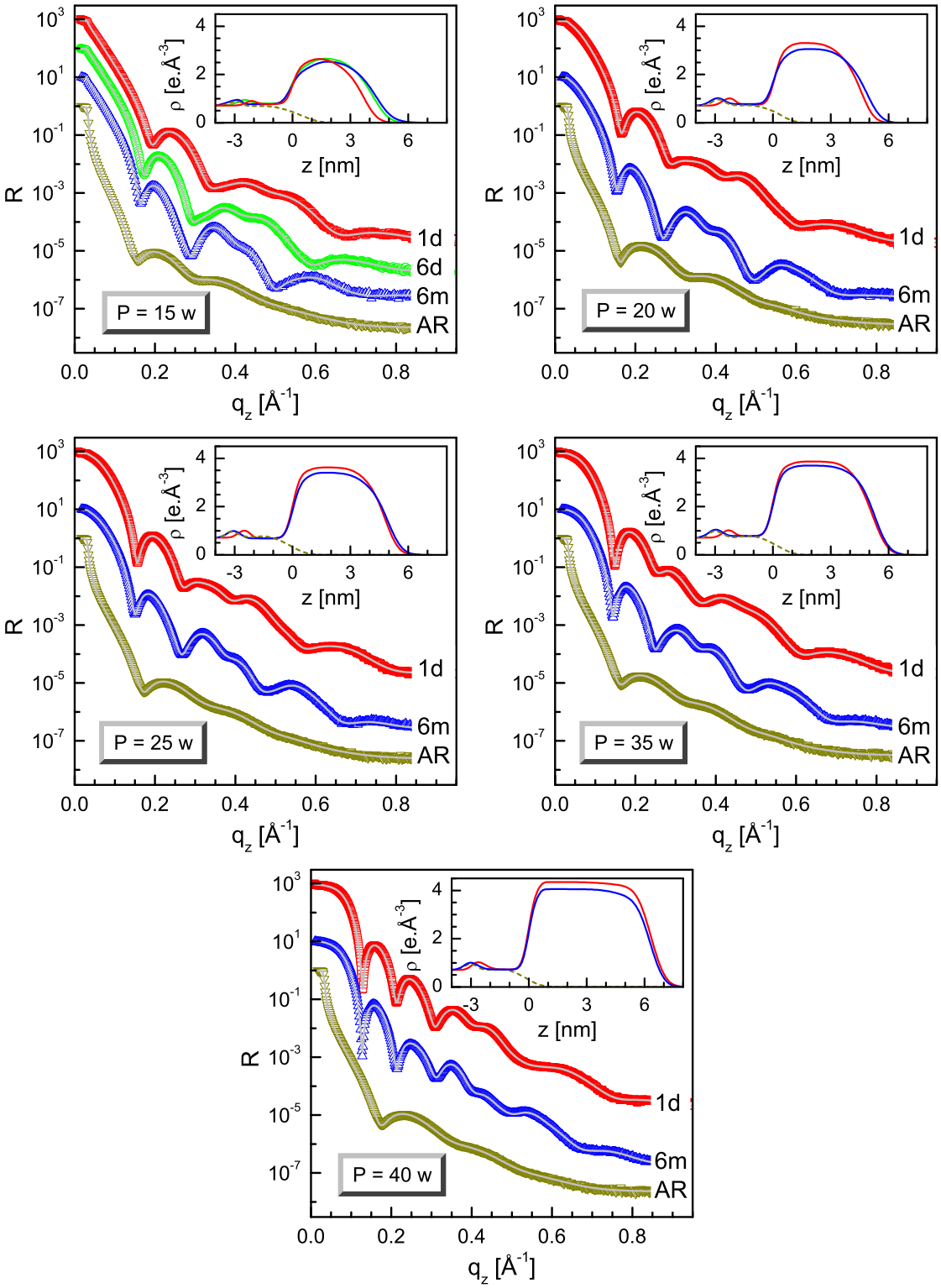

Figure 65: XR data (different symbols) collected within a day (1d), during sixth month (6m) and after AR treatment along with the analysed curves (solid lines) of the Au/O-Si films deposited at different power (P). Curves are shifted vertically for clarity. Insets: corresponding analysed EDPs.

significantly with increase in deposition power as revealed in Fig. 66. Though there is not much change in the layer thickness of the diffused Au inside SiO_2

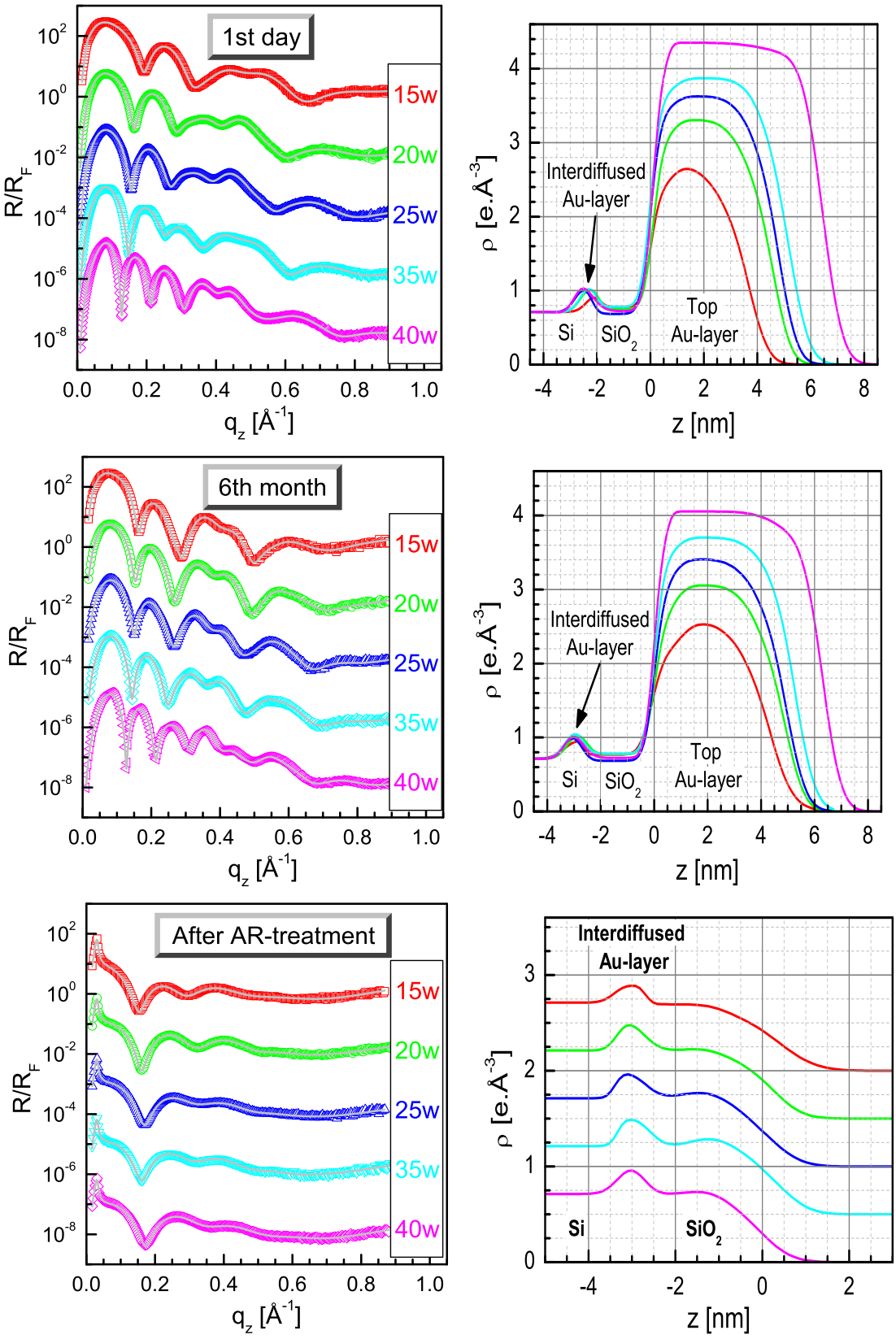

Figure 66: Top panels: Normalized XR data (different symbols) and also the analysed curves (solid lines) of the Au/O-Si films deposited at different power (P) and collected within a day, during sixth month and after AR treatment . Curves are shifted vertically for clarity. Bottom panels: Corresponding analysed EDPs

there is a noticeable change in the peak electron density of the layer. This proves the increase in Au diffusion i.e. the diffusion coefficient as the deposition power increases.

For the films deposited at constant power but different time shows significant increase in the upper Au layer with increasing time as shown in Fig. 67. For larger time duration increase in coverage is as expected from the normalised comparison of the XR profiles and EDPs as shown in Fig. 68. But the inter diffused Au layers are not following any particular behaviour as we have expected. The peak position of EDPs vary upto 1 nm. For 20 s the depth of diffused layer is least and then it increases. For 60 and 90 s, Au reaches maximum depth and layer thickness and peak electron density is almost same. But for 120 s,where the upper layer coverage is maximum, quantity of diffused Au decreases.

8.3.3 Au/O-Si nanolayers after sixth months

But after a significant time of about 6 months, there is a change in peak electron density for the larger Au layer, Fig. 66. The peak values decrease for all the films where as the FWHM increases making the total coverage almost conserved. The inter diffused Au layers for different films show equal property i.e. same peak position and width. This indicates saturation of inter diffused au layer thickness value with time. No more diffusion is expected through the porous oxide layer. Another interesting fact as revealed from the EDPs of 15 W film, Fig. 65, is that the decrease in peak electron density is very fast initially (EDP after 6 day) and the rate decreases afterwards. The EDPs collected after 6 days and 6 months show a very little change in peak density. This gradual decrease in the rate indicates a diffusion rate similar to the exponential one.

For the films deposited for different time duration, the upper Au layers show the same behaviour as the films deposited at different wattage. the peak electron density decreases and FWHM increases. But all the diffused Au layers shift along -z axis that means almost 0.5 nm. But the in difference maximum and minimum

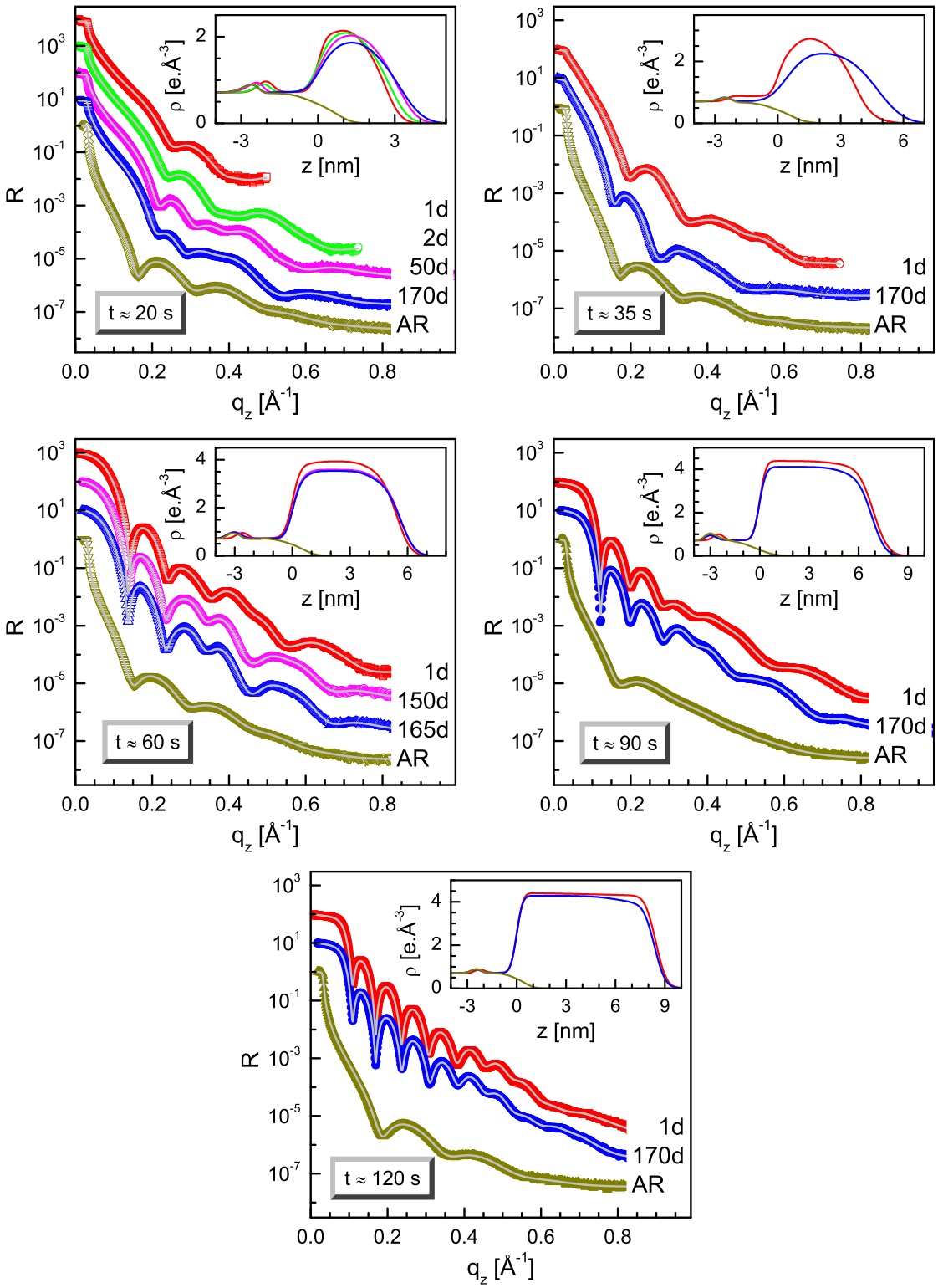

Figure 67: XR data (different symbols) collected within a day (1d), after different days (nd) and after AR treatment along with the analysed curves (solid lines) of the Au/O-Si films deposited for different time (t). Curves are shifted vertically for clarity. Insets: corresponding analysed EDPs.

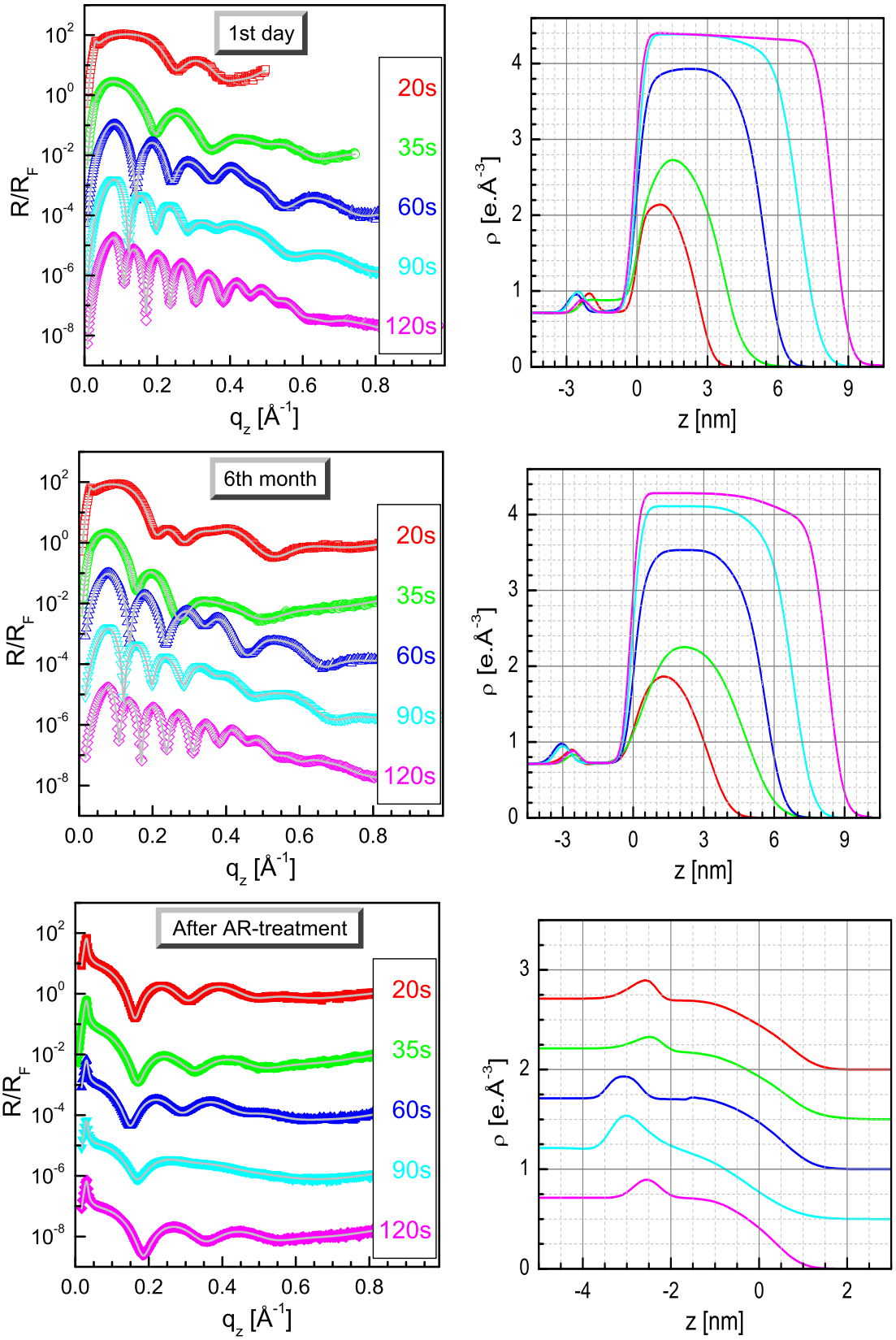

Figure 68: Top panels: Normalized XR data (different symbols) and also the analysed curves (solid lines) of the Au/O-Si films deposited for different time (t) and collected within a day, during sixth month and after AR treatment. Curves are shifted vertically for clarity. Bottom panels: Corresponding analysed EDPs.

peak positions remains same in nature as shown in Fig. 68. The EDPs of the film deposited for 20 s after 1, 2, 50 and 170 days show a gradual decrease in peak electron density, as shown in Fig. 67. Similarly film deposited for 60 s show a gradual decrease in peak electron density which leads likely to a saturation value. Thus, a gradual decrease in diffusion rate of the inter diffused Au layer occurs.

8.3.4 Au/O-Si nanolayers after AR-treatment

The AR treated Au-films (initially deposited at various wattage) shows some Au still in the upper layer. The diffused Au layer is almost unaffected but a small decrease in peak electron density is obvious from the EDPs as revealed from the EDPs shown in Fig. 66. The peak positions are same as that of the 6 months old films as revealed from the EDPs.

In case of the AR treated Au-films (deposited for different time duration), behaviour of the etched Au layer is same, shown in Fig. 68. Au layers with a very coverage are present in all the films. While the position of the inter diffused Au layers remain same but the peak electron density decreases compared the initial as-grown films. But the FWHM of the peaks remain same as compared to the untreated films after 6 months..

8.4 Conclusions

The structure of the as-deposited films and after AR treatment are investigated using XR technique. In case of Au films deposited at different power, it is clear that the cluster size changes with deposition power and this induces different diffusion coefficient. On the other hand, for the films with increasing coverage with increasing deposition time, the diffused layer thickness initially increases but then decreases. For both types of films after AR treatment show decrease in peak density but no change in position w.r.t the aged Au films. Since the AR treatment was done just after taking the initial XR data within a day, it can be concluded

that the diffused layers shift very quickly through the oxide layer and attain the saturation depth compared to the untreated films where the shifting take almost 6 months to reach the ultimatum depth. Further analysis of the system is needed for a more strong and definite conclusion.

9

SUMMARY

9.1 General conclusions

In this section we briefly state the main findings from our studies and mention the inferences that can be drawn from them. The studies on the DT-AuNPs can be classified into the following two categories. The first category includes (i) growth of DT-AuNPs thin films, both monolayer and multilayer, due to different deposition conditions (i.e. different Π values for LS technique) and varying substrate passivation and (ii) evolution of structure after deposition with varying time and upon exposure to radiation. The second category is based on the diffusion of Au into Si substrate and the evolution of diffused layer with time as a function of different deposition conditions. In what follows we discuss these points in short

1. The structures of the single-transferred DT-AuNP/H-Si LS films, deposited at different Π-values were first estimated using XR and GISAXS techniques and then confirmed using an AFM technique. The films are predominantly made of a monolayer structure and such a monolayer is made of networked disk-like islands with some voids. The size of the islands increases with increasing Π. The average separation between DT-AuNPs (d) either decreases or increases with Π-value depending upon the competitive effects of packing and flipping due to compression. Such structures can very well be considered as the structures of the Langmuir monolayes.

2. The time evolution of single-transferred DT-AuNPs LS films on H-Si substrate reveals that the bilayer signature initially present in the films diminishes with time at ambient conditions and the electron density of first layer increases

due to material gathering from second layer i.e. the fluctuation decreases with time, which is quite unusual. While the single-transferred DT-AuNPs LS films on OTS-Si substrate forms near perfect monolayer during deposition but deviates gradually with time. The different behaviour of two systems can be understood considering the film-substrate inter facial instability and/or room-temperature thermal energy.

3. The in-plane evolution of the structures of the DT-AuNPs LS films with time under X-ray radiation is evident from GISAXS techniques, where relatively large correlation appear in expense of original particle particle correlation within the disk-like islands due to the agglomeration of certain AuNPs with their first nearest neighbours after damage or modification of thiol coated layer in presence of X-ray radiation.

4. The structure of the multi-transferred DT-AuNP/H-Si LS films is found to form with disk like islands of similar size, where the initial number of layers matches with the number of transfer, but with time the packing or coverage increases and the number of layer decreases. In fact, DT-AuNP monolayer films of nearly full coverage are formed from partially covered bilayer LS films with time at ambient conditions.

5. The diffusion of Au into Si substrate has been studied at room temperature, for SiO_2/Si surface. The XR profiles suggest that the diffused layer thickness increases with increasing power of deposition.

9.2 Scope for future studies

Although we have encountered several interesting features of DT-AuNPs thin films in this thesis, a lot more can be done using such NPs. In fact, we have stressed only on the structural aspects of the films. Obtaining a correlation between the structure and properties of these films will be an interesting option for future research.

Yet another possibility is to explore the effect of the size change of the AuNPs in the structure and evolution of LS films. During LS deposition of the multi-layered films, the coverage area decreases with increasing number of strokes. And these multi-layered films show evolution toward NUT. By choosing different portion of the trough during multiple transfer of Langmuir film, higher coverage is expected for bilayer and tetra layer. It will be interesting to investigate the evolution of these films especially to explore if nearly unique thickness proposal is valid for fully covered films.

To study the room temperature evolution of the as-deposited thin films and to compare the effect with irradiation induced evolution is also an important and interesting scope of future studies. Simultaneously, exploring the surface morphology of the films with the help of microscopy techniques as well as using X-ray photoelectron spectroscopy to investigate the change in chemical composition of the films is also necessary.

PUBLICATIONS

Publications related to this thesis

1. Growth of thiol-coated Au-nanoparticle Langmuir monolayers through a 2D-network of disk-like islands, **M. Mukhopadhyay** and S. Hazra, *RSC Adv*. **6**, 12326 (2016). See also: Correction, *RSC Adv*. **6**, 16481 (2016).

2. Interfacial and thermal energy driven growth and evolution of Langmuir-Schaefer monolayers of Au-nanoparticles, **M. Mukhopadhyay** and S. Hazra, *Phys. Chem. Chem. Phys*. **20**, 1051 (2018).

3. Evolution of ligand-capped nanoparticle multilayers toward a near unique thickness, **M. Mukhopadhyay** and S. Hazra, *Soft Matter* **15**, 1869 (2019).

4. Radiation-induced regrowth of Au-nanoparticles within Langmuir-Schaefer films, **M. Mukhopadhyay** and S. Hazra, *Under preparation*.

5. Growth and evolution of gold nanolayers on native oxide coated Si substrates, **M. Mukhopadhyay** and S. Hazra, *Under preparation*.

Other contributed articles

1. Chitosan-fatty acid interaction mediated growth of Langmuir monolayer and Langmuir-Blodgett films, I. Ahmed, L. Dildar, A. Haque, P. Patra, **M. Mukhopadhyay**, S. Hazra, M. Kulkarni, S. Thomas, J. R. Plaisier, S. B. Dutta and J. K. Bal, *J. Colloid Interf. Sci.* **514**, 433 (2018).

2. Near 5% DMSO is the best: A structural investigation of PEDOT:PSS thin films with strong emphasis on surface and interface for hybrid solar cell, S. Mahato, J. Puigdollers, C. Voz, **M. Mukhopadhyay**, M. Mukherjee and S. Hazra, *Communicated*.

BIBLIOGRAPHY

[1] Mihail C Roco, R Stanley Williams, and Paul Alivisatos. *Nanotechnology research directions: IWGN workshop report: vision for nanotechnology in the next decade*. Springer Science & Business Media, 2000.

[2] Hari Singh Nalwa. *Nanostructured materials and nanotechnology: concise edition*. Gulf Professional Publishing, 2001.

[3] Robert Kelsall, Ian W Hamley, and Mark Geoghegan. *Nanoscale science and technology*. John Wiley & Sons, 2005.

[4] Guozhong Cao. *Nanostructures and nanomaterials: synthesis, properties and applications*. World Scientific, 2004.

[5] Z. Tang, N. A. Kotov, and M. Giersig. Spontaneous organization of single CdTe nanoparticles into luminescent nanowires. *Science*, 297:237, 2002.

[6] Robert B Grubbs. Nanoparticle assembly: solvent-tuned structures. *Nat. Mater.*, 6:553–555, 2007.

[7] Q. Ji, S. Acharya, J. P. Hill, G. J. Richards, and K. Ariga. Multi-dimensional control of surfactant-guided assemblies of quantum gold particles. *Adv. Mater.*, 20:4027–4032, 2008.

[8] Ph Buffat and Jean Pierre Borel. Size effect on the melting temperature of gold particles. *Physical review A*, 13(6):2287, 1976.

[9] Inder P Batra, S Ciraci, GP Srivastava, JS Nelson, and CY Fong. Dimensionality and size effects in simple metals. *Physical Review B*, 34(12):8246, 1986.

[10] J. K. Bal and S. Hazra. Interfacial role in room-temperature diffusion of Au into Si substrates. *Phys. Rev. B*, 75:205411, 2007.

[11] J. K. Bal and S. Hazra. Atmospheric pressure induced atomic diffusion into solid crystal. *Phys. Rev. B*, 79:155405, 2009.

[12] J. K. Bal and S. Hazra. Time-evolution growth of Ag nanolayers on differently-passivated Si(001) surfaces. *Phys. Rev. B*, 79:155412, 2009.

[13] F. Silly, A. O. Gusev, A. Taleb, F. Charra, and M.-P. Pileni. Coupled plasmon modes in an ordered hexagonal monolayer of metal nanoparticles: a direct observation. *Phys. Rev. Lett.*, 84:5840, 2000.

[14] S. Vial, I. Pastoriza-Santos, J. Pérez-Juste, and L. M. Liz-Marzán. Plasmon coupling in layer-by-layer assembled gold nanorod films. *Langmuir*, 23: 4606–4611, 2007.

[15] Rupak Banerjee. *Ordering and pattern formation in self-assembled nanostructured materials*. PhD dissertation, University of Calcutta, 2011.

[16] M. Brust, M. Walker, D. Bethell, D. J. Schiffrin, and R. Whyman. Synthesis of thiol-derivatised gold nanoparticles in a two-phase liquid-liquid system. *J. Chem. Soc., Chem. Commun.*, page 801, 1994.

[17] Tran Thanh Tung, Tae Young Kim, and Kwang S Suh. Nanocomposites of single-walled carbon nanotubes and poly (3, 4-ethylenedioxythiophene) for transparent and conductive film. *Organic Electronics*, 12(1):22–28, 2011.

[18] Harold W Kroto, James R Heath, Sean C O'Brien, Robert F Curl, and Richard E Smalley. C60: Buckminsterfullerene. *Nature*, 318(6042):162, 1985.

[19] Nasser Peyghambarian, Brian Fluegel, Daniele Hulin, Arnold Migus, Manuel Joffre, Andre Antonetti, Stephen W Koch, and Markus Lindberg. Femtosecond optical nonlinearities of cdse quantum dots. *IEEE journal of quantum electronics*, 25(12):2516–2522, 1989.

[20] VJ Mohanraj and Y Chen. Nanoparticles-a review. *Tropical journal of pharmaceutical research*, 5(1):561–573, 2006.

[21] Sarita Kango, Susheel Kalia, Annamaria Celli, James Njuguna, Youssef Habibi, and Rajesh Kumar. Surface modification of inorganic nanoparticles for development of organic–inorganic nanocomposites-a review. *Progress in Polymer Science*, 38(8):1232–1261, 2013.

[22] U Banin, M Bruchez, AP Alivisatos, T Ha, S Weiss, and DS Chemla. Evidence for a thermal contribution to emission intermittency in single cdse/cds core/shell nanocrystals. *The Journal of chemical physics*, 110(2): 1195–1201, 1999.

[23] Guowen Meng, Yung Joon Jung, Anyuan Cao, Robert Vajtai, and Pulickel M Ajayan. Controlled fabrication of hierarchically branched nanopores, nanotubes, and nanowires. *Proceedings of the National Academy of Sciences*, 102 (20):7074–7078, 2005.

[24] Donald R Paul and Lioyd M Robeson. Polymer nanotechnology: nanocomposites. *Polymer*, 49(15):3187–3204, 2008.

[25] Byron D Gates, Qiaobing Xu, Michael Stewart, Declan Ryan, C Grant Willson, and George M Whitesides. New approaches to nanofabrication: molding, printing, and other techniques. *Chemical reviews*, 105(4):1171–1196, 2005.

[26] Abraham Ulman. Formation and structure of self-assembled monolayers. *Chemical reviews*, 96(4):1533–1554, 1996.

[27] Cosmin Farcau, Helena Moreira, Benoit Viallet, Jérémie Grisolia, and Laurence Ressier. Tunable conductive nanoparticle wire arrays fabricated by convective self-assembly on nonpatterned substrates. *ACS nano*, 4(12): 7275–7282, 2010.

[28] Artur Ciesielski, Carlos-Andres Palma, Massimo Bonini, and Paolo Samorì. Towards supramolecular engineering of functional nanomaterials: Pre-programming multi-component 2d self-assembly at solid-liquid interfaces. *Advanced Materials*, 22(32):3506–3520, 2010.

[29] Steven De Feyter and Frans C De Schryver. Two-dimensional supramolecular self-assembly probed by scanning tunneling microscopy. *Chemical Society Reviews*, 32(3):139–150, 2003.

[30] Marian Kaholek, Woo-Kyung Lee, Bruce LaMattina, Kenneth C Caster, and Stefan Zauscher. Fabrication of stimulus-responsive nanopatterned polymer brushes by scanning-probe lithography. *Nano Letters*, 4(2):373–376, 2004.

[31] Zhihong Chen, Yu-Ming Lin, Michael J Rooks, and Phaedon Avouris. Graphene nano-ribbon electronics. *Physica E: Low-dimensional Systems and Nanostructures*, 40(2):228–232, 2007.

[32] Kostya S Novoselov, Andre K Geim, Sergei V Morozov, D Jiang, Y_ Zhang, Sergey V Dubonos, Irina V Grigorieva, and Alexandr A Firsov. Electric field effect in atomically thin carbon films. *science*, 306(5696):666–669, 2004.

[33] M Brust, J Fink, D Bethell, DJ Schiffrin, and C Kiely. Synthesis and reactions of functionalised gold nanoparticles. *Journal of the Chemical Society, Chemical Communications*, 16:1655–1656, 1995.

[34] Sharbari Palmal, SK Basiruddin, Amit Ranjan Maity, Sekhar C Ray, and Nikhil R Jana. Thiol-directed synthesis of highly fluorescent gold clusters and their conversion into stable imaging nanoprobes. *Chemistry–A European Journal*, 19(3):943–949, 2013.

[35] Daniel V Leff, Pamela C Ohara, James R Heath, and William M Gelbart. Thermodynamic control of gold nanocrystal size: experiment and theory. *The Journal of Physical Chemistry*, 99(18):7036–7041, 1995.

[36] Nikhil R Jana, Latha Gearheart, and Catherine J Murphy. Seed-mediated growth approach for shape-controlled synthesis of spheroidal and rod-like gold nanoparticles using a surfactant template. *Advanced Materials*, 13(18): 1389–1393, 2001.

[37] Matthew E Stewart, Christopher R Anderton, Lucas B Thompson, Joana Maria, Stephen K Gray, John A Rogers, and Ralph G Nuzzo. Nanostructured plasmonic sensors. *Chemical reviews*, 108(2):494–521, 2008.

[38] Jeffrey N Anker, W Paige Hall, Olga Lyandres, Nilam C Shah, Jing Zhao, and Richard P Van Duyne. Biosensing with plasmonic nanosensors. In *Nanoscience and Technology: A Collection of Reviews from Nature Journals*, pages 308–319. World Scientific, 2010.

[39] Yong Yang, Shigemasa Matsubara, Masayuki Nogami, and Jianlin Shi. Controlling the aggregation behavior of gold nanoparticles. *Materials Science and Engineering: B*, 140(3):172–176, 2007.

[40] Anthony J Morfa, Kathy L Rowlen, Thomas H Reilly III, Manuel J Romero, and Jao van de Lagemaat. Plasmon-enhanced solar energy conversion in organic bulk heterojunction photovoltaics. *Applied Physics Letters*, 92(1): 013504, 2008.

[41] Seok-Soon Kim, Seok-In Na, Jang Jo, Dong-Yu Kim, and Yoon-Chae Nah. Plasmon enhanced performance of organic solar cells using electrodeposited ag nanoparticles. *Applied Physics Letters*, 93(7):305, 2008.

[42] Woo-Jun Yoon, Kyung-Young Jung, Jiwen Liu, Thirumalai Duraisamy, Rao Revur, Fernando L Teixeira, Suvankar Sengupta, and Paul R Berger. Plasmon-enhanced optical absorption and photocurrent in organic bulk heterojunction photovoltaic devices using self-assembled layer of silver nanoparticles. *Solar Energy Materials and Solar Cells*, 94(2):128–132, 2010.

[43] Andrea Tao, Prasert Sinsermsuksakul, and Peidong Yang. Tunable plasmonic lattices of silver nanocrystals. *Nature nanotechnology*, 2(7):435, 2007.

[44] Yan Gao, Xiaoqiang Chen, Hao Xu, Yunlong Zou, Renpeng Gu, Mingsheng Xu, Alex K-Y Jen, and Hongzheng Chen. Highly-efficient fabrication of nanoscrolls from functionalized graphene oxide by langmuir–blodgett method. *Carbon*, 48(15):4475–4482, 2010.

[45] Michael Faraday. X. the bakerian lecture-experimental relations of gold (and other metals) to light. *Philosophical Transactions of the Royal Society of London*, 147(X):145–181, 1857.

[46] M. C. Daniel and D. Astruc. Gold nanoparticles: Assembly, supramolecular chemistry, quantum-size-related properties, and applications toward biology, catalysis, and nanotechnology. *Chem. Rev.*, 104:293–346, 2004.

[47] Marek Grzelczak, Jorge Pérez-Juste, Paul Mulvaney, and Luis M Liz-Marzán. Shape control in gold nanoparticle synthesis. *Chemical Society Reviews*, 37 (9):1783–1791, 2008.

[48] Huajun Feng, Yanmei Yang, Yumeng You, Gongping Li, Jun Guo, Ting Yu, Zexiang Shen, Tom Wu, and Bengang Xing. Simple and rapid synthesis of ultrathin gold nanowires, their self-assembly and application in surface-enhanced raman scattering. *Chemical Communications*, 15:1984–1986, 2009.

[49] Krishnendu Saha, Sarit S. Agasti, Chaekyu Kim, Xiaoning Li, and Vincent M. Rotello. Gold nanoparticles in chemical and biological sensing. *Chemical Reviews*, 112(5):2739–2779, 2012. doi: 10.1021/cr2001178. URL https://doi.org/10.1021/cr2001178. PMID: 22295941.

[50] Andrew N Shipway, Eugenii Katz, and Itamar Willner. Nanoparticle arrays on surfaces for electronic, optical, and sensor applications. *ChemPhysChem*, 1(1):18–52, 2000.

[51] Christopher B Murray, a CR Kagan, and MG Bawendi. Synthesis and characterization of monodisperse nanocrystals and close-packed nanocrystal assemblies. *Annual review of materials science*, 30(1):545–610, 2000.

[52] Mathias Brust and Christopher J Kiely. Some recent advances in nanostructure preparation from gold and silver particles: a short topical review. *Colloids and Surfaces A: Physicochemical and Engineering Aspects*, 202(2-3): 175–186, 2002.

[53] Günter Schmid, Monika Bäumle, Marcus Geerkens, Ingo Heim, Christoph Osemann, and Thomas Sawitowski. Current and future applications of nanoclusters. *Chemical Society Reviews*, 28(3):179–185, 1999.

[54] Günter Schmid and Benedetto Corain. Nanoparticulated gold: syntheses, structures, electronics, and reactivities. *European Journal of Inorganic Chemistry*, 2003(17):3081–3098, 2003.

[55] A Paul Alivisatos, Kai P Johnsson, Xiaogang Peng, Troy E Wilson, Colin J Loweth, Marcel P Bruchez Jr, and Peter G Schultz. Organization of'nanocrystal molecules' using dna. *Nature*, 382(6592):609, 1996.

[56] Stefan A Maier, Mark L Brongersma, Pieter G Kik, Sheffer Meltzer, Ari AG Requicha, and Harry A Atwater. Plasmonics-a route to nanoscale optical devices. *Advanced materials*, 13(19):1501–1505, 2001.

[57] M Quinten, Alfred Leitner, Joachim R Krenn, and Franz R Aussenegg. Electromagnetic energy transport via linear chains of silver nanoparticles. *Optics letters*, 23(17):1331–1333, 1998.

[58] Stefan A Maier, Mark L Brongersma, Pieter G Kik, and Harry A Atwater. Observation of near-field coupling in metal nanoparticle chains using far-field polarization spectroscopy. *Physical Review B*, 65(19):193408, 2002.

[59] M Salerno, N Felidj, JR Krenn, A Leitner, FR Aussenegg, and JC Weeber. Near-field optical response of a two-dimensional grating of gold nanoparticles. *Physical Review B*, 63(16):165422, 2001.

[60] Uwe Kreibig and Michael Vollmer. Theoretical considerations. In *Optical Properties of Metal Clusters*, pages 13–201. Springer, 1995.

[61] Ronald P Andres, Thomas Bein, Matt Dorogi, Sue Feng, et al. " coulomb staircase" at room temperature in a self-assembled molecular nanostructure. *Science*, 272(5266):1323, 1996.

[62] Janos H Fendler. Self-assembled nanostructured materials. *Chemistry of Materials*, 8(8):1616–1624, 1996.

[63] Arnim Henglein. Physicochemical properties of small metal particles in solution:" microelectrode" reactions, chemisorption, composite metal particles, and the atom-to-metal transition. *The Journal of Physical Chemistry*, 97(21):5457–5471, 1993.

[64] Jacqueline Belloni. Metal nanocolloids. *Current opinion in colloid & interface science*, 1(2):184–196, 1996.

[65] Ghenadii Korotcenkov, Vladimir Brinzari, and Beong K Cho. Conductometric gas sensors based on metal oxides modified with gold nanoparticles: a review. *Microchimica Acta*, 183(3):1033–1054, 2016.

[66] Hank Wohltjen and Arthur W Snow. Colloidal metal- insulator- metal ensemble chemiresistor sensor. *Analytical Chemistry*, 70(14):2856–2859, 1998.

[67] Sherine O Obare, Rachel E Hollowell, and Catherine J Murphy. Sensing strategy for lithium ion based on gold nanoparticles. *Langmuir*, 18(26): 10407–10410, 2002.

[68] Amanda J Haes, Shengli Zou, George C Schatz, and Richard P Van Duyne. A nanoscale optical biosensor: the long range distance dependence of the

localized surface plasmon resonance of noble metal nanoparticles. *The Journal of Physical Chemistry B*, 108(1):109–116, 2004.

[69] Youngjin Kim, Robert C Johnson, and Joseph T Hupp. Gold nanoparticle-based sensing of "spectroscopically silent" heavy metal ions. *Nano Letters*, 1 (4):165–167, 2001.

[70] Stephen D Evans, Simon R Johnson, Yaling L Cheng, and Tiehan Shen. Vapour sensing using hybrid organic–inorganic nanostructured materials. *Journal of Materials Chemistry*, 10(1):183–188, 2000.

[71] S-H Kim, G Medeiros-Ribeiro, DAA Ohlberg, R Stanley Williams, and JR Heath. Individual and collective electronic properties of ag nanocrystals. *The Journal of Physical Chemistry B*, 103(47):10341–10347, 1999.

[72] James R Heath, Charles M Knobler, and Daniel V Leff. Pressure/temperature phase diagrams and superlattices of organically functionalized metal nanocrystal monolayers: the influence of particle size, size distribution, and surface passivant. *The Journal of Physical Chemistry B*, 101 (2):189–197, 1997.

[73] Bernadette M Quinn, Peter Liljeroth, Virginia Ruiz, Timo Laaksonen, and Kyösti Kontturi. Electrochemical resolution of 15 oxidation states for monolayer protected gold nanoparticles. *Journal of the American Chemical Society*, 125(22):6644–6645, 2003.

[74] Kohei Fukumi, Akiyoshi Chayahara, Kohei Kadono, Toru Sakaguchi, Yuji Horino, Masaru Miya, Kanenaga Fujii, Junji Hayakawa, and Mamoru Satou. Gold nanoparticles ion implanted in glass with enhanced nonlinear optical properties. *Journal of applied physics*, 75(6):3075–3080, 1994.

[75] Daven Compton, Lesley Cornish, and Elma van der Lingen. The third order nonlinear optical properties of gold nanoparticles in glasses, part i. *Gold Bulletin*, 36(1):10–16, Mar 2003.

[76] Donka Andreeva, Tatjana Tabakova, Vasko Idakiev, Pirin Christov, and Rudolf Giovanoli. Au/α-fe203 catalyst for water–gas shift reaction prepared by deposition–precipitation. *Applied Catalysis A: General*, 169(1):9–14, 1998.

[77] H Sakurai and M Haruta. Synergism in methanol synthesis from carbon dioxide over gold catalysts supported on metal oxides. *Catalysis Today*, 29 (1-4):361–365, 1996.

[78] George M Whitesides and Bartosz Grzybowski. Self-assembly at all scales. *Science*, 295(5564):2418–2421, 2002.

[79] Cheolmin Park, Jongseung Yoon, and Edwin L Thomas. Enabling nanotechnology with self assembled block copolymer patterns. *Polymer*, 44(22): 6725–6760, 2003.

[80] Jacob Sagiv. Organized monolayers by adsorption. 1. formation and structure of oleophobic mixed monolayers on solid surfaces. *Journal of the American Chemical Society*, 102(1):92–98, 1980.

[81] J Christopher Love, Lara A Estroff, Jennah K Kriebel, Ralph G Nuzzo, and George M Whitesides. Self-assembled monolayers of thiolates on metals as a form of nanotechnology. *Chemical reviews*, 105(4):1103–1170, 2005.

[82] Richard D Tilley and Satoshi Saito. Preparation of large scale monolayers of gold nanoparticles on modified silicon substrates using a controlled pulling method. *Langmuir*, 19(12):5115–5120, 2003.

[83] Rodolfo Zanella, Suzanne Giorgio, Claude R Henry, and Catherine Louis. Alternative methods for the preparation of gold nanoparticles supported on tio2. *The Journal of Physical Chemistry B*, 106(31):7634–7642, 2002.

[84] TG Schaaff and DA Blom. Deposition of au- nanocrystals on tio2 crystallites. *Nano Letters*, 2(5):507–511, 2002.

[85] John C Hulteen, Charles J Patrissi, David L Miner, Erin R Crosthwait, Elizabeth B Oberhauser, and Charles R Martin. Changes in the shape and optical properties of gold nanoparticles contained within alumina membranes due to low-temperature annealing. *The Journal of Physical Chemistry B*, 101(39):7727–7731, 1997.

[86] J Garcıa-Serrano and U Pal. Synthesis and characterization of au nanoparticles in al203 matrix. *International journal of hydrogen energy*, 28(6):637–640, 2003.

[87] Tetsu Yonezawa, Shin-ya Onoue, and Toyoki Kunitake. Growth of closely packed layers of gold nanoparticles on an aligned ammonium surface. *Advanced Materials*, 10(5):414–416, 1998.

[88] L Bardotti, B Prevel, P Jensen, M Treilleux, P Mélinon, A Perez, J Gierak, G Faini, and D Mailly. Organizing nanoclusters on functionalized surfaces. *Applied surface science*, 191(1-4):205–210, 2002.

[89] Eugene WL Chan and Luping Yu. Chemoselective immobilization of gold nanoparticles onto self-assembled monolayers. *Langmuir*, 18(2):311–313, 2002.

[90] Tao Zhu, Xu Zhang, Jian Wang, Xiaoyi Fu, and Zhongfan Liu. Assembling colloidal au nanoparticles with functionalized self-assembled monolayers. *Thin Solid Films*, 327:595–598, 1998.

[91] JK Bal and S Hazra. Interfacial role in room-temperature diffusion of au into si substrates. *Physical Review B*, 75(20):205411, 2007.

[92] L Braicovich, CM Garner, PR Skeath, CY Su, PW Chye, I Lindau, and WE Spicer. Photoemission studies of the silicon-gold interface. *Physical Review B*, 20(12):5131, 1979.

[93] CB Collins, RO Carlson, and CJ Gallagher. Properties of gold-doped silicon. *Physical Review*, 105(4):1168, 1957.

[94] G Le Lay. Physics and electronics of the noble-metal/elemental-semiconductor interface formation: A status report. *Surface Science*, 132 (1-3):169–204, 1983.

[95] Akio Hiraki. Low temperature reactions at si/metal interfaces; what is going on at the interfaces? *Surface Science Reports*, 3(7):357–412, 1983.

[96] SL Molodtsov, C Laubschat, G Kaindl, AM Shikin, and VK Adamchuk. Formation and chemical structure of the au/si (111) interface. *Physical Review B*, 44(16):8850, 1991.

[97] A Cros and P Muret. Properties of noble-metal/silicon junctions. *Materials science reports*, 8(6-7):271–367, 1992.

[98] Li Ma, Jianguang Wang, Qiliang Lu, and Guanghou Wang. Chemisorption of co on h-passivated si (1 0 0) surface. *Chemical physics letters*, 405(1-3): 208–213, 2005.

[99] J-J Yeh, J Hwang, K Bertness, DJ Friedman, R Cao, and I Lindau. Growth of the room temperature au/si (111)-7× 7 interface. *Physical review letters*, 70(24):3768, 1993.

[100] Kjeld Pedersen and Per Morgen. Room-temperature deposition and growth of au on clean and oxygen passivated si (111) surfaces investigated by optical second-harmonic generation. *Journal of Physics: Condensed Matter*, 9 (44):9497, 1997.

[101] C Grupp and A Taleb-Ibrahimi. A u/h: S i (111)-(1× 1) interface versus a u/s i (111)-(7× 7). *Physical Review B*, 57(11):6258, 1998.

[102] JH Kim, G Yang, S Yang, and AH Weiss. Study of the growth and stability of ultra-thin films of au deposited on si (1 0 0) and si (1 1 1). *Surface science*, 475(1-3):37–46, 2001.

[103] Yuichi Haruyama, Kazuhiro Kanda, and Shinji Matsui. Electronic structure of the au–si (1 1 1) interface as a function of au coverage. *Radiation Physics and Chemistry*, 75(11):1943–1947, 2006.

[104] Young-Seok Shon and Hosun Choo. [60] fullerene-linked gold nanoparticles: synthesis and layer-by-layer growth on a solid surface. *Chemical Communications*, 21:2560–2561, 2002.

[105] Luqi Liu, Tongxin Wang, Junxin Li, Zhi-Xin Guo, Liming Dai, Deqing Zhang, and Daoben Zhu. Self-assembly of gold nanoparticles to carbon nanotubes using a thiol-terminated pyrene as interlinker. *Chemical physics letters*, 367(5-6):747–752, 2003.

[106] H-G Boyen, Th Herzog, G Kästle, F Weigl, P Ziemann, Joachim P Spatz, M Möller, R Wahrenberg, MG Garnier, and P Oelhafen. X-ray photoelectron spectroscopy study on gold nanoparticles supported on diamond. *Physical Review B*, 65(7):075412, 2002.

[107] Toshiharu Teranishi, Akira Sugawara, Takami Shimizu, and Mikio Miyake. Planar array of 1d gold nanoparticles on ridge-and-valley structured carbon. *Journal of the American Chemical Society*, 124(16):4210–4211, 2002.

[108] Torsten Reuter, Olivia Vidoni, Viktoria Torma, Günter Schmid, Lu Nan, Michael Gleiche, Lifeng Chi, and Harald Fuchs. Two-dimensional networks via quasi one-dimensional arrangements of gold clusters. *Nano Letters*, 2(7): 709–711, 2002.

[109] Takeo Oku and Katsuaki Suganuma. Carbon nanocage structures formed by one-dimensional self-organization of gold nanoparticles. *Chemical Communications*, 23:2355–2356, 1999.

[110] Ron Blonder and Laila Sheeney. Three-dimensional redox-active layered composites of au–au, ag–ag and au–ag colloids. *Chemical Communications*, 13:1393–1394, 1998.

[111] Fumitaka Mafuné, Jun-ya Kohno, Yoshihiro Takeda, and Tamotsu Kondow. Nanoscale soldering of metal nanoparticles for construction of higher-order structures. *Journal of the American Chemical Society*, 125(7):1686–1687, 2003.

[112] Leif O Brown and James E Hutchison. Formation and electron diffraction studies of ordered 2-d and 3-d superlattices of amine-stabilized gold nanocrystals. *The Journal of Physical Chemistry B*, 105(37):8911–8916, 2001.

[113] Sang-Keun Oh, Yong-Gu Kim, Heechang Ye, and Richard M Crooks. Synthesis, characterization, and surface immobilization of metal nanoparticles encapsulated within bifunctionalized dendrimers. *Langmuir*, 19(24):10420–10425, 2003.

[114] Wei Li, Lihua Huo, Dongmei Wang, Guangfu Zeng, Shiquan Xi, Bing Zhao, Jijun Zhu, Jing Wang, Yaochun Shen, and Zuhong Lu. Self-assembled multilayers of alternating gold nanoparticles and dithiols: approaching to superlattice. *Colloids and Surfaces A: Physicochemical and Engineering Aspects*, 175(1-2):217–223, 2000.

[115] Yvonne Joseph, Isabelle Besnard, Miriam Rosenberger, Berit Guse, Heinz-Georg Nothofer, Jurina M Wessels, Ute Wild, Axel Knop-Gericke, Dangsheng Su, Robert Schlögl, et al. Self-assembled gold nanoparticle/alkanedithiol films: preparation, electron microscopy, xps-analysis, charge transport, and vapor-sensing properties. *The Journal of Physical Chemistry B*, 107(30):7406–7413, 2003.

[116] Giuseppe Compagnini, Alessandro A Scalisi, and Orazio Puglisi. Ablation of noble metals in liquids: a method to obtain nanoparticles in a thin polymeric film. *Physical Chemistry Chemical Physics*, 4(12):2787–2791, 2002.

[117] Hnin Yu Yu Ko, Minoru Mizuhata, Akihiko Kajinami, and Shigehito Deki. Fabrication of high performance thin films from metal fluorocomplex aque-

ous solution by the liquid phase deposition. *Journal of fluorine chemistry*, 120 (2):157–163, 2003.

[118] JJ Diao, FS Qiu, GD Chen, and ME Reeves. Surface vertical deposition for gold nanoparticle film. *Journal of Physics D: Applied Physics*, 36(3):L25, 2003.

[119] Weimin Huang and Jianlin Shi. Synthesis and properties of zro2 films dispersed with au nanoparticles. *Journal of sol-gel science and technology*, 20 (2):145–151, 2001.

[120] Hisao Yanagi and Takayuki Ohno. Nanofabrication of gold particles in glass films by afm-assisted local reduction. *Langmuir*, 15(14):4773–4776, 1999.

[121] Zhong-Ze Gu, Rumiko Horie, Shoichi Kubo, Yasuhiro Yamada, Akira Fujishima, and Osamu Sato. Fabrication of a metal-coated three-dimensionally ordered macroporous film and its application as a refractive index sensor. *Angewandte Chemie International Edition*, 41(7):1153–1156, 2002.

[122] SR Johnson, SD Evans, SW Mahon, and Abraham Ulman. Synthesis and characterisation of surfactant-stabilised gold nanoparticles. *Supramolecular Science*, 4(3-4):329–333, 1997.

[123] Thomas J Krinke, Knut Deppert, Martin H Magnusson, Frank Schmidt, and Heinz Fissan. Microscopic aspects of the deposition of nanoparticles from the gas phase. *Journal of Aerosol Science*, 33(10):1341–1359, 2002.

[124] Wei Chen, Weiping Cai, Liang Zhang, Guozhong Wang, and Lide Zhang. Sonochemical processes and formation of gold nanoparticles within pores of mesoporous silica. *Journal of colloid and interface science*, 238(2):291–295, 2001.

[125] W Chen, WP Cai, CH Liang, and LD Zhang. Synthesis of gold nanoparticles dispersed within pores of mesoporous silica induced by ultrasonic irradi-

ation and its characterization. *Materials research bulletin*, 36(1-2):335–342, 2001.

[126] Jian Wang, Tao Zhu, Jiaqing Song, and Zhongfan Liu. Gold nanoparticulate film bound to silicon surface with self-assembled monolayers. *Thin Solid Films*, 327:591–594, 1998.

[127] Kensuke Akamatsu and Shigehito Deki. Tem investigation and electron diffraction study on dispersion of gold nanoparticles into a nylon 11 thin film during heat treatment. *Journal of colloid and interface science*, 214(2): 353–361, 1999.

[128] P. L. Geissler E. Rabani, D. R. Reichman and L. E. Brus. Drying-mediated self-assembly of nanoparticles. *Nature*, 426:271–274, 2003.

[129] T. P. Bigioni, X.-M. Lin, T. T. Nguyen, E. I. Corwin, T. A. Witten, and H. M. Jager. Kinetically driven self assembly of highly ordered nanoparticlemonolayers. *Nat. Mater.*, 5:265, 2006.

[130] S. Narayanan, J. Wang, and X.-M. Lin. Dynamical self-assembly of nanocrystal superlattices during colloidal droplet evaporation by in-situ small angle x-ray scattering. *Phys. Rev. Lett.*, 93:135503, 2004.

[131] Axel Huerre, Fernando Cacho-Nerin, Vincent Poulichet, Christiana E Udoh, Marco De Corato, and Valeria Garbin. Dynamic organization of ligand-grafted nanoparticles during adsorption and surface compression at fluid–fluid interfaces. *Langmuir*, 34(3):1020–1028, 2017.

[132] S. Liu, R. Maoz, and J. Sagiv. Colloidal gold via self-assembly on hierarchically assembled organic bilayer template patterns with in-situ generated terminal amino functionality. *Nano Lett.*, 4:845–851, 2004.

[133] M. Mukhopadhyay and S. Hazra. Growth of thiol-coated au-nanoparticle langmuir monolayers through a 2d-network of disk-like islands. *RSC Adv.*, 6:12326–12336, 2016.

[134] V. Santhanam, J. Liu, R. Agarwal, and R. P. Andres. Self-assembly of uniform monolayer arrays of nanoparticles. *Langmuir*, 19:7881–7887, 2003.

[135] B. Kim, M. A. Carignano, S. L. Tripp, and A. Wei. Cluster size analysis of two-dimensional order in colloidal gold nanoparticle arrays. *Langmuir*, 20: 9360–9365, 2004.

[136] S. J. Khan, F. Pierce, C. M. Sorensen, and A. Chakrabarti. Self-assembly of ligated gold nanoparticles: Phenomenological modeling and computer simulations. *Langmuir*, 25:13861–13868, 2009.

[137] C. P. Joshi, Y. Shim, T. P. Bigioni, and J. G. Amar. Critical island size, scaling, and ordering in colloidal nanoparticle self-assembly. *Phys. Rev. E*, 90:032406, 2014.

[138] C. B. Murray, C. R. Kagan, and M. G. Bawendi. Synthesis and characterization of monodisperse nanocrystals and close-packed nanocrystal assemblies. *Annual Review of Materials Science*, 30:545–610, 2000.

[139] K. Holmberg, D. O. Shah, and M. J. Schwuger, editors. *Handbook of Applied Surface and Colloid Chemistry*, volume 1. John Wiley & Sons Ltd., 2002.

[140] P. Colson, R. Cloots, and C. Henrist. Experimental design applied to spin coating of 2d colloidal crystal masks: A relevant method? *Langmuir*, 27: 12800–12806, 2011.

[141] T. Ishida, Y. Tachikiri, T. Sako, Y. Takahashi, and S. Yamada. Structural characterization and plasmonic properties of two-dimensional arrays of hydrophobic large gold nanoparticles fabricated by langmuir-blodgett technique. *Appl. Surf. Sci*, 404:350–356, 2017.

[142] Z. Nie, A. Petukhova, and E. Kumacheva. Properties and emerging applications of self-assembled structures made from inorganic nanoparticles. *Nat. Nanotech.*, 5:15, 2010.

[143] Ashavani Kumar, AB Mandale, and Murali Sastry. Sequential electrostatic assembly of amine-derivatized gold and carboxylic acid-derivatized silver colloidal particles on glass substrates. *Langmuir*, 16(17):6921–6926, 2000.

[144] R Banerjee, S Hazra, S Banerjee, and MK Sanyal. Nanopattern formation in self-assembled monolayers of thiol-capped au nanocrystals. *Physical Review E*, 80(5):056204, 2009.

[145] H. F. Okorn-Schmidt. Characterization of silicon surface preparation processes for advanced gate dielectrics. *IBM J. Res. Dev.*, 43:351–366, 1999.

[146] P. Chatterjee and S. Hazra. Time evolution of a Cl-terminated Si surface at ambient conditions. *J. Phys. Chem. C*, 118:11350–11356, 2014.

[147] Raj Kumar Gupta, KA Suresh, and Sandeep Kumar. Monolayer of amphiphilic functionalized gold nanoparticles at an air-water interface. *Physical Review E*, 78(3):032601, 2008.

[148] Karol Vegso, Peter Siffalovic, Eva Majkova, Matej Jergel, Monika Benkovicova, Teodora Kocsis, Martin Weis, Stefan Luby, Kim Nygård, and Oleg Konovalov. Nonequilibrium phases of nanoparticle langmuir films. *Langmuir*, 28(28):10409–10414, 2012.

[149] M. Fukuto, R. K. Heilmann, P. S. Pershan, A. Badia, and R. B. Lennox. Monolayer/bilayer transition in langmuir films of derivatized gold nanoparticles at the gas/water interface: An x-ray scattering study. *J. Chem. Phys.*, 120: 3446–3459, 2004.

[150] David G Schultz, Xiao-Min Lin, Dongxu Li, Jeff Gebhardt, Mati Meron, James Viccaro, and Binhua Lin. Structure, wrinkling, and reversibility of langmuir monolayers of gold nanoparticles. *The Journal of Physical Chemistry B*, 110(48):24522–24529, 2006.

[151] M. K. Bera, M. K. Sanyal, S. Pal, J. Daillant, A. Datta, G. U. Kulkarni, D. Luzet, and O. Konovalov. Reversible buckling in monolayer of gold nanoparticles on water surface. *Europhys. Lett.*, 78:56003, 2007.

[152] Venugopal Santhanam, Jia Liu, Rajan Agarwal, and Ronald P Andres. Self-assembly of uniform monolayer arrays of nanoparticles. *Langmuir*, 19(19): 7881–7887, 2003.

[153] R. Banerjee, S. Hazra, S. Banerjee, and M. K. Sanyal. Nanopattern formation in self-assembled monolayers of thiol-capped au nanocrystals. *Phys. Rev. E*, 80:056204, 2009.

[154] C Vericat, ME Vela, G Benitez, P Carro, and RC Salvarezza. Self-assembled monolayers of thiols and dithiols on gold: new challenges for a well-known system. *Chemical Society Reviews*, 39(5):1805–1834, 2010.

[155] Trevor M Willey, Andrew L Vance, T Van Buuren, C Bostedt, LJ Terminello, and CS Fadley. Rapid degradation of alkanethiol-based self-assembled monolayers on gold in ambient laboratory conditions. *Surface Science*, 576 (1-3):188–196, 2005.

[156] J. K. Bal, S. Kundu, and S. Hazra. Growth and stability of langmuir-blodgett films on oh-, h-, or br-terminated si(001). *Phys. Rev. B*, 81:045404, 2010.

[157] E Yablonovitch, RM Swanson, WD Eades, and BR Weinberger. Electron-hole recombination at the si-sio2 interface. *Applied Physics Letters*, 48(3):245–247, 1986.

[158] E Yablonovitch, DL Allara, CC Chang, T Gmitter, and TB Bright. Unusually low surface-recombination velocity on silicon and germanium surfaces. *Physical review letters*, 57(2):249, 1986.

[159] Mala Mukhopadhyay and S Hazra. Evolution of ligand-capped nanoparticle multilayers toward a near unique thickness. *Soft matter*, 15(8):1869–1878, 2019.

[160] Mala Mukhopadhyay and S Hazra. Interfacial and thermal energy driven growth and evolution of langmuir–schaefer monolayers of au-nanoparticles. *Physical Chemistry Chemical Physics*, 20(2):1051–1062, 2018.

[161] Mala Mukhopadhyay and S Hazra. Growth of thiol-coated au-nanoparticle langmuir monolayers through a 2d-network of disk-like islands. *RSC Advances*, 6(15):12326–12336, 2016.

[162] Xiaoge Gregory Zhang. *Electrochemistry of Silicon and its Oxide*. Springer Science & Business Media, 2007.

[163] Yaping Dan, Kwanyong Seo, Kuniharu Takei, Jhim H Meza, Ali Javey, and Kenneth B Crozier. Dramatic reduction of surface recombination by in situ surface passivation of silicon nanowires. *Nano letters*, 11(6):2527–2532, 2011.

[164] U Mohideen, WS Hobson, SJ Pearton, F Ren, and RE Slusher. Gaas/algaas microdisk lasers. *Applied physics letters*, 64(15):1911–1913, 1994.

[165] Paramita Chatterjee. *Surfactant-mediated growth of mesoporous and nanostructured films*. PhD dissertation, University of Calcutta, 2014.

[166] GW Trucks, Krishnan Raghavachari, GS Higashi, and YJ Chabal. Mechanism of hf etching of silicon surfaces: A theoretical understanding of hydrogen passivation. *Physical Review Letters*, 65(4):504, 1990.

[167] X Zhang, Eric Garfunkel, YJ Chabal, SB Christman, and EE Chaban. Stability of hf-etched si (100) surfaces in oxygen ambient. *Applied physics letters*, 79 (24):4051–4053, 2001.

[168] Frank Schreiber. Self-assembled monolayers: from 'simple'model systems to biofunctionalized interfaces. *Journal of Physics: Condensed Matter*, 16(28): R881, 2004.

[169] Frank Schreiber. Structure and growth of self-assembling monolayers. *Progress in surface science*, 65(5):151–257, 2000.

[170] Touraj Manifar, Asad Rezaee, Mehdi Sheikhzadeh, and Silvia Mittler. Formation of uniform self-assembly monolayers by choosing the right solvent: Ots on silicon wafer, a case study. *Applied Surface Science*, 254(15):4611–4619, 2008.

[171] Anne Kathrena A Aliganga, Zhehui Wang, and Silvia Mittler. Chemical vapor deposition of mercury on alkanedithiolate self-assembled monolayers. *The Journal of Physical Chemistry B*, 108(30):10949–10954, 2004.

[172] Mark J Stevens. Thoughts on the structure of alkylsilane monolayers. *Langmuir*, 15(8):2773–2778, 1999.

[173] Richard D Peters, Paul F Nealey, Jason N Crain, and Franz J Himpsel. A near edge x-ray absorption fine structure spectroscopy investigation of the structure of self-assembled films of octadecyltrichlorosilane. *Langmuir*, 18 (4):1250–1256, 2002.

[174] David L Angst and Gary W Simmons. Moisture absorption characteristics of organosiloxane self-assembled monolayers. *Langmuir*, 7(10):2236–2242, 1991.

[175] Leanne G Britcher, David C Kehoe, Janis G Matisons, Roger SC Smart, and A Geoffrey Swincer. Silicones on glass surfaces. 2. coupling agent analogs. *Langmuir*, 9(7):1609–1613, 1993.

[176] P Fontaine, M Goldmann, and F Rondelez. Influence of headgroup cross-linking on chain packing in langmuir monolayers of n-alkyltrialkoxysilanes. *Langmuir*, 15(4):1348–1352, 1999.

[177] Julio Gun and Jacob Sagiv. On the formation and structure of self-assembling monolayers: Iii. time of formation, solvent retention, and release. *Journal of colloid and interface science*, 112(2):457–472, 1986.

[178] Zhong Lin Wang. Structural analysis of self-assembling nanocrystal superlattices. *Advanced Materials*, 10(1):13–30, 1998.

[179] Krisanu Bandyopadhyay, V Patil, K Vijayamohanan, and Murali Sastry. Adsorption of silver colloidal particles through covalent linkage to self-assembled monolayers. *Langmuir*, 13(20):5244–5248, 1997.

[180] R Griffith Freeman, Katherine C Grabar, Keith J Allison, Robin M Bright, Jennifer A Davis, Andrea P Guthrie, Michael B Hommer, Michael A Jackson, Patrick C Smith, Daniel G Walter, et al. Self-assembled metal colloid monolayers: an approach to sers substrates. *Science*, 267(5204):1629–1632, 1995.

[181] M Giersig and P Mulvaney. Formation of ordered two-dimensional gold colloid lattices by electrophoretic deposition. *The Journal of Physical Chemistry*, 97(24):6334–6336, 1993.

[182] Murali Sastry and KS Mayya. Hetero-colloidal metal particle multilayer films grown using electrostatic interactions at the air–water interface. *Journal of Nanoparticle Research*, 2(2):183–190, 2000.

[183] KS Mayya and Murali Sastry. Electrostatic complexation of carboxylic acid derivatized silver colloidal particles with fatty amine langmuir monolayers. role of neutral spacer molecules in the monolayer. *Langmuir*, 14(1):74–78, 1998.

[184] Vijaya Patil, KS Mayya, SD Pradhan, and Murali Sastry. Evidence for novel interdigitated bilayer formation of fatty acids during three-dimensional self-assembly on silver colloidal particles. *Journal of the American Chemical Society*, 119(39):9281–9282, 1997.

[185] KS Mayya and Murali Sastry. A new technique for the spontaneous growth of colloidal nanoparticle superlattices. *Langmuir*, 15(6):1902–1904, 1999.

[186] Vijaya Patil, RB Malvankar, and Murali Sastry. Role of particle size in individual and competitive diffusion of carboxylic acid derivatized colloidal

gold particles in thermally evaporated fatty amine films. *Langmuir*, 15(23): 8197–8206, 1999.

[187] Murali Sastry, V Patil, and KS Mayya. Incorporation of colloidal metal particles in thermally evaporated fatty amine films via selective electrostatic interactions. *Langmuir*, 13(16):4490–4492, 1997.

[188] Fu-Ken Liu, Yu-Cheng Chang, Fu-Hsiang Ko, Tieh-Chi Chu, and Bau-Tong Dai. Rapid fabrication of high quality self-assembled nanometer gold particles by spin coating method. *Microelectronic Engineering*, 67:702–709, 2003.

[189] M Clemente-Leon, B Agricole, C Mingotaud, CJ Gomez-Garcia, E Coronado, and P Delhaes. Toward new organic/inorganic superlattices: Keggin polyoxometalates in langmuir and langmuir- blodgett films. *Langmuir*, 13 (8):2340–2347, 1997.

[190] Abraham Ulman. *Ultrathin organic films: From Langmuir-Blodgett to self assembly*. Academic Press, 1991.

[191] R Vijayalakshmi, A Dhathathreyan, M Kanthimathi, V Subramanian, Balachandran Unni Nair, and T Ramasami. Penetration of dna into mixed monolayers of 1, 3-bis (salicylideneamino) propanechromium (iii) perchlorate and octadecylamine at an air/water interface. *Langmuir*, 15(8): 2898–2900, 1999.

[192] A Riccio, M Lanzi, F Antolini, C De Nitti, C Tavani, and C Nicolini. Ordered monolayer of cytochrome c via chemical derivatization of its outer arginine. *Langmuir*, 12(6):1545–1549, 1996.

[193] Janos H Fendler and Fiona C Meldrum. The colloid chemical approach to nanostructured materials. *Advanced Materials*, 7(7):607–632, 1995.

[194] Marko Burghard, Günther Philipp, Siegmar Roth, Klaus von Klitzing, Raphael Pugin, and Günter Schmid. Multilayered langmuir–blodgett films

of thiol-substituted ultrasmall gold clusters. *Advanced Materials*, 10(11): 842–845, 1998.

[195] W Li, R Xu, L Wang, H Cui, and S Xi. Mol. cryst. liq. cryst. sci. technol. *Sect. A.*, 337:185, 1999.

[196] Jean-Philippe Bourgoin, Christophe Kergueris, Elisabeth Lefèvre, and Serge Palacin. Langmuir–blodgett films of thiol-capped gold nanoclusters: fabrication and electrical properties. *Thin Solid Films*, 327:515–519, 1998.

[197] Murali Sastry, V Patil, KS Mayya, DV Paranjape, P Singh, and SR Sainkar. Organization of polymer-capped platinum colloidal particles at the air–water interface. *Thin Solid Films*, 324(1-2):239–244, 1998.

[198] Samuel L Kleinman, Renee R Frontiera, Anne-Isabelle Henry, Jon A Dieringer, and Richard P Van Duyne. Creating, characterizing, and controlling chemistry with sers hot spots. *Physical Chemistry Chemical Physics*, 15 (1):21–36, 2013.

[199] Hyunhyub Ko, Srikanth Singamaneni, and Vladimir V Tsukruk. Nanostructured surfaces and assemblies as sers media. *Small*, 4(10):1576–1599, 2008.

[200] Ihor Tokarev and Sergiy Minko. Tunable plasmonic nanostructures from noble metal nanoparticles and stimuli-responsive polymers. *Soft Matter*, 8 (22):5980–5987, 2012.

[201] Marek Grzelczak, Jan Vermant, Eric M. Furst, and Luis M. Liz-Marzán. Directed self-assembly of nanoparticles. *ACS Nano*, 4(7):3591–3605, 2010. doi: 10.1021/nn100869j. URL https://doi.org/10.1021/nn100869j. PMID: 20568710.

[202] Matthew N Martin, James I Basham, Paul Chando, and Sang-Kee Eah. Charged gold nanoparticles in non-polar solvents: 10-min synthesis and 2d self-assembly. *Langmuir*, 26(10):7410–7417, 2010.

[203] Shouheng Sun, Christopher B Murray, Dieter Weller, Liesl Folks, and Andreas Moser. Monodisperse fept nanoparticles and ferromagnetic fept nanocrystal superlattices. *science*, 287(5460):1989–1992, 2000.

[204] Jongnam Park, Kwangjin An, Yosun Hwang, Je-Geun Park, Han-Jin Noh, Jae-Young Kim, Jae-Hoon Park, Nong-Moon Hwang, and Taeghwan Hyeon. Ultra-large-scale syntheses of monodisperse nanocrystals. *Nature materials*, 3(12):891, 2004.

[205] Dmitri V Talapin, Elena V Shevchenko, Maryna I Bodnarchuk, Xingchen Ye, Jun Chen, and Christopher B Murray. Quasicrystalline order in self-assembled binary nanoparticle superlattices. *Nature*, 461(7266):964, 2009.

[206] Michael C Petty. *Langmuir-Blodgett films: an introduction*. Cambridge University Press, 1996.

[207] A-L Barabási and Harry Eugene Stanley. *Fractal concepts in surface growth*. Cambridge university press, 1995.

[208] Jacob N Israelachvili. *Intermolecular and surface forces*. Academic press, 2015.

[209] Brian A Korgel and Donald Fitzmaurice. Condensation of ordered nanocrystal thin films. *Physical review letters*, 80(16):3531, 1998.

[210] Mathieu Maillard, L Motte, AT Ngo, and MP Pileni. Rings and hexagons made of nanocrystals: A marangoni effect. *The Journal of Physical Chemistry B*, 104(50):11871–11877, 2000.

[211] C. P. Martin, M. O. Blunt, and P. Moriarty. Nanoparticle networks on silicon: Self-organized or disorganized? *Nano Lett.*, 4:2389, 2004.

[212] Stephan Herminghaus, Karin Jacobs, Klaus Mecke, Jörg Bischof, Andreas Fery, Mohammed Ibn-Elhaj, and Stefan Schlagowski. Spinodal dewetting in liquid crystal and liquid metal films. *Science*, 282(5390):916–919, 1998.

[213] Andrew Stannard, Christopher P Martin, Emmanuelle Pauliac-Vaujour, Philip Moriarty, and Uwe Thiele. Dual-scale pattern formation in nanoparticle assemblies. *The Journal of Physical Chemistry C*, 112(39):15195–15203, 2008.

[214] Kevin S Schneider, Wei Lu, Thomas M Owens, Daniel R Fosnacht, MM Banaszak Holl, and BG Orr. Monolayer pattern evolution via substrate strain-mediated spinodal decomposition. *Physical review letters*, 93(16):166104, 2004.

[215] F áL Leibowitz et al. Size and shape evolution of core–shell nanocrystals. *Chemical Communications*, (13):1211–1212, 1999.

[216] Ronald P Andres, Jeffery D Bielefeld, Jason I Henderson, David B Janes, Venkat R Kolagunta, Clifford P Kubiak, William J Mahoney, and Richard G Osifchin. Self-assembly of a two-dimensional superlattice of molecularly linked metal clusters. *Science*, 273(5282):1690–1693, 1996.

[217] Mathew M Maye, Wenxia Zheng, Frank L Leibowitz, Nam K Ly, and Chuan-Jian Zhong. Heating-induced evolution of thiolate-encapsulated gold nanoparticles: a strategy for size and shape manipulations. *Langmuir*, 16(2):490–497, 2000.

[218] T Pradeep, S Mitra, A Sreekumaran Nair, and R Mukhopadhyay. Dynamics of alkyl chains in monolayer-protected au and ag clusters and silver thiolates: A comprehensive quasielastic neutron scattering investigation. *The Journal of Physical Chemistry B*, 108(22):7012–7020, 2004.

[219] A Gibaud, N Cowlam, G Vignaud, and T Richardson. Evidence of self-affine rough interfaces in a langmuir-blodgett film from x-ray reflectometry. *Physical review letters*, 74(16):3205, 1995.

[220] J. Daillant and A. Gibaud, editors. *X-Ray and Neutron Reflectivity: Principles and Applications*. Springer, Paris, 1999.

[221] Metin Tolan. *X-ray scattering from soft-matter thin films*. Springer, 1999.

[222] M Delheusy, A Stierle, N Kasper, RP Kurta, A Vlad, H Dosch, C Antoine, Andrea Resta, Edvin Lundgren, and J Andersen. X-ray investigation of subsurface interstitial oxygen at nb/oxide interfaces. *Applied Physics Letters*, 92(10):101911, 2008.

[223] Brent Fultz and James M Howe. *Transmission electron microscopy and diffractometry of materials*. Springer Science & Business Media, 2012.

[224] Debbie Stokes. *Principles and practice of variable pressure/environmental scanning electron microscopy (VP-ESEM)*. John Wiley & Sons, 2008.

[225] Xiu-Hong Li, Ming Li, and Zhen-Hong Mai. Kinetic roughening of the interfaces of langmuir-blodgett films. *Physical Review B*, 69(23):235407, 2004.

[226] Ryan Muszynski, Brian Seger, and Prashant V Kamat. Decorating graphene sheets with gold nanoparticles. *The Journal of Physical Chemistry C*, 112(14): 5263–5266, 2008.

[227] Roland Wiesendanger. *Scanning probe microscopy and spectroscopy: methods and applications,*. Cambridge University Press, Cambridge, 1994.

[228] C Julian Chen. *Introduction to scanning tunneling microscopy*, volume 2. Oxford University Press New York, 1993.

[229] Lyman G Parratt. Surface studies of solids by total reflection of x-rays. *Physical review*, 95(2):359, 1954.

[230] Alain Gibaud. *Specular reflectivity from smooth and rough surfaces*. Springer, 1999.

[231] Paramita Chatterjee and Satyajit Hazra. Time evolution of a cl-terminated si surface at ambient conditions. *The Journal of Physical Chemistry C*, 118(21): 11350–11356, 2014.

[232] W Kern and DA Puotinen. Rca cleaning. *RCA-Review*, pages 187–190, 1970.

[233] Harald F Okorn-Schmidt. Characterization of silicon surface preparation processes for advanced gate dielectrics. *ibm Journal of Research and Development*, 43(3):351–326, 1999.

[234] SA Mirji. Octadecyltrichlorosilane adsorption kinetics on si (100)/sio2 surface: contact angle, afm, ftir and xps analysis. *Surface and Interface Analysis: An International Journal devoted to the development and application of techniques for the analysis of surfaces, interfaces and thin films*, 38(3):158–165, 2006.

[235] Yongan Yang, Alexander M Bittner, Steve Baldelli, and Klaus Kern. Study of self-assembled triethoxysilane thin films made by casting neat reagents in ambient atmosphere. *Thin Solid Films*, 516(12):3948–3956, 2008.

[236] John Turkevich, Peter Cooper Stevenson, and James Hillier. A study of the nucleation and growth processes in the synthesis of colloidal gold. *Discussions of the Faraday Society*, 11:55–75, 1951.

[237] Günter Schmid, Reinhard Pfeil, Roland Boese, Friedhelm Bandermann, Sonja Meyer, Gijs Calis, Jan WA van der Velden, et al. Au55 [p (c6h5) 3] 12ci6-ein goldcluster ungewöhnlicher größe. *Chemische Berichte*, 114(11): 3634–3642, 1981.

[238] Mathias Brust, Merryl Walker, Donald Bethell, David J Schiffrin, and Robin Whyman. Synthesis of thiol-derivatised gold nanoparticles in a two-phase liquid–liquid system, 1994.

[239] WP Halperin. Quantum size effects in metal particles. *Reviews of Modern Physics*, 58(3):533, 1986.

[240] A. M. Fox. Optical properties of solids, 2003.

[241] Johannes Antonius Albertus Joseph Perenboom, Peter Wyder, and Felix Meier. Electronic properties of small metallic particles. *Physics Reports*, 78 (2):173–292, 1981.

[242] K Lance Kelly, Eduardo Coronado, Lin Lin Zhao, and George C Schatz. The optical properties of metal nanoparticles: the influence of size, shape, and dielectric environment, 2003.

[243] JJ Mock, M Barbic, DR Smith, DA Schultz, and S Schultz. Shape effects in plasmon resonance of individual colloidal silver nanoparticles. *The Journal of Chemical Physics*, 116(15):6755–6759, 2002.

[244] Philip Moriarty. Nanostructured materials. *Reports on Progress in Physics*, 64(3):297, 2001.

[245] Christopher A Palmer and Erwin G Loewen. *Diffraction grating handbook*. Newport Corporation New York, 2005.

[246] www.chemguide.co.uk. Uv-visible spectroscopy, 2019. URL https://www.chemguide.co.uk/analysis/uvvisible/spectrometer.gif. [Online; accessed June 3, 2019].

[247] Helmut Kohl and Ludwig Reimer. *Transmission Electron Microscopy: Physics of Image Formation*. Springer-Verlag New York, 2008.

[248] Goerg H Michler. High-impact rubber-modified polymers. *Electron Microscopy of Polymers*, pages 351–371, 2008.

[249] Jinfeng Yang, Yoichi Yoshida, and Hidehiro Yasuda. Ultrafast electron microscopy with relativistic femtosecond electron pulses. *Microscopy*, 67(5): 291–295, 2018.

[250] Irving Langmuir. The constitution and fundamental properties of solids and liquids. ii. liquids. 1. *Journal of the American Chemical Society*, 39(9): 1848–1906, 1917.

[251] Katharine B Blodgett. Films built by depositing successive monomolecular layers on a solid surface. *Journal of the American Chemical Society*, 57(6): 1007–1022, 1935.

[252] Katharine B Blodgett and Irving Langmuir. Built-up films of barium stearate and their optical properties. *Physical Review*, 51(11):964, 1937.

[253] Daniel K Schwartz. Langmuir-blodgett film structure. *Surface Science Reports*, 27(7):245–334, 1997.

[254] I. Langmuir and V. J. Schaefer. Activities of urease and pepsin monolayers. *J. Am. Chem. Soc.*, 60:1351–1360, 1938.

[255] Peter J Goodhew, John Humphreys, and Richard Beanland. *Electron microscopy and analysis*. CRC Press, 2014.

[256] www.eng atoms.msm.cam.ac.uk. Scanning electron microscopy, 2019. URL https://www.eng-atoms.msm.cam.ac.uk/Images/SEMScheme. [Online; accessed June 3, 2019].

[257] Gerd Binnig, Heinrich Rohrer, Ch Gerber, and Edmund Weibel. Surface studies by scanning tunneling microscopy. *Physical review letters*, 49(1):57, 1982.

[258] Agilent Technologies. *Agilent Technologies 5500 Scanning Probe Microscope User's Guide*. Agilent Technologies, September 2008.

[259] I Horcas, Rs Fernández, JM Gomez-Rodriguez, JWSX Colchero, JWSXM Gómez-Herrero, and AM Baro. Wsxm: a software for scanning probe microscopy and a tool for nanotechnology. *Review of scientific instruments*, 78(1):013705, 2007.

[260] Yiping Zhao, Gwo-Ching Wang, and Toh-Ming Lu. *Characterization of Amorphous and Crystalline Rough Surface–Principles and Applications*, volume 37. Elsevier, 2000.

[261] Ph Dumas, B Bouffakhreddine, Claude Amra, O Vatel, E Andre, R Galindo, and F Salvan. Quantitative microroughness analysis down to the nanometer scale. *EPL (Europhysics Letters)*, 22(9):717, 1993.

[262] Angela Duparre, Josep Ferre-Borrull, Stefan Gliech, Gunther Notni, Jörg Steinert, and Jean M Bennett. Surface characterization techniques for determining the root-mean-square roughness and power spectral densities of optical components. *Applied optics*, 41(1):154–171, 2002.

[263] Wilhelm Conrad Röntgen. On a new kind of rays. *Science*, pages 227–231, 1896.

[264] David Attwood and Anne Sakdinawat. *X-rays and extreme ultraviolet radiation: principles and applications*. Cambridge university press, 2017.

[265] Jean Daillant and Alain Gibaud. *X-ray and neutron reflectivity: principles and applications*, volume 770. Springer, 2008.

[266] M Born and E Wolf. Principles of optics, reprinted, 1993.

[267] Jens Als-Nielsen and Des McMorrow. *Elements of modern X-ray physics*. John Wiley & Sons, 2011.

[268] David J Griffiths and R Colleger. Introduction to electrodynamics, prentice hall upper saddle river. *New Jersey*, 7458, 1999.

[269] John David Jackson. Classical electrodynamics, 1999.

[270] Heinz Kiessig. Interferenz von röntgenstrahlen an dünnen schichten. *Annalen der Physik*, 402(7):769–788, 1931.

[271] M Piecuch and L Nevot. X-ray and neutron characterization of multilayer systems. In *Materials Science Forum*, volume 59, pages 93–140. Trans Tech Publ, 1990.

[272] JK Basu and Milan K Sanyal. Ordering and growth of langmuir–blodgett films: X-ray scattering studies. *Physics reports*, 363(1):1–84, 2002.

[273] S. K. Sinha, E. B. Sirota, S. Garoff, and H. B. Stanley. X-ray and neutron scattering from rough surfaces. *Phys. Rev. B*, 38:2297–2311, Aug 1988. doi: 10.1103/PhysRevB.38.2297. URL https://link.aps.org/doi/10.1103/PhysRevB.38.2297.

[274] JK Basu and MK Sanyal. Capillary waves in langmuir-blodgett interfaces and formation of confined cds layers. *Physical review letters*, 79(23):4617, 1997.

[275] MK Sanyal. X-ray scattering studies of surfaces and interfaces. *Radiation Physics and Chemistry*, 51(4-6):487–495, 1998.

[276] George H Vineyard. Grazing-incidence diffraction and the distorted-wave approximation for the study of surfaces. *Physical Review B*, 26(8):4146, 1982.

[277] Gilles Renaud, Rémi Lazzari, and Frédéric Leroy. Probing surface and interface morphology with grazing incidence small angle x-ray scattering. *Surface Science Reports*, 64(8):255–380, 2009.

[278] Jan Skov Pedersen. Determination of size distribution from small-angle scattering data for systems with effective hard-sphere interactions. *Journal of applied crystallography*, 27(4):595–608, 1994.

[279] C Braun. Parratt32-the reflectivity tool. *HMI Berlin*, 99, 1997.

[280] Julian Schwinger. On the classical radiation of accelerated electrons. *Physical review*, 75(12):1912, 1949.

[281] G. Margeritondo. *Introduction to Synchrotron Radiation Research*. Oxford University Press,Oxford, 1988.

[282] SV Roth, H Walter, M Burghammer, C Riekel, B Lengeler, C Schroer, M Kuhlmann, T Walther, A Sehrbrock, R Domnick, et al. Combinatorial

investigation of the isolated nanoparticle to coalescent layer transition in a gradient sputtered gold nanoparticle layer on top of polystyrene. *Applied physics letters*, 88(2):021910, 2006.

[283] CG Schroer, M Kuhlmann, SV Roth, R Gehrke, N Stribeck, A Almendarez-Camarillo, and B Lengeler. Mapping the local nanostructure inside a specimen by tomographic small-angle x-ray scattering. *Applied physics letters*, 88(16):164102, 2006.

[284] SV Roth, T Autenrieth, G Grübel, C Riekel, M Burghammer, R Hengstler, L Schulz, and P Müller-Buschbaum. In situ observation of nanoparticle ordering at the air-water-substrate boundary in colloidal solutions using x-ray nanobeams. *Applied Physics Letters*, 91(9):091915, 2007.

[285] W. P. Halperin. Quantum size effects in metal particles. *Rev. Mod. Phys.*, 58: 533–606, 1986.

[286] C. P. Collier, R. J. Saykally, J. J. Shiang, S. E. Henrichs, and J. R. Health. Reversible tuning of silver quantum dot monolayers through the metal-insulator transition. *Nano Lett.*, 277:1978, 1997.

[287] G. Schmid, editor. *Clusters and Colloids: From Theory to Applications*. John Wiley & Sons, 2008.

[288] J. F. Galisteo-López, M. Ibisate, R. Sapienza, L. S. Froufe-Pérez, A. Blanco, and C. López. Self-assembled photonic structures. *Adv. Mater.*, 23:30–69, 2011.

[289] K. Holmberg, D. O. Shah, and M. J. Schwuger, editors. *Handbook of Applied Surface and Colloid Chemistry*, volume 1. John Wiley & Sons Ltd., 2002.

[290] P. Du, M. Li, K. Douki, X. Li, C.-B.-W. Garcia, A. Jain, D.-M. Smilgies, L.-J. Fetters, S.-M. Gruner, U. Wiesner, and C.-K. Ober. Additive-driven phase-selective chemistry in block copolymer thin films: The convergence of top-down and bottom-up approaches. *Adv. Mater.*, 16:953–957, 2004.

[291] R. Lazzari, F. Leroy, and G. Renaud. Grazing-incidence small-angle x-ray scattering from dense packing of islands on surfaces: Development of distorted wave born approximation and correlation between particle sizes and spacing. *Phys. Rev. B*, 76:125411, 2007.

[292] S. V. Roth, G. Herzog, V. Körstgens, A. Buffet, M. Schwartzkopf, J. Perlich, M. M. Abul Kashem, R. Döhrmann, R. Gehrke, A. Rothkirch, K. Stassig, W. Wurth, G. Benecke, C. Li, P. Fratzl, M. Rawolle, and P. Müller-Buschbaum. In-situ observation of cluster formation during nanoparticle solution casting on a colloidal film. *J. Phys: Condens. Matter*, 23:254208, 2011.

[293] I. Horcas, R. Fernández, J. M. Gómez-Rodriguez, J. Colchero, J. Gómez-Herrero, and A. M. Baro. Wsxm: A software for scanning probe microscopy and a tool for nanotechnology. *Rev. Sci. Instrum.*, 78:013705, 2007.

[294] L. G. Parratt. Surface studies of solids by total reflection of X-rays. *Phys. Rev.*, 95:359–369, 1954.

[295] I. Roy and S. Hazra. Solvent dependent ordering of poly(3-dodecylthiophene) in thin films. *Soft Matter*, 11:3724–3732, 2015.

[296] M. Maaza, A. Gibaud, C. Sella, B. Pardo, F. Dunsteter, J. Corno, F. Bridou, G. Vignaud, A. Desert, and A. Menelle. X-ray scattering by nano-particles within granular thin films, investigation by grazing angle X-ray reflectometry. *Eur. Phys. J. B*, 7, 1999.

[297] S. Hazra, A. Gibaud, and C. Sella. Role of ceramic matrix and Au fraction on the morphology and optical properties of cosputtered Au-ceramic thin films. *J. Appl. Phys.*, 101:113532, 2007.

[298] J. Merle Elson and J. M. Bennett. Calculation of the power spectral density from surface profile data. *Appl. Opt.*, 34:1, 1995.

[299] S. J. Fang, S. Haplepete, W. Chen, C. R. Helms, and H. Edwards. Analyzing atomic force microscopy images using spectral methods. *J. Appl. Phys.*, 82: 5891, 1997.

[300] G. Schmid, editor. *Clusters and Colloids: From Theory to Applications*. John Wiley & Sons, 2008.

[301] S. Srivastava, D. Nykypanchuk, M. Fukuto, and O. Gang. Tunable nanoparticle arrays at charged interfaces. *ACS Nano*, 8:9857–9866, 2014.

[302] Y. Min, M. Akbulut, K. Kristiansen, Y. Golan, and J. Israelachvili. The role of interparticle and external forces in nanoparticle assembly. *Nat. Mater.*, 7: 527, 2008.

[303] I. K. Robinson and D. J. Tweet. Surface x-ray diffraction. *Rep. Prog. Phys.*, 55:599, 1992.

[304] S. Hazra, A. Gibaud, A. Désert, V. Gacem, and N. Cowlam. X-ray scattering studies of imperfect manganese stearate langmuir-blodgett films. *Physica B*, 283:45–48, 2000.

[305] H. C. Hamaker. The london-van der waals attraction between spherical particles. *Physica*, 4:1058–1072, 1937.

[306] D. G. Schultz, X.-M. Lin, D. Li, J. Gebhardt, M. Meron, P. James Viccaro, and B. Lin. Structure, wrinkling, and reversibility of langmuir monolayers of gold nanoparticles. *J. Phys. Chem. B*, 110:24522–24529, 2006.

[307] P. C. Ohara, D. V. Leff, J. R. Heath, and W. M. Gelbart. Crystallization of opals from polydisperse nanoparticles. *Phys. Rev. Lett.*, 75:3466–3469, 1995.

[308] G. J. Kluth, M. M. Sung, and R. Maboudian. Thermal behavior of alkylsiloxane self-assembled monolayers on the oxidized si(100) surface. *Langmuir*, 13:3775–3780, 1997.

[309] S. A. Mirji. Octadecyltrichlorosilane adsorption kinetics on si(100)/sio_2 surface: Contact angle, afm, ftir and xps analysis. *Surf. Interface Anal.*, 38: 158–165, 2006.

[310] J. K. Bal, S. Kundu, and S. Hazra. Hydrophobic to hydrophilic transition of hf-treated si surface during langmuir-blodgett film deposition. *Chem. Phys. Lett.*, 500:90–95, 2010.

[311] J. Drelich, E. Chibowski, D. D. Meng, and K. Terpilowski. Hydrophilic and superhydrophilic surfaces and materials. *Soft Matter*, 7:9804–9828, 2011.

[312] Jin Luo, Vivian W Jones, Li Han, Mathew M Maye, Nancy N Kariuki, and Chuan-Jian Zhong. Afm probing of thermal activation of molecularly linked nanoparticle assembly. *The Journal of Physical Chemistry B*, 108(28): 9669–9677, 2004.

[313] Nigel M Kirby, Stephen T Mudie, Adrian M Hawley, David J Cookson, Haydyn DT Mertens, Nathan Cowieson, and Vesna Samardzic-Boban. A low-background-intensity focusing small-angle x-ray scattering undulator beamline. *Journal of Applied Crystallography*, 46(6):1670–1680, 2013.

[314] G David and J Pérez. Combined sampler robot and high-performance liquid chromatography: a fully automated system for biological small-angle x-ray scattering experiments at the synchrotron soleil swing beamline. *Journal of applied crystallography*, 42(5):892–900, 2009.

[315] P Pernot, P Theveneau, T Giraud, R Nogueira Fernandes, D Nurizzo, D Spruce, J Surr, S McSweeney, A Round, F Felisaz, et al. New beamline dedicated to solution scattering from biological macromolecules at the esrf. In *Journal of Physics: Conference Series*, volume 247, page 012009. IOP Publishing, 2010.

[316] Jesse B Hopkins and Robert E Thorne. Quantifying radiation damage in biomolecular small-angle x-ray scattering. *Journal of applied crystallography*, 49(3):880–890, 2016.

[317] Nicholas Jon Hardy, Marcus D Hanwell, and Tim H Richardson. Temperature effects on the electrical conductivity of thiol encapsulated gold nanoparticle thin films. *Journal of Materials Science: Materials in Electronics*, 18(9):943–949, 2007.

[318] NJ Hardy and TH Richardson. Temperature effects on the optical properties of thiol encapsulated gold nanoparticle thin films. *Colloids and Surfaces A: Physicochemical and Engineering Aspects*, 321(1-3):285–291, 2008.

[319] Yu Chen, Richard E Palmer, and Jess P Wilcoxon. Sintering of passivated gold nanoparticles under the electron beam. *Langmuir*, 22(6):2851–2855, 2006.

[320] Mathew M Maye, WX Zheng, FL Leibowitz, NK Ly, HH Eichelberger, and CJ Zhong. An ivestigation of temperature-manipulated size and shape evolution of preformed core-shell nanoparticles. *MRS Online Proceedings Library Archive*, 580, 1999.

[321] Jiadao Wang, Shuai Chen, Kai Cui, Dangguo Li, and Darong Chen. Approach and coalescence of gold nanoparticles driven by surface thermodynamic fluctuations and atomic interaction forces. *ACS nano*, 10:2893–2902, 2016.

[322] SookYoung Moon, Shun-ichiro Tanaka, and Tohru Sekino. Crystal growth of thiol-stabilized gold nanoparticles by heat-induced coalescence. *Nanoscale research letters*, 5(5):813, 2010.

[323] A Courty, A-I Henry, N Goubet, and M-P Pileni. Large triangular single crystals formed by mild annealing of self-organized silver nanocrystals. *Nature materials*, 6(11):900, 2007.

[324] Calvin H Bartholomew. Mechanisms of catalyst deactivation. *Applied Catalysis A: General*, 212(1-2):17–60, 2001.

[325] Laurent J Lewis, Pablo Jensen, and Jean-Louis Barrat. Melting, freezing, and coalescence of gold nanoclusters. *Physical Review B*, 56(4):2248, 1997.

[326] Martin S Kunz, Kenneth R Shull, and Andrew J Kellock. Morphologies of discontinuous gold films on amorphous polymer substrates. *Journal of applied physics*, 72(9):4458–4460, 1992.

[327] Suresh Narayanan, Dong Ryeol Lee, Rodney S Guico, Sunil K Sinha, and Jin Wang. Real-time evolution of the distribution of nanoparticles in an ultrathin-polymer-film-based waveguide. *Physical review letters*, 94(14): 145504, 2005.

[328] LA Baker, AR Laracuente, and LJ Whitman. Hydrogen termination following cu deposition on si (001). *Physical Review B*, 71(15):153302, 2005.